DEFORMATION AND ULTIMATE LOAD OF REINFORCED SOIL STRUCTURES, Theory and Experiment

GYANESWOR POKHAREL

DEFORMATION AND ULTIMATE LOAD OF REINFORCED SOIL STRUCTURES, Theory and Experiment

A dissertation submitted in partial fulfillment of the requirements for the Degree of Doctor of Engineering

GYANESWOR POKHAREL

Civil Engineering Special Program
DEPARTMENT OF CIVIL ENGINEERING
NAGOYA UNIVERSITY
JAPAN

MARCH 1995

ABSTRACT

The mechanism and behavior of reinforced soils are studied under both the initial loading and the limit equilibrium state of the soil mass. A new concept of computation of the initial load-settlement relation, bearing capacity/safety factor, distribution of axial and shear (or bending) forces in the reinforcement, velocity vectors and stress distribution in reinforced soil structures is presented.

Brief literature review of the existing philosophies on the reinforced soil systems, the concept and the applications is carried out. Need for a new simplified and realistic tool for the analysis and design of reinforced soil structures has been derived based on the deficiency observed in the existing analysis and design tools and the over-conservatism in their performances.

A new formulation of the mechanism of reinforcing a soil mass is presented. The reinforced effect is coupled in the conventional rigid plastic finite element method (RPFEM) by introducing a set of linear constraint conditions of "*no length change*" and "*no-bending*" upon plastic flow of the soil element nodes corresponding to the reinforcement at limit equilibrium state of soil mass. These constraint conditions are shown to be equally applicable in formulating the reinforced effect at the initial loading state of soil mass by coupling it with the conventional linear elastic finite element method (LEFEM).

These two new linear constraint conditions are subsequently incorporated in two energy functions: stored energy function for the linear elastic problems and the plastic energy dissipation function for the limit state problems. The corresponding Lagrange multipliers are shown to be representing the axial force and the shear force (/bending moment) in the reinforcing material per unit length, respectively.

Behaviors of reinforced soil structures under both the initial loading state and at the limit state of reinforced soil mass are investigated employing the proposed concept. The proposed methodology is tested numerically in a bearing capacity problem with strip footing loading, and in slope stability and excavation problems under gravity loading. Later, applicability of the proposed numerical method is examined through analyzing the results of a series of medium scale 1g model tests of the reinforced soil slopes. Using these observations on the real model tests, advantages and limitations of the proposed method are assessed.

Effect of the soil reinforcement is shown through the improvements in the load-deformation relations, bearing capacity values, the reinforcement axial force, stress distribution and displacement/ or velocity fields in the soil mass. The effect of facing rigidity on the soil is explained through the bending moments developed in the facing.

The computed factor of safety shows that the reinforcement is more effective in frictional (c-ϕ) material than in purely cohesive clay. The reinforcement in the frictional (c-ϕ) material acts like an anchor while in the purely cohesive clay the bar does not show such kind of effects. The axial force in the reinforcement is treated as an internal stress that develops because of the soil-reinforcement interaction and cannot be controlled from outside the soil system.

Substantial improvement in the response of the soil structure due to the soil reinforcement is demonstrated through the model test results and then, supported by the numerical simulation results obtained by employing the proposed numerical method.

Through numerical investigations of the excavation problems, a new concept on the positioning of vertical reinforcements has been recommended depending on the reinforcement types, axial or bending member.

Overall, conclusion is that the proposed methodology offers promising features and wide applicability for the analysis and design of complex reinforced soil structures. The results presented through this study provide enough confidence to the practicing engineers to adopt the methodology in the practice.

ACKNOWLEDGMENTS

At the outset, the author expresses his deepest gratitude to *Professor Minoru Matsuo* who as a Dean of School of Engineering admitted in his laboratory as a Doctoral Student. Prof. Matsuo's valuable suggestions and gesture of helps in various affairs concerning research as well as private matters are also gratefully acknowledged. It was a matter of great pleasure to have him as a committee member.

The author takes this great opportunity to express his profound gratitude to his academic advisor *Professor Akira Asaoka* for his superlative flow of ideas and guidance as well as moving inspirations all throughout the period of this research. It was a matter of great pleasure to sail through several turbulent phases of this work with him. He is a great sailor, indeed.

The author owes a lot to *Dr. T. Kyoya*, Associate Professor for his kind gesture in serving as a committee member and for his very detailed comments for amendment and improvements of the first draft of this thesis.

Author is really grateful to *Dr. Satoru Ohtsuka*, Assoc. Professor for his nice gesture of helps especially in the first few months of stay in Japan and continuing encouragement.

Dr. Takeshi Kodaka, a senior doctoral student during first year of this study and later as research associate in the same laboratory, is a very special person to be acknowledged here. He is the one who in-spite-of his busy periods helped to understand various secrets of the research techniques in this laboratory. His kind help during the experimental model tests is greatly appreciated.

The author fondly acknowledges the inspiring efforts of *Dr. Y. Suzuki, Dr. M. Sugai, Dr. M. Nakano* and *Dr. T. Noda* for their wonderful ideas and personal helps those proved helpful in completing this work. Additionally *Mr. T. Miyagawa* and *Mr. Moritomo*, masters students who helped in conducting the experimental model tests and in the numerical computations without their help the research report wouldn't look as it is now. Author is also grateful to Masters students: *Mr. S. Baba*, *Mr. Onishi* and *Mr. Y. Kato* for their assistance in preparing some of the figures.

Mr. T. Ochiai and *Mr. T. Katoh*, Yahagi Corporation who provided model testing facility and the instruments as well as sponsored financially to make the experiment successful, are sincerely appreciated and very many thanks to *Mr. Kodama* for his help throughout model testing period.

A sincere thanks is also due for the Monbusho Scholarship Program, Ministry of Education and Culture, Japanese Government for providing the scholarship that made it possible for this author to spend a most gratifying period of study in Nagoya university.

A special thanks extends to *Mr. M. Nozu* and *Mr. G.S.K. Fernando*, fellow doctoral students for their wonderful ideas and thought-provoking remarks those proved to be instrumental in wrapping up the thesis and other private communications in the laboratory. The author appreciates *Mr. H Hazarika*, a fellow doctoral student for his sincere help in proof reading the manuscript. Nonetheless, very many masters and bachelor students in this laboratory who helped directly or indirectly are gratefully acknowledged.

A special note of sincere appreciation also extends to *Dr. Yusuke Honjo*, *Professor Yudhbir* and *Professor A.S. Balasubramaniam* for their continuing inspirations. Sincere appreciation goes to all those who helped in numerous ways in succeeding this piece of research work.

A very special debt of deep gratitude is offered to author's parents and parents-in-law for their unceasing sacrifices, endeavors and encouragement.

Finally, thanks are due to wife *Ila*, son *Asit* and daughter *Anu* for their forbearance and affection althroughout the research period. This piece of work is dedicated to them.

Gyaneswor Pokharel

March 27, 1995 Nagoya University, Japan

TABLE OF CONTENTS

CHAPTER **TITLE** **PAGE**

CHAPTER **TITLE** **PAGE**

CHAPTER **TITLE** **PAGE**

CHAPTER 1 INTRODUCTION

1.1 GENERAL

The past three decades have shown great achievements in the advancement of reinforced soil system using stiff metal to flexible/extensible geosynthetic materials as reinforcing elements. Many reinforced soil structures have been performing well and are considered safe and convenient in construction. Parallel to the advancement in the construction technology, in these years a lot of efforts has been devoted to find a suitable method/procedure for the analysis and design (e.g. Vidal, 1966; Schlosser and Long, 1972; Haussman, 1976; Chapius, 1978; Yang, 1972; ASCE, 1978; Jarret et al., 1987), Tatsuoka, 1992; Yamanouchi et al., 1978; Ochiai, 1992). Many assumptions have been postulated and many solution procedures have been proposed about the mechanism of different components comprising these systems (e.g. reinforcement force, soil-reinforcement-facing interaction) and the mechanism is still not well understood. The commonly accepted analysis and design method is still lagging.

In the analysis of most soil engineering problems, specially reinforced soil structure, stability and deformation are considered both critical and independent but they are always dealt separately. In this dissertation, these two aspects of the behavior of reinforced soil structures are studied introducing some mechanisms to model the facing, reinforcement and soil interactions. The mechanism of axial force development in the reinforcement is also newly proposed. The length along reinforcing element is assumed to be constant by imposing a constrained condition of no-length change. Similarly, the flexural (bending i.e. shear force) rigidity is modeled by imposing additional constrained condition of "*no-angle change*". Further, the difference between soil anchors and soil reinforcement is distinguished through the axial/shear forces developed along the soil reinforcement and soil anchors. In the former, the axial force can be controlled externally (out

side the soil/anchor system) while in the latter (i.e. soil reinforcement) case, the axial force is not externally controllable, rather develops internally due to soil-reinforcement interaction depending on the confining pressure. In this context, the conventional methods of the reinforced soil structures that require the tensile force distribution along reinforcements be prescribed, as an initial condition cannot be accepted, at least, from the theoretical point of view.

Thus, the deformation behavior of reinforced soil structure under a initial loading stage is studied by introducing these newly proposed mechanisms in the linear elastic finite element method (LEFEM). LEFEM is used as a numerical tool in all deformation analyses. The proposed numerical method is demonstrated through some typical soil engineering deformation problems and the results reveal that the reinforcement is much effective in reducing the lateral deformation in addition to vertical settlements of reinforced soil mass.

Similarly, a detailed investigation of the behaviors of reinforced soil structures at limiting equilibrium state is attempted to examine how plastic velocities and axial/shear force develop in the reinforcement. Such an investigation is also extended to excavation problems where axial/shear forces are obtained. Rigid Plastic Finite Element Method (RPFEM) is used throughout this research as a numerical tool in the study of stability problems. Thus, these illustrations will offer the practicability of the proposed mechanism in the design and analysis of the reinforced soil structure considering both serviceability and stability aspects.

A series of medium sized 1g model tests were carried out to verify the methodology in addition to the ideal foundation, excavation, slope stability problems. Steep and mild slope surfaces were unreinforced, reinforced and reinforcement connected with flexible and rigid facing panels were tested. The steep slope was tested under long reinforcements in addition to the reinforcement lengths equal to footing width. The tests clearly shows the effectiveness of reinforcements and use of facing panels shows more effectiveness in the distribution of reinforcement force, prevention of local failures near slope faces and reduction in vertical and horizontal deformations. It is shown by numerical simulations that the proposed mechanism and numerical procedure work well in such real data in addition to the aforesaid typical ideal soil engineering problems.

Through applications of the proposed methodology to some typical ideal example problems and model test simulations, the general tendency of solutions provides information/confidence enough for practicing engineers in order to make up their engineering judgment whether the method is applicable to daily design works or not.

1.2 SCOPES AND OBJECTIVES OF STUDY

An attempt is made to formulate a set of mechanism of reinforced soil mass from initial loading to the limiting equilibrium state. The RPFEM and LEFEM are used as general framework in this study because these methods appeal to only very few assumption/idealizations instead of depending on large number of unrealistic idealizations. Comprehensive medium sized 1 g model test were carried out on unreinforced, reinforced and reinforced with panel faced soil slopes.

In this study, a set of mechanisms to describe the behavior of reinforced soils is developed based on some assumptions and hypotheses in conjunction with well known constitutive models in the theory of elasticity and plasticity. A rigid plastic stress-strain model to describe the Mises material e.g. purely cohesive clay is extended to the non-dilatant frictional (c-ϕ) material. An attempt is made to describe the non-dilatant plastic material as an assembly of inhomogeneous Mises material whose strength depends on the confining stress. The prediction of F_S, s, $\boldsymbol{u}$, n, x.... from proposed model will then be compared with other predictions as well as the model test results.

This research reviews the development of design criteria for reinforced soil structures especially for foundations, embankment, retaining walls, slope and excavations, with a special attention to the use of linear elastic and stability analysis of these reinforced soil structures. The history and development of soil reinforcement is briefly discussed and the limit analysis based on the rigid plastic finite element model originally pioneered by Tamura et al. (1984) in the field of Geotechnical Engineering, is discussed in detail. Tamura's model is extended to the Stability analysis of reinforced soil structures. The applicability of the proposed scheme is examined/illustrated/demonstrated through some typical soil engineering problems. In this perspective, the current research of the author complement the previous works by Asaoka et al.(1990, 1992) to the reinforced soil structure as a new area of application.

1.3 ORGANIZATION OF THE DISSERTATION

Following the introductory chapter which describes the aim and scope of the work in relation to the current status on the understanding of behavior and mechanism of reinforced soil structure, Chapter II is devoted to a review of the literature associated with the author's work. It deals with history and developments of reinforced soil structures to the philosophy behind the analysis and design of reinforced soil structure and its different components e.g. fill material, reinforcement, facing, to elasto-plastic theories used in the analysis. RPFEM and LEFEM are reviewed in detail in the context of the author's present work.

Chapter III describes the mathematical modeling/formulation of the proposed mechanism of the reinforced soil structure and their incorporation into the LEFEM and RPFEM. The mathematical derivation of the non-dilatant Frictional (c-ϕ) material as assemble of inhomogeneous Mises material is explained and incorporated into the RPFEM. In Chapter IV, some numerical investigations of the proposed model is presented through some typical soil engineering problems where soil is reinforced. In this chapter it is also shown that the axial/shear force along reinforcement develops due to internal action and also shown that the axial/shear force along reinforcement can not be controlled from outside the reinforced soil system in contrast to anchoring of a soil mass to bed rock.

First part of Chapter V is devoted on describing the model-testing program, the testing procedures, test results and discussions. Three series of medium sized 1 g model tests were conducted on silty sand slopes. First series was on mild face slope (1V:0.5H), others were on steep slopes(1V:0.2H) where first two series had reinforcement lengths same as footing length while the third series was on steep slope but the length of reinforcement was longer then the footing length. In the first two series, there were four models in each case while on the last series only two models were tested. The four models series cases had 1. Unreinforced plain slope 2. Reinforced without facing 3. Reinforced with thin panel facing (thickness 3mm) and 4. Reinforced with thick panel facing (5mm thick). In the case of last series where only 2 models were tested, had 1. Reinforced with steel bars without facings and 2. Reinforced with thick facing panels. All models were loaded till failure.

Latter part of the Chapter V presents numerical simulations of the model test results employing the proposed numerical formulation on the mechanism of reinforced soils. Out of the first two series of aforementioned model tests, total six models (3 from each series) are simulated employing the proposed numerical method. As stated before, novel feature of the results presented in Chapter V is that good agreement between the model test results and numerical analysis results were obtained.

Chapter VI presents a typical excavation of soft clay ground. The horizontal reinforcement, e.g. soil nailing, and vertical reinforcements, e.g. 'I' shaped sections or sheet pile are analyzed through the proposed method. A new concept on the vertical reinforcement positioning is proposed based on the reinforcement type. Thus, two types of reinforcements are distinguished, a. reinforcements capable to carry axial forces while the other type is the reinforcements offering very high flexural resistance.

Concluding remarks are made at the end of each chapter and an overall conclusion is also made in Chapter VII.

CHAPTER II REVIEW ON DEVELOPMENTS IN REINFORCED SOIL SYSTEMS

2.1 GENERAL

Strength of the natural /fill soil in earth structures is improved by various techniques, e.g., mechanical processes, chemical process, inserting a strong material into the soil mass (sand compaction piles, bamboo strip, straw, etc.) and the interesting one is natural plant roots. Besides these natural and traditional techniques, the important development of Reinforced Earth®, and the concept of reinforced soil as construction material, introduced by its inventor French architect H. Vidal, in the sixties, have introduced the modern form of soil reinforcement technique (Schlosser and Delage, 1987). This technique has been used in various structures, e.g. slopes and embankment, retaining walls, foundations, dams and others. Mitchell (1981) noted that no other soil improvement techniques have been so intensively studied and having advanced application in the past several years, as has soil reinforcement.

The concept of soil reinforcement is based on the existence of strong soil-reinforcement interaction like roots, due to their tensile strength and frictional or adhesion properties reinforce the soil. Many hypotheses have been postulated, in the past 25 years, about the load transfer between the soil and reinforcement and their interaction. A lot of research has been carried out to find suitable method for the analysis and design of reinforced soil structures.

There are three basic categories of literature available relevant to this research work. The first category is on the type of reinforced soil structures e.g. foundations, embankments, retaining wall, slopes and excavations. The second, the most important category is on the development of the components of the reinforced soils. The third category is devoted on analysis and design of the reinforced soil structures. The selection of the material contained in this chapter is perhaps

somewhat deliberate in the sense that it covers those aforesaid three aspects of reinforced soil structures.

2.2 HISTORY AND DEVELOPMENTS ON REINFORCING SYSTEMS

Development of Reinforced Earth®:

Henri Vidal in 1963 invented the Reinforced Earth® and much of the current development can be attributed to his pioneering work. Vidal introduced the basic mechanism underlying reinforced soil behaviors in his first paper published in 1966. Reinforced Earth® is a composite construction material (Fig. 2.1a) in which the strength of fill is enhanced by the addition of strong inextensible as well as extensible reinforcing materials. The basic mechanism of Reinforced Earth involves the generation of frictional interaction between soil and reinforcements (Schlosser and Delage, 1987).

York Method:

Jones (1973) developed the York method (Fig. 2.1b), which is similar to the Reinforced Earth technique except two minor differences, regarding facing units and sliding mechanism of reinforcements. The York method is the first reinforced soil wall totally built with plastic material (Schlosser and Delage, 1987). According to Jones (1978), differential settlements can easily be accommodated in the sliding mechanism.

GRS-RW System:

Geosynthetic-reinforced soil retaining wall (GRS-RW) system, developed in Japan, is a hybrid wall system of mechanically reinforced earth wall with a cast-in-place full-height rigid facing and a schematic diagram is shown in (Fig. 2.1c). Some advantages of GRS-RW system are small lateral deformation due to full height continuous rigid facing, and excavation may not be required because of short reinforcements. This system can be used in sites e.g. bridge abutment or laterally loaded walls.

Miscellaneous:

There are several other reinforcing systems developed by many manufacturers used for particular purpose and suitable for typical site conditions. Tervoile, Websol system, Cellular Confining system, Genesis Highway Wall System consisting of Tensar structural geogrids, Con-wall system, etc. are interesting systems to be noted here.

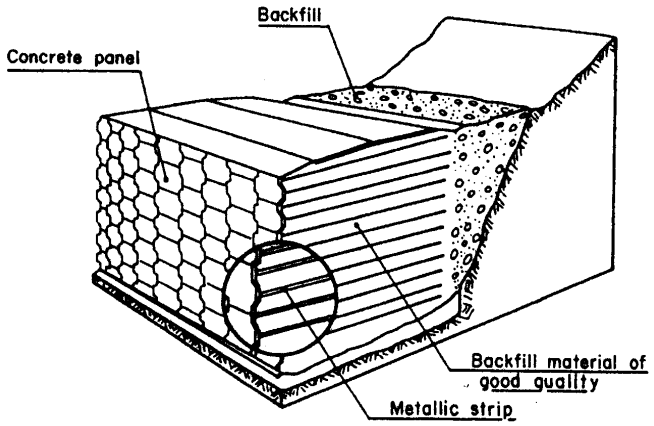

(a) Typical *Reinforced Earth*® system (*Schlosser and Delage*, 1987)

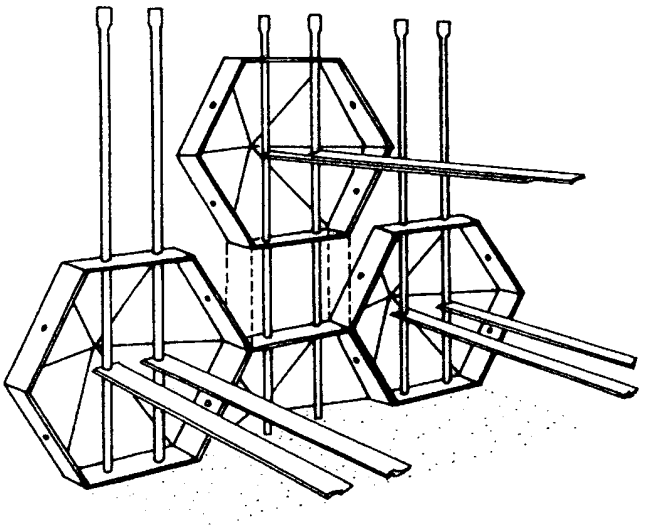

(b) York Method (Sliding method of construction) (*Jones*, 1992)

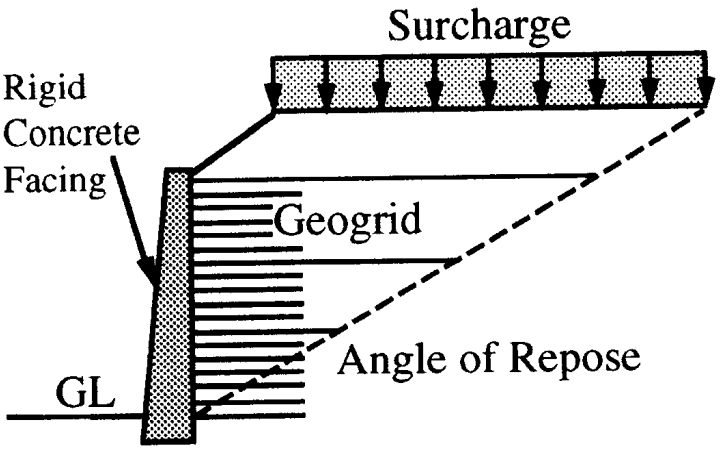

(c) Geosynthetic reinforced soil-rigid wall (GRS-RW) system (*Tatsuoka*, 1994)

Figure 2.1 Schematic diagram of typical reinforced soil systems.

2.3 TYPES OF REINFORCING MATERIALS

In the literature, there mainly two groups of reinforcements, extensible and inextensible, are discussed with respect to the stress-strain response of soil mass. Stress-strain characteristics of typical inextensible and extensible reinforcing materials are illustrated in Fig. 2.2. McGown et al. (1978) originally defined inextensible and extensible reinforcements and Bonaparte et al. (1987) extended as follows:

a. Inextensible reinforcement is reinforcement used in such a way that the tensile strain in the reinforcement is significantly less than the horizontal extension required to develop an active plastic state in the soil. An "absolutely" inextensible reinforcement is so stiff that equilibrium is achieved at virtually zero horizontal extension (K_o conditions prevail)

b. Extensible reinforcement is reinforcement used in such a way that the tensile strain in the reinforcement is equal to or larger than the horizontal extension required developing an active plastic state in the soil. An "absolutely" extensible reinforcement has such a low modulus that virtually no tensile forces are introduced to the soil mass at the strain required to develop an active plastic state (K_a conditions theoretically prevail)

Bonaparte et al. (1987) considered steel reinforcement as an inextensible reinforcement and geosynthetic reinforcing materials as extensible reinforcements, for almost all practical applications. Thus, an inextensible metallic reinforcement makes the structure brittle and the extensible geosynthetic increases the ductility of the reinforced soil structure (Fig. 2.3).

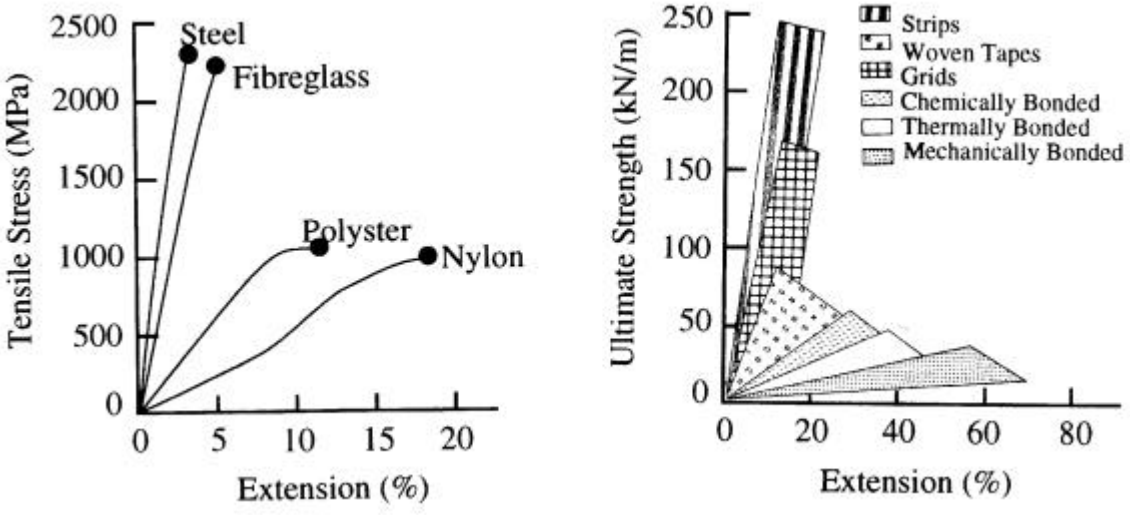

(a) Different material fibers (*Schlosser and Delage*, 1987)

(b) Geosynthetic products (*John*, 1987)

Figure 2.2 Stress-strain characteristics of typical reinforcing materials

2.3.1 Inextensible reinforcements

Steel Bars/fiber glass reinforcements:

The choices on the reinforcing material vary from inextensible reinforcements like steel, fiberglass to extensible polyester resins. Galvanized steel has been used in wide variety of environments over very long periods, thus, its corrosion mechanism and the rate of corrosion have been known for long time. Similarly, polyester coated fiberglass, stainless steel and aluminum are also used. The corrosion rate of these metals is faster than galvanized steel. Despite these drawbacks, the steel and fiberglass reinforcing materials have also gained popularity specially when the construction requires less post construction deformation such as in the case of bridge abutments, railway embankments, etc. The advantage of steel and fiberglass is due to their unique combination of elasticity, ductility/stiffness and favorable economics. Bonaparte et al.(1987) states that the tensile stiffness of steel reinforcements is stiff enough to keep the state of soil stress close to the at-rest (K_O) condition.

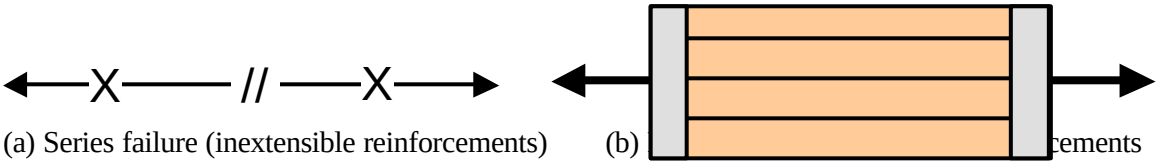

(a) Series failure (inextensible reinforcements) (b) cements

Figure 2.3 Analogy of reinforced soil fail mechanisms (*Jones*, 1992).

2.3.2 Extensible Reinforcements

Geosynthetic and related products:

Major geosynthetic materials currently used as reinforcements in soil structures are geogrid sheet (*see* Fig.2.4), woven and non-woven geotextile sheet, coated fiber strips, rigid plastic strips, composites and three-dimensional honeycomb type products. Geosynthetic materials have large ranges of deformation modulus and tensile strengths compared to metals (see Fig.2.2). Geosynthetic materials also exhibit creep behavior. Bonaparte et al.(1987) has grouped geosynthetic reinforcements as extensible reinforcements, thus, the state of soil stress is far from at-rest (K_o) condition.

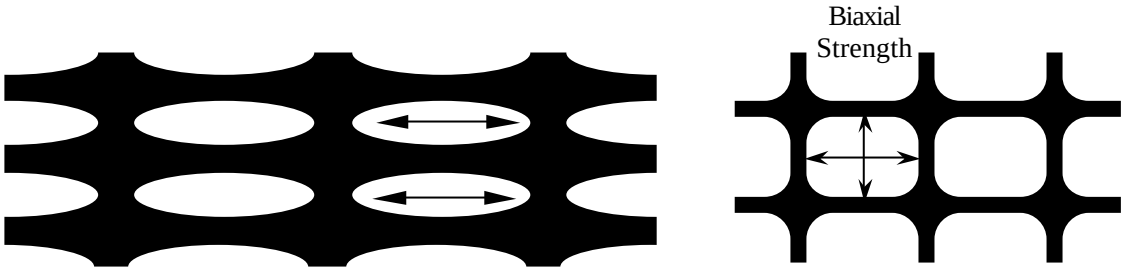

(a) Uniaxial geogrid (b) Biaxial geogrid

Figure 2.4 Typical geogrids used as soil reinforcements (*John*, 1987).

2.3.3 Miscellaneous

There are several other types of reinforcing materials used for particular purposes. Small inclusions (fibers, small plates) or continuous filaments (e.g. Texsol) are some typical reinforcing materials. Sometime natural materials (e.g. bamboo, jute) are also used as reinforcing material. In UK and USA, redundant car tires have been used as reinforcement.

2.4 APPLICATIONS OF REINFORCED SOILS

More common applications of reinforced soil are in the form of retaining walls. Reinforced soil structures can be grouped into three classes (Ingold, 1982), (a) Embankment and retaining walls, (b) Foundations / sub-soil reinforcements and (c) In-situ reinforcement (*soil nailing*)- existing slopes and excavations.

2.4.1 Embankments/ Retaining Walls

Several reinforcing systems with varieties of reinforcing materials and facings have been successfully used to construct many reinforced embankment and retaining walls (e.g. Yamanouchi, 1988; McGown et al., 1991; Ochiai et al., 1992). Some of them are very tall and long e.g. 2000m of 2~3m height (Tatsuoka et al., 1994).

A primary role of reinforcement in an embankment or a retaining wall is to support the outward earth pressure (lateral thrust) in the fill while maintaining the full bearing capacity in the foundation (e.g. Ingold, 1982; Gourc, 1993). The reinforcement provided at the embankment base prevents lateral displacements of the embankment and foundations soils, subsequently the bearing capacity of the soft soil and stability of embankments are increased significantly (Madhav, 1993). Purpose of these reinforcements is to perform as (i) superficial slope reinforcement and edge stiffening; (ii) main body reinforcement; (iii) reinforcement at the base of the retaining walls. Reinforcement in the main body is essentially the major application of reinforcement in reinforced embankment or retaining wall structures.

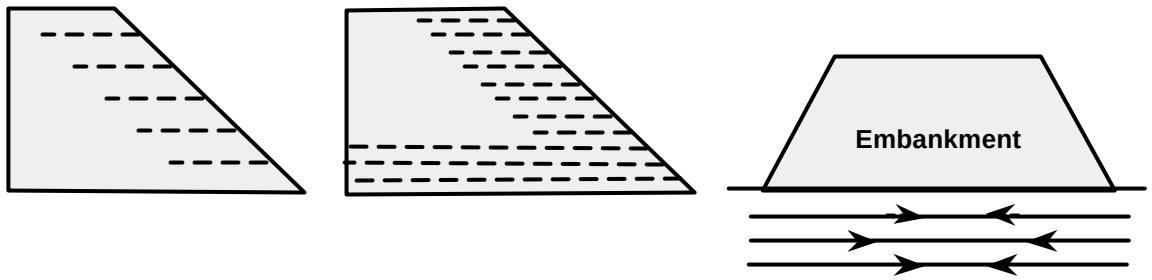

(a) Superficial reinforcement (b) Body reinforcement (c) Foundation reinforcement

Figure 2.5 Embankment reinforcing modes (*Ingold*, 1984).

2.4.2 Subsoil Reinforcement Beneath Foundations

In the soil beneath the reinforced soil foundation two distinct zones are formed (e.g., Binquet - Lee, 1975), and John, 1987) as shown in Fig. 2.6. In the first zone, the wedge of soil directly beneath the structure is forced vertically downwards (punching failure) whilst outside the footing, there are symmetrical zones which have both lateral and upward movements, the function of an effective reinforcement being to hold these two zones together. Binquet-Lee (1975), Oka et al. (1992), Takemura et al.(1992) and other researchers reported that the maximum bearing capacity ratio occurs at a depth ratio 0.8 to 1.0.

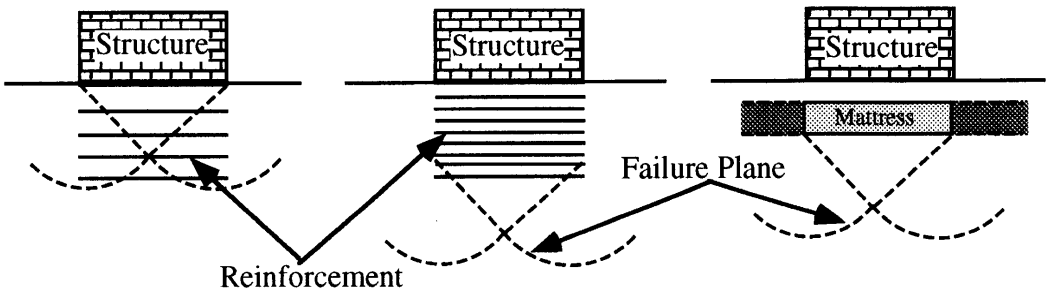

(i) Sparcely layered system (ii) Densly layered system (iii) Mattress Foundation

(a) Critical zones beneath reinforced foundations (*Fukuda et al.*, 1987)

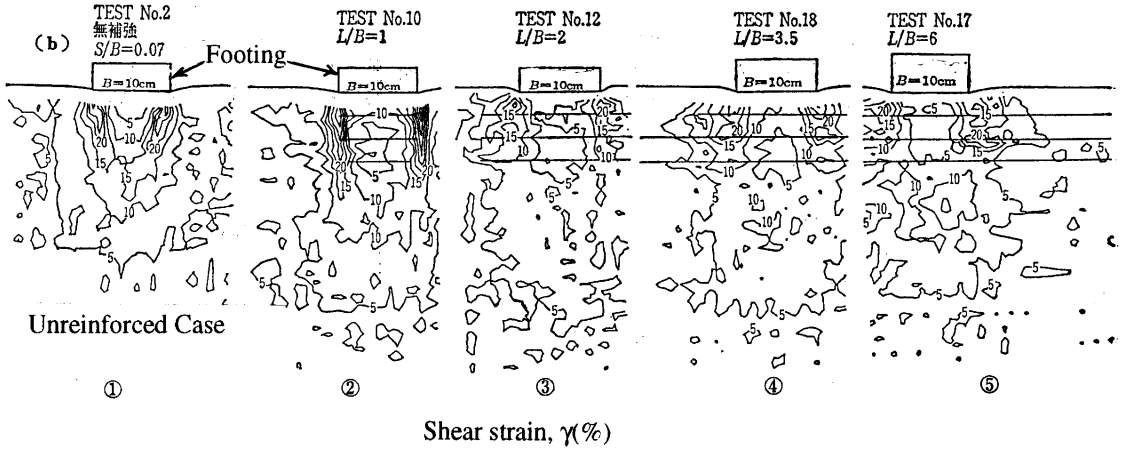

(b) Experimental observation (*Tatsuoka*, 1992)

Figure 2.6 Effect of sub-soil reinforcements.

2.4.3 In-situ Reinforcement (*soil nailing*): *slope stability/excavation*.

Soil nailing is an in-situ soil reinforcement technique, which has been used during the last two decades. Soil nailing is being used at present to stabilize natural slopes, cuts or excavation, walls in stiff clays, granular soils (with some suction) and also soft rocks. The purpose of this technique is essentially to limit the decompression and the opening of pre-existing discontinuities by restraining the deformations. They are usually steel rods 20-30 mm in diameter that are inserted into the soil either by simple driving or by grouting in predrilled borehole (Fig.2.7). Soil nailed slopes behave like a reinforced soil wall although there are some major differences between these two techniques (John, 1987), e.g.,

i. Construction method: Soil nailed slopes have top-downwards construction method whereas reinforced soil walls are constructed from the bottom upwards
ii. Shear and bending stresses may develop in soil nails depending on the stiffness of the nails relative to soil, while this is not generally observed in soil reinforcements.
iii. Soil nailing is applied to existing soil slopes and may therefore involve more cohesive soils than the selected fills used for reinforced soil walls.
iv. Soil reinforcement sheets or strips are usually laid horizontally, whereas soil nails are usually driven at an inclined angle.

Schlosser (1982) observed that the active failure zone for nailed slopes was similar to, but larger than, that of a reinforced soil wall. In both cases, the active failure zone is smaller than the standard Coulomb active wedge assumed with the other retaining structures. He suggested that this difference in behavior is attributable to the inclination of the soils nails.

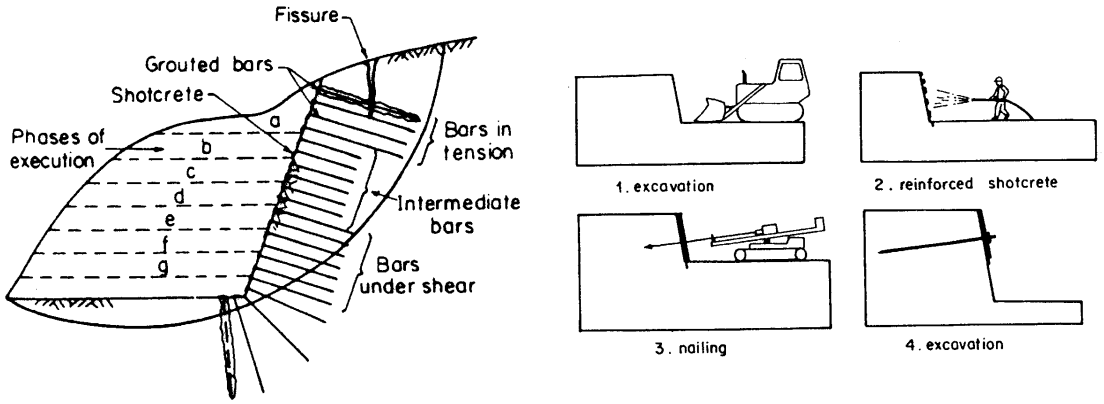

(a) Typical soil nailed structure. (*Schlosser and Juran*, 1980)

(b) Construction steps (*Schlosser and Delage*, 1987)

Figure 2.7 Typical in-situ soil-reinforcing techniques.

2.5 CONCEPTS AND MECHANISM OF REINFORCED SOIL

Several experimental and theoretical investigations have been performed since the invention of Reinforced Earth wall (Vidal, 1963) to understand the concepts and mechanism of reinforced soil structure and interaction among its basic components, generally, reinforcing elements, backfill soil and facing. H. Vidal, the pioneer of Reinforced Earth system seems to be the first person to propose a general and realistic concept of reinforcing a soil.

Anisotropic Cohesion Concept

Schlosser and Long (1972) indicated that the reinforced soil has higher shear strength than unreinforced plain samples (Fig.2.8a). Hausemann (1976) independently postulated a more unified anisotropic cohesion theory. They have shown that two failure modes can develop in such reinforced sand samples: (a) failure by slippage of the reinforcement at low confining pressure leading to a curved yield line passing through the origin and (b) failure by reinforcement breakage at higher confining pressure leading to a straight failure line which proves that the reinforced sand behaves as a cohesive material having the same frictional angle as the original sand and an anisotropic pseudo-cohesion due to reinforcements as shown in Fig. 2.8b. This pseudo-cohesion is very rapidly mobilized at low axial deformations.

Enhanced Cohesion Concept

Chapius (1972) and Yang (1972) independently presented *enhanced confining pressure concept* on the mechanism of reinforcing a soil mass. This concept is based on the assumption that the horizontal and vertical planes are no longer principal stress planes due to the shear stresses induced between the soil and reinforcements. Mohr's circle of stress is shifted due to reinforcing of the soil mass (Fig. 2.8b) while failure envelope remained same for both reinforced and unreinforced samples. Such effect is called enhanced confining pressure effect.

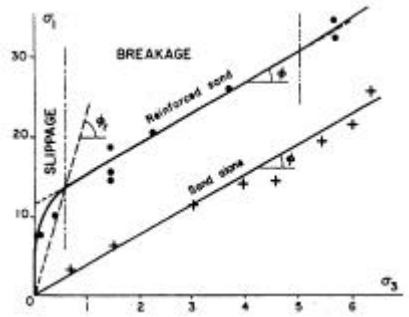

Figure 2.8a Reinforced and unreinforced samples in triaxial tests (*Schlosser et al., 1972*)

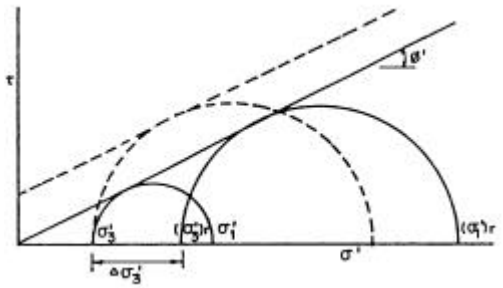

Figure 2.8b Anisotropic Cohesion and Enhanced Cohesion Concepts (*Ingold*, 1984)

Basset and Last (1978)

Basset and Last (1978) considered that the mechanism of tensile reinforcement involves anisotropic restraint of the soil deformations in the directions of the reinforcements. Using Roscoe's failure criteria for sands based on zero extension concepts, they demonstrated that the presence of the reinforcement leads to rotation of the principal directions of the deformation tensors. Reinforcements should be aligned with the zero extension lines, thus, exhibiting a vertical failure surface. Thus, the stress and the strain patterns are greatly modified due to the soil-reinforcement interaction (Fig.2.9).

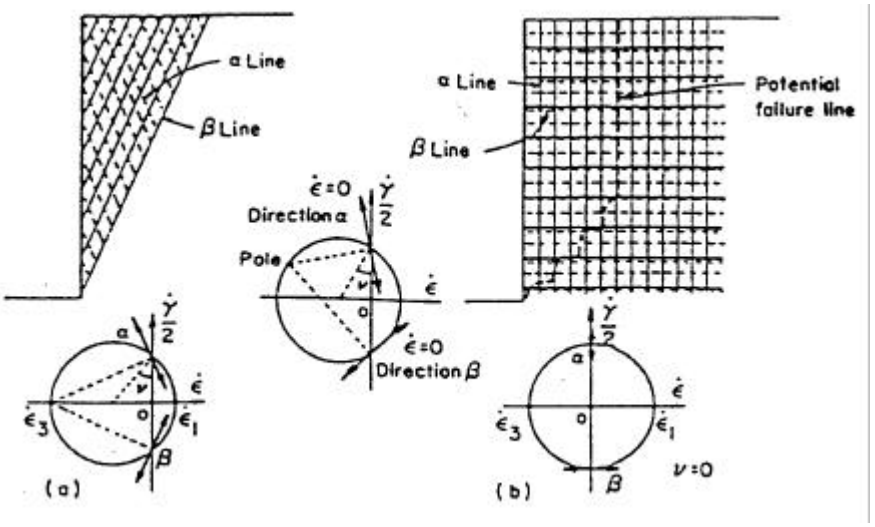

Figure 2.9 Influence of reinforcements on potential failure lines (*Basset and Last*, 1978)

2.6 BEHAVIOR OF REINFORCED SOIL STRUCTURES

In the analysis and design of reinforced soil structure, stability and deformation are considered both critical and independent concerns for a soil structure and they are always dealt separately. Past research reveals that major work was concentrated on stability analysis compared to the deformation problems. In deformation analysis, serviceability with respect to excessive differential settlement and horizontal deformation of the slope face are considered important. The stability analysis of reinforced soil structures is divided into internal and external stability analyses (Gourc, 1992; Rowe and Ho, 1992) as will be illustrated in later sub-sections.

Rowe and Ho (1993) suggested that the overall behavior of a reinforced soil structure may be considered known if one understands:

a. State of stress within the reinforced soil mass.
b. State of strain in both the soil and the reinforcement.
c. Axial force distribution in the reinforcement.
d. Horizontal soil pressure acting at the back of the reinforced soil mass and the vertical soil

pressure at the base.

e. Vertical soil stress on each reinforcement layer.
f. Horizontal soil pressure acting at the face.
g. Horizontal and vertical forces transferred to the wall face.
h. Horizontal deformation of the reinforced soil mass
i. Effect of varying the design parameters (i.e. reinforcement stiffness, soil properties, facing stiffness, foundation stiffness, surcharge condition, construction procedures, etc.) on the response of the system.

2.6.1 Vertical and Horizontal Soil Stress Distribution:

Several types of vertical stress distribution patterns are assumed in the analysis and design of reinforced soil mass. Uniform, trapezoidal, Meyerhof distributions and 2:1 stress dispersion method are typical examples. Maximum stress is attained within the reinforced zone. Close to the far end of reinforced zone the vertical soil stress reaches a minimum. Further away into the unreinforced retained fill, the vertical soil stress attains the minimal value. The vertical soil stress close to the facing depends on the facing rigidity (Tatsuoka, 1993). Rigid facing decreases the vertical soil stress close to the facing due to load transfer from the soil to the facing. Such effect of the facing leads to higher reinforcement force and requires higher bearing capacity in the design of foundations.

Horizontal soil stress primarily depends on the number of reinforcement layer, the stiffness and the creep of the reinforcement and the degree of yielding of the wall face as shown in Fig.2.10. Relative deformation of the wall face and soil with the reinforcement results increased transfer of horizontal stress to reinforcement rather than to facing. The horizontal soil stress increases as the number of reinforcement layers is increased. Rowe and Ho (1993) noted that there are no literatures giving any real observed information on the horizontal soil stress distribution further back into the reinforced soil.

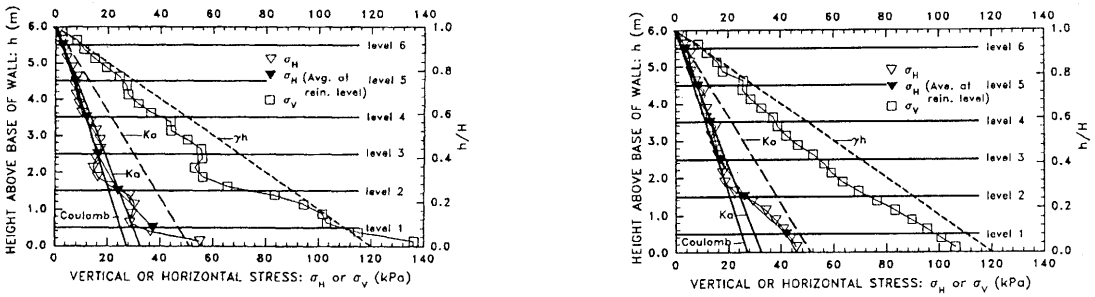

(a) at wall face (b) at back of reinforced soil block

Figure 2.10 Vertical and Horizontal soil stress distributions from numerical analysis (*Ho and Rowe*, 1992)

2.6.2 Force in Reinforcement

The magnitude of reinforcement force primarily depends on the shear strength mobilized in the backfill, the horizontal soil strain, the stiffness of the reinforced system, and the creep of reinforcements. Maximum tensile force close to toe is usually observed less than predicted by the Rankine active condition (Lesniewska, 1992; Bathurst et al.,1988). Fannin (1991), Jewel (1987) and Ho-Rowe (1992) indicated that the maximum force in reinforcement becomes more uniform with decreasing reinforcement stiffness and lower near the bottom due to the influence of foundation.

Variation in soil properties and construction methods results shifting of the position of maximum tensile forces away from the failure plane. It also depends on the length and stiffness of reinforcements. Jewell (1987) stated that the locus of maximum tensile force will always be inclined to 45 + ϕ/2 to the horizontal if the soil-reinforcement interface is sufficiently bonded, otherwise, the locus will move towards the facing. The maximum tensile force shifts towards the facing in the case of short reinforcements.

Force distribution in a reinforcement layer: The force distribution in a reinforcement layer is most influenced by the construction method, the existence of facing, the lateral restraint of facing during construction and the facing reinforcement connections. There are two general type axial force distributions (e.g. Muramatsu et al., 1992 and Tatsuoka, 1992) as shown in Fig.2.11(a).

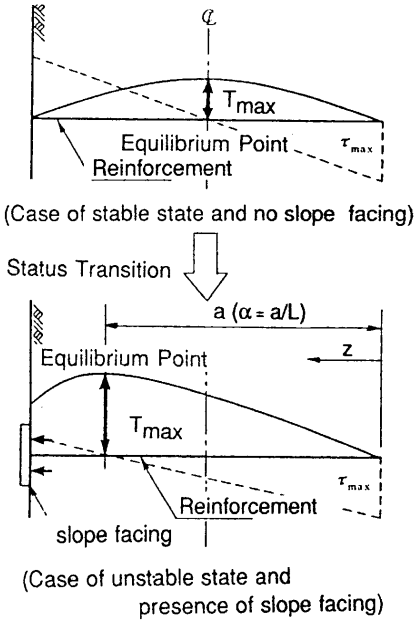

(a) Muramatsu et al. (1992)

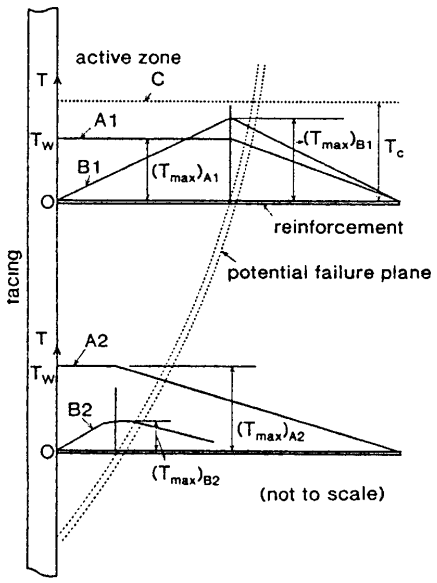

(b) Tatsuoka (1992)

Figure 2.11 General tensile force distribution patterns along a reinforcement.

Type A: This pattern is observed when lateral deformation of the wall face is restrained till the end of construction, e.g., ideal pull-out test. In this situation the maximum tensile force is induced at the back of the facing and remains more or less constant up to the potential failure plane and decreases to zero close to inner end of the reinforcement (e.g., Jowell, 1987 and Tatsuoka, 1993) When perfect lateral restraining of facing during construction is not possible, the tensile force in the reinforcement at the back of facing may be much smaller than its maximum value attained near the potential failure surface.

Type B: The parabolic tensile force distribution is observed when facing provides little or no lateral restraint against deformation e.g. wrapped back facing, slope face without any facing. The maximum force in the reinforcement is assumed to occur at the potential failure plane as shown in Fig. 2.11(b).

2.6.3 Horizontal Displacement

Magnitude of horizontal movement depends on the interaction between various components of reinforced soil structure and construction methods. Higher reinforcement density and stiffness reduce the strain in the soil, and larger shear strength of fill results in less force in the reinforcement, being required to maintain equilibrium and hence less deformation. The soil movement behind the reinforced zone depends on the strain level of the unreinforced zone above the stable slope.

2.6.4 Role of Facing rigidity:

Currently, facing material ranges from rigid full-faced concrete facing to flexible wrapped around geosynthetic facing as shown in Fig. 2.12(a~h). Most of the soil reinforced stabilization techniques assume that facing does not play a significant structural role; they are rather used for aesthetic reason (e.g. Vidal, 1978; Bruce and Jewell, 1986). However, Tatsuoka (1993) has demonstrated the roles of the facing in improving the stability of reinforced soil structures based on extensive literature review. Horizontal movement of the wall face and subsequent earth pressure development within the reinforced zone as well as the reinforcement force are significantly affected by the facing rigidity.

Tatsuoka (1993) has classified various types of facing according to the degree of facing rigidity. The facing rigidity increases the stability of wall in the following three ways:

1. Rigid facings (Types D and E) support the combination of earth pressure and tensile force in reinforcement.
2. Weight of backfill is partly transmitted to the facing through the frictional force on the back face.
3. Due to high confining pressure behind rigid facing, the location of the overall reaction force becomes closer to the facing.

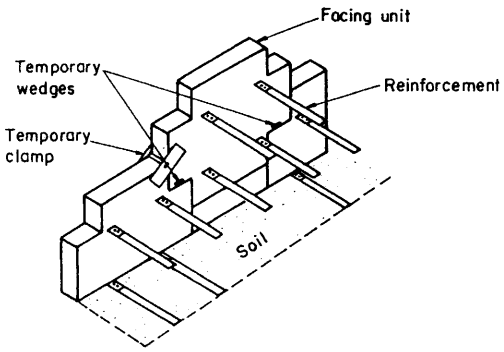

(a) Concrete Panel facing (*Reinforced Earth® system*)

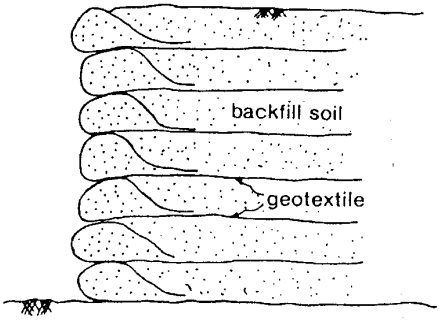

(b) Wrapped around facing

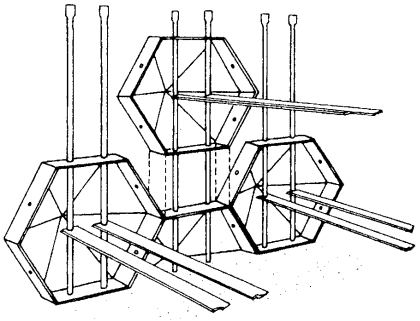

(c) York wall facing (*Jones*, 1992)

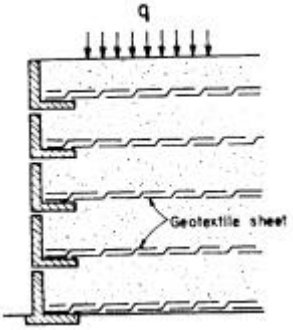

(d) L-shaped concrete facing (*Broms*, 1988)

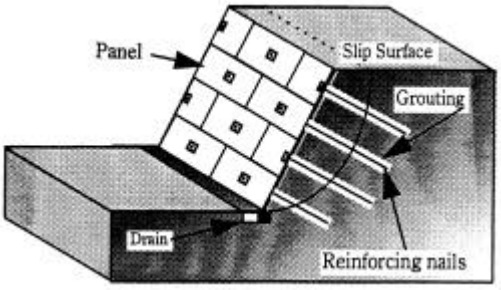

(e) Reinforced Concrete Panel (Japanese system)

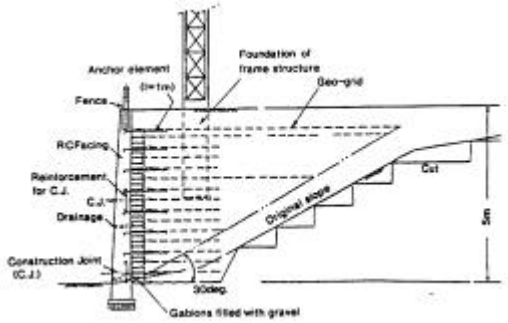

(f) Full Height Rigid Reinforced Concrete Facing (GRS-RW System)

Figure 2.12 Currently used typical facings in reinforced soil structures.

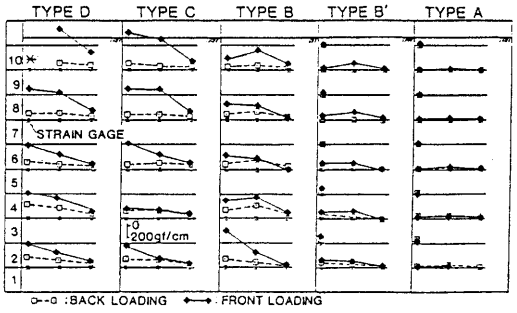

Figure 2.13 Observed tensile force distributions along reinforcement corresponding to different facing rigidities (*Tatsuoka et al.*, 1989)

Tatsuoka et al. (1989) studied the effect of facing rigidity in a set of GRS-RWs model tests having facing Types A~D. The test result reveals that the location of failure surface moved from an intermediate elevation to the bottom of the facing depending on the facing rigidity. The ratio of earth pressure p_f on the back of the facing to q_u remained almost constant with the facing rigidity. Similarly, the tensile force just behind the facing is greatly influenced by the facing rigidity (see Fig.2.13). Location of T_{max} (Fig. 2.11) approaches back of the facing with increasing facing rigidity. Thus, the contribution of the facing rigidity on the stability of the reinforced soil structure was clearly demonstrated and similar conclusions are also reported by several other researchers (e.g., Juran-Schlosser, 1978, Bolton-Pang, 1982, and Koga et al., 1992).

2.7 TYPICAL CURRENT DESIGN METHODS

For the analysis and design of reinforced soil structures numerous approaches have been developed. All methods are either empirical in nature or based on limit equilibrium analysis. These methods don't consider either the stress-deformation characteristics of the structure or the interactions between the wall components e.g. the soil, the reinforcement, the facing and the foundation. Their main purpose is to compute the factor of safety against several modes of failure. In general, the design methods use the allowable strengths (corresponding to each components) which are significantly lower than the ultimate strengths and further partial safety factors are applied to account for the uncertainties in the behavior of the reinforcement and soil/reinforcement interaction mechanism. As a consequence, these methods are lagging in adequately describing the real behavior of the reinforced soil structures. Hence, their application typically introduces an extra level of conservatism. Rimoldi (1988) based on eight case histories reported that current design methods are conservative.

Most of the current design methods can be divided into two main categories. The first category use simple force equilibrium analysis where the horizontal forces developed in the reinforcement balance the destabilizing horizontal force from the soil. The forces considered in these methods are: a. the vertical soil stress, b. the horizontal soil stress, c. the stress in the reinforcement and d. the horizontal resistance to pull-out of the reinforcement behind the potential failure plane. Two independent factors of safety, for reinforcement rupture and pullout resistance, are calculated for each layer of reinforcement.

The methods in the second category evaluate the force and or moment equilibrium on an assumed failure surface similar to conventional slope stability analysis but with the inclusion of the balancing force/moment developed in the reinforcement.

2.7.1 Force Equilibrium Methods

Some of the widely used force equilibrium methods for the design of numerous reinforced soil structures are as follows:

1. Jewell method (1987)- This method was proposed and applied first to predict the performance of Royal Military College trial wall in 1987. In this method, the reinforced soil structure is divided into 3 zones based on the reinforcement force as shown in Fig.2.14

   Zone-1: The zone between the wall face and the most critical surface where the reinforcement force required to maintain equilibrium is constant (i.e. between the surface and wall face). Thus, the most critical surface was defined as a surface through the toe that requires the greatest total reinforcement force to maintain equilibrium on this surface. The surface in vertical wall case is inclined at an angle $\theta=(45+\phi/2)$ to the horizontal as shown in Fig.2.14

   Zone-2: This zone is confined between the aforesaid most critical surface and the locus of zero required force as shown in Fig.2.14. A surface beyond which no additional stresses are required from the reinforcement to maintain equilibrium is called the locus of zero required force. Ideally beyond this zone the reinforcement can be truncated and equilibrium can be maintained by soil itself. Such length of the reinforcement is called the ideal reinforcement length.

   Zone-3: The zone beyond the locus of zero required force is in equilibrium without requiring any reinforcements.

Jewell (1987) proposed uniform spacing and ideal spacing pattern for reinforcement spacing. He further explained a truncated length concept and consequences of the truncation in the design. He also provided several design charts.

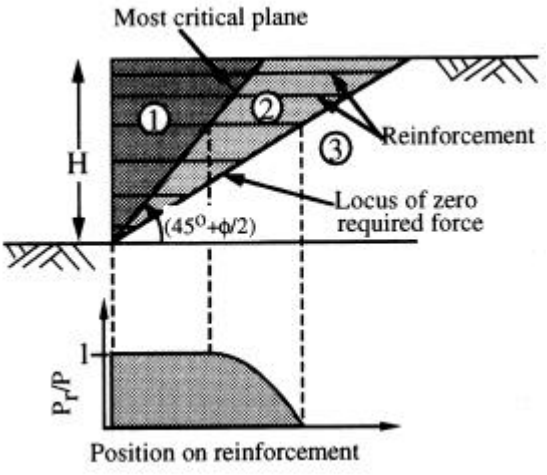

Figure 2.14 Reinforcement layout and force distribution for ideal length case.
(*Jowell, 1987*)

2. Bonaparte et al. method (1987) - In this design method, the extensible and inextensible reinforcements are clearly distinguished. Then, the influence of reinforcement extensions is evaluated by defining hyperbolic relations between $K \sim \varepsilon_h$. Detailed explanation about the method may be referred to Bonaparte et al.(1987).
3. Tie back design method (1978)- Tie back method was originally developed by the U.K. Department of Transport (1978) and is based upon limit equilibrium methods. It is independent of the reinforcement material and is used with both inextensible and extensible reinforcement and with anchors.

2.7.2 Slope Stability Methods

Many basic methods have been derived from the conventional slope stability studies; the most widely used (Rowe and Ho, 1992; Smith, 1992) being the Fellenius or Bishop methods or the Wedges methods. There are three noticeable differences among these methods as follow: a. the shape of the failure surface b. the distribution of force in the reinforcement and c. the means by which a surcharge is considered. Typical slope stability methods are as follows:

Fellenius Method:

In this method, it is assumed that for each slice the resultant of the interslice forces is zero. Taga et al.(1992) have summarized all the possible combination of various forces based on the Fellenius (simplified) method used in the analysis and design of reinforced soil structures where the basic computational formula used is as follows (*refer* Fig. 2.15):

$$\textit{Sliding Safety Factor, } F_S = \frac{\textit{Force resisting sliding}}{\textit{Force inducing sliding}} = \frac{\sum \left[cb + W \cos a \tan f \right]}{\sum W \sin a} \qquad ...(2.1)$$

where,
- W: weight of sliced blocks
- b: length of sliding plane in sliced block
- f: Internal friction angle of sliding surface
- c: cohesion of sliding surface
- α: inclination of sliding surface with horizontal.

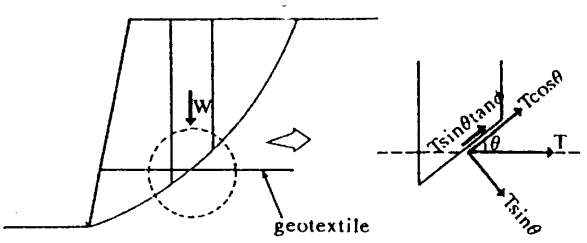

Figure 2.15 Fellenius method of analyzing reinforced soil structures

There are two reinforcement effects of the tensile force generated in the reinforcements in the sliding surface (see Fig. 2.15).

(1) Anchoring effect, T cosα

(2) Confining effect, T sinα . tan ϕ

Regarding the confining effect (2), involves the equation, Eq.(2.1), and regarding the anchoring effect, two possible conditions arise, it may be considered as a resisting force (numerator) and as a sliding forced (denominator). Sometime, both effects are considered simultaneously together depending on the problem. Thus following five combinations can be derived by coupling these two effects with the Eq.(2.1).

Formula (a)

$$F_S = \frac{\sum [cb + W\cos a \tan f + T\cos a]}{\sum W \sin a} \qquad ...(2.2)$$

Formula (b)

$$F_S = \frac{\sum [cb + W\cos a \tan f]}{\sum (W \sin a - T\cos a)} \qquad ...(2.3)$$

Formula (c)

$$F_S = \frac{\sum [cb + W\cos a \ \tan f + T\sin a \ \tan f]}{\sum W \sin a} \qquad ...(2.4)$$

Formula (d)

$$F_S = \frac{\sum [cb + W\cos a \ \tan f + T\cos a + T\sin a \ \tan f]}{\sum W \sin a} \qquad ...(2.5)$$

Formula (e)

$$F_S = \frac{\sum [cb + W\cos a \ \tan f + T\sin a \ \tan f]}{\sum (W \sin a - T\cos a)} \qquad ...(2.6)$$

***Bishop's Method**:*

In this method, it assumed that the resultant forces on the sides of the slices are horizontal. Thus, moment equilibrium is checked in this method as follows (refer Fig. 3.16):

$$Fs = (M_R + \Delta M_R)/M_D \qquad ...(2.7)$$

where M_D = sliding moment, M_R =resisting moment of soil, ΔM_R =resisting moment of geogrid, ΔM_R =R? T_i, R=radius of slip circle, and ? T_i =sum of tensile strengths of geogrid. A typical formula for computing the factor of safety based on Bishop's Method is:

$$F_S = \frac{\sum \left[cb + \left(W - ub + P + T \sin g \right) \tan f \right]}{\sum \left[W \sin a + P \sin a - T \cos(a + g) \right]} \qquad ...(2.8)$$

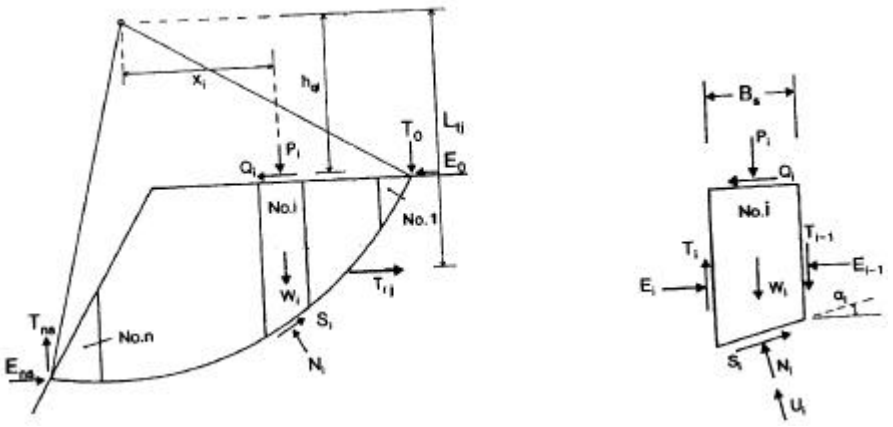

Figure 2.16 Bishop's Simplified Method of analyzing reinforced soil structures

Trial Wedges Method:

Slip surfaces in the trail wedge method can be assumed to be two straight-line slips caused by the horizontal earth pressure, similar to the experimental data.

$$F_S = \frac{\sum T_i}{P_H} \qquad ...(2.9)$$

In this equation, P_H = horizontal earth pressure and $\sum T_i$ = sum of tensile strengths of the geogrid. Total horizontal earth pressure components P_H, of the two straight-line slips, divided into two areas, Zone-1 and Zone-2, as shown in Fig. 2.17, can be obtained based on the concept of force polygons. It can be determined that the embankment is stable when the external force of restraining wall acting is larger than P_H.

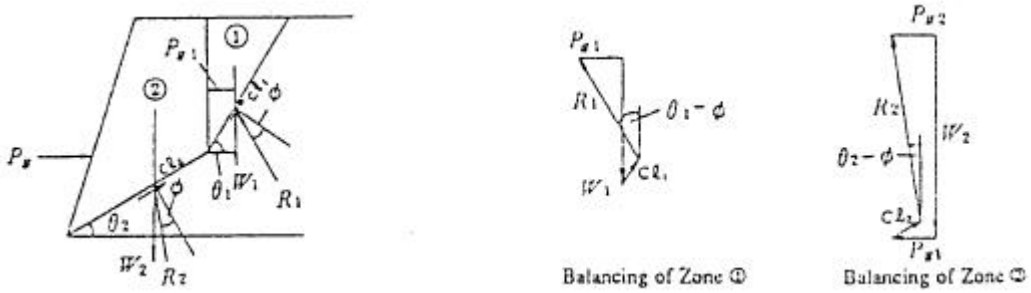

Figure 2.17 Trial wedge method of analyzing reinforced soil structures (*Taga* et al., 1992)

2.7.4 Failure Modes

Sometimes several possible failure modes are checked in reinforced soil walls depending on type of the structure itself and the field conditions. Generally, five independent types of failure (i.e. limit) modes are suggested sufficient enough for most of the geotechnical design problems (Bolton, 1989). These failure modes are grouped into two (external and internal) stability criteria. Typical failure modes that are checked (Jones, 1993) in the design of reinforced soil structures are as mentioned below:

External Stability (Fig. 2.18~19)

a. Vertical and horizontal deformations resulting into unacceptable differential settlement.
b. Lateral sliding of reinforced soil.
c. Overturning failure due to rotation about toe of the wall.
d. Bearing capacity failure (punching) of the foundation soil under the reinforced soil.
e. Overall collapse of the reinforced wall or embankment or nailed slope.

Internal Stability

a. Rupture failure of reinforcement
b. Pull-out failure of reinforcement

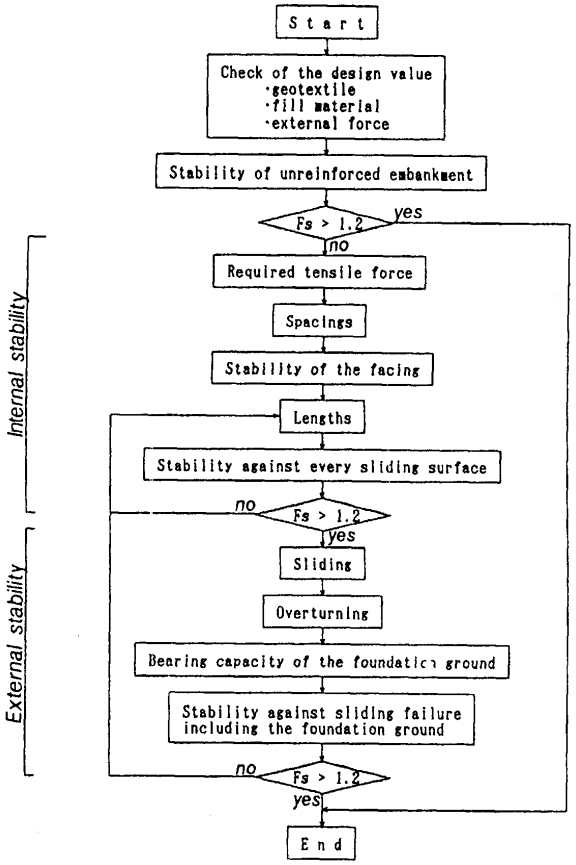

Figure 2.18 Typical flow chart for the analysis and design of reinforced soil structures. (*Onodera* et al., 1992)

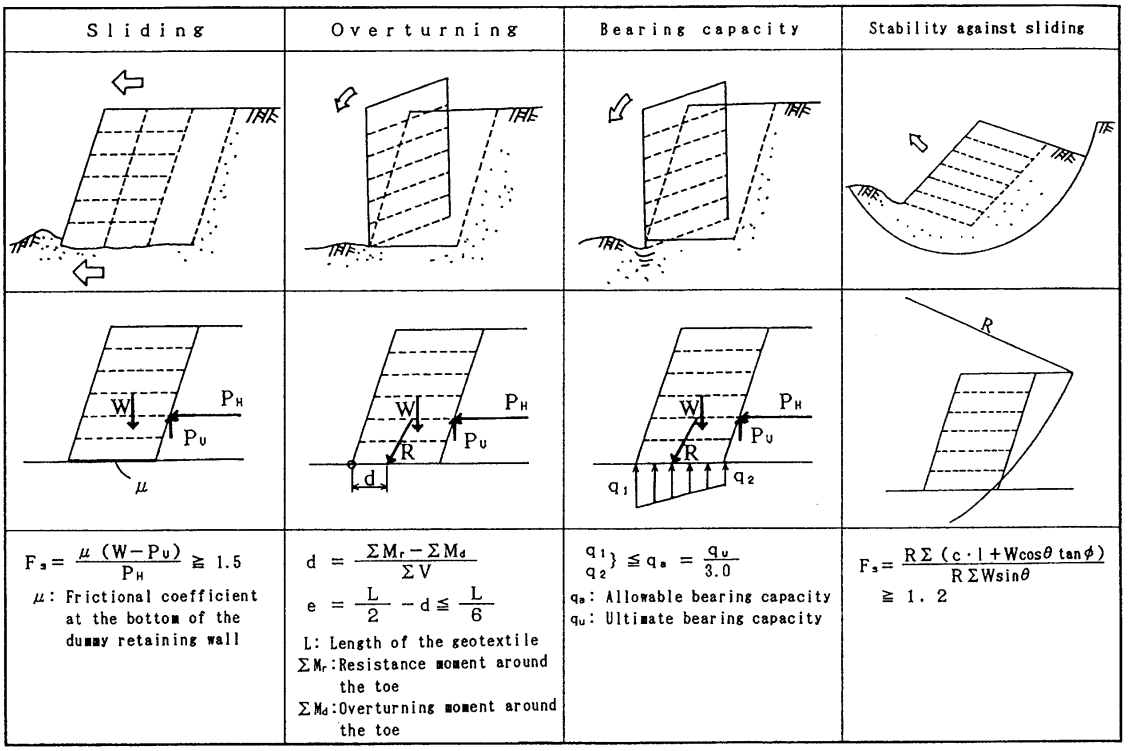

Figure 2.19(a) Typical failure modes to be examined in the design of reinforced soil walls (*Onodera et al.*, 1992)

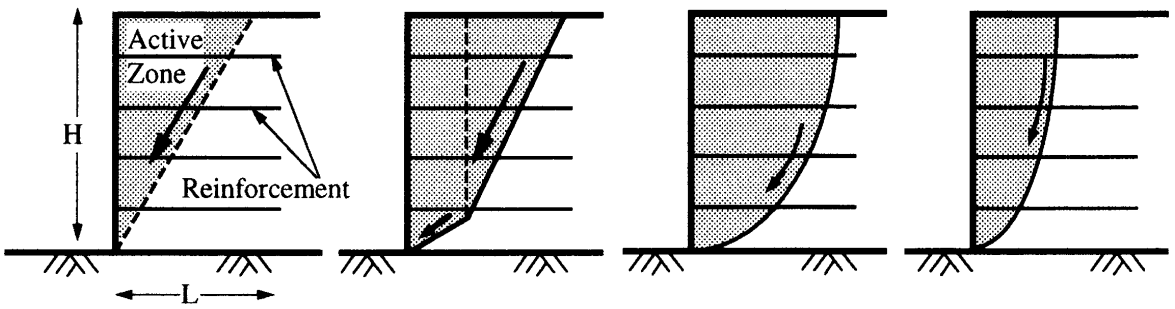

(a) Straight wedge (b) Two-part wedge (c) Circular arc (d) Logarithmic spiral

Figure 2.19(b) Common shapes for potential failure surfaces for Limit Equilibrium Analysis techniques

2.8 FINITE ELEMENT ANALYSIS

Finite element method (FEM) is vigorous well known method of numerically solving boundary value problems which can accommodate highly non-linear stress-strain relations of materials including even creep, any geometrical configuration with complex boundaries, construction sequence, etc. FEM has been used as the standard tool for the design and analysis (e.g. prediction of safety factor and settlement analysis) of many geotechnical structures. Similarly, it is becoming a design and analysis tool for the reinforced soil structures. These features of FEM can be achieved only when material parameters, constitutive equations and boundaries are appropriately defined or modeled.

2.8.1 Modeling of Components: *soil, reinforcement and facing*

The incorporation of mechanism of soil-reinforcement-facing interaction in the FEM are greatly influenced by the construction method, compaction, propping of facing during construction and its release later including the boundary conditions (loading on top, etc.), thus, making it difficult to model the problem.

Soil: most researchers as pointed out by Gourc, 1992, have adopted non-linear elastic or elasto-plastic models. The initial deformation is sometime calculated using linear elastic constitutive models and failure load is calculated using limiting equilibrium methods employing appropriate constitutive models e.g. Mises or Mohr-Coulomb, Drucker-Prager etc.

Reinforcement: Reinforcement is generally modeled by linear bar element capable of taking only axial tensile forces. Behavior of extensible geosynthetic materials is generally nonlinear. Sometime metallic reinforcements are also modeled as continuous beam element (Kalikan and Xi, 1992) and the bending moment is calculated in addition to the axial force.

2.8.2 Modeling of Soil Reinforcement Interface

Several authors have proposed various types of interface elements to model the interface behavior. Most of the interface elements, originally developed in rock mechanics, are used in the analysis of reinforced soils. Interface elements can be classified (Gens et al.,1989) into the following categories:

a. Standard finite elements of small thickness
b. Quasi-continuum elements possessing a weakness plane in the direction of the interface.
c. Linkage elements in which only the connections between opposite nodes are considered
d. Interface elements in which relative displacement between opposite nodes are the primary deformation variables. They can have finite or zero thickness.

Several differences exist among these methods and the main argument concerns the physical existence of shearing band of soil around reinforcement. FEM methods are based on continuity of soils except the contact plane between soils and reinforcing materials. Goodman element

(1968) is the original interface element introduced in the geotechnical contact problems. This type of interface element is extensively used in the reinforced soil problems. A typical interface element is illustrated in Fig.2.20 below.

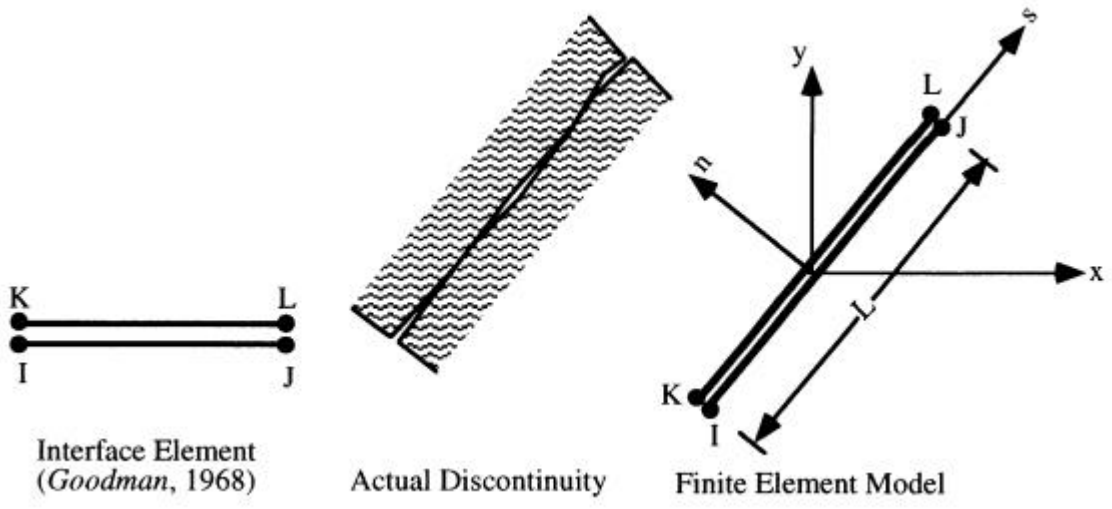

Figure 2.20 A typical interface element used in the modeling of the soil-reinforcement interfaces (*Goodman, 1968*)

2.9 SUMMARY AND CONCLUDING REMARKS

In this chapter, literatures on the existing philosophies of reinforced soil system have been reviewed. The review clearly shows a lot of progress has been achieved since the early publication of Vidal's (1966) concept of soil reinforcement. As Mitchell also pointed out that the research in this field of soil improvement technique has been leading extensively compared to other contemporary soil improvement techniques. In this chapter, the current patterns of the analysis and design of reinforced soil structures are illustrated. It shows similarity as well as diversity in the methodologies and interpretations of results. The following conclusion is drawn based on those preceding sections:

1. Overall strength of the reinforced soil structures increases substantially. Shear stress develops along the reinforcement axis, thus principal stresses also get rotated. The confining pressure and bond length control the maximum tensile force in the reinforcement, and thus, the failure mode of reinforcement is either slippage or rupture.
2. Real reinforcements lie in between two boundaries: inextensible and extensible, which controls the response of the reinforced soil structures. The horizontal earth pressure distribution in the former types (e.g. steel) approaches to K_O condition while in the latter type, it approaches to K_A condition. Creep also affect the structural response and varies with time.
3. Essentially two types of tensile force distribution patterns, with the stiff facing material and without facing material, exist in the literature. The real structure lies in between these two extremes because of yielding during construction.
4. The review by Tatsuoka (1992) on the role of facing has shown significant structural role of the facing in contrast to the conventional assumptions.
5. Force equilibrium and slope stability methods are currently used design methods with some minor modifications. Internal and external stability are checked. All most all the design procedures are over-conservative in nature because of two many unrealistic idealizations. It is because most of the design method are oversimplified and also consist of a lot of design parameters to model the reinforced soil structures. These parameters are difficult to quantify/ identify accurately in the design of real structures.
6. Finite element method (FEM) is getting popular, but, still confined in the research purposes compared to the analysis and design of reinforced soil structures in practice. There are no simple and realistic concepts on modeling the reinforcement and soil-reinforcement interaction and is the main reason for lagging in the application of the FEM into the design of real reinforced soil structures. This aspect is the main fulcrum of the present research.

CHAPTER III FORMULATION OF REINFORCED SOIL SYSTEM

3.1 GENERAL

The aim of the present research work is to present a realistic and simplified numerical method for the analysis and design of real reinforced soil structures. The word "simplified" here implies to the less assumptions made while idealizing a real complex reinforced structures, so that the prediction is close to the performance of the structure after it is erected. Conventional methods of analysis and design of slope stability problems and retaining walls are applied to the complex reinforced soil structures where a lot of assumptions are made before commencing the computation, e.g. computation of factor of safety, reinforcement force distribution, reinforcement soil interface friction, etc., thus, all most all the reinforced structures are over designed (Yako et al, 1987). Unlike these conventional analyses and design methods, the numerical methodology presented in this chapter can compute such variables without making any assumptions before commencing the computation, i.e., the methodology can compute all the variables simultaneously.

This chapter starts with some review on the essence of plasticity theories, then advances to summarization of the rigid plastic finite element method and finally, a new formulation of the reinforced soil system is derived and incorporated into the rigid plastic finite element method (RPFEM). The formulation of the mechanism of a reinforced soil system, derived at the limit state of soil mass is equally applicable to initial loading stage. Thus, the formulation is illustrated by incorporating into the linear elastic finite element method (LEFEM). The applicability of the methodology is illustrated through some typical reinforced soil problems in the next chapter.

3.2 ESSENCE OF *RPFEM* IN SOIL STRUCTURES

In this section, the existing theoretical basis of upper bound theorem for rigid plastic material is briefly discussed and gradually a new formulation is presented in the context of reinforced soil structure. The detailed formulation on RPFEM can be referred to Tamura et al. (1984, 1987), Asaoka et al. (1990, 1992, 1993, 1994) and Kodaka (1993).

3.2.1 Basics on Plasticity Theories

Before we proceed to formulate the soil structure at limit state, some important terms and postulates are summarized. At the outset, a relation between the stresses and the plastic strains is presented based on the Drucker's fundamental quasi-thermo dynamic postulate, also called the Drucker's stability postulate.

***Drucker's Stability Postulate*:**

The Drucker's fundamental quasi-thermo dynamic postulate (Drucker, 1951) states that:

a. If σ_{ij} is a state of stress on the yield surface in which non-vanishing plastic strain rates $\dot{e}_{ij}^{p}$ occur

$$\left(s_{ij} - s_{ij}^{a}\right)\cdot\dot{e}_{ij}^{p} \geq 0 \qquad ...(3.1)$$

for all "allowable" states of stress s_{ij}^{a}. Koiter (1962) has geometrically explained implications of Drucker's principle of maximum work (Eq. 3.1). Koiter (1962) stated that no change in the plastic strains, $\dot{e}_{ij}^{p}$, of an element is assumed to occur if the stress, s_{ij}, point lies in a elastic domain; such a state of stress is called "safe" s_{ij}^{s}. Increments of the plastic strains, $\dot{e}_{ij}^{p}$, can only occur if the stress point is at the boundary of the elastic domain, which is called as yield limit, or in geometric terms the yield surface. A state of stress that is either in the elastic domain or on the yield surface is called "allowable" s_{ij}^{a}. He further stated that the aforesaid condition (Eq. 3.1) has very significant implications and restriction on the shape of yield surface. Thus, Drucker's fundamental postulate entails the following consequences:

b. If ds_{ij} are the stress rates corresponding to the plastic strain rates $\dot{e}_{ij}^{p}$, then the strain rate vector, $\dot{e}_{ij}^{p}$ is normal to the yield surface (Fig. 3.1). Mathematically-

$$ds_{ij}\cdot\dot{e}_{ij}^{p} = 0 \qquad ...(3.2)$$

c. The yield surface is convex.

It should be noted that Drucker's fundamental postulate has consequences only for the plastic strain rates; no statement can be made on the total plastic strains unless the entire history of the element has been specified.

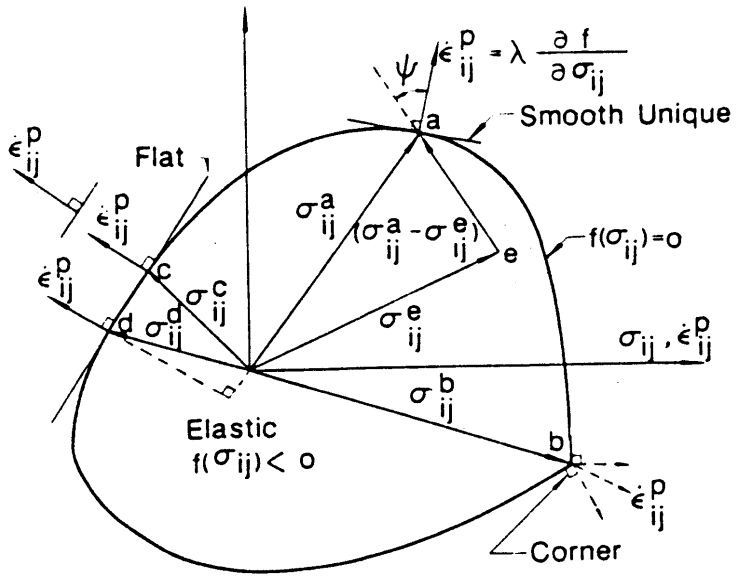

Figure 3.1 Graphical representation of yield surface (*Chen and Liu, 1991*)

Rate of Plastic Energy Dissipation

The rate of plastic energy dissipation per unit volume (i.e. specific volume) is:

$$D(\dot{e}_{ij}^{p}) = s_{ij} \cdot \dot{e}_{ij}^{p} \qquad ...(3.3)$$

where s_{ij} is the state of stress on the yield surface in which the non-vanishing plastic strain rates $\dot{e}_{ij}^{p}$ occur. It is a single valued function of the plastic strain rates that increases proportionally with the increase of the plastic strain rates. The properties of the rate of plastic energy dissipation may be summarized as follows:

a. Since s_{ij} is independent of the magnitude of $\dot{e}_{ij}^{p}$, then $D(\dot{e}_{ij}^{p})$ is linear with $\dot{e}_{ij}^{p}$.

b. The differential of D, is $dD = s_{ij}.d\dot{e}_{ij}^{p} + ds_{ij}.\ \dot{e}_{ij}^{p}$ and $ds_{ij}.\dot{e}_{ij}^{p}$ is zero based on the normality rule. Thus, $dD = s_{ij}.d\dot{e}_{ij}^{p}$.

c. $D(\dot{e}_{ij}^{p})$ is convex in $\dot{e}_{ij}^{p}$ if it is continuously differentiable, e.g. $D(\dot{e}_{ij}^{p})$. (Fig. 3.2).

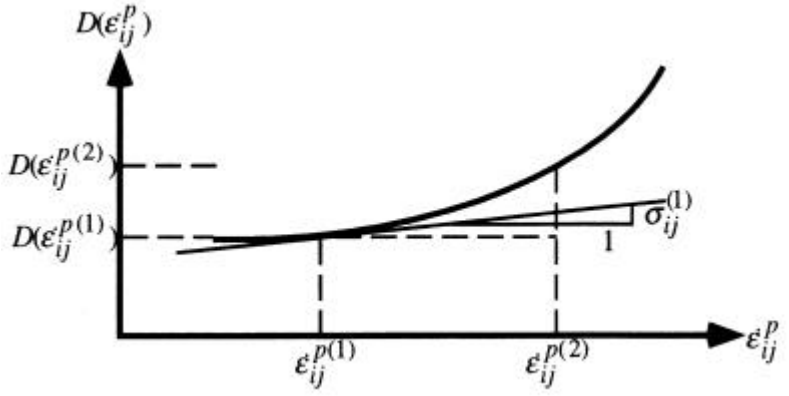

Figure 3.2 Graphical explanation of the convexity and continuously differentiability of the energy function (*Kodaka*, 1993)

d. Though non-vanishing plastic strain rate, $\dot{e}_{ij}^{\,p}$, occurs, Mises material exhibits additional special feature with respect to the rate of volumetric strain at limit state.

Yield function for Mises material, $f(s_{ij}) = \frac{1}{2}(s_{ij}\, s_{ij} - s_o^{\,2})$ ...(3.4)

where, s_o is Mises constant. The corresponding plastic strain rate, $\dot{e}_{ij}^{\,p}$, can be derived following the normality rule:

$$\dot{e}_{ij}^{\,p} = l\,\frac{\partial f}{\partial s_{ij}} = l\, S_{ij} \qquad ...(3.5)$$

here, $l = \dfrac{\bar{\dot{e}}}{s_0}$ is plastic multiplier, and $\bar{\dot{e}} = \sqrt{\dot{e}_{ij}\dot{e}_{ij}}$ is equivalent plastic strain rate. Eq. (3.5) gives the plastic volumetric strain rate, $\dot{e}_v^{\,p}$,as follows:

$$\text{Volumetric plastic strain:} \qquad \dot{e}_v^{\,p} = \dot{e}_{ii}^{\,p} = 0 \qquad ...(3.6)$$

Therefore, when the plastic flow of Mises material is discussed, the plastic strain rate with non-vanishing volumetric component cannot be employed for the computation of plastic energy dissipation. The plastic energy dissipation rate, $D(\dot{e}_{ij}^{\,p})$ for Mises material is given by

$$D(\dot{e}_{ij}^{\,p}) = s_0\,\bar{\dot{e}} \qquad ...(3.7)$$

Likewise some constraint conditions should be imposed on the plastic flow, $\dot{e}_{ij}^{\,p}$, depending on the type of yield function adopted in the analysis.

***Compatibility Condition*:**

The plastic strain rate, $\dot{e}_{ij}^{p}$, can be derived from the velocity, $\dot{u}_i$, by means of the following formula called compatibility relation for small deformation theory:

$$\dot{e}_{ij}^{p} = \frac{1}{2}\left(\dot{u}_{i,j} + \dot{u}_{j,i}\right) \quad in \quad V \qquad ...(3.8)$$

where a comma preceding a subscript *i* denotes partial differentiation with respect to the coordinate X_i. The velocity satisfies the boundary conditions on S_u

$$\dot{u}_i = \dot{u}_{i0} \qquad ...(3.9)$$

***Load Factor*:**

Safety factor/load factor, r corresponding to a given system of external loads X_i, T_i (considering X_i be the body force distribution in V and T_i be the traction on the traction boundary S_σ) is defined as the positive multiplier with the property that the loads rX_i and rT_i constitute a limit load system. In certain cases, the pair (X_i, T_i) implies the external forces of unit magnitude.

***Limiting Equilibrium State*:**

The limit state is defined as the state of equilibrium of forces at which all the soil elements have reached the failure state and their associated plastic strain rates satisfy compatibility conditions with continuous, non-zero velocity field. At limit state, thus, a rigid plastic material (e.g., purely cohesive clay) exhibits following characteristics:

(a) The plastic strain rate, $\dot{e}_{ij}^{p}$, of soil element is indeterminate at the failure state of soil.

(b) The stress, s_{ij}^{*}, on the yield surface, which is derived from, $\dot{e}_{ij}^{p}$, through the associated flow rule, forms a equilibrium state with the external forces $(r^{*}X_i, r^{*}T_i)$.

(c) The volumetric plastic strain rate is zero. ($\dot{e}_{ij}^{p}$=0).

***Upper Bound Theorem*:**

Consider that the X_i, T_i are the given external forces and a new subset Kp ($\grave{I}$ K) may be introduced as follows:

$$K_p = \left\{ \left(\dot{e}_{ij}^{p}, \dot{u}_i\right) \in K \middle| \int_V X_i \dot{u}_i \; dV + \int_{S_s} T_i \dot{u}_i \; dS \geq 0 \right\} \qquad ...(3.10)$$

For any given kinematically admissible strain rate and velocity fields, $(\dot{e}_{ij}^{\,p}, \dot{u}_i) \in K$, the load factor, r, may be defined as follows:

$$r = \frac{\int_V D(\dot{e}_{ij}^{\,p})\ dV}{\int_V X_i \dot{u}_i\ dV + \int_{S_s} T_i \dot{u}_i\ dS} \qquad ...(3.11)$$

The upper bound theorem states

$$r \geq r^* \qquad ...(3.12)$$

where r^* is the load factor at the limit state and this condition introduces the minimization problem of r with respect to $\dot{u}_i$.

As mentioned before, $D(\dot{e}_{ij}^{\,p})$ is linear with $\dot{e}_{ij}^{\,p}$ (or equivalently $\dot{u}_i$.) and other terms in the denominator are also linear with $\dot{u}_i$, therefore, problem of minimization of r with respect to $\dot{u}_i$ can be equivalently replaced by the following problem. In this case, the global shape of spatial distribution of external forces is assumed to be of unit magnitude. There exist an additional constraint condition of no volume change at limit state of soil. Such that the problem reduces to:

Problem A

$$Minimize \int_V D(\dot{u}_i)\ dV \qquad ...(3.13)$$

$$Subject\ to \int_V X_i \dot{u}_i\ dV + \int_{S_s} T_i \dot{u}_i\ dS = 0 \quad and \quad \dot{e}_{kk} = 0 \qquad ...(3.14)$$

3.2.2 Rigid Plastic Finite Element Method (*RPFEM*)

The detailed procedure for the minimization of the internal plastic energy dissipation rate, $D(\dot{u}_i)$, with respect to kinematically admissible velocity field which reduces the upper bound theorem in plasticity to the equilibrium equation of forces at limit state was clearly explained by Tamura et al.(1984) using the finite element discretization technique. In this section, referring Tamura et al.(1984), the limiting equilibrium equations are illustrated through finite element discretized notations. This finite element discretization technique has been called the rigid plastic finite element method (RPFEM) which was pioneered by Tamura et al.(1984) in the field of geotechnical engineering. The following Problem B equivalently replaces using FE discretized notations, the earlier Problem A:

Problem B

$$\begin{aligned} &Minimize \int_V D(\dot{\boldsymbol{u}})\ dV \\ &Subject\ to \begin{cases} \boldsymbol{F}^T \dot{\boldsymbol{u}} = 1 \\ L\,\dot{\boldsymbol{u}} = \boldsymbol{0} \end{cases} \end{aligned} \qquad ...(3.15)$$

in which $\boldsymbol{F}$ is the vector of all nodal forces expressing the shape of external forces of an unit magnitude. L is the matrix defined such as, where $L\dot{\boldsymbol{u}} = \dot{\boldsymbol{v}}$ is the vector of all nodal velocities, while $\dot{\boldsymbol{v}}$ is the rate of volume changes in all elements. The constraint condition, $\boldsymbol{F}^T \dot{\boldsymbol{u}} = 1$, in Eq.(3.15) defines the provisional norms of velocity vector and the other one, $L\,\dot{\boldsymbol{u}} = \boldsymbol{0}$ indicates that no rates of volume change should occur at all elements in the limit state, which reflects the non-dilatant characteristics of the Mises material described later.

The problem defined above falls in the category of a convex programming problem where a local minimum is the global minimum. Introducing the Lagrange multipliers l & m and finally minimizing the following functional have applied the limit analysis based on the upper bound theorem,

$$j\left(\dot{\boldsymbol{u}}, l, m\right) = \int_V D(\dot{\boldsymbol{u}})\, dV + l^T \left(L\dot{\boldsymbol{u}} - \boldsymbol{0}\right) + m\left(\boldsymbol{F}^T \dot{\boldsymbol{u}} - \boldsymbol{1}\right) \qquad ...(3.16)$$

As $D(\dot{\boldsymbol{u}})$ is the convex function of $\dot{\boldsymbol{u}}$, a stationary condition of J gives the global minimum of J. Thus, the finite element formulation of the limit state problems is considered as a problem of finding out the stationary condition for the above functional.

The stationary condition for the above functional corresponding to any virtual variations $d\dot{\boldsymbol{u}}$, dl and dm can be given as follows:

$$\int_V dD(\dot{\boldsymbol{u}})\ dV + l^T L d\dot{\boldsymbol{u}} + m\boldsymbol{F}^T d\dot{\boldsymbol{u}} = 0 \qquad ...(3.17)$$

$$dl^T\ L\dot{\boldsymbol{u}} = 0 \qquad ...(3.18)$$

$$dm\left(\boldsymbol{F}^T \dot{\boldsymbol{u}} - 1\right) = 0 \qquad ...(3.19)$$

Since, $dD = s_{ij}^T\, d\dot{e}_{ij}^p = s^T (B\, d\dot{\boldsymbol{u}}^T)$, then, Eq. (3.17) can be written as:

$$\int_V (s^T B)\ dV + l^T L d\dot{\boldsymbol{u}} + m\boldsymbol{F}^T d\dot{\boldsymbol{u}} = 0 \qquad ...(3.20)$$

In the above equations (Eqs. 3.18~20) $d\dot{\boldsymbol{u}}$, dl and dm can be completely arbitrary provided they are continuous. Therefore, the following equilibrium equations are obtained by eliminating these terms:

Problem C

$$\int_V B^T \boldsymbol{s}\, dV + L^T l + m\boldsymbol{F} = \boldsymbol{0} \qquad \text{...(3.21)}$$

$$L\dot{\boldsymbol{u}} = 0 \qquad \text{...(3.22)}$$

$$\boldsymbol{F}^T \dot{\boldsymbol{u}} = 1 \qquad \text{...(3.23)}$$

in which $\boldsymbol{s}$ denotes deviator stress vector while m is interpreted as load factor of external forces and l as the indeterminate isotropic stress in V**.**

These equilibrium equations can be directly obtained after minimizing the function J with respect to the velocity field, $\dot{\boldsymbol{u}}$, and Lagrange multipliers, l and m, respectively.

Problem D

Often some relations among velocity components at the displacement boundary are assigned a priori such as in the case of loading through the rigid plate. For example, consider the following problem:

$$\text{Minimize } \int_V D(\dot{\boldsymbol{u}})\, dV$$
$$\text{Subject to } \begin{cases} C\dot{\boldsymbol{u}} = \boldsymbol{a} \\ L\dot{\boldsymbol{u}} = \boldsymbol{0} \end{cases} \qquad \text{...(3.24)}$$

in which $\boldsymbol{a}$ is the prescribed vector and Eq. (3.24) is a linear constraint for $\dot{\boldsymbol{u}}$. The function J can be replaced by a new function, Y, as:

$$j(\dot{\boldsymbol{u}}, l, m) = \int_V D(\dot{\boldsymbol{u}})\, dV + l^T(\boldsymbol{L}\dot{\boldsymbol{u}} - \boldsymbol{0}) - m^T(\boldsymbol{C}\dot{\boldsymbol{u}} - \boldsymbol{a}) \qquad \text{...(3.25)}$$

in this problem. Hence, following the similar procedure as before, the stationary condition of Y can be derived in the following form:

$$\int_V B^T \boldsymbol{s}\, dV + L^T l = C^T m \qquad \text{...(3.26)}$$

which can be regarded as the equilibrium condition corresponding to each nodes.
Rigid smooth footing case

$$\dot{u}_{v0} = \dot{u}_0 \qquad \text{...(3.27)}$$

Rigid rough footing plate exhibits following conditions:

$$\dot{u}_{v0} = \dot{u}_0 \text{ and } \dot{u}_{h0} = 0 \qquad \text{...(3.28)}$$

3.2.3 Constitutive Relationship of Soils at the Limiting Equilibrium State

Eqs. (3.21)-(3.23) define statically indeterminate limiting equilibrium problems and they are solved with the aid of a constitutive relationship of soils at the limit state. Two types of soil are considered in the present study and both soils are assumed to exhibit non-dilatant characteristics at limit state. Then, they are assumed to follow the Mises type plastic flow at limit state. In this sub-section, the constitutive relationship of soils at limit state are discussed and compared with the well-known Cam-clay model at the critical state.

Yield Function of Soil and Limiting Equilibrium State

Terzaghi (1936) introduced the concept of effective stress and the mathematical relationship between total stress, effective stress and pore pressure. He defined the effective stress, as *"All measurable effects of a change of stress, such as compression, distortion and a change of shearing resistance are due exclusively to changes of effective stress The effective stress s' is related to the total stress* (s) *and pore pressure* (u) *by* $s' = s - u$". Thus,

$$s'_{ij} = s_{ij} - u\delta_{ij} \qquad \text{...(3.29)}$$

where, s'_{ij} = the effective stress,
s_{ij} = the total stress,
u = the pore pressure and
δ_{ij} = Kroneckor delta (δ_{ij} =1 if i=j, else δ_{ij} =0)

Based on Henkel (1960), it can be stated that the volumetric strain is caused by the effective stress components and independent of stress path. The volumetric strain can be mathematically represented as:

$$\varepsilon_v = \varepsilon_v(s'_{ij}, s'_{ij0}) \qquad \text{...(3.30)}$$

The total volumetric strain can be separated into two elastic and plastic components, $\varepsilon_v = \varepsilon_v^e + \varepsilon_v^p$. The elastic component of the volumetric strain, i.e. $\varepsilon_v^e = \varepsilon_v^e(s'_{ij}, s'_{ij0})$, is reversible.

In the present study soils are assumed to follow the associated flow rule with the following type of yield function in terms of effective stresses:

$$\varepsilon_v^p = f(s'_{ij}, s'_{ij0}) \qquad \text{...(3.31)}$$

in which the plastic volumetric strain, ε_v^p, is considered as a hardening parameter, s'_{ij} represent the current effective stress and $s'_{ij\,o}$ represent initial effective stress which gives reference state from which plastic strain rate begins to be measured, i.e., $\dot{\varepsilon}_v^p$ =0 when $s'_{ij} = s'_{ij\,o}$.

From Eq. (3.31),

$$de_v^p = df = \frac{\partial f}{\partial s'_{kl}} ds'_{kl} \qquad ...(3.32)$$

The critical state is defined here as the state at which the magnitude of plastic strain increment becomes indeterminate even when no increments of stresses(ds'_{kl} =0) are applied. When no increments of stresses are considered, it follows from Eq.(3.32) that

$$\dot{e}_v^p = \dot{e}_v^e = 0 \qquad \text{at critical state.} \qquad ...(3.33)$$

Note that ($de_{ij}^p = \dot{e}_{ij}^p \, dt$ *where dt is a scalar quantity*)

Now, based on the associated flow rule,

$$de_{ij}^p = \lambda \frac{\partial f}{\partial s'_{ij}} \qquad ...(3.34)$$

After some mathematical manipulations of Eq. (3.33~3.34), one gets the plastic multiplier as follows:

$$\lambda = \frac{\frac{\partial f}{\partial s'_{kl}} ds'_{kl}}{\frac{\partial f}{\partial s'_{mn}} . d_{mn}} \qquad ...(3.35)$$

Finally, the plastic strain rate is given by:

$$de_{ij}^p = \frac{\frac{\partial f}{\partial s'_{kl}} ds'_{kl}}{\frac{\partial f}{\partial s'_{mn}} d_{mn}} \frac{\partial f}{\partial s'_{ij}} \qquad ...(3.36)$$

Thus, based on the normality assumption [Eq. (3.34)], the critical state condition in terms of effective stresses is obtained so that plastic multiplier [Eq. (3.35)] may become indeterminate under no incremental stress condition, that is

$$\frac{\partial f}{\partial s'_{mn}} d_{mn} = 0 \qquad ...(3.37)$$

At the critical state, it should also be noted that no rate of volume change should occur, whereas the magnitude of other plastic strain rate components, $\dot{e}_{ij}^p$, are still indeterminate [Eq. (3.36)].

In this study, the state of equilibrium of forces at which all the soil elements have reached the critical state is called the limit equilibrium state. Their associated plastic strain rates at limit state should satisfy compatibility conditions with non-zero velocity field.

At the critical state, the stress-strain rate relationship can be written concretely only when yield function is identified. The stress-strain rate relationship is demonstrated through the well-known yield function for the Cam-clay model.

Critical State of Soils in the Perspective of Cam-clay Model

Researchers at Cambridge University derived a very simple theoretical formulation of the critical state of soils during 1960s (e.g., Roscoe et al., 1963). Over the years many researchers have modified the original Cambridge Model called "*Cam-clay Model*" (Roscoe-Burland, 1968; Sekiguchi-Ohta, 1977; etc.). All the theories within the Cam clay family are basically similar. The state boundary surface is taken as a yield surface as well as a plastic potential surface, and the hardening is related to the plastic volumetric strain given by following equation:

$$e_v^p = f = M D \ln\frac{p'}{p'_o} + D\, h' \qquad ...(3.38)$$

where, f = yield function,

M = material parameter of soil at critical state,

D = dilatancy parameter of soil

p' = σ_m', mean effective stress,

p_o' = mean effective stress at reference state such that (when q=0, p'=p_o')

q = $\sqrt{\frac{3}{2} s_{ij} s_{ij}}$ deviator stress = $\sqrt{\frac{3}{2}} s_o$ (for Mises Material)

h' = effective stress ratio=q/p',

The critical state condition (Eq. 3.37)

$$\frac{\partial f}{\partial s'_{mn}} d_{mn} = 0 \qquad ...(3.39)$$

After simple manipulations, Eq.(3.38) at the critical state condition reduces to the following simple form:

$$q = M p' \qquad ...(3.40)$$

where M is a critical state parameter. Following the associated flow rule, $de_{ij}^p = \lambda \frac{\partial f}{\partial s'_{ij}}$, the plastic strain rate de_{ij}^p in Cam-clay model at critical state is as follows:

$$de_{ij}^{p} = \lambda \left(\frac{D}{p'} \frac{\partial q}{\partial s'_{ij}} \right) \qquad ...(3.41)$$

Differentiating $q = \sqrt{\frac{3}{2} s_{ij} s_{ij}}$, one gets,

$$\frac{\partial q}{\partial s'_{ij}} = \frac{3}{2} \left(\frac{3}{2} s_{ij} s_{ij} \right)^{-\frac{1}{2}} s_{ij} \qquad ...(3.42)$$

Then, de_{ij}^{p} is simplified as:

$$de_{ij}^{p} = \lambda \frac{D}{p'} \frac{3}{2} \left(\frac{3}{2} s_{ij} s_{ij} \right)^{-\frac{1}{2}} s_{ij} \qquad ...(3.43)$$

Defining a new term called equivalent plastic strain rate:

$$\bar{\dot{e}} = \sqrt{\dot{e}_{ij} \dot{e}_{ij}} = \sqrt{\frac{3}{2}} \lambda \frac{D}{p'} \qquad ...(3.44)$$

Thus, the plastic multiplier in the Cam-clay model is:

$$\lambda = \frac{\bar{\dot{e}}}{\sqrt{\frac{3}{2}} \frac{D}{p'}} \qquad ...(3.45)$$

Substituting Eq.(3.45) in Eq.(3.43) and after some mathematical manipulations, one gets,

$$\dot{e}_{ij}^{p} = \sqrt{\frac{3}{2}} \frac{\bar{\dot{e}}}{M} \lambda \frac{1}{p'} s_{ij} \qquad ...(3.46)$$

Thus, the normality rule uniquely determines the direction of plastic strain rate in terms of stresses at the critical state whereas the norm of strain rate is still remains indeterminate. Eq.(3.46) shows that the plastic flow of Cam clay at critical state is absolutely identical to the plastic flow of rigid plastic Mises material, i.e. $d\varepsilon_{ij}^{p} = \lambda s_{ij}$.

The plastic energy dissipation rate in Cam-clay model at critical state can be obtained by substituting Eq.(3.45) in Eq.(3.46) and after some mathematical steps as follows:

$$\begin{aligned} D(\dot{e}_{ij}^{p}) &= d s_{ij} \dot{e}_{ij}^{p} \\ &= \sqrt{\frac{2}{3}} M p' \bar{\dot{e}} \end{aligned} \qquad ...(3.47)$$

For Mises material, $q = \sqrt{\frac{3}{2}} s_0$, the plastic energy dissipation rate is given by,

$$D(\dot{e}_{ij}^{p}) = s_0 \, \bar{\dot{e}} \qquad ...(3.48)$$

Cam-clay model at the critical state and Mises material resembles similarity regarding the plastic energy dissipation rate.

Generally, the limiting equilibrium state of saturated soil is solved taking into account of drainage conditions during loading state before reaching the limit state. In the present study, non-dilatant characteristics are assumed at the limit state. Two distinct states are usually discussed, first one is undrained problem and the other, fully drained problem. Most real problems lie in between these two extreme states during loading over saturated soil mass; however, these two states are discussed here for the illustration purposes.

UNDRAINED CONDITION (e.g. *purely cohesive clay*)

In the analysis of undrained problems, no flow of water into or out of any soil element during entire loading procedure is assumed and called as the undrained loading. Because of undrained condition, the soil is assumed to exhibit constant volume throughout the undrained loading procedure. This characteristics provides unique undrained path from the initial stress state to the critical state of the soil element, thus exhibit unique shear strength at failure. When undrained loading for the Cam-clay model is considered, the mean effective stress state at limit state can be determined from the initial effective stress state, and is independent of the boundary conditions for the undrained loading. The mean effective stress state at the limit state for undrained loading is given by:

$$(p')_f = p'_0 \, exp(-L), \quad where \quad L = 1 - \frac{k}{l} \qquad ...(3.49)$$

where l and κ are compression and swelling indices, respectively. In real problems, the soil exhibiting very low permeability is assumed to reach the failure state under undrained condition, therefore the shear strength of the soil, i.e. material constant, is already known before loading procedure is commenced. Such a soil is generally known as "purely cohesive soil".

In Japanese practice, the unconfined compressive strength, c_u, is frequently used in the design and analysis of grounds having such purely cohesive clays. The undrained strength of such clay, c_u, is shown to give following relationship:

$$c_u = \frac{s_1 - s_3}{2} \qquad ...(3.50)$$

in which s_1 and s_3 are the maximum and the minimum principal stresses, respectively. Since

deviator stress, q, is $\sqrt{3}c_u$ in the plane strain conditions, the following relationship is derived:

$$\sigma_0 = \sqrt{2}c_u \qquad ...(3.51)$$

FULLY DRAINED CONDITION (*e.g. Sandy soils*)

In the fully drained loading problems, the excess pore pressure distribution at limit state is always assumed dissipated (Du_f=0). Thus, the flow of water in such fully drained (Du_f=0) soil mass can be computed independent of failure mechanism. Such a condition usually observed in the case of soils exhibiting high permeability e.g. sandy soils. In the fully drained problems, therefore, the mean effective stress at critical state is given by:

$$(p')_f = (p)_f - u_s \qquad ...(3.52)$$

when, $$(Du)_f = 0 \qquad ...(3.53)$$

where u_S is the pore pressure distribution at limit state assigned as priori (before loading) and p_f is the mean total stress that should be given by a solution of l in limiting equilibrium equations. Then, Eq.(3.52) should be solved simultaneously with Eqs.(3.21~23), and with constitutive equations at critical state, Eq. (3.43). In this numerical method, the mean effective stress is assumed arbitrarily in the very first step of the iterations and is modified in all the subsequent steps using Eq.(3.52) at the limit state solutions. The limit state reached under fully drained condition has no effect of the initial stress. Thus, the fully drained analysis using aforementioned numerical procedure (Cam-clay model at critical state) requires only one additional material parameter, the critical state parameter, *M* in addition to the unit weight of soil. Furthermore, the similarity between Cam-clay model at the critical state and Mises material has been demonstrated. The Mises constant, s_o, is considered to exhibit similarity with the critical state parameter, *M*, in Cam-clay model and the relationship can be written as follows:

$$\sigma_o = \sqrt{\frac{2}{3}}\, Mp'_f \qquad ...(3.54)$$

In the case of purely cohesive soil, $p'_f(s_o)$ is unique for each soil element before loading procedure as an independent of the boundary conditions. But, in this drained condition, the p'_f is the solution of the boundary value problem because the $p'_f(s_o)$ depends on the p_f as shown earlier in Eq. (3.52). Therefore, the iterative method is required to solve this problem as stated before. It should be noted here that the shear strength in this case are different for each element because the void ratio can be easily changed due to the flow of pore water.

In real problems, especially, when the reinforced soil in sandy soil slopes is considered the

fully drained cases are very few whereas almost all the cases are either in dry or in unsaturated conditions where the pore water flow does not exist. The relationship between p'_f and p' in such cases can, therefore, be written as follows:

$$p'_f = p_f \qquad \text{...(3.55)}$$

In the practical design, the internal friction angle, f, is frequently used. As the relationship between f and M is written as $M = \sqrt{3}\ \sin f$ under the plane strain condition, then the Mises constant σ_o can be expressed as follows:

$$s_0 = \sqrt{2}\ p_f \sin f \qquad \text{...(3.56)}$$

As far as the unsaturated soil is concerned, the cohesion, c, should also be taken into account. Referring both the Drucker-Prager type failure criteria as well as the Mohr's circle envelope, the following relation is obtained for the plane strain condition (Tamura et al., 1987).

$$s_0 = \sqrt{2}\ c \cos f + \sqrt{2}\ p'_f \sin f \qquad \text{...(3.57)}$$

It should be noted that Eq. (3.57) is not a yield function but just a failure criteria adopted in this study exactly same as $q=Mp'$. In the case of sandy soil (c=0), Eq. (3.57) reduces to Eq. (3.56) and in the case of f=0, purely cohesive soil, Eq. (3.57) reduces to Eq. (3.51). As the principle of effective stress cannot be discussed concerning the unsaturated soils, therefore, it is not yet known whether the unsaturated soil exhibits the Mises flow at the critical state. However, Mises flow is assumed in the present study it as in the saturated purely cohesive soil.

The structure of sandy soil is; therefore, modeled as an assembly of the inhomogeneous Mises materials where each soil part consists of different σ_o with respect to corresponding confining pressure, *see* Fig. 3.3. In this case, the limit equilibrium equation is solved iteratively because the Mises constant σ_o here is a function of the mean effective stress l (i.e., p_f') as shown in Eq. (3.57). The iterative procedure is illustrated through the flow chart as shown in Fig. 3.4. Through the flow chart (Fig. 3.4), it can be observed that this problem seems to follow the non-associated flow rule (Tamura et al., 1987), however, the solutions obtained by iterative calculations satisfy the associated flow rule once convergence is achieved.

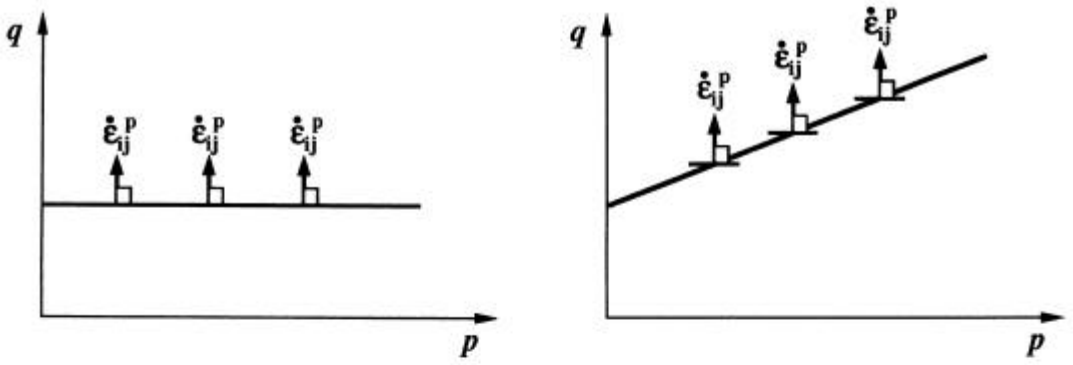

Figure 3.3 Idealization of the frictional (c-ϕ) as an assembly of inhomogeneous Mises materials of varying, σ_O.

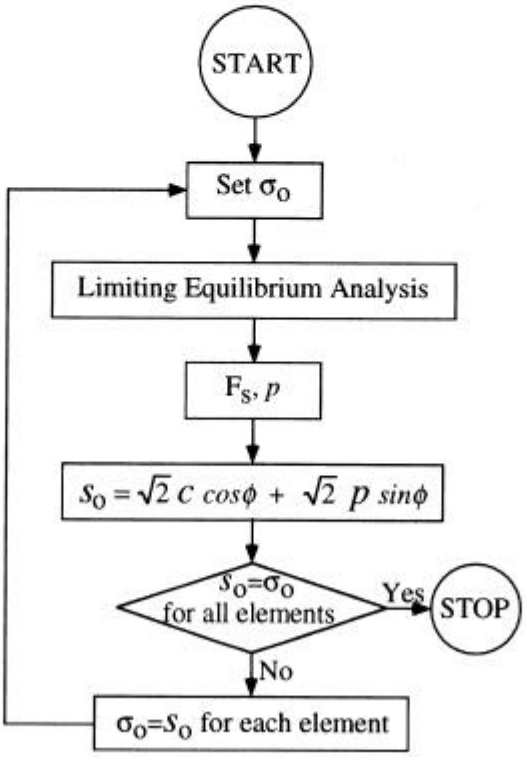

Figure 3.4 Flow Chart adopted for the Numerical Simulations based on RPFEM

3.2.4 Numerical Procedures and Example

Assume that the whole region is in plastic state without unloading. Substituting Eq.(3.5) in to Eq.(3.21) we have the following system of non linear equations for $\dot{\boldsymbol{u}}$, l and m.

$$\left(s_0 \int_V \frac{B^T Q B}{\bar{\dot{e}}} \right) \dot{\boldsymbol{u}} + \boldsymbol{L}^T l = m\boldsymbol{F} \qquad ...(3.58)$$

$$L\dot{\boldsymbol{u}} = 0 \qquad ...(3.59)$$

$$\boldsymbol{F}^T \dot{\boldsymbol{u}} = 1 \qquad ...(3.60)$$

In the above σ_0 is the only one material constant for the analysis. The plastic strain rate calculated by Eq.(3.57) has obviously no volumetric component.

$$\bar{\dot{e}} = \sqrt{\dot{\boldsymbol{u}}^T B^T Q B \dot{\boldsymbol{u}}} \qquad ...(3.61)$$

where , $$Q = \begin{bmatrix} 1 & 0 & 0 \\ 0 & 1 & 0 \\ 0 & 0 & \frac{1}{2} \end{bmatrix} \qquad ...(3.62)$$

The equation, Eq.(3.61), can be derived as follows:

$$\begin{aligned} \bar{\dot{e}} &= \sqrt{\dot{e}_{ij}^p \dot{e}_{ij}^p} = \sqrt{\dot{e}_x \dot{e}_x + \dot{e}_z \dot{e}_z + 2\dot{e}_{xz} \dot{e}_{xz}} \\ &= \sqrt{\dot{e}_x \dot{e}_x + \dot{e}_z \dot{e}_z + 2\dot{g}_{xz} \dot{g}_{xz}} \\ &= \sqrt{\dot{e}^? Q \dot{e}} = \sqrt{\dot{\boldsymbol{u}}^? B^T Q B \dot{\boldsymbol{u}}} \end{aligned} \qquad ...(3.63)$$

The above set of simultaneous equations, Eqs. (3.58~60) are iteratively solved. Thus, $\dot{\boldsymbol{u}}_{(n)} = \dot{\boldsymbol{u}}_{(n-1)} + aD\dot{\boldsymbol{u}}_{(n-1)}$, $a \geq 0$ in every nth step of calculations. The multiplier α is used to control the rate of convergence and generally varies between 0.1 and 1.0 depending on the state of convergence. In all the calculation, the $\Delta \dot{\boldsymbol{u}}_{(n)}$ computed till it practically diminishes to zero i.e. $\dot{\boldsymbol{u}}_{(n)} = \dot{\boldsymbol{u}}_{(n-1)}$.

$$\left(s_0 \int_V \frac{B^T Q B}{\bar{\dot{e}}} \right) (\dot{\boldsymbol{u}} + D\dot{\boldsymbol{u}}) + \boldsymbol{L}^T l - m\boldsymbol{F} = 0 \qquad ...(3.64a)$$

or,

$$\left(s_0 \int_V \frac{B^T Q B}{\bar{\dot{e}}} \right) \dot{\boldsymbol{u}} + \boldsymbol{L}^T l - m\boldsymbol{F} + \frac{\partial \left\{ \left(s_0 \int_V \frac{B^T Q B}{\bar{\dot{e}}} \right) \dot{\boldsymbol{u}} \right\}}{\partial \dot{\boldsymbol{u}}} D\dot{\boldsymbol{u}} = 0 \qquad \text{...(3.64b)}$$

or,

$$\frac{\partial \left\{ \left(s_0 \int_V \frac{B^T Q B}{\bar{\dot{e}}} \right) \dot{\boldsymbol{u}} \right\}}{\partial \dot{\boldsymbol{u}}} = \left(s_0 \int_V \frac{B^T Q B}{\bar{\dot{e}}} \right) - \left(s_0 \int_V \frac{B^T Q B \dot{\boldsymbol{u}}_e}{\bar{\dot{e}}^2} \right) \bullet \frac{\partial \bar{\dot{e}}}{\partial \dot{\boldsymbol{u}}_e} \qquad \text{...(3.65)}$$

$$= \int_V s_0 \left(\frac{B^T Q B}{\bar{\dot{e}}} - \frac{B^T Q B \dot{\boldsymbol{u}}_e \dot{\boldsymbol{u}}_e B^T Q B}{\bar{\dot{e}}^3} \right) dV$$

Thus,

$$\frac{\partial \bar{\dot{e}}}{\partial \dot{\boldsymbol{u}}_e} = \frac{\partial \sqrt{(B\dot{\boldsymbol{u}}_e)^T Q B \dot{\boldsymbol{u}}_e}}{\partial \dot{\boldsymbol{u}}_e} = \frac{1}{\bar{\dot{e}}} \dot{\boldsymbol{u}}_e{}^T B^T Q B \qquad \text{...(3.66)}$$

Similarly,

$$L\dot{\boldsymbol{u}} + LD\dot{\boldsymbol{u}} = 0 \qquad \text{...(3.67)}$$

$$\boldsymbol{F}^T \dot{\boldsymbol{u}} + \boldsymbol{F}^T D\dot{\boldsymbol{u}} = 1 \qquad \text{...(3.68)}$$

Finally, the following equations are solved for $D\dot{\boldsymbol{u}}$, l and m.

$$\int_V s_0 \left(\frac{B^T Q B}{\bar{\dot{e}}} - \frac{B^T Q B \dot{\boldsymbol{u}}_e \dot{\boldsymbol{u}}_e B^T Q B}{\bar{\dot{e}}^3} \right) dV \, D\dot{\boldsymbol{u}} + \boldsymbol{L}^T l - m\boldsymbol{F} = -\left(\int_V s_0 \frac{B^T Q B}{\bar{\dot{e}}} \right) \dot{\boldsymbol{u}} \qquad (3.69a)$$

$$LD\dot{\boldsymbol{u}} = -L\dot{\boldsymbol{u}} \qquad \text{…(3.69b)}$$

$$\boldsymbol{F}^T D\dot{\boldsymbol{u}} = 1 - \boldsymbol{F}^T \dot{\boldsymbol{u}} \qquad \text{…(3.69c)}$$

3.3 FORMULATION OF REINFORCED SOIL SYSTEM

3.3.1 Axial Force: *"no-length change" Condition*

As mentioned in the introduction, the concept we assume is that the length between arbitrary soil element nodes touching the reinforcement material does not change in the soil mass at failure. In other words, the soil elements flow with the reinforcing material keeping the length constant in the soil mass at the limiting equilibrium state. Under this condition the reinforcing material restrains the flow of soil elements (i.e. plastic flow) keeping the nodal distance constant. It should be noted that the real reinforcing steel bars or geotextiles never appear in this computational work.

Let us incorporate this reinforced mechanism in RPFEM. Referring Fig. 3.6, let A and B are soil element nodes touching the reinforcing material and having positions vectors $\boldsymbol{X}_1$ and $\boldsymbol{X}_2$, respectively. Now, consider $\boldsymbol{l}$ ($=\boldsymbol{X}_2-\boldsymbol{X}_1$) is displaced to $\boldsymbol{l}+D\,\boldsymbol{l}$ in arbitrary small time dt at failure. Meanwhile, it is assumed that the relative position between A and B remains constant during plastic flow. Mathematically,

$$|\boldsymbol{l}\quad| = |\,\boldsymbol{l}+D\,\boldsymbol{l}\,| \qquad ...(3.70)$$

Therefore,

$$(\boldsymbol{l}+D\,\boldsymbol{l}\quad)^T\quad(\boldsymbol{l}+D\,\boldsymbol{l}\,) - \quad \boldsymbol{l}^T\boldsymbol{l}\quad =0 \qquad ...(3.71)$$

$$\boldsymbol{l}^T\boldsymbol{l} + \boldsymbol{l}^T D\,\boldsymbol{l}\quad + D\,\boldsymbol{l}^T\boldsymbol{l}\quad + D\,\boldsymbol{l}^T D\,\boldsymbol{l}\quad - \quad \boldsymbol{l}^T\boldsymbol{l}\quad = \boldsymbol{0} \qquad ...(3.72)$$

where T implies the transpose of vector (or Matrix)

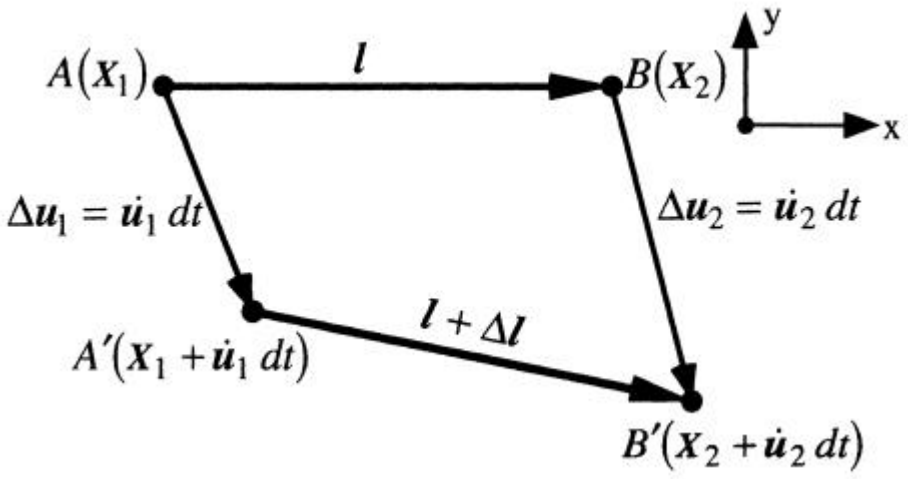

Figure 3.6 Concept of "*no-length change*" condition at limiting equilibrium state.

After some mathematical manipulations, i.e. neglecting higher order terms, Eq.(3.72) is reduced to the following form,

$$\boldsymbol{l}^T D\,\boldsymbol{l} = 0 \qquad \text{...(3.73)}$$

Referring Fig. 3.6, the vector $D\,\boldsymbol{l}$ can be expanded as follows:

$$\boldsymbol{l} + D\boldsymbol{l} = \boldsymbol{X}_2 + D\boldsymbol{u}_2 - (\boldsymbol{X}_1 + D\boldsymbol{u}_1) \qquad \text{...(3.74)}$$

or, $$\boldsymbol{l} + D\boldsymbol{l} = \boldsymbol{X}_2 - \boldsymbol{X}_1 + (D\boldsymbol{u}_2 - D\boldsymbol{u}_1) \qquad \text{...(3.75)}$$

Since $\boldsymbol{l} = (\boldsymbol{X}_2 - \boldsymbol{X}_1)$ in Fig. 3.6, then vector $D\,\boldsymbol{l}$ reduced to the following form:

$$D\boldsymbol{l} = D\boldsymbol{u}_2 - D\boldsymbol{u}_1 = \dot{\boldsymbol{u}}_2 dt - \dot{\boldsymbol{u}}_1 dt \; D\boldsymbol{l} = D\boldsymbol{u}_2 - D\dot{\boldsymbol{u}}_1 = \dot{\boldsymbol{u}}_2 dt - \dot{\boldsymbol{u}}_1 dt \qquad \text{...(3.76)}$$

where $D\,\dot{\boldsymbol{u}}_1$ and $D\,\dot{\boldsymbol{u}}_2$ are the displacements of A and B in arbitrary time dt and $\dot{\boldsymbol{u}}_1$ and $\dot{\boldsymbol{u}}_2$ are the velocities corresponding to A and B respectively. After eliminating the scalar quantity dt the equation reduces to

$$(\boldsymbol{X}_2 - \boldsymbol{X}_1)^T (\dot{\boldsymbol{u}}_2 - \dot{\boldsymbol{u}}_1) = 0 \qquad \text{...(3.77)}$$

Since $\boldsymbol{X}_1 \neq \boldsymbol{X}_2$ the velocities obtained by employing the constrained condition of no length change should satisfy either of the following relations:

$$\text{Either} \quad \dot{\boldsymbol{u}}_1 = \dot{\boldsymbol{u}}_2 \quad \text{or} \quad (\boldsymbol{X}_2 - \boldsymbol{X}_1) \perp (\dot{\boldsymbol{u}}_2 - \dot{\boldsymbol{u}}_1) \qquad \text{...(3.78)}$$

Now, expanding the position vectors and velocity vectors

$$\boldsymbol{X}_1 = \begin{pmatrix} x_1 \\ y_1 \end{pmatrix} \quad \boldsymbol{X}_2 = \begin{pmatrix} x_2 \\ y_2 \end{pmatrix} \quad \dot{\boldsymbol{u}}_1 = \begin{pmatrix} \dot{u}_{x1} \\ \dot{u}_{y1} \end{pmatrix} \quad \dot{\boldsymbol{u}}_2 = \begin{pmatrix} \dot{u}_{x2} \\ \dot{u}_{y2} \end{pmatrix} \qquad \text{...(3.79)}$$

and incorporating these terms in Eq. (3.77)

$$(x_2 - x_1)(\dot{u}_{x2} - \dot{u}_{x1}) + (y_2 - y_1)(\dot{u}_{y2} - \dot{u}_{y1}) = 0 \qquad \text{...(3.80)}$$

The equation Eq.(3.80) can be presented in the following matrix form:

$$\begin{Bmatrix} (x_2 - x_1) & (y_2 - y_1) & -(x_2 - x_1) & -(y_2 - y_1) \end{Bmatrix} \begin{Bmatrix} \dot{u}_{x1} \\ \dot{u}_{y1} \\ \dot{u}_{x2} \\ \dot{u}_{y2} \end{Bmatrix} = 0 \qquad \text{...(3.81)}$$

Since Eq. (3.77)(or Eq. (3.80)) is a linear algebraic equation, we can easily incorporate this in the RPFEM/LEFEM as a constrained condition. This constrained condition represents a basic reinforcing element and it can be extended to other continuous reinforcing members by discretizing them into finite numbers of such basic discrete elements. Such procedure is illustrated in the next paragraphs.

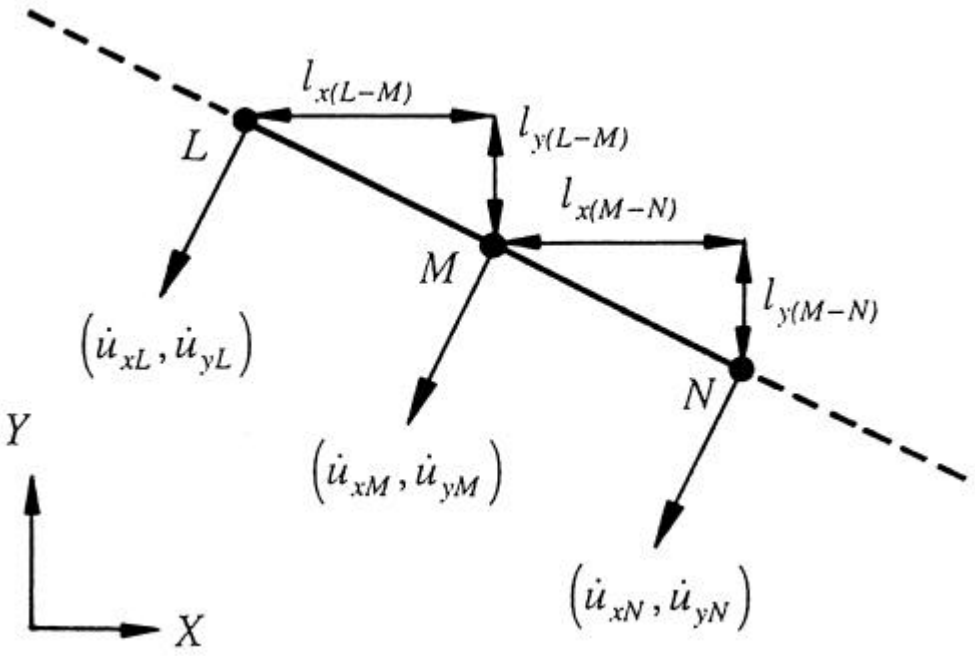

Figure 3.7 Graphical explanation of length components for a typical reinforcing element under axial tension.

Consider three nodes L, M and N are constrained by the reinforcing system as shown in Figs. 3.7 and 3.8. Then, the x and y components of the length vector between nodes L and M are:

$$l_{x(L-M)} = x_2 - x_1 \qquad \text{and} \qquad l_{y(L-M)} = y_2 - y_1 \qquad ...(3.82)$$

Thus, replacing the Cartesian components by absolute length components, the constrained condition corresponding to nodes L & M can be simplified to:

$$\begin{pmatrix} l_{x(M-N)} & l_{y(M-N)} & -l_{x(M-N)} & -l_{y(M-N)} \end{pmatrix} \begin{Bmatrix} \dot{u}_{xM} \\ \dot{u}_{yM} \\ \dot{u}_{xN} \\ \dot{u}_{yN} \end{Bmatrix} = 0 \qquad ...(3.83)$$

and similarly for nodes M & N:

$$\left(l_{x(M-N)} \quad l_{y(M-N)} \quad -l_{x(M-N)} \quad -l_{y(M-N)}\right)\begin{Bmatrix} \dot{u}_{xM} \\ \dot{u}_{yM} \\ \dot{u}_{xN} \\ \dot{u}_{yN} \end{Bmatrix} = 0 \qquad \text{...(3.84)}$$

Such equations corresponding to all reinforcing element nodes can be finally assembled into the following single equation:

$$C_t \ \dot{\boldsymbol{u}} = 0 \qquad \text{...(3.85)}$$

which is equivalent to Eq. (3.77) or Eq. (3.80). The matrix C_t produces a set of equations similar to Eq.(3.80) when all nodal velocity vectors are multiplied by C_t . Thus, these equations represent the "*constrained conditions*" for the respective reinforcing element nodes.

The assembled positions of the aforementioned reinforcing element nodes is illustrated in the following expanded form of matrix C_t .

$$(C_t) = \begin{pmatrix} & .... & .... & .... & .... & .... & .... & \\ 0 & l_{x(L-M)} & l_{y(L-M)} & -l_{x(L-M)} & -l_{y(L-M)} & 0 & 0 & 0 \\ 0 & 0 & 0 & l_{x(M-N)} & l_{y(M-N)} & -l_{y(M-N)} & -l_{y(M-N)} & 0 \\ & & .... & .... & .... & .... & .... & \end{pmatrix} \text{.(3.86)}$$

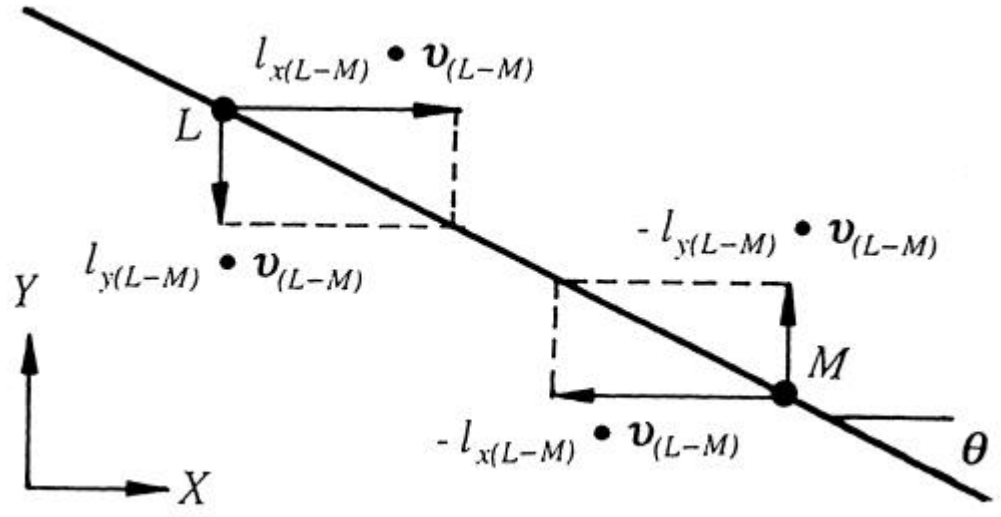

Figure 3.8 Graphical explanation of Lagrange multipliers corresponding to the linear constraint condition of "*no-length change*" condition.

3.3.2 Shear Force/Bending Moment: "*no-bending*" *Condition*

In this study, it is assumed that the soil elements along a reinforcing material that is practically rigid in bending (e.g. facing panel, shotcrete, sheet pile, etc.) do not change their relative positions during the plastic flow of soil elements at limit state.

In Figure 3.9, the three points A, B and C make a straight line and maintain the straight line throughout the limiting equilibrium state of soil mass. The no-bending condition, here, is formulated along with the no-length change condition imposed on the corresponding reinforced soil element nodes. Mathematically, the no-length change condition for a reinforcement means the displacement components parallel to the reinforcement are assumed to be constant as follows:

$$|D\boldsymbol{u}_i| \cos\beta_i = \text{constant} \qquad ...(3.87)$$

or, in velocity terms

$$|\dot{\boldsymbol{u}}_i| \cos\beta_i \, dt = \text{constant} \qquad ...(3.88)$$

where dt is a scalar quantity and thus satisfies. $|\dot{\boldsymbol{u}}_i| = |\boldsymbol{u}_i| \, dt$ Then, referring the Figs.3.9~3.11,

$$|\dot{\boldsymbol{u}}_1| \cos\beta_1 = |\dot{\boldsymbol{u}}_2| \cos\beta_2 = |\dot{\boldsymbol{u}}_3| \cos\beta_3 \qquad ...(3.89)$$

In order to formulate the no-bending condition under the no-length change assumption (Eq. 3.87), the following condition is introduced in this study:

$$|l_1| : (|\dot{\boldsymbol{u}}_2| \sin\beta_2 - |\dot{\boldsymbol{u}}_1| \sin\beta_1) = |l_2| : (|\dot{\boldsymbol{u}}_3| \sin\beta_3 - |\dot{\boldsymbol{u}}_2| \sin\beta_2) \qquad ...(3.90)$$

which yields,

$$-|l_2||\dot{\boldsymbol{u}}_1| \sin\beta_1 + (|l_1| + |l_2|)|\dot{\boldsymbol{u}}_2| \sin\beta_2 - |l_1||\dot{\boldsymbol{u}}_3| \sin\beta_3 = 0 \qquad ...(3.91)$$

The first term of Eq. (3.91) is simplified as follows:

$$\begin{aligned} |l_2|\,|\dot{\boldsymbol{u}}_1| \sin\beta_1 &= |l_2| AD = |l_2| A'E = |l_2|(A'E' - E'E) = |l_2|(A'E' - FF') \\ &= |l_2|\,|\dot{\boldsymbol{u}}_1| \sin(\alpha+\beta_1)\cos\alpha - |l_2|\,|\dot{\boldsymbol{u}}_1| \cos(\alpha+\beta_1)\sin\alpha \\ &= |l_2| \cos\alpha\, |\dot{\boldsymbol{u}}_1| \sin(\alpha+\beta_1) - |l_2| \sin\alpha\, |\dot{\boldsymbol{u}}_1| \cos(\alpha+\beta_1) \\ &= l_{2x}\, \dot{u}_{1y} - l_{2y}\, \dot{u}_{1x} \end{aligned} \qquad ...(3.92)$$

in which the subscripts x and y express the Cartesian components of vectors. Geometrically various components of velocity $\dot{\boldsymbol{u}}_1$ are illustrated in Fig.3.11. The length components for a typical bending element are illustrated in Fig. 3.11.

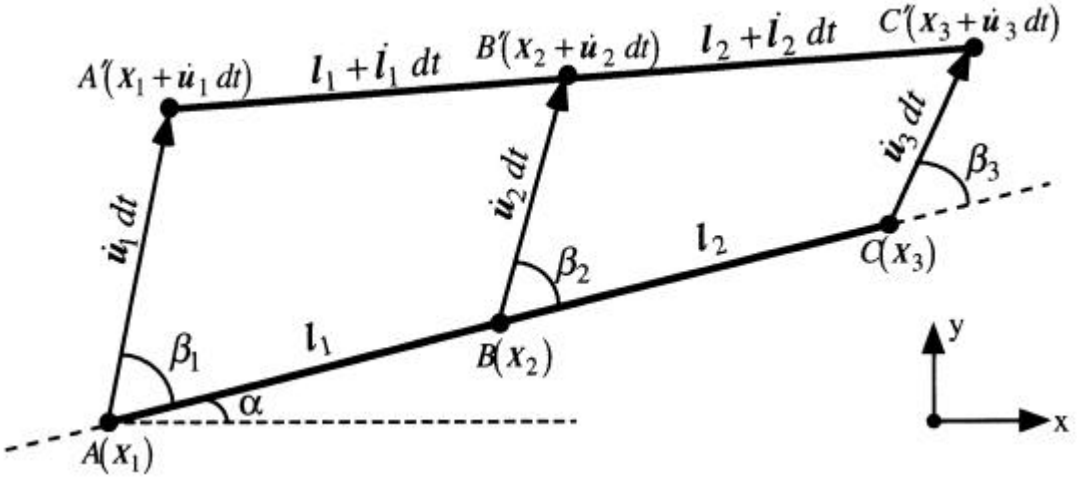

Figure 3.9 Concept of "*no-bending*" condition at limiting equilibrium state

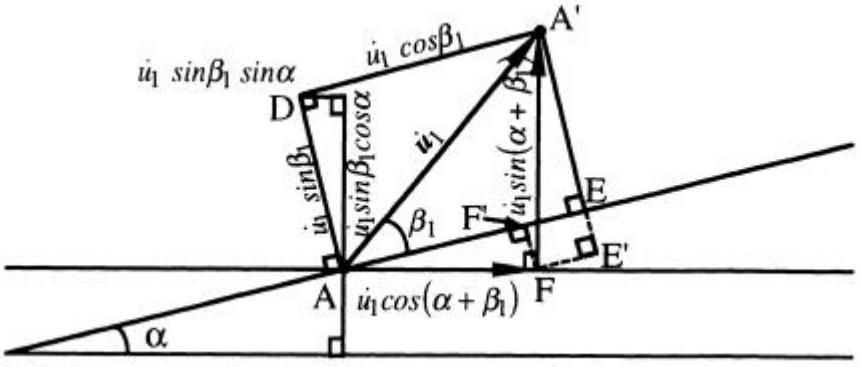

Figure 3.10 Graphical details of length components for a typical velocity vector.

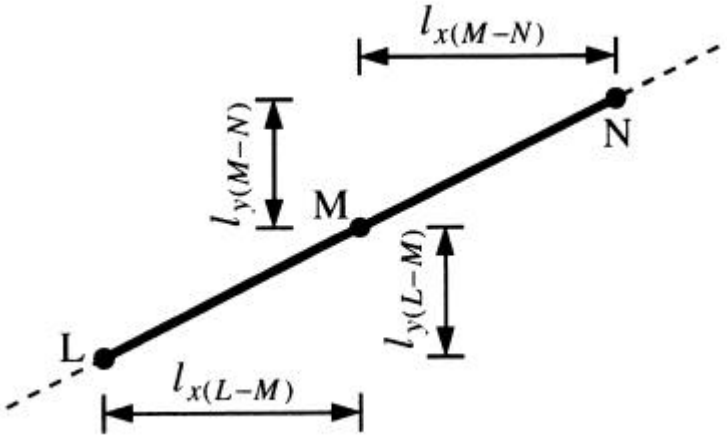

Figure 3.11 Graphical explanation of length components for a typical bending element.

Meanwhile, such simplified forms (e.g. Eq.3.92) can be obtained for the last two terms in Eq. (3.91) following the similar procedure. Thus, the simplified forms corresponding to these two terms are as follows:

$$(|l_1|+|l_2|)|\dot{u}_2|\sin\beta_2 = (l_{1x}+l_{2x})\dot{u}_{2y} - (l_{1y}+l_{2y})\dot{u}_{2x} \qquad ..(3.93)$$

and

$$|l_3|\,|\dot{u}_3|\sin\beta_3 = l_{1x}\,\dot{u}_{3y} - l_{1y}\,\dot{u}_{3x} \qquad ..(3.94)$$

Thus, the equation, Eq.(3.91) can be expressed in the following simplified form:

$$-(l_{2x}\,\dot{u}_{1y} - l_{2y}\,\dot{u}_{1x}) + (l_{1x}+l_{2x})\dot{u}_{2y} - (l_{1y}+l_{2y})\dot{u}_{2x} - (l_{1x}\,\dot{u}_{3y} - l_{1y}\,\dot{u}_{3x}) = 0 \qquad ..(3.95)$$

or, $$l_{2y}\,\dot{u}_{1x} - l_{2x}\,\dot{u}_{1y} - (l_{1y}+l_{2y})\dot{u}_{2x} + (l_{1x}+l_{2x})\dot{u}_{2y} + l_{1y}\,\dot{u}_{3x} - l_{1x}\,\dot{u}_{3y} = 0 \qquad ...(3.96)$$

Finally, the "*ho bending condition*" (i.e. Eq.3.91 or Eq.3.96) can be expressed in the matrix form as a linear constrained condition on the velocity corresponding to three reinforced points as shown in Fig.3.9.

$$\left(l_{2y}, -l_{2x}, -(l_{1y}+l_{2y}), (l_{1x}+l_{2x}), l_{1y}, -l_{1x}\right).\left(\dot{u}_{1x}, \dot{u}_{1y}, \dot{u}_{2x}, \dot{u}_{2y}, \dot{u}_{3x}, \dot{u}_{3y}\right)^T = 0 \qquad ...(3.97)$$

This equation can be also expanded to assemble all the nodal velocity vectors using the matrix C_b similarly as in the "*no length change condition*", *see* Eq. (3.86), i.e. the matrix, C_t.

$$C_b\ \dot{\boldsymbol{u}} = 0 \qquad ...(3.98)$$

where C_b in the case shown in Fig.3.11 can be expressed as follows:

$$C_b = \begin{pmatrix} \cdots & \cdots & \cdots & \cdots & \cdots & \cdots & \cdots & \cdots \\ \cdots & l_{y(M-N)} & -l_{x(M-N)} & -(l_{y(L-M)} + l_{y(M-N)}) & -(l_{x(L-M)} + l_{x(M-N)}) & l_{y(L-M)} & -l_{x(L-M)} & \cdots \\ \cdots & \cdots & \cdots & \cdots & \cdots & \cdots & \cdots & \cdots \end{pmatrix} \qquad ...(3.99)$$

Points L, M and N form a basic (unit) reinforcing system for all the reinforcement under bending.

3.4 INCORPORATIONS OF CONSTRAINT CONDITIONS

3.4.1 Incorporating into the RPFEM

On the basis of the upper bound theorem on plasticity, the rigid plastic finite element method (RPFEM) is obtained through minimizing the rate of internal plastic energy dissipation with respect to the kinematically admissible velocity field under several linear constraint conditions (Tamura et al. 1984). In this study, these are summarized as follows: (1) soils are assumed to exhibit no rate of volume change at the limit state like the plastic flow of Mises material. (2) Loading is made through a velocity/displacement boundary like through a rigid footing. In addition to these constraints, (3) "*no length change*" and (4) "*no-bending*" conditions are imposed upon the velocity along reinforcements. Mathematically, these are all linear constraint conditions.

The formulation is employed by introducing the Lagrange multipliers l, m, n and x to solve the minimization problem under constraint conditions. Finally, the following function is minimized.

$$\varphi(\dot{\boldsymbol{u}}, \boldsymbol{\lambda}, \boldsymbol{\mu}, \boldsymbol{\nu}, \boldsymbol{\xi}) = \int_V D(\dot{\boldsymbol{u}})dV + \boldsymbol{\lambda}^T(L\dot{\boldsymbol{u}} - \mathbf{0}) + \boldsymbol{\mu}(C\dot{\boldsymbol{u}} - \boldsymbol{a}) + \boldsymbol{\nu}^T(C_t\dot{\boldsymbol{u}} - \mathbf{0}) + \boldsymbol{\xi}^T(C_b\dot{\boldsymbol{u}} - \mathbf{0}) \quad ...(3.100)$$

in which $\boldsymbol{D}$ is the rate of internal plastic energy dissipation. L is the matrix defined such as $L\dot{\boldsymbol{u}} = \dot{\boldsymbol{v}}$ where $\dot{\boldsymbol{v}}$ is the rate of volume changes in all elements. Therefore the first constraint condition, $L\dot{\boldsymbol{u}}$=0 indicates that no rates of volume change occur in all the elements at the limit state. The vector $\boldsymbol{a}$ is a prescribed vector only at the displacement boundary and the matrix C retrieves the velocity vector at the displacement boundary when all nodal velocity vectors, $\dot{\boldsymbol{u}}$, are multiplied by C. Therefore, the second constraint condition, $C\dot{\boldsymbol{u}} = \boldsymbol{a}$ defines the provisional norms of velocity vector beneath the rigid loading plate. The third constraint condition, $C_t\dot{\boldsymbol{u}} = \mathbf{0}$ indicates the "no length change condition", *see* Eq. (3.88), while the forth one, $C_b\dot{\boldsymbol{u}} = \mathbf{0}$, indicates the "no-bending condition", *see* Eq. (3.93). As the rate of internal plastic energy dissipation, $D(\dot{\boldsymbol{u}})$ is the convex function of $\dot{\boldsymbol{u}}$, a local stationary condition of J gives the global minimum of J. Then taking the derivative of function, J, one has the following equilibrium equation of forces at limit state and accompanied constraint conditions.

$$\int_V B^T\boldsymbol{s}\,dV + L^T l + C^T m + C_t{}^T n + C_b{}^T x = \mathbf{0} \quad ...(3.101)$$

$$L\dot{\boldsymbol{u}} = 0 \quad ...(3.102)$$

$$C\dot{\boldsymbol{u}} = \boldsymbol{a} \quad ...(3.103)$$

$$C_t\dot{\boldsymbol{u}} = \mathbf{0} \quad ...(3.104)$$

$$C_b\dot{\boldsymbol{u}} = \mathbf{0} \quad ...(3.105)$$

in which $\boldsymbol{s}$ denotes deviator stress vector while Lagrange multipliers l and m are interpreted as the indeterminate isotropic stress and the contact pressure at the prescribed displacement boundary, respectively (Tamura et al., 1984). Interpretation of the other two newly introduced

Lagrange multipliers (n and x) are mentioned in the following section.

3.4.2 Interpretation of the Lagrange Multipliers

The Lagrange multiplier n is interpreted as the unit nodal forces acting on constrained nodes along the reinforcement direction, while x is also interpreted as the unit nodal forces acting on constrained nodes but along the perpendicular direction to the reinforcement. In other words, the forces calculated as x appear at the reinforced system that remains straight, e. g. points A, B and C in Fig. 3.9, to resist the bending moment in the reinforced system. For instance, the

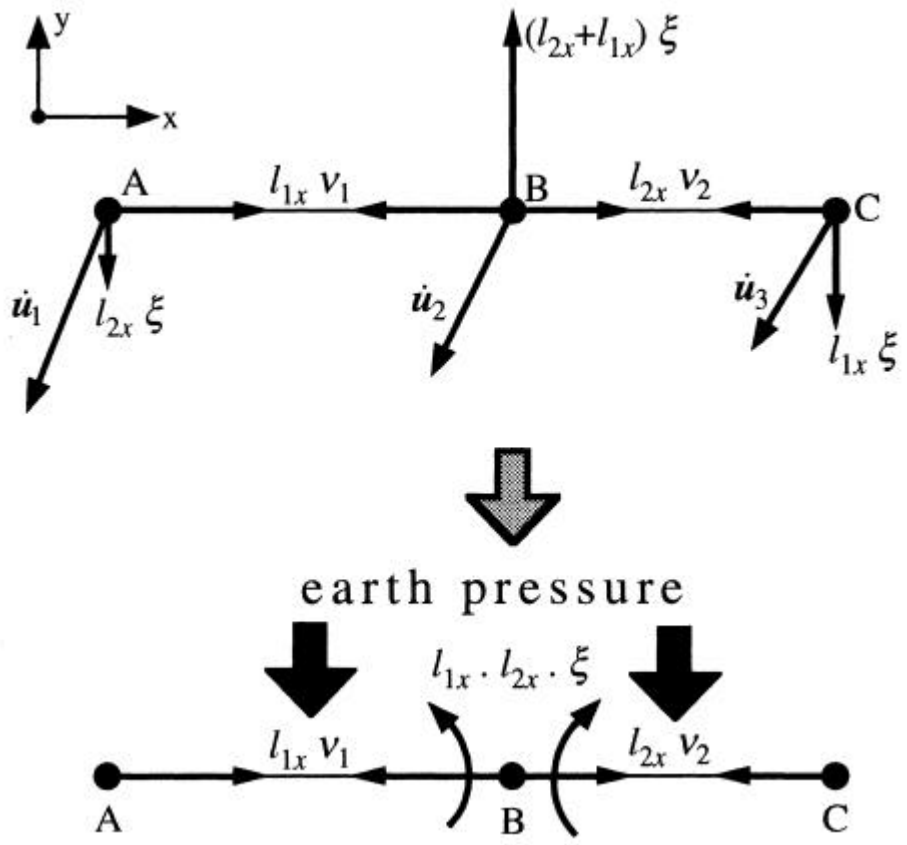

Figure 3.12 Graphical explanation of Lagrange multipliers corresponding to the linear constraint condition of "*no-bending*" conditions.

forces calculated as n and x in the horizontal reinforcement as shown in Figs. 3.8 and 3.12 are described. The fourth term in Eq.(3.101), $C_t^T n$, can be rewritten by the x, y component of the points A, B and C as follows:

$$C_t^T n = \left(l_{1x} n_1,\ 0,\ l_{2y},\ -l_{1x} n_1 + l_{2x} n_2,\ 0,\ -l_{2x} n_2,\ 0\right)^T \quad ...(3.106)$$

These forces act to resist extension of the distance between the constrained nodes along the reinforcement during failure. The fifth term in Eq. (3.101), $C_b^T x$ can be rewritten similarly to Eq. (3.104) as follows:

$$C_t^T x = \left(0,\ -l_{2x} x,\ 0,\ (l_{2x}+l_{1x})x,\ 0,\ -l_{1x} x\right)^T \quad (3.107)$$

These forces, which are interpreted as shear forces, resist bending of the straight line due to the earth pressure during failure. Furthermore the resistant to bending moment occur in the reinforced system is calculated as follow:

$$l_{1x} . l_{2x} . x \quad (3.108)$$

A complete reinforced system that is designed to resist developed bending moment in the system can be modeled by having such bending elements in series where neighboring three nodes can overlap each other in series. The resistant to bending moments can be superimposed.

3.4.3 Incorporating into the LEFEM

Strain-displacement compatibility:

The strain tensor, e_{ij}, can be derived from the displacements u_i by means of the following compatibility relation assuming small strain:

$$e_{ij} = \frac{1}{2}\left(u_{i,j} + u_{j,i}\right) \quad in \ V \quad ...(3.109)$$

where a comma preceding a subscript i denotes partial differentiation with respect to the coordinate x_i.

Boundary condition The displacements satisfy the boundary conditions on S_u

$$u_i = u_{io} \quad ...(3.110)$$

Equilibrium equation: Neglecting the geometry change due to the deformation in deriving the equations of equilibrium, it is immaterial whether the symmetric stress tensor σ_{ij} is referred to the undeformed or the deformed state. Denoting the body forces per unit volume by X_i and the surface tractions by T_i, the equations of equilibrium in the interior of the body are

$$s_{ij,j} + X_i = 0 \qquad \text{...(3.111)}$$

and the boundary conditions on the surface are

$$s_{ij} n_j = T_i \qquad \text{...(3.112)}$$

where n_i is the unit outward normal vector to the surface and the summation convention for repeated subscripts has been employed .

The conditions of equilibrium may be compressed into a single equation

$$\int_V s_{ij}\, e_{ij} dV = \int_{S_s} T_i\, \delta u_i \; dS + \int_V X_i \delta u_i \; dV \qquad \text{...(3.113)}$$

holding for any stress distribution s_{ij} in equilibrium with the external loads X_i, T_i and for any displacement field u_i with its corresponding strain distribution e_{ij}. This equilibrium equation is the basic tool in the derivation of linear elastic finite element formulations.

***General stress-strain relations*:**

The tensor of elastic coefficient has the properties of symmetry

$$\sigma D = \varepsilon \qquad \text{...(3.114)}$$

or, $$\sigma = D^{-1}\varepsilon \qquad \text{...(3.115)}$$

The elastic strain energy per unit volume

$$\Pi(\boldsymbol{u}, n, x) = \int_V \frac{1}{2} s^T e \, dV \qquad \text{...(3.116)}$$

unless all stresses are zero and the inversion of the relations Eq.(3.114) is also unique.

The initial tangential load-deformation curve of the reinforced soil structure is estimated in this study approximately by using the linear elastic theory (E,υ).

The potential energy is minimized introducing constraint conditions on the deformation field, which is almost the same as that in minimizing the rate of internal plastic dissipation corresponding to the aforementioned RPFEM. The energy function in Eq.(3.116) is modified to satisfy the constraint conditions, as follows:

$$F(\boldsymbol{u}, n, x) = \int_V \frac{1}{2} s^T e \, dV + n^T (C_t \boldsymbol{u} - \boldsymbol{0}) + x^T (C_b \boldsymbol{u} - \boldsymbol{0}) - F \boldsymbol{u}^T \qquad \text{...(3.117)}$$

Minimization of this energy function yields a set of simultaneous equations with constraint conditions is as follows:

$$\int_V B^T DB \; dV \; \boldsymbol{u} + C_t^T \, n + C_b^T \, x - F = \mathbf{0} \qquad ...(3.118)$$

$$C_t \boldsymbol{u} = \mathbf{0} \qquad ...(3.119)$$

$$C_b \boldsymbol{u} = \mathbf{0} \qquad ...(3.120)$$

in which the matrix D defines the constitutive relationship of the linear elastic material based on the Hook's law. These Lagrange multipliers can be interpreted similarly as in the RPFEM.

3.5 SUMMARY AND CONCLUDING REMARKS

A simplified tool for the analysis and design of complex reinforced soil structures is formulated based on plasticity theories at the limit state of soil mass. This method presents a new concept of computation of bearing capacity/safety factor, distribution of axial and shear (/bending) forces as well as velocity vectors and the stress distribution in the reinforced soil structures is simultaneously formulated. The reinforced effect is coupled in the conventional rigid plastic finite element method by introducing a set of linear constraint conditions of *"no length change*" and "*no-bending*" upon the soil element nodes corresponding to reinforcement at the limit equilibrium state.

The conclusions drawn from the present chapter on formulation of the reinforced soil system are as follows:

1. The mechanism of the reinforcement and facing can be modeled by introducing the two new linear constraint conditions, "*no-length change*" and "*no-bending*", in the two energy functions: stored energy function in linear elastic problems and the plastic energy dissipation function in limit state problems.
2. Lagrange multipliers corresponding to these constraint conditions represent the axial force and shear force (/bending moment) in the reinforcing material per unit length, respectively.
3. The effect of rigid panel facing in bending can also be formulated using the same concept. It can be explained with the bending moment developed in the facing.
4. Frictional material can be modeled as an assembly of inhomogeneous Mises material whose shear strength depends on the confining pressure.

CHAPTER IV NUMERICAL INVESTIGATIONS OF REINFORCED SOIL STRUCTURES

4.1 GENERAL

In the preceding chapter, Chapter III, existing methodologies (RPFEM and LEFEM) based on plasticity and linear elastic theories have been reviewed and a new formulation to model the reinforced soil system is derived. Finally, the newly introduced formulations of the reinforced soil system have been incorporated into these numerical methods. In this chapter, the capability of the proposed methodology will be numerically investigated through some typical reinforced soil engineering problems, e.g. bearing capacity problems, slope stability problems, etc. It will be further illustrated that the methodology can solve an indeterminate axial force and shear force (/bending moment) distributions acting along the reinforcing members together with the load factor (a safety factor of the applied force) and velocity field of soils at limiting equilibrium state, simultaneously. As already explained in the previous chapter that nothing has been assumed in advance of the analysis unlike the conventional limiting equilibrium methods.

The general tendency of the solutions presented in this chapter is expected to provide enough confidence for the practicing engineers in order to make up their engineering judgment whether the method is applicable to daily design works or not. The example problems discussed in the present study are aimed at this purpose.

4.2 BEARING CAPACITY PROBLEMS

4.2.1 General

The first problem taken is a bearing capacity problem of a long shallow foundation idealized as a typical plane strain problem. The soil deposit beneath the footing is reinforced by a reinforcing material (e.g. geotextile /steel). For simplicity, first homogeneous clay under undrained condition (Mises material) is considered, and then another clay is considered whose undrained shear strength linearly increases along the depth. Due to symmetry of the foundation along the centerline, only right half of the soil mass is discretized by putting roller along the centerline (Fig. 4.1). All displacement boundary conditions are either roller or fixed support types. Flexible loading, rigid-smooth and rigid-rough footings are separately discussed.

A single reinforcing member is placed at different elevations in order to search an optimum position of the reinforcement where the maximum ultimate bearing capacity, q_f, can be obtained. The ultimate bearing capacity, q_f, is computed and also the initial footing loading~settlement relations are studied, employing the methodology proposed in the previous chapter, Chap. III (RPFEM and LEFEM). The corresponding computed tensile force distributions along the reinforcement; nodal velocity vectors are illustrated for each case dealt. Such figures demonstrate the effect of reinforcements at the limit equilibrium state of the soil mass. Detailed explanation is presented in the following paragraphs for each cases dealt separately.

4.2.2 Homogeneous Clay

The soil mass is assumed to be homogeneous clay with c_u=9.8 kPa as undrained shear strength. The thickness of the clay deposit is 20 m and the width is 30 m. The width of the footing is equal to the depth of the clay (H=B(=2b)=20m). Thus, the foundation rock beneath the soil has no direct influence over the failure mechanism.

Flexible Loading

The loading is assumed to be flexible enough like an embankment so that it exhibits no restrains against the velocity or displacement of the soil mass. The theoretical bearing capacity of the soil mass under a footing was ideally derived by Prandtl and is equal to $q_f=(\pi+2)\ c_u = 5.14\ c_u$. Before describing the bearing capacity results for the reinforced cases, the computed bearing capacity of the footing employing rigid plastic finite element method (RPFEM) is discussed. In the previous sections, it was shown that the RPFEM solutions require several cycles of iterations, so the aforesaid analytical solutions for an ideal case can be achieved after much iteration. Considering the time and cost constraints, further computation steps are terminated upon achieving fairly accurate results (fairly accurate refers to personal judgments). Thus, the computed factor of safety for unreinforced soil is 5.168 that is little more than Prandtl's analytical solutions

and assumed to be accurate enough for the practical purposes. The distribution of the velocity vectors is shown in Fig. 4.2.

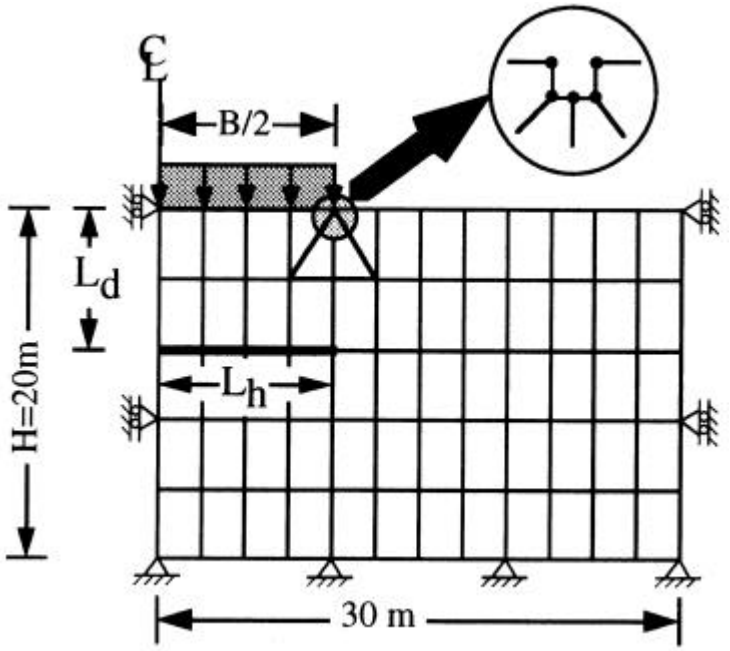

Figure 4.1 Finite element mesh for the bearing capacity problems

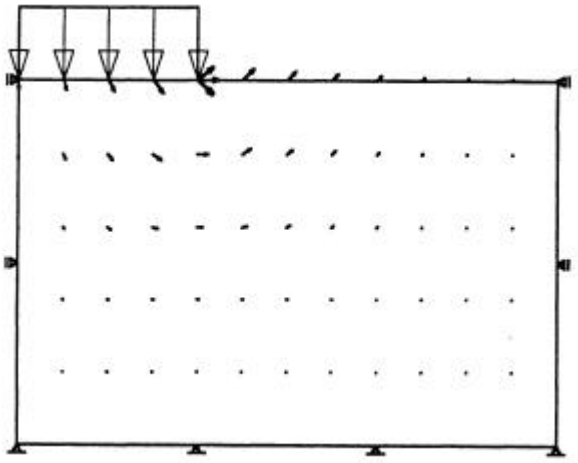

Figure 4.2 Velocity field in an unreinforced soil mass at limit state of soil mass (*flexible footing*)

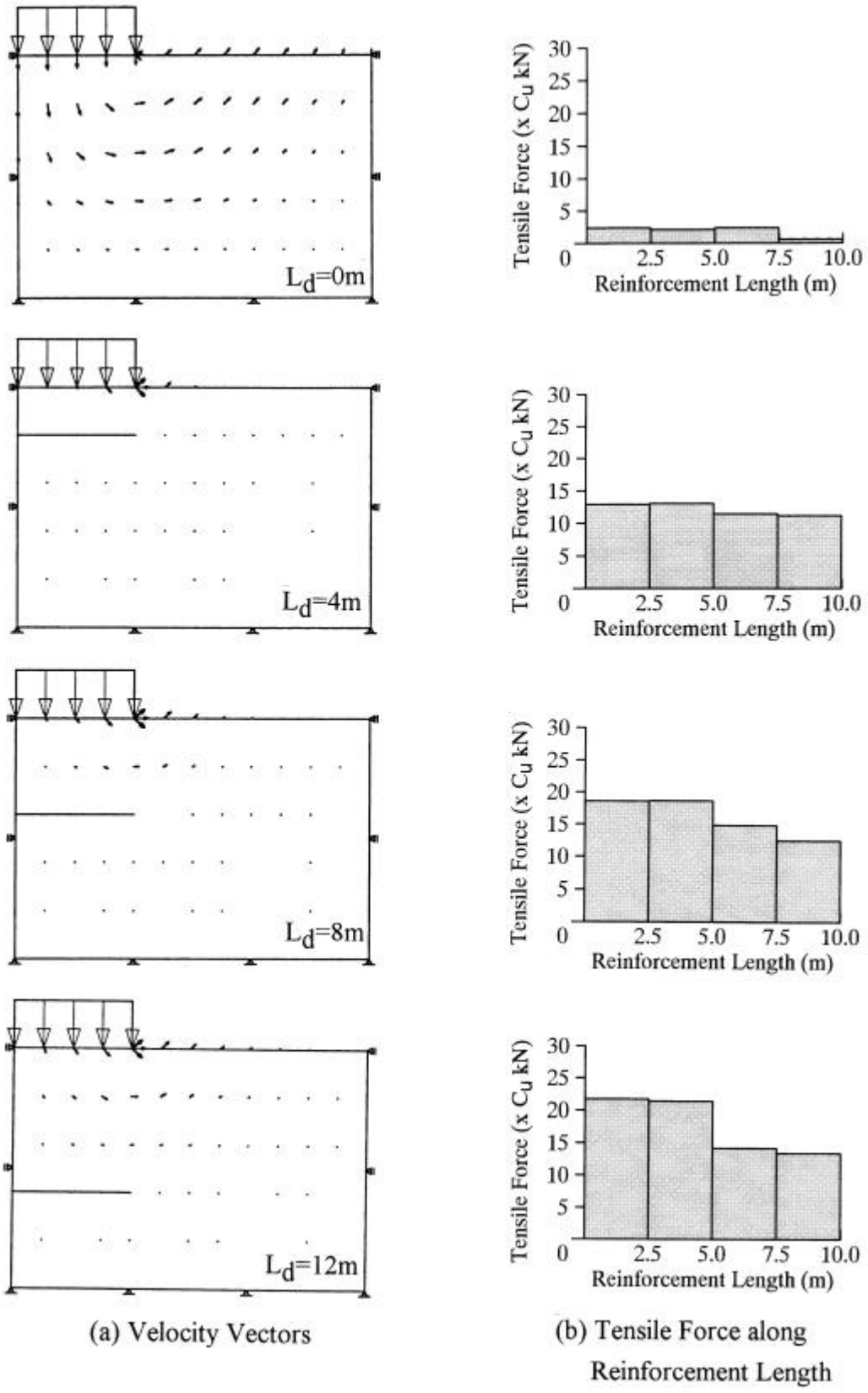

Figure 4.3 Effect of reinforcement on velocity field at limit state of soil mass and axial force distributions along reinforcement (*flexible loading*)

Table 4.1 Computed ultimate bearing capacity and normalized bearing capacity factors for the flexible loading.

Reinforcement Position L_d (m)	Ultimate Bearing Capacity q_{fc}(xc u (kN/m^2)	Normalized Bearing Capacity Factor (q_{fc}/q_{fu})
-	5.168	1.000
0.0	5.254	1.017
4.0	5.294	1.024
8.0	5.206	1.007

The positions of 20 m long reinforcement (equal to the footing width) are shown in Fig. 4.3. The computed ultimate bearing capacity corresponding to these different positions are tabulated in Table 4.1. The c_u is undrained shear strength of the clay deposit estimated to $1/\sqrt{2}\,\sigma_o$ under plane strain condition. For comparison purposes the computed bearing capacity ($q_{f\_computed}$) is normalized with respect to the bearing capacity of unreinforced ($q_{f\_unreinforced}$) soil media (q_{fc}/q_{fu}). Thus, the normalized bearing capacity factor for unreinforced case is unit (i.e. 1.00). In the case of reinforcements placed just under the footing reveals (Table 4.1) an increase in the ultimate bearing capacity compared to the unreinforced case. Further lowering the reinforcement position gradually increases the bearing capacity up to a certain depth and afterwards it starts decreasing that finally reduces to the unreinforced bearing capacity value. The maximum increment after reinforcing the soil is about 2.4% compared to the unreinforced case. Optimum position of the reinforcement was about, L_d=4m (L_d/b=0.4). The very low positioned reinforcement (e.g. L_d=12m) has almost no influence over the soil mass because the shearing of soil is confined near the surface. While the higher positions also could not increase the bearing capacity because the directions of the velocity vector around that position before placing the reinforcement was perpendicular to the current reinforcement axis as shown in Fig. 4.3(a). The velocity vectors at and around the optimum position before placing the reinforcement were almost parallel to the current reinforcement axis. This illustrates the best possible orientation for reinforcement is parallel to the velocity vectors. Figure 4.3(b) shows the computed reinforcement force along the reinforcement length for various positions. The axial force gradually increases when the reinforcement positions are lowered.

***Rigid-smooth Footing*:**

The footing is assumed perfectly rigid-smooth such that the vertical component of velocities (i.e. along y-direction) just under the footing are equal throughout the plastic flow of soil mass and the velocities are allowed to rotate freely provided the vertical components are maintained equal. Thus, this problem is very similar to the former problem (flexible loading) except the footing rigidity. The other boundary conditions, finite element array and various positions and length of

reinforcement also remained unchanged.

At first, the computation work is carried out for the unreinforced case of the rigid-smooth footing. The ultimate bearing capacity is q_f=5.176 which is almost the same as the flexible loading case (q_f=5.167). This q_f is used in the normalization of the ultimate bearing capacity for comparison with the bearing capacity of reinforced soil cases. The distribution of the nodal velocity vectors in the unreinforced case is shown in the Fig. 4.4.

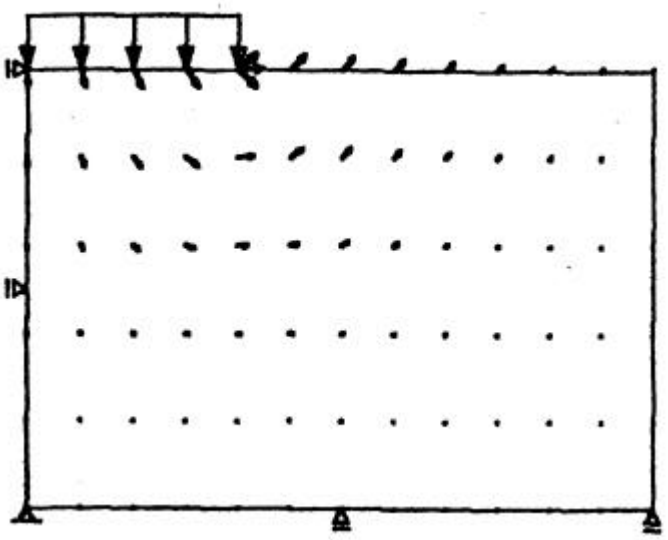

Figure 4.4 Velocity field in an unreinforced soil mass at limit state (*rigid-smooth footing*)

Table 4.2 Computed ultimate bearing capacity and normalized bearing capacity factors for the rigid-smooth footing.

Reinforcement Position L_d (m)	Ultimate Bearing Capacity q_{fc}(xc_u (kN/m^2)	Normalized Bearing Capacity Factor (q_{fc}/q_{fu})	LEFEM D=0.01m P_c/P_{uo}
-	5.172	1.000	1.000
4.0	5.669	1.096	1.372
8.0	5.303	1.025	1.447
12.0	5.187	1.003	1.318
16.0	5.172	1.000	1.145

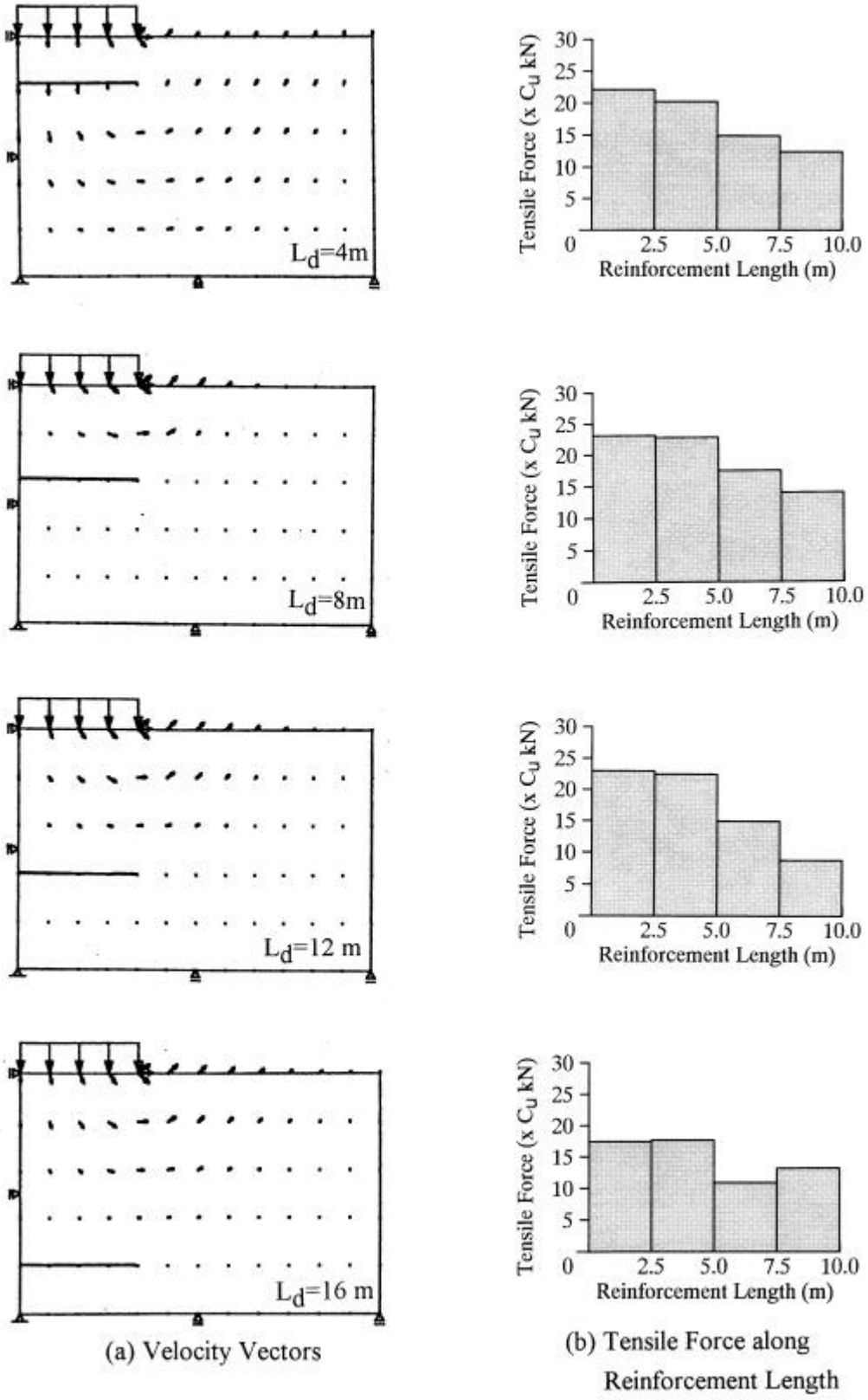

Figure 4.5 Effect of reinforcement on velocity field at limit state of soil mass and axial force distributions along reinforcement (*rigid-smooth footing*)

The positions of 20 m long reinforcement (equal to the footing width) are shown in Fig. 4.5. The computed ultimate bearing capacity corresponding to these different positions are tabulated in Table 4.2. The normalized bearing capacity factors ($q_{f\_computed}$ /$q_{f\_unreinforced}$) are also presented in the same table. The reinforcement placed under the footing (L_d=4m) reveals substantial increment (about 10%) in the ultimate bearing capacity compared to the unreinforced case. Further lowering the reinforcement position gradually decreases the ultimate bearing capacity, q_f, which finally reduces to the unreinforced bearing capacity value. Optimum position of the reinforcement is L_d=4m (L_d/b=0.4) where maximum increment in the bearing capacity is about 10%. The nodal velocity vectors are shown in Fig.4.5 for each cases mentioned in the table. The lowermost reinforcement (L_d=16m) shows no influence over the soil mass because of the localized shearing of the soil near the footing. In this case also maximum ultimate bearing capacity, q_f, is obtained for the reinforcement position where the velocity vectors before placing the reinforcement were almost parallel to the current reinforcement axis. This also support the best orientation for a reinforcement noted in the previous example. Figure 4.5 shows the computed axial force along the reinforcement length for various reinforcement positions. The axial force gradually increased when the reinforcement positions are lowered up to the optimum and further lowering resulted gradual decrease in the ultimate bearing capacity, q_f, to the value for the unreinforced case.

***Rigid-rough Footing*:**

The footing is assumed perfectly rigid such that the vertical component of velocities (i.e. along y-direction) just under the footing is equal at the limit equilibrium state of the soil mass, same as in the previous example. In this case, the lateral component of velocities under the footing are not allowed to rotate which means $\dot{u}_h = 0$ This problem is very similar to the previous example (rigid-smooth) except the footing smoothness. The other boundary conditions, finite element array and various positions and length of reinforcement also remained same.

Similar to the previous examples, this example also starts with the computation for the unreinforced soil. The computed ultimate bearing capacity is q_f=5.248 which is higher than the rigid-smooth case (q_f=5.171) because of the rough footing. Ultimate bearing capacities computed later in the reinforced cases are normalized with respect to this unreinforced bearing capacity as in earlier examples. The distribution of the nodal velocity vectors in the unreinforced case is shown in the Fig. 4.6.

The reinforcement positions are similar to the previous cases (*see* Fig.4.5). The computed ultimate bearing capacity and the normalized bearing capacity factors are tabulated in Table 4.3. The reinforcement placed under the footing reveals an increase in the ultimate bearing capacity compared to the unreinforced case. Further lowering the reinforcement position gradually increases the bearing capacity up to certain depth (L_d=8m) and afterwards it starts decreasing

which finally reduced to the unreinforced bearing capacity value. The maximum increment after reinforcing the soil is about 13% compared to the unreinforced case. The optimum position of the reinforcement was about, L_d=8m (L_d/b=0.8). The nodal velocity vectors (Fig.4.7a) are similar to the previous examples. Negligible effect of the lower positioned reinforcement was observed which can be attributed to the localized shearing of soil near the footing toe. Figure 4.7(b) resembles similarity with the axial force distribution patterns illustrated in the previous examples (*see* Fig. 4.5b). The reinforcement force gradually increases as the reinforcement positions are lowered up to the optimum position. Further lowering of the reinforcement position after the optimum position also gradually reduces the reinforcement forces as shown in Fig.4.7.

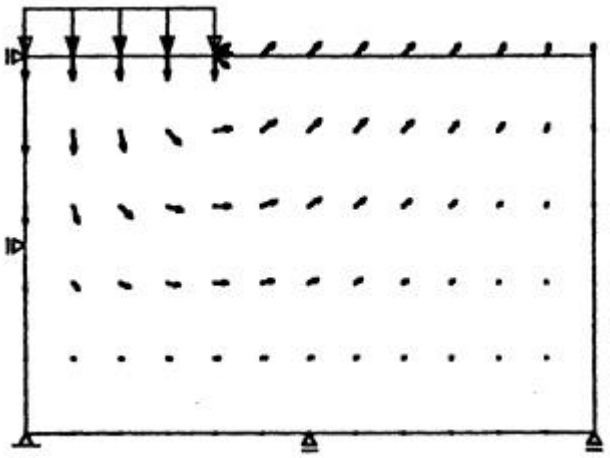

Figure 4.6 Velocity field in an unreinforced soil mass at limit state. (*rigid-rough footing*)

Table 4.3 Computed ultimate bearing capacity and normalized bearing capacity factors for the rigid-rough footing.

Reinforcement Position L_d (m)	Ultimate Bearing Capacity q_{fc}(xc u (kN/m^2)	Normalized Bearing Capacity Factor (q_{fc}/q_{fu})	LEFEM D=0.01m P_c/P_{uo}
-	5.248	1.000	1.000
4.0	5.868	1.114	1.351
8.0	5.956	1.131	1.517
12.0	5.432	1.031	1.392
16.0	5.286	1.003	1.177

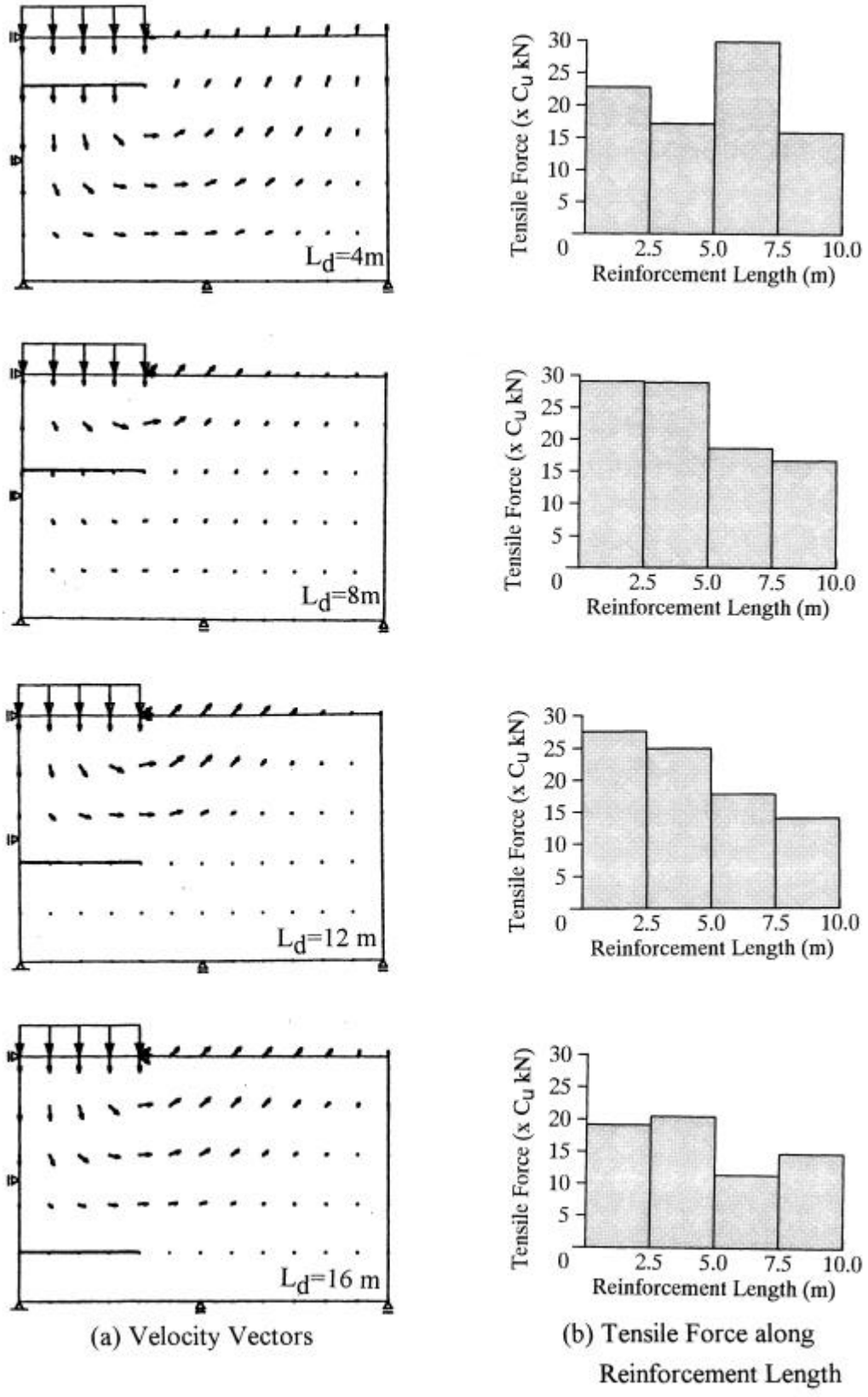

Figure 4.7 Velocity field in reinforced soil mass and axial force distributions at the limit state of the reinforced soil structure (*rigid-rough footing*)

DEFORMATION ANALYSIS

The deformation analysis in this research deals mainly with the initial load~settlement relations and the displacement field computations. The computations (Figs. 4.8~4.12) are based on the linear elastic finite element method (LEFEM), discussed in the preceding chapter, Chapter III. The reinforcement positions and length remained same as mentioned in the preceding bearing capacity problems. The Young's modulus of elasticity is computed based on an empirical equation, $E=210 \times C_u = 210 \times 9.8 = 2058$ kPa. The soil is assumed fully saturated, thus, the Poisson's ratio, υ, is assumed equal to 0.5 as an incompressible material ($\varepsilon_v=0$).

The displacement field of the unreinforced plain soil mass, loaded through rigid footing under smooth and rough surfaces is illustrated in Fig. 4.8. Likewise, the computed displacement field (Figs. 4.9~10) corresponding to reinforced soil cases are shown in Figs. 4.9~10. Similarly, computed footing stress-settlement relations for the unreinforced and the reinforced soil foundations are presented in Figs. 4.11 and 4.12, which clearly show that the optimum position giving maximum effect on the footing stress-settlement relations corresponding to the rigid-rough footing is very similar to the bearing capacity problems, while the optimum position in the case of the rigid-smooth footing is deeper than the bearing capacity problem.

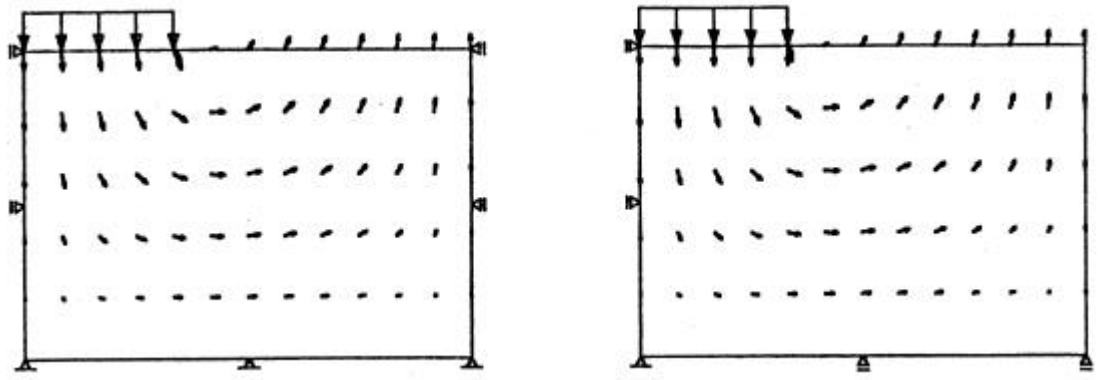

Figure 4.8 Displacement field in unreinforced soil mass based on LEFEM.

Figures 4.9(a) and 4.10(a) clearly show that the influence area is wide for all the reinforcement positions. Compared to the velocity field at the limit state, it may be considered as one major contrast. Two distinct displacement fields could be noticed either side of the reinforcements placed at or around the optimum positions. Such a effect could not be noticed for the reinforcements positioned either very close to the footing or at very low elevations.

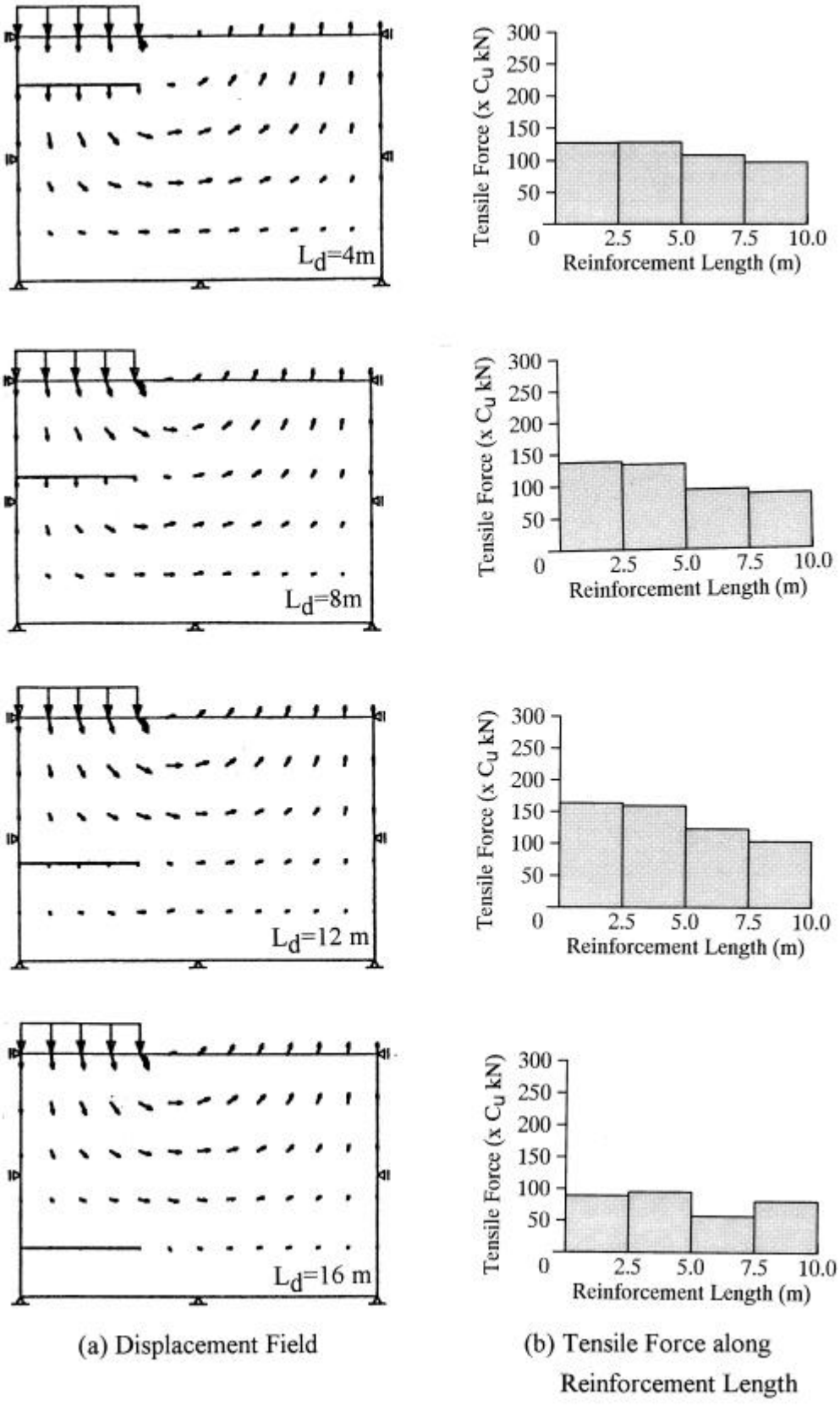

Figure 4.9 Displacement field in the reinforced soil mass and axial force distributions along reinforcements (*rigid-smooth footing*)

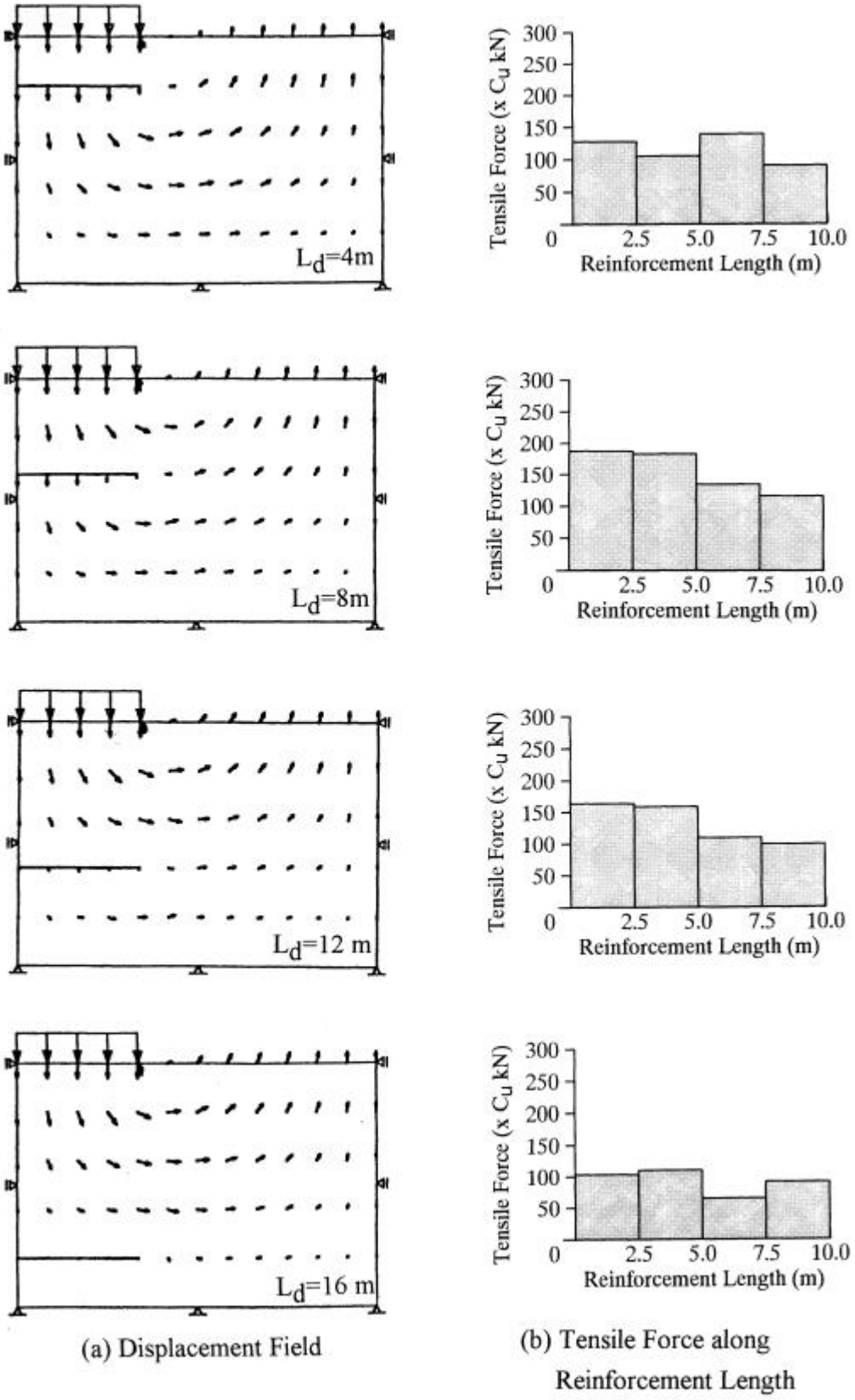

Figure 4.10 Displacement field in the reinforced soil mass and axial force distributions along reinforcements (*rigid-rough footing*)

Corollary, the footing stress is very high for the reinforcement positions where displacement fields are separated into two distinct zones either side of the reinforcements. The magnitudes and distribution pattern of the reinforcement tensile force are almost similar for all the reinforcement positions. The tensile force distribution pattern in the reinforcement is very similar to the patterns observed at the limit state, i.e. bearing capacity problems.

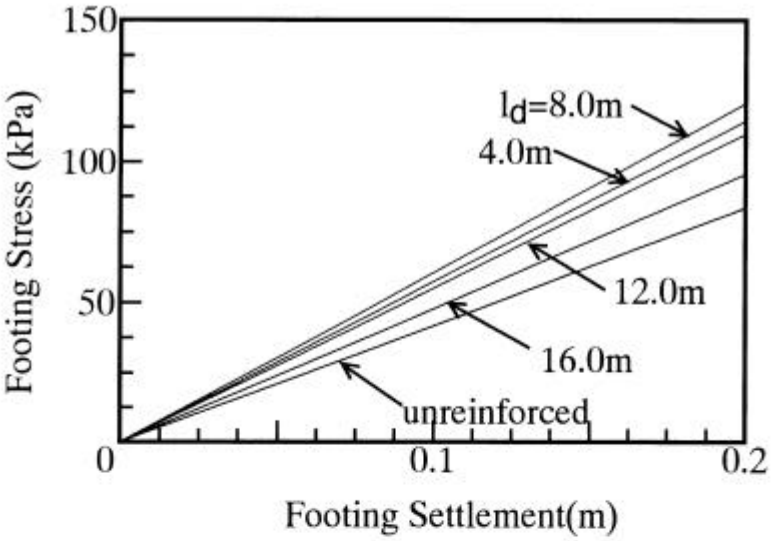

Figure 4.11 Footing stress versus footing settlement relation. (*rigid-smooth footing*)

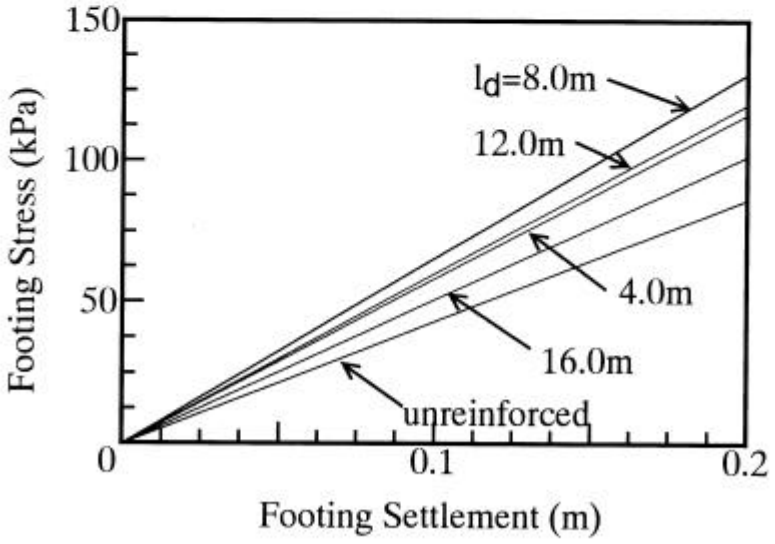

Figure 4.12 Footing stress versus footing settlement relation based on LEFEM. (*rigid-rough footing*)

4.2.3 Clay: *Linearly increasing Shear Strength along Depth*

General

The normally consolidated clay in nature exhibits linear increase in the undrained shearing strength along the depth. It can be equivalently represented by multi-layered system as shown in Fig.4.13. Asaoka and Kodaka (1993) have illustrated the solution procedure using RPFEM. In this study, the same procedure is employed to solve the reinforced soil when the undrained shear strength of clay increases linearly with depth. For simplicity, the finite element array, the boundary conditions and the loading pattern assumed to be same as in the earlier examples of the homogeneous clay sub-section. The soil strength on the surface is equal to the strength of the homogeneous clay (c_u=9.8kPa). It increases linearly with depth and becomes doubled (c_u =2 x 9.8 =19.6kPa) at the bottom of the soil. The shear strengths assigned to different finite elements at the corresponding elevations assuming the equivalent multi-layered system is shown in Fig.4.13.

In this soil type, only two case: the flexible loading and the rigid-rough footing are presented. The trend of the results obtained employing the proposed methodology is similar to the earlier examples, therefore, only these two cases are illustrated for the sake of completeness.

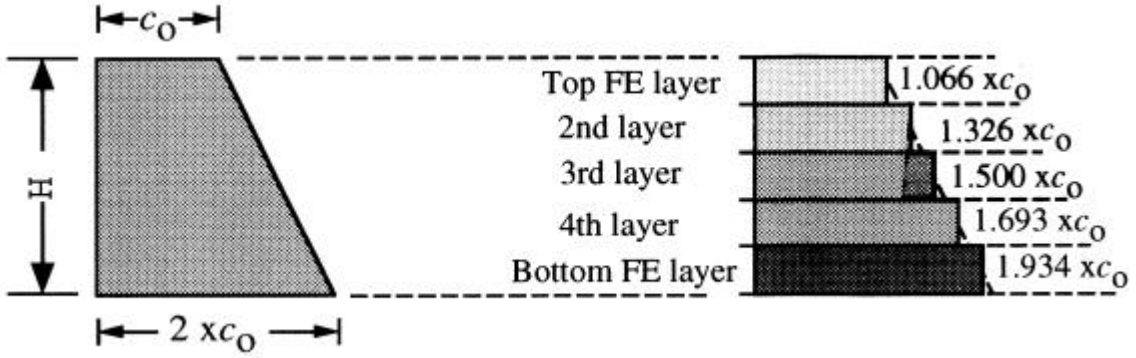

Figure 4.13 Discretization of the linearly increasing shear strength along depth.

***Flexible Loading*:**

Flexible loading similar to the first example explained for the homogeneous clay is considered. Before describing the bearing capacity results for the reinforced cases, the computed bearing capacity of the unreinforced soil mass employing the rigid plastic finite element method (RPFEM) is briefed. The computed ultimate bearing capacity for the unreinforced soil is 5.643. The distribution of the velocity vectors is shown in the Fig. 4.14. It clearly shows the influence of increasing shear strength. The failure zone is exclusively localized near the surface especially around the footing edge.

The reinforcement length and positions here, too, are similar to the earlier examples. The

computed ultimate bearing capacity and the normalized bearing capacity factors ($q_{f\_computed}$ /$q_{f\_unreinforced}$) corresponding to these different positions are tabulated in Table 4.4. The result clearly reveals that the lower positioned reinforcements have no influence over the bearing capacity as well as the influence area before and after reinforcing the soil (Fig. 4.15a). Interestingly, the reinforcement force still increases gradually as the reinforcement position is lowered.

Table 4.4 Computed ultimate bearing capacity and normalized bearing capacity factors in the case of the flexible-loading.

Reinforcement Position L_d (m)	Ultimate Bearing Capacity $q_{fu} x c_u$ (kN/m^2)	Normalized Bearing Capacity Factor (q_{fu}/q_{fc})
-	5.643	1.000
0.0	6.202	1.099
4.0	5.643	1.000
8.0	5.643	1.000
12.0	5.643	1.000

***Rigid-rough Footing*:**

The vertical component of the velocities just under the rigid-rough footing is equal at limiting equilibrium state of soil. The lateral component of velocities under the footing are always kept zero, $\dot{u}_h = 0$. This problem is very similar to the last example (rigid-rough footing) described under the homogeneous clay problems. The difference is due to the linearly increasing undrained shear strength of the soil in the present example. The other boundary conditions, the finite element array and the various positions and length of the reinforcements also remained same.

Similar to the previous examples, an unreinforced case of rigid-rough footing is investigated first. The reason for higher ultimate bearing capacity, q_f=6.871, compared to the homogeneous clay under similar rigid-rough footing (q_f=5.248) may be attributed to the increasing strength of the soil with depth. The distribution of the nodal velocity vectors is shown in the Fig. 4.16. Which clearly shows the reduced influence area.

The reinforcement positions are shown in Fig. 4.17(a). The computed ultimate bearing capacity and normalized bearing capacity factors corresponding to different positions are tabulated in Table 4.5. The reinforcement placed under the footing reveals an initial increase in the ultimate bearing capacity up to the optimum position and gradually decreases for reinforcements positioned at lower elevations. The pattern of ultimate bearing capacity variation with the

reinforcement position (depth) is very similar to the previous examples. Because of the increasing shear strength of the soil along the depth, the optimum position shifted upward close to the footing (e.g. current L_d=4m compared to previous example of the rigid-rough footing in homogeneous example, L_{do}=8m) The maximum increment after reinforcing the soil is about 25% compared to the unreinforced case, while in the homogeneous clay it was only 13%. The nodal velocity vectors are shown in Fig.4.17 (a) for each cases mentioned in the table. The direction of the velocity vectors at optimum position before and after reinforcing the soil is also similar to the results presented in the homogeneous clay. Fig. 4.17(b) shows the computed reinforcement force along the reinforcement length for various reinforcement positions. The reinforcement force gradually increases when the reinforcement positions are lowered up to the optimum position. Further lowering of the reinforcement position after the optimum position also gradually reduces the reinforcement forces as shown in Fig.4.17 (b).

Table 4.5 Computed ultimate bearing capacity and normalized bearing capacity factors in the case of the rigid-rough footing.

Reinforcement Position L_d (m)	Ultimate Bearing Capacity q_{fu} xc u (kN/m^2)	Normalized Bearing Capacity Factor (q_{fu}/q_{fc})
-	6.871	1.000
0.0	6.871	1.000
4.0	8.725	1.269
8.0	7.116	1.036
12.0	6.871	1.000

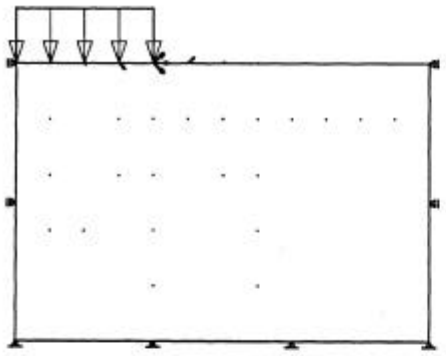

Figure 4.14 Velocity field in a unreinforced soil mass at limit state. (*flexible loading*)

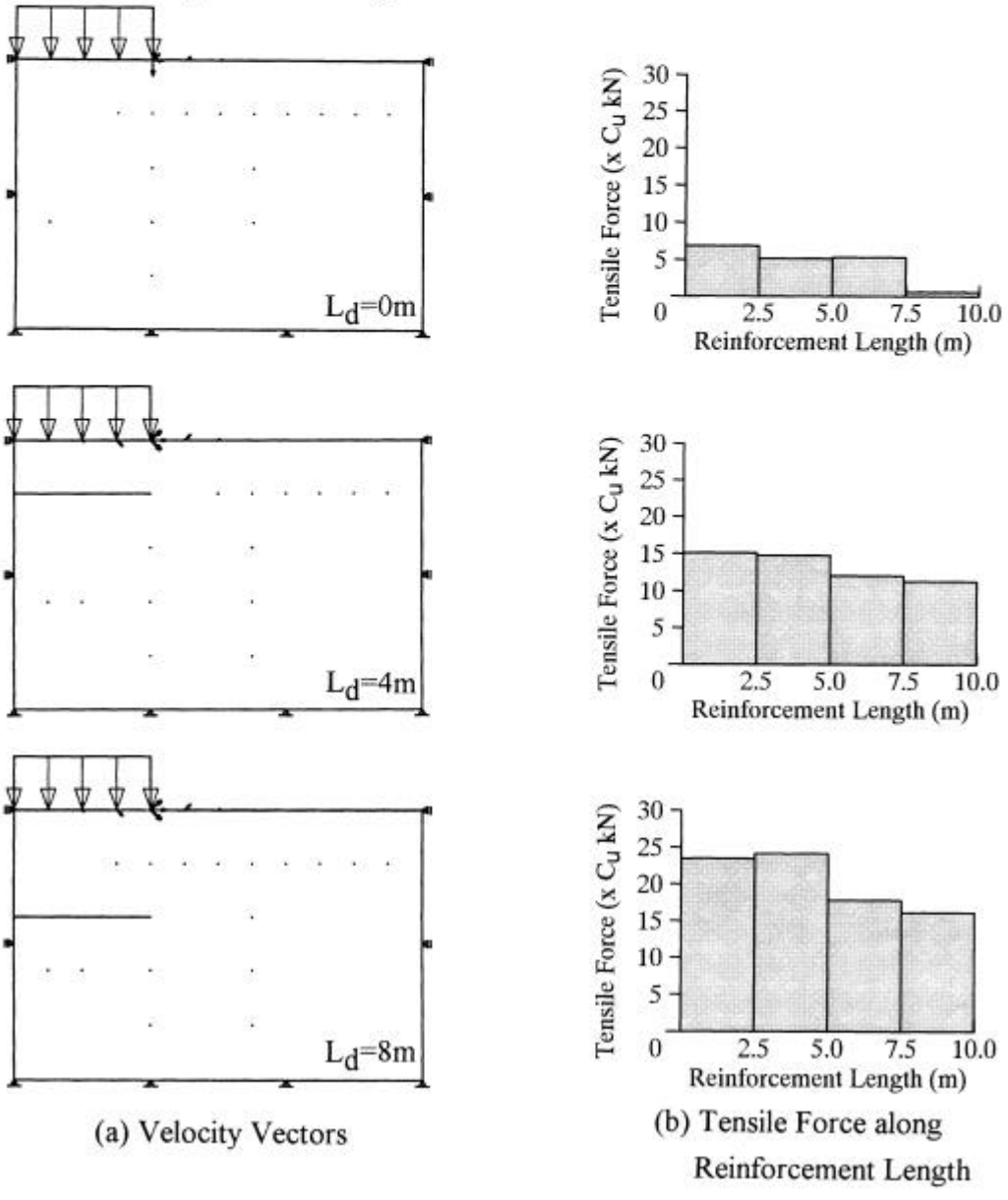

Figure 4.15 Velocity field in reinforced soil mass and axial force distributions at the limit state of the reinforced soil structure (*flexible loading*)

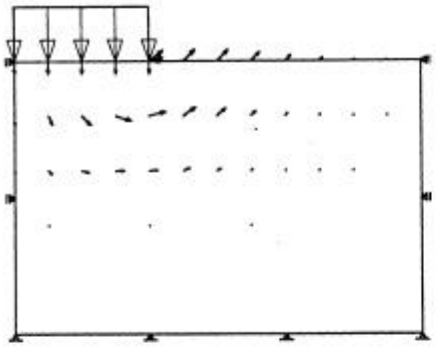

Figure 4.16 Velocity field in an unreinforced soil mass at limit state. (*rigid-rough footing*)

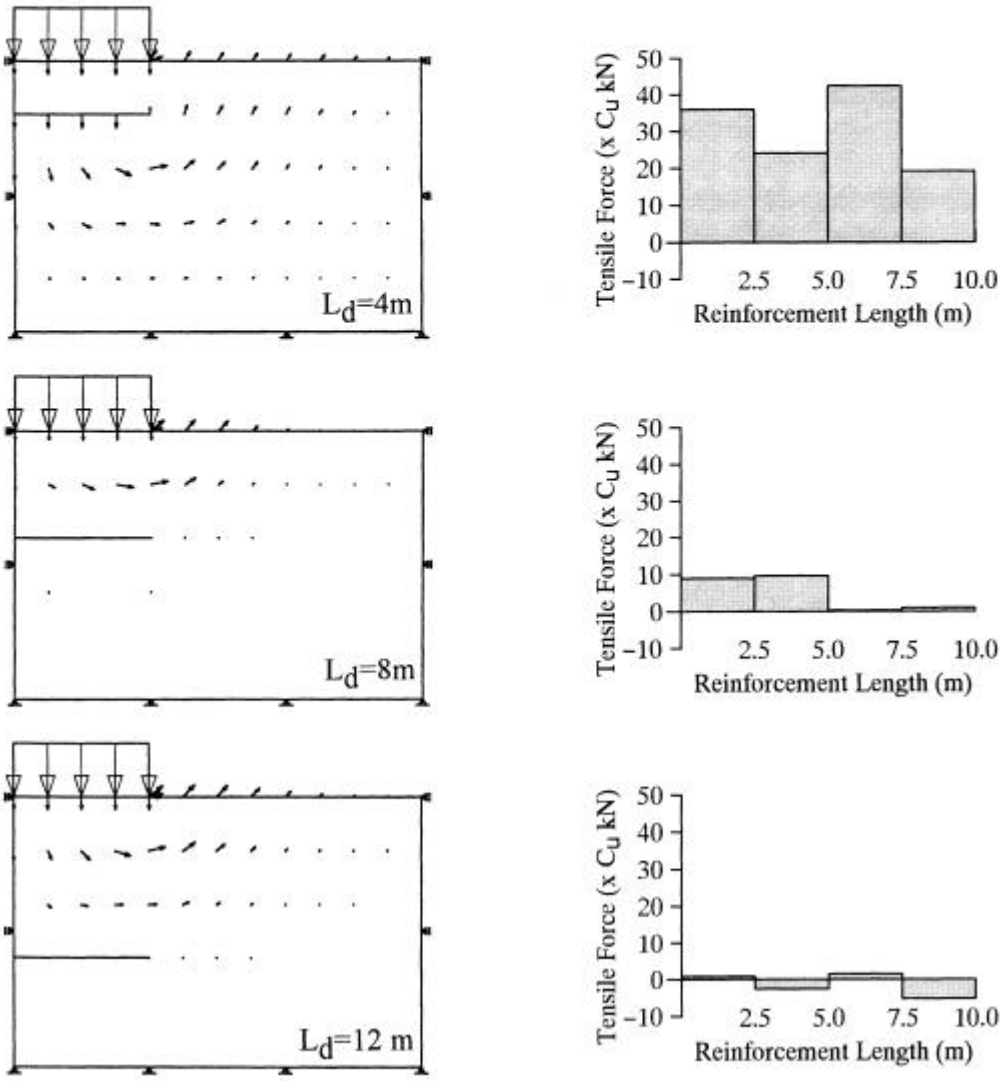

Figure 4.17 Velocity field in reinforced soil mass and axial force distributions at the limit state of the reinforced soil structure (*rigid-rough footing*)

4.3 SLOPE STABILITY PROBLEMS

4.3.1 General

The second representative problem chosen is a slope stability problem. The slope is reinforced by inserting a reinforcing material (e.g. steel bar) from the face like soil nails. For simplicity, first purely cohesive clay under undrained condition (Mises material) is considered, and latter the c-ϕ material, i.e. sandy soil, will be discussed. Velocity boundary conditions are either roller or fixed support types. The failure is caused by the stresses developed due to the body force of soil mass. The isoparametric quadrilateral elements are used in all the examples.

Effect of reinforcement length is investigated by inserting reinforcing member(s) at different elevations. The effect of single reinforcement is also compared with the multiple reinforcements placed simultaneously at different elevations. Safety factor is computed using RPFEM incorporating the proposed mechanism. The factor of safety, F_S corresponding to the present slope stability problems is the same as load factor, μ, introduced in Eq.(3.101). The computed principal stress distributions mean confining stress contours in soil mass and tensile force distributions along the reinforcement are illustrated. The computed nodal velocity vectors are also explained for each case. Detailed explanation is presented in the following sub-sections for each cases dealt with.

4.3.2 Purely Cohesive Clay (*Mises Material*)

Example 1: *Horizontal Reinforcement*

Fig. 4.18 shows a typical finite element array and detailed boundary conditions used in this example. The slope stability problem is considered under plane strain condition assuming close spacing of reinforcements. The grading of the slope face is **1**(*Horizontal*): **2**(*Vertical*), i.e. 67^o with horizontal. The soil properties of the Mises material are chosen in such a way that the unreinforced soil under prescribed boundary conditions gives the factor of safety, F_S=1.0. Thus, the soil properties for the present example are c_u= 12.3 kPa and γ_t=16.3 kN/m3.

Reinforcements are placed horizontally at three elevations as shown in Fig. 4.18(b). In case of single reinforcement, the middle position is only explained. The computed factor of safety corresponding to different length of the reinforcements is plotted in Fig.4.19. The initial rate of increase of the safety factor is slow for relatively shorter reinforcements. The safety factor gradually increases as the reinforcement length is extended and after some length the rate is very rapid (Fig. 4.19). The computed safety factor is also higher when the number of reinforcement is increased to three. It should be noted here that the absolute increase in safety factor is still relatively small compared to c-ϕ material cases discussed later

The computed nodal velocity vectors are also plotted in Fig. 4.21(a); the figure shows that the

influence area widens as the length increases. The tensile force diagram along reinforcement (Fig. 4.21b) also reveals an increase in tensile force magnitudes with respect to the reinforcement length increments. The computed tensile force distribution pattern is very similar to the experimental observations (Nagao et al., 1988 and Hada et al., 1988).

Figure 4.22(a) shows the velocity field and the tensile force distribution along three 5m long reinforcements placed at three different elevations. In this case, computation is carried out with fine FE mesh to avoid the influence of the FE mesh. The FE layers between the consecutive reinforcements are divided into two layers as shown in Fig.4.18 (b). It shows that a clear tensile force distribution can be obtained without any computational disorder thus avoiding the direct interference effect of the reinforcements. The higher confining pressure at lower elevations because of the gravity loading produced higher magnitude in the tensile force distributions for reinforcements placed at lower elevations.

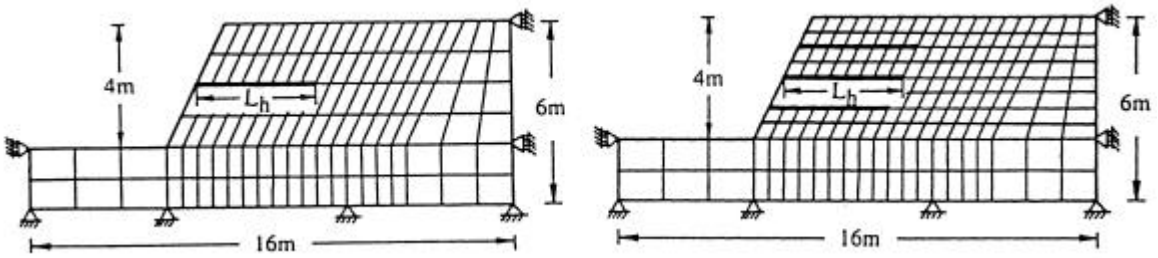

(a) Single Reinforcement Cases (b) Multiple Reinforcements Cases

Figure 4.18 Finite element array for the stability analysis of the reinforced soil slopes.

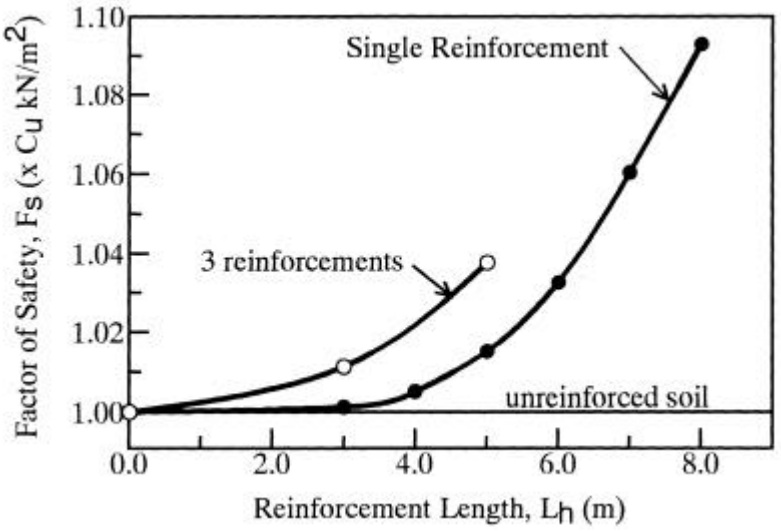

Figure 4.19 Computed factor of safety versus reinforcement length relation in a reinforced purely cohesive clay slope (*Mises material*).

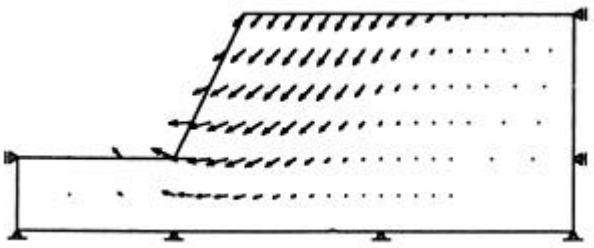

Figure 4.20 Velocity field at limit equilibrium state of the soil mass without any reinforcing material.

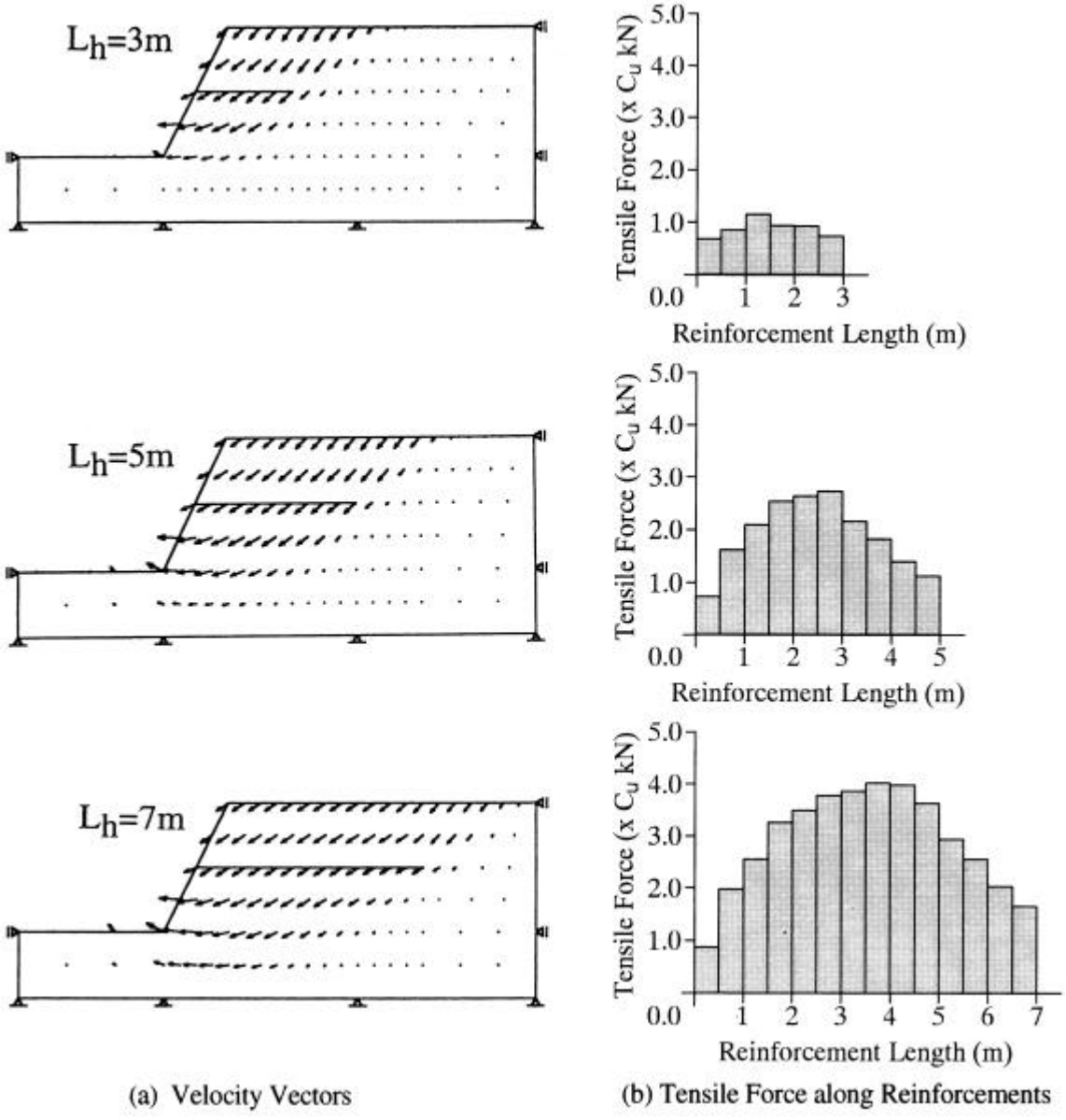

Figure 4.21 Effect of reinforcement lengths on velocity field and the axial force along reinforcements.

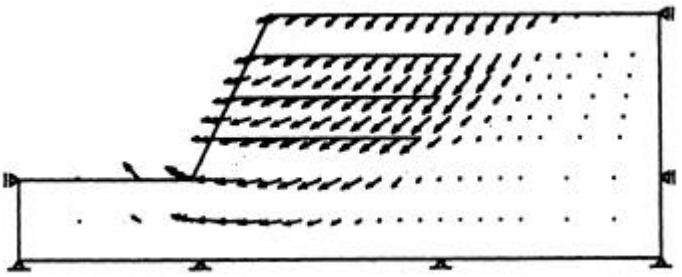

(a) Velocity Vectors

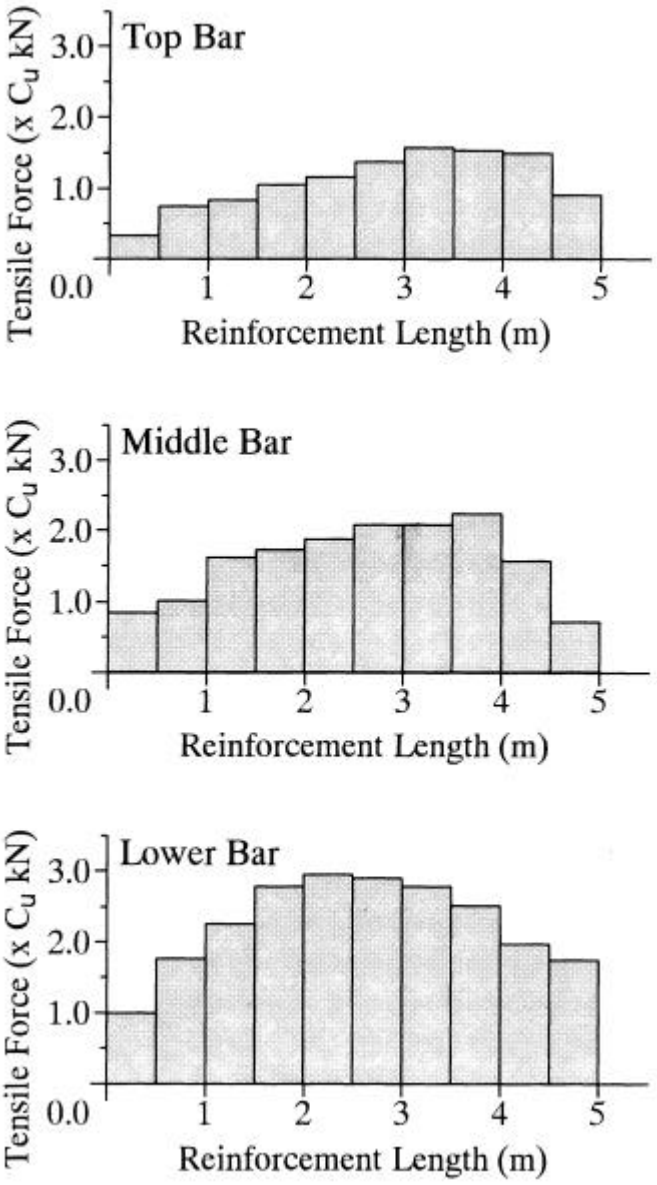

(b) Tensile Force along Reinforcements

Figure 4.22 Effect of multiple reinforcements on velocity field and the axial force distribution along the reinforcements.

Example 2: ***Inclined Reinforcement***

In this example, a reinforcing material is placed at different angles and locations. The length of reinforcement is kept constant, 5m. The total thickness of the soil in previous example is increased by 2m for convenience in placing the reinforcement at different angles. Figure 4.23 shows a typical finite element array and detailed boundary conditions used in this example. The safety factor is computed for three positions (top, middle and bottom) along vertical directions and at five different inclinations corresponding to each position as shown in Fig. 4.24. Factor of safety gradually increases (Fig. 4.24) as the reinforcement position is lowered and or inclination is increased or the number of reinforcements are increased. The figure shows that the lower position is relatively more effective. It should also be noted here that the absolute increase in safety factor is relatively smaller than the frictional (c-ϕ) material case to be discussed later.

Though the factor of safety for the top, middle and bottom positions are presented; the velocity vectors, the reinforcement force and the principal stress distributions are discussed in detail only for the middle position.

The computed nodal velocity vectors are plotted in Fig. 4.26a; the figure reveals that the failure region goes on widening with respect to increase in the reinforcement inclination. Figures. 4.25b and 4.26b show the principal stresses corresponding to the unreinforced and the reinforced cases respectively. The directions of principal stresses are smoothly changing in unreinforced soil while the principal stress directions in reinforced soil are abruptly rotated around these inclined reinforcements. Such rotation may be attributed to the soil-reinforcement interface friction.

Figure 4.26c shows the tensile force distribution in a reinforcement corresponding to the middle position. The horizontal position gives the parabolic distribution, but, as the inclination of the reinforcement becomes steeper, the tensile force distribution diagram tends to be uniform. Though the maximum tensile force decreases due to the steeper inclinations of the reinforcements, the safety factor is still increasing.

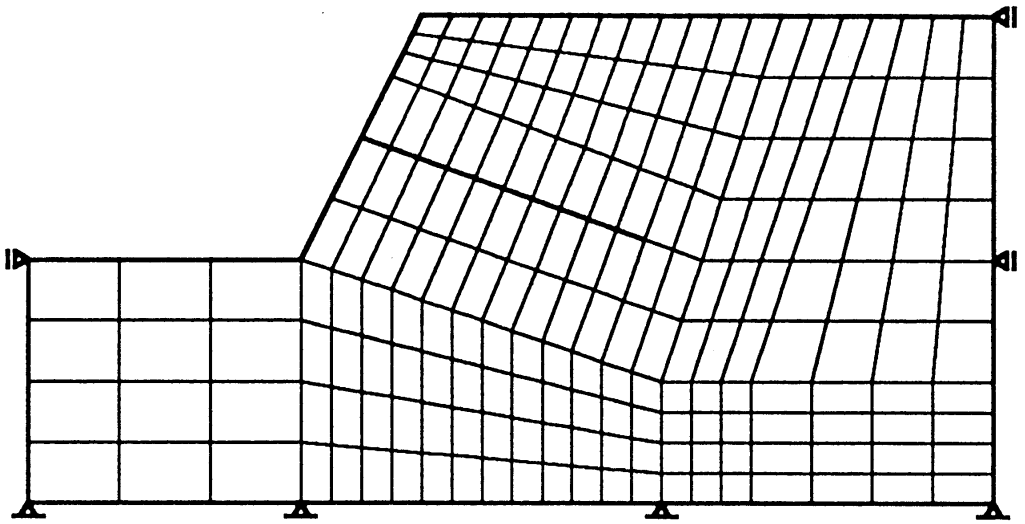

Figure 4.23 A typical finite element array for the slopes reinforced with the inclined reinforcements.

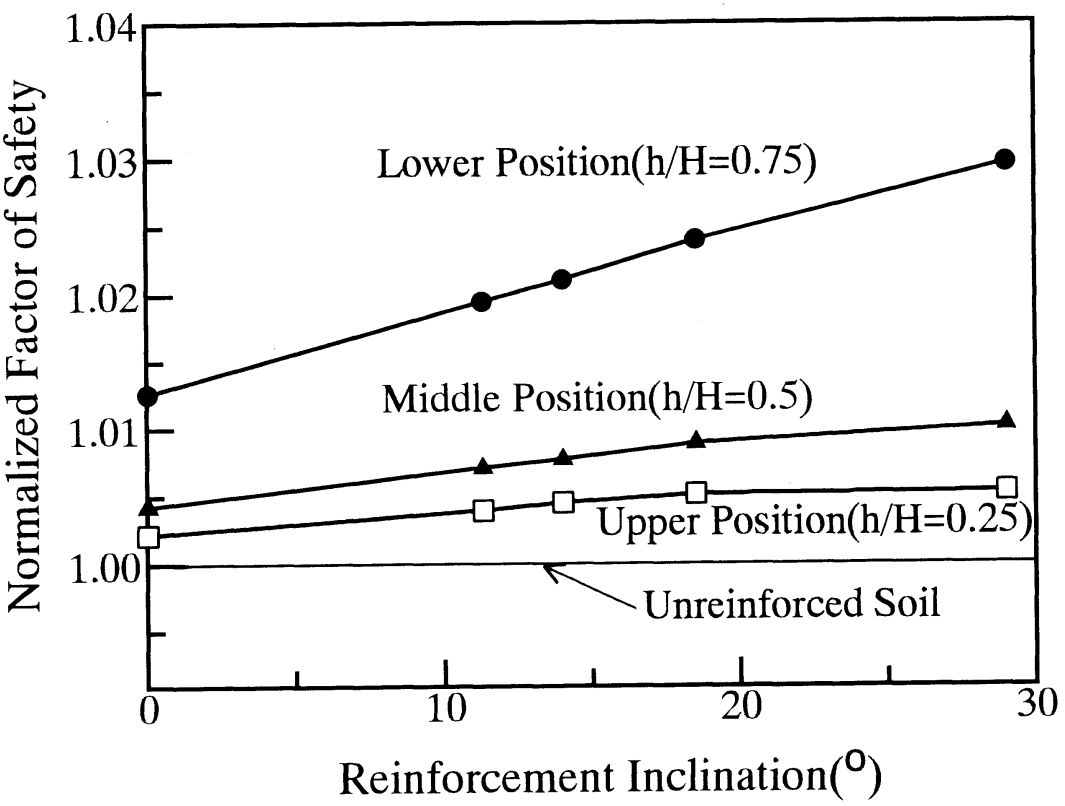

Figure 4.24 Computed factor of safety versus reinforcement inclination relations for a reinforced purely cohesive clay slope (*Mises material*).

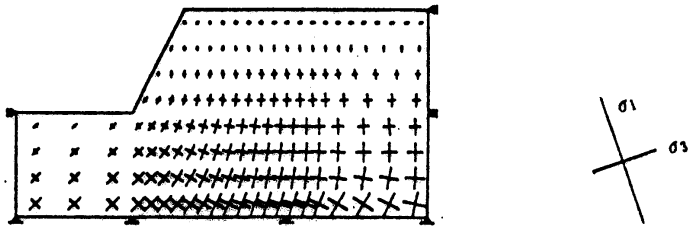

Figure 4.25 Velocity field and principal stress orientations in the unreinforced cohesive clay slope.

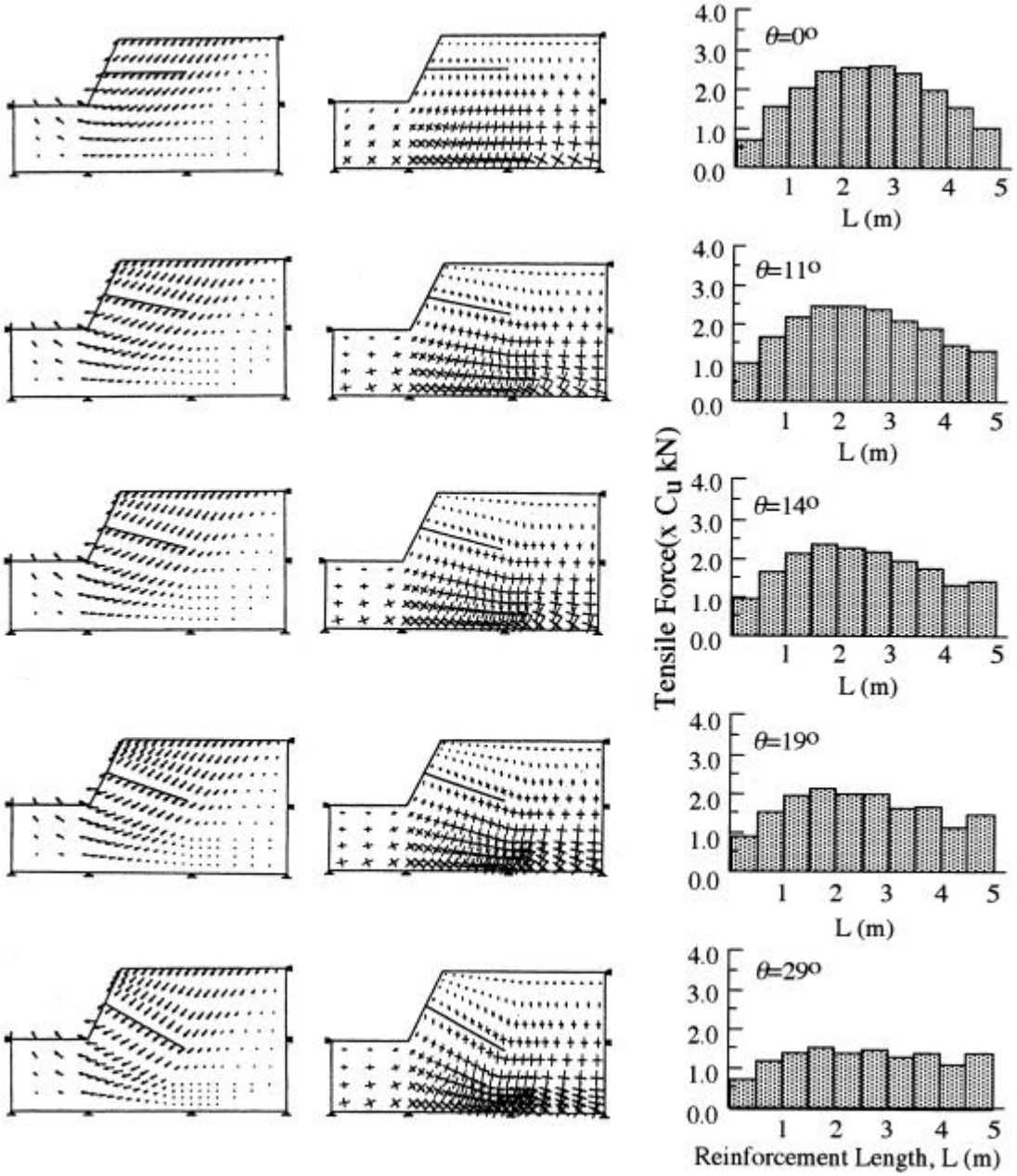

Figure 4.26 Effect of reinforcement inclinations on velocity field, principal stress orientations and the axial force distribution along reinforcements.

Example 3: ***Reinforced Slope with Facing Material***

In this example, the facing panels are installed in order to examine the effect of facing on the slope rigidity as shown in Figs. 4.27 & 4.28. Facings are assumed rigid enough; therefore, the formulation for the "*no-bending*" condition presented in the Chapter III is employed. The facings are discretized in two ways: (a) Panel facing with pin-joints at the connection (Fig. 4.28a). (b) Rigid continuous facing, e.g., full height RCC facing or panel facings with rigid connections at the joints (Fig. 4.28b). The latter type can be modeled by overlapping several basic bending elements in series as shown in Fig.4.28b. As facing is assumed to follow the "*no-bending*" condition, the distance between nodes representing facing also does not change at the limiting equilibrium state, such that the thickness of the facing does not explicitly appear in the numerical analysis.

The slope configuration is same as in the Example 1 where a 5m long reinforcing material is connected to facing panels (Fig. 4.29). The axial force distributions along reinforcement lengths (Figs. 4.30 & 4.31) and shear force(or bending moment) distributions along facing are computed. The computed bending moment is presented in Fig. 4.32. Very high bending moment at the facing-reinforcement connection clearly reveals the resistance by panel facing to bending due to the lateral earth pressure. The factor of safety in this case is Fs=1.036. When compared with the no-facing case, the effect of the facing is same as the effect of three reinforcements case without facing (*see* Tables 4.6 and 4.7).

Table 4.6 Computed safety factor for the facing connected to the single reinforcement cases

Type	Factor of Safety, F_S
Unreinforced case	1.000
Reinforcement alone (without facing)	1.015
Reinforcement connected to facing. Facing discretized by technique, T-1	1.025
Reinforcement connected to facing. Facing discretized by technique, T-2	1.039

Effect of the facing connected to multiple reinforcements is investigated, where the facing is discretized by the aforesaid techniques. The velocity vectors and the reinforcement force distributions corresponding to these two techniques are compared with the multiple reinforcements without facing (*see* Figs. 4.33 & 4.34). The nodal velocity vectors acting on the facing nodes are parallel to each other for the continuous rigid type of facing in contrast to the no-facing case or three reinforcements with facing modeled by the first method. The facing does not exhibit significant effect on the velocity field. The magnitude of the velocity vectors away from toe is very high compared to the no-facing case and the facing discretized by the first technique.

Thus, the soil rotation is above the toe in no-facing case or in pin-jointed panel facing case and the rotation is about the toe when facing is a rigid continuous type. The axial force distribution pattern is parabolic. The lower reinforcement exhibits maximum axial force close to the slope face and gradually decreasing towards the inner end of the reinforcements. The top and middle positioned reinforcements have axial force distribution very similar to the no-facing case. The bending moment diagram (Figs. 4.34 & 4.35) using both the facing discretization technique produces almost similar peaks while the distribution is better represented in the second method.

Table 4.7 Computed safety factor for the facing connected to the three reinforcements

Type	Factor of Safety, F_S
Unreinforced case	1.000
Reinforcement alone (without facing)	1.037
Reinforcement connected to facing. Facing discretized by technique, T-1	1.050
Reinforcement connected to facing. Facing discretized by technique, T-2	1.054

In addition to the aforementioned facing discretization techniques, another alternative approach (Fig. 4.36) is also attempted. In this method, the lengths between all nodes on both sides of this panel facing area (Fig.4.36) are assumed to follow only the "*no-length change*" condition. The thickness of the facing appears in the numerical analysis (Figs. 4.36 & 4.37). Therefore, both the compressive and the tensile force distributions could be computed. The computed results shown in Fig. 4.38 clearly demonstrate that the inner side of the facing is under tension while outside is under compression. This verifies that the panel facing resists the bending moment induced due to the lateral earth pressure. The factor of safety in this case is Fs=1.039. As compared with the no-facing case (Fig.4.22), the effect of the facing is same as the effect of the three-reinforcement case without facing.

The velocity vectors and the tensile force distribution along reinforcement shown in Fig. 4.39(b) exhibits similarity with Fig.4.30 (a). The directions of the velocity vectors on the panel facing nodes are restrained due to the existence of facing while the velocity vectors away from the slope toe have relatively wider influence area and larger relative magnitudes. The tensile force distribution near the facing becomes larger than the no-facing case and has almost similar pattern as that observed in many experiments (e.g. Schlosser, 1990 and Tatsuoka et al., 1992).

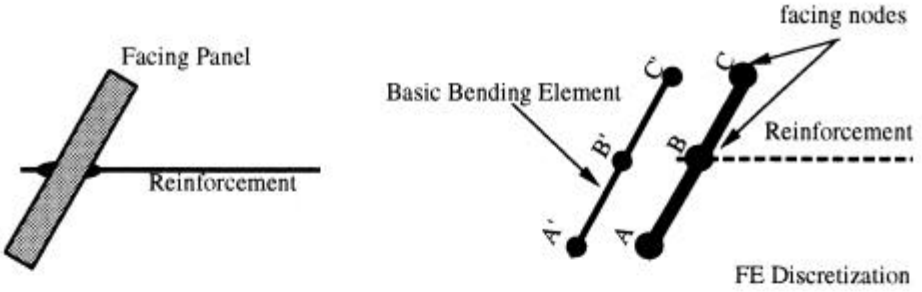

Figure 4.27 FE discretization of a single facing panel as a basic bending element.

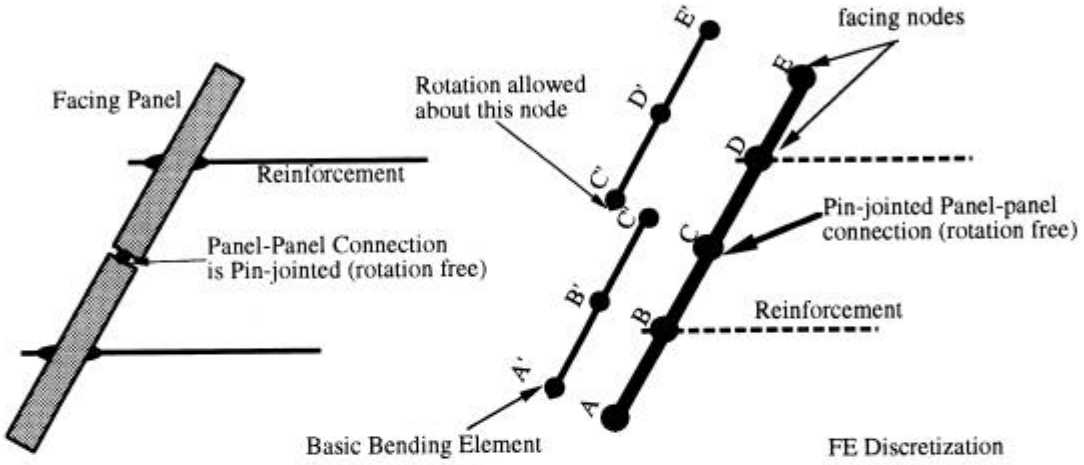

Multiple panels having pin joint connection at the panel-panel interface..

(a) Facing Discretization Technique-1

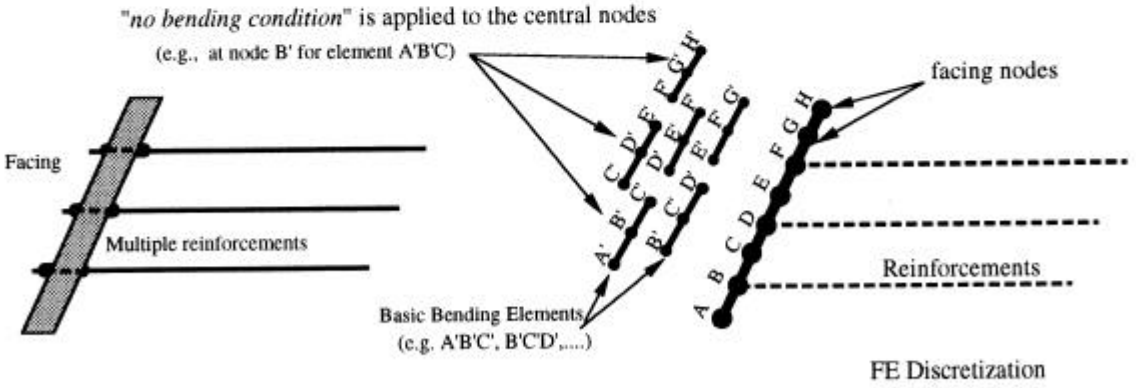

Multiple reinforcements connected to a full height rigid concrete facing or multiple facing panels with rigid panel-panel joints.

(b) Facing Discretization Technique-2

Figure 4.28 FE discretization techniques for a continuous and a discrete rigid facing material.

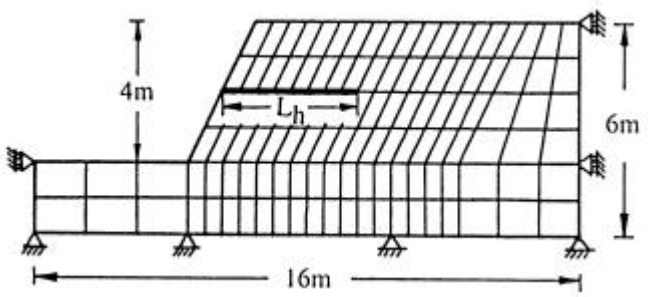

Figure 4.29 A typical finite element array for the reinforced slopes with facing material.

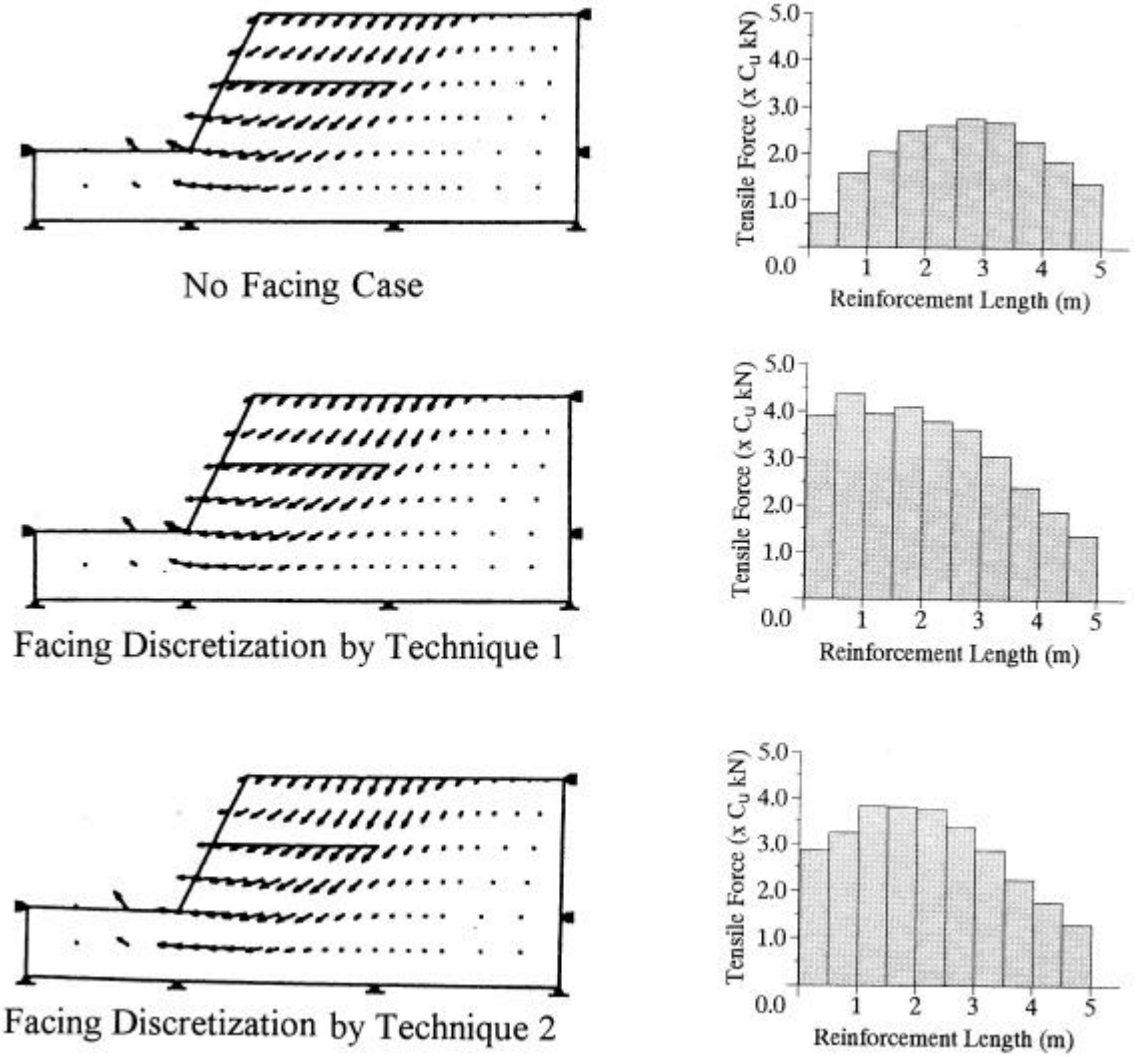

(a) Velocity Vectors (b) Tensile Force along Reinforcements

Figure 4.30 Effect of facings on velocity field and axial force distributions in bars.

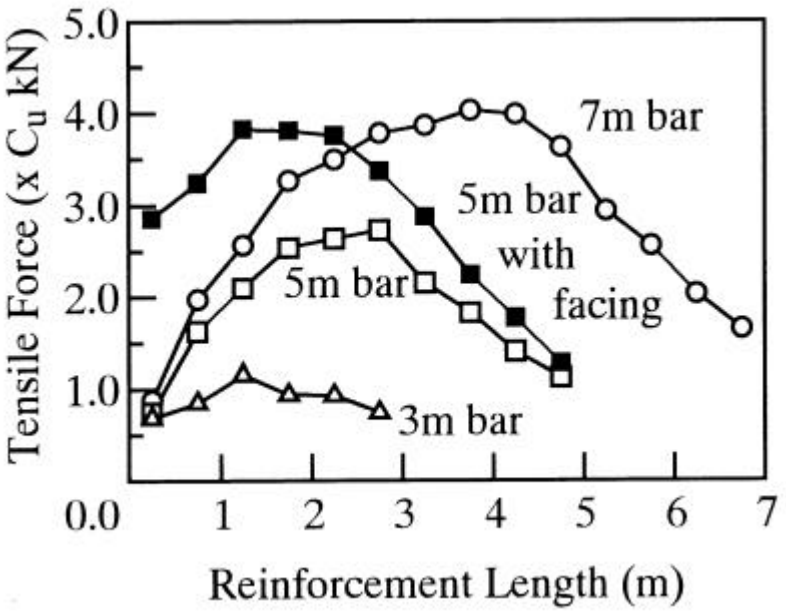

Figure 4.31 Comparisons of axial force distributions along reinforcements with and without facing materials.

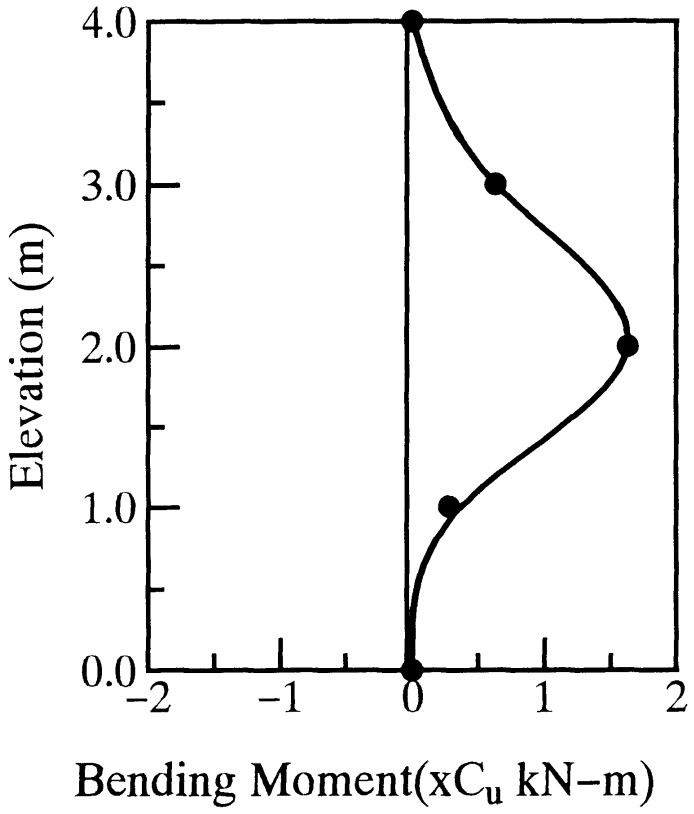

Figure 4.32 Computed bending moment distribution along a facing panel connected to single reinforcement.

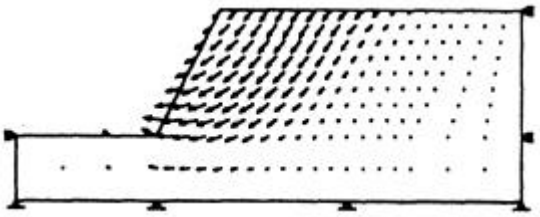

Figure 4.33 Velocity field in the unreinforced soil mass at limit state.

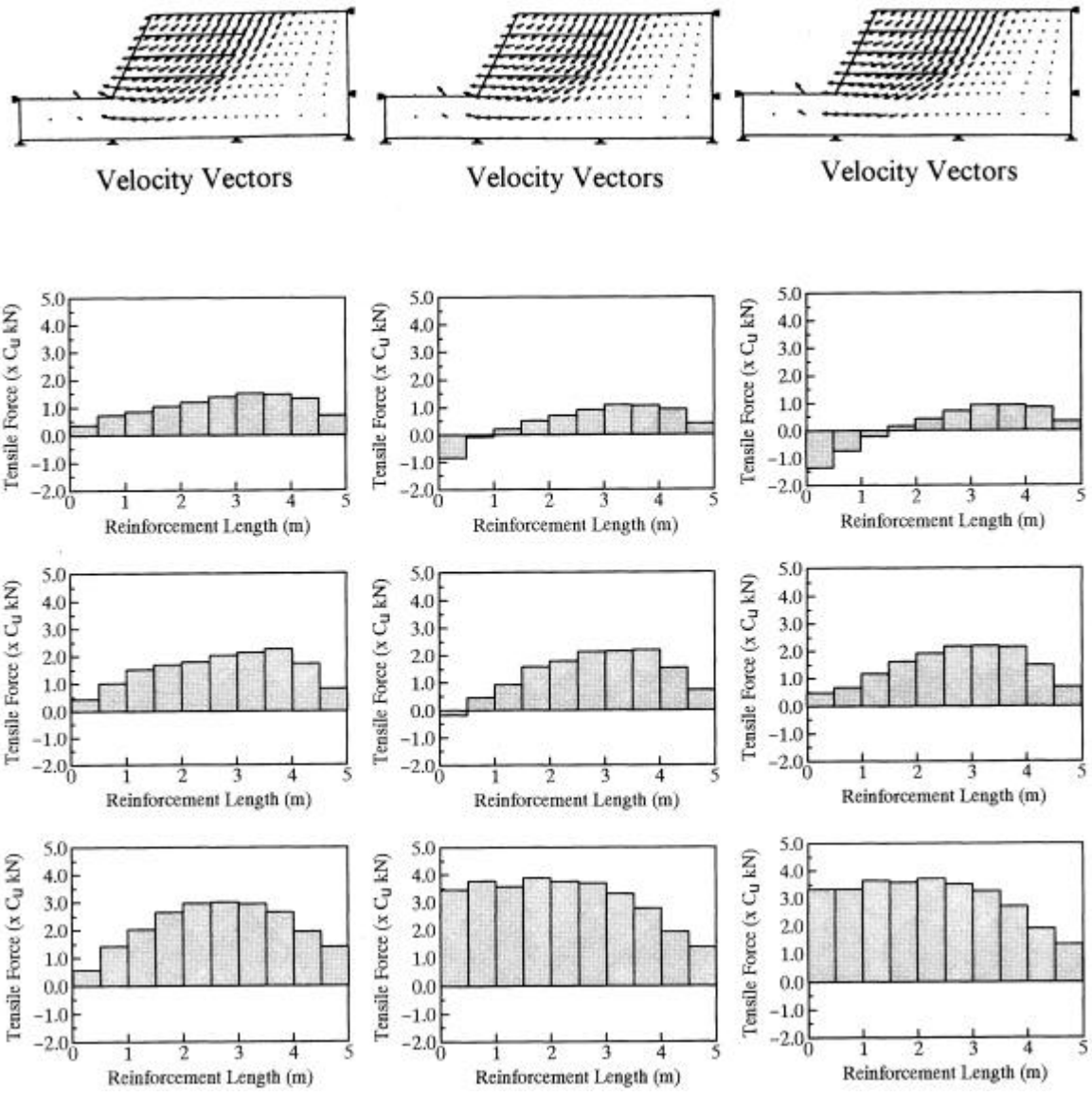

(a) No-facing case (b) Facing Discretization by Technique 1 (c) Facing Discretization by Technique 2

Figure 4.34 Effect of facings connected to multiple reinforcements on velocity field and the axial force distributions along reinforcements.

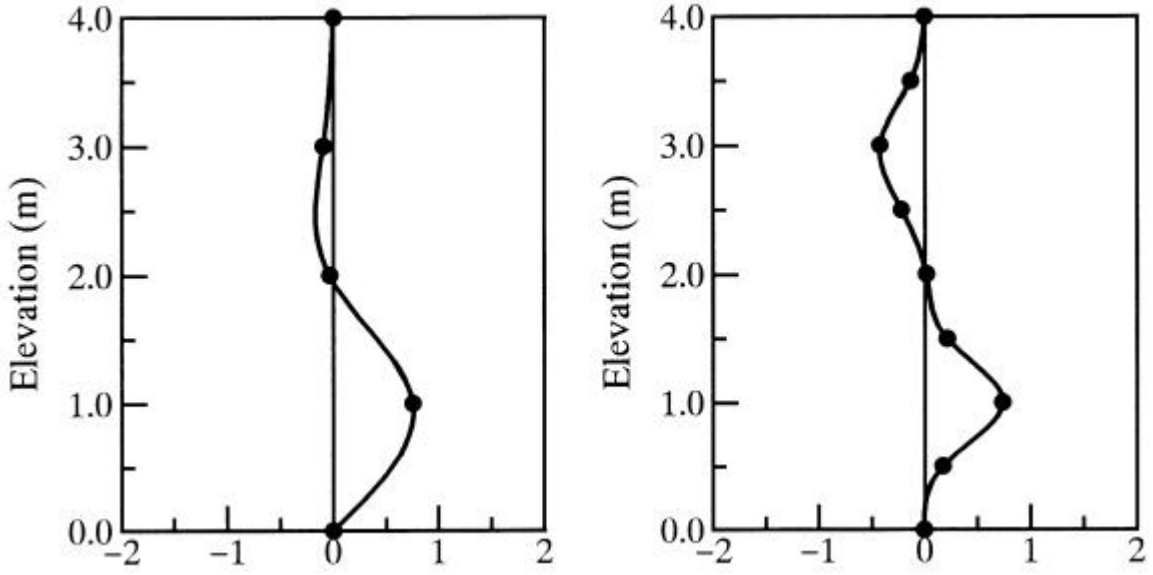

(a) Facing Discretization by Technique 1 (b) Facing Discretization by Technique 2

Figure 4.35 Computed bending moment distribution along the facing connected to a set of multiple reinforcements.

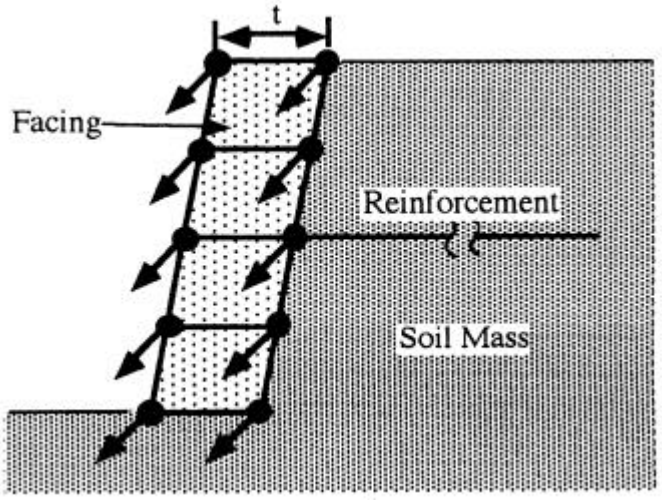

Figure 4.36 An alternative method of modeling the facing employing only the *no-length change* condition.

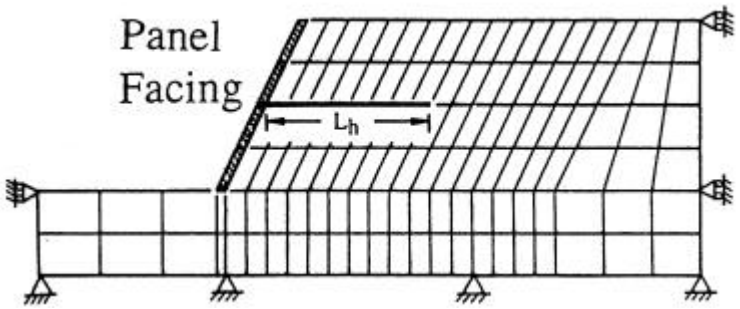

Figure 4.37 Finite Element Mesh used in used in the alternative method.

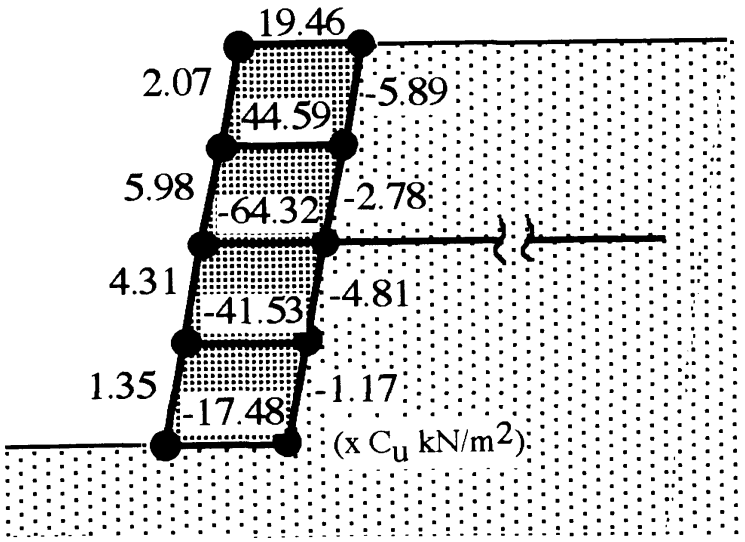

Figure 4.38 Tensile and compressive forces in the panel facing connected to facing.

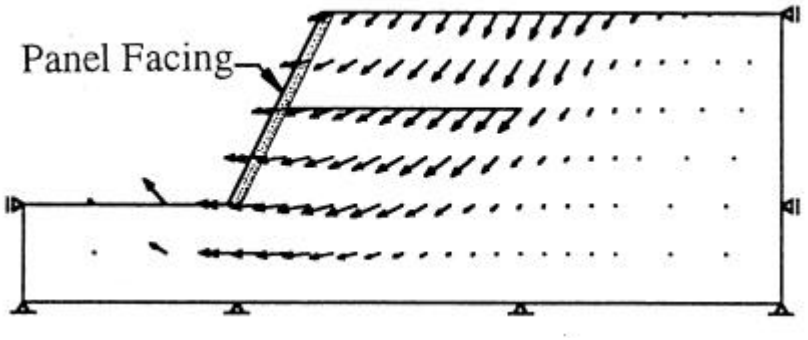

(a) Velocity Vectors

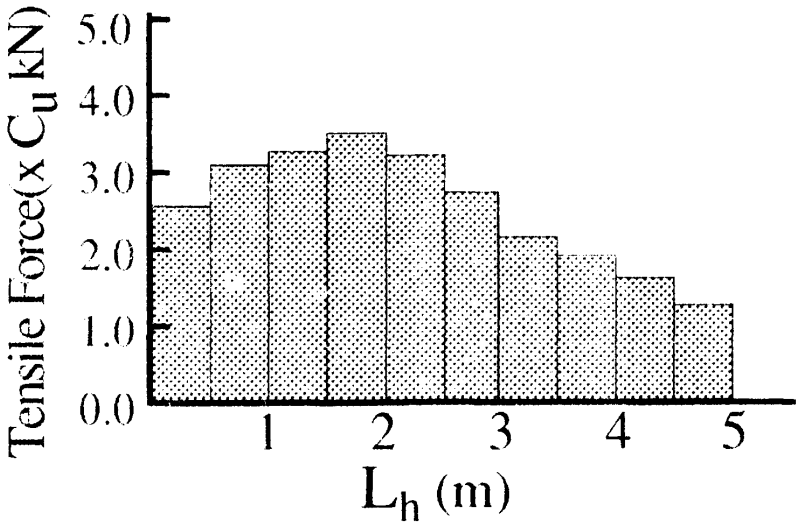

(b) Tensile Force along the Reinforcement Length

Figure 4.39 Effect of the panel facing on velocity field and axial force distributions.

4.3.3 Sandy Soil (*c-f material*)

The last representative problem taken is the stability analysis of a sandy slope (i.e. frictional, *c-f*, material: c=4.4 kPa, $\phi=30^{o}$). As stated in the second chapter, *c-f* material is analyzed as inhomogeneous Mises material satisfying the Mohr-Coulomb failure criteria at the limit state. The boundary conditions of the slope discussed in this example are shown in Fig. 4.40 that is similar to *Example 1* in this section concerning the slope face grading, thickness of the soil layer and the reinforcement positions. Two sets of analyses were carried out, first with single reinforcement and latter, with multiple reinforcements (Figs.4.41~4.44). Figure 4.41 shows the relationship of the computed factor of safety and the length of reinforcement in the former two cases. The reinforcing effect of the sandy (c-ϕ) material is larger than that of the purely cohesive clay. Even a single short reinforcement produced the factor of safety as much as two times of the unreinforced soil (*see* Fig.4.45). Factor of safety considerably increases when soil is reinforced with multiple reinforcements, e.g., three reinforcements give about 5 times of the unreinforced slope.

Figure 4.42 shows the velocity field, the principal stress distributions and the mean confining stress distribution in the soil mass without reinforcement. The failure zones are very narrow and close to the slope face compared with the failure regions observed in the purely cohesive clay slope (Fig. 4.21).

The computed velocity fields, the principal stress distributions, the mean confining stress distributions and the tensile force distributions along the reinforcement are shown in Fig. 4.43 for a single reinforcement of varying lengths. For relatively short reinforcements, e.g. 1.5m, the widening effect of velocity field bears resemblance with the Mises material discussed in the earlier sub-section. Further increase in the reinforcement length divides the velocity field into two small zones on either side of the reinforcement as shown in Fig.4.43 (a). The inner end of the reinforcement also reaches rigid area ($\dot{\bar{e}} = 0$, *see* Eq.3.40). The magnitude of the mean confining stress in soil mass around reinforcements shows a significant increase. The magnitude of the tensile force along reinforcements in such sandy soil mass is directly influenced by the magnitude of the mean confining pressure around the reinforcement. For the reinforcements approaching a high confining pressure zone, the tensile force magnitude increases substantially towards the zone (Fig. 4.43b). This behavior can be compared with an anchor used for rock bolting. Thus, the high confining stress in the sandy soil equivalently acts like a rock bolt.

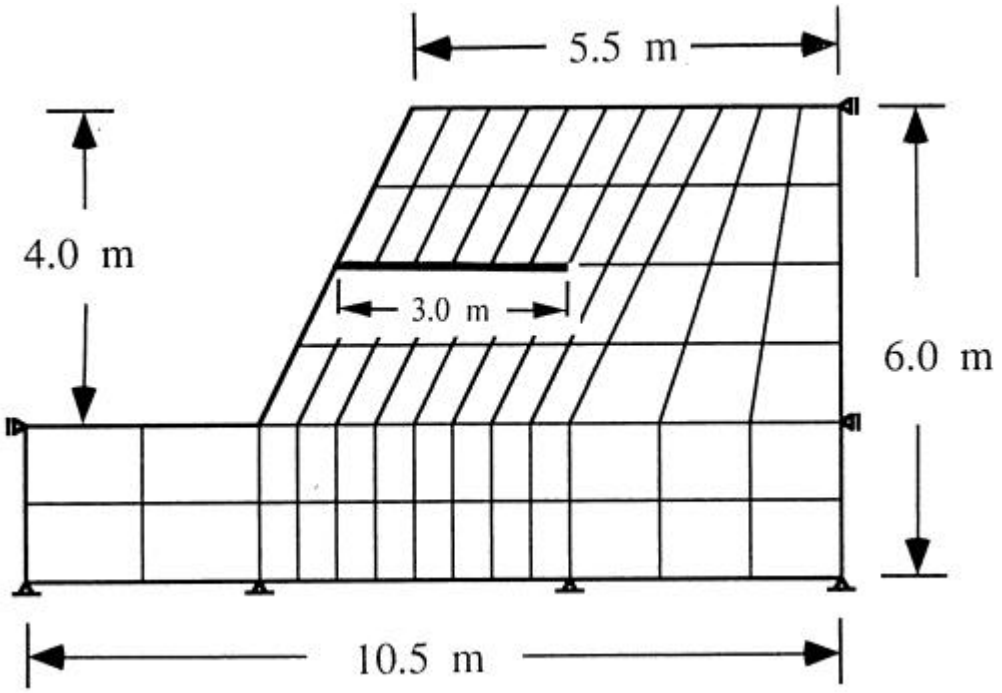

Figure 4.40 A typical finite element array for FE analysis of the reinforced slopes with frictional (c-ϕ) material.

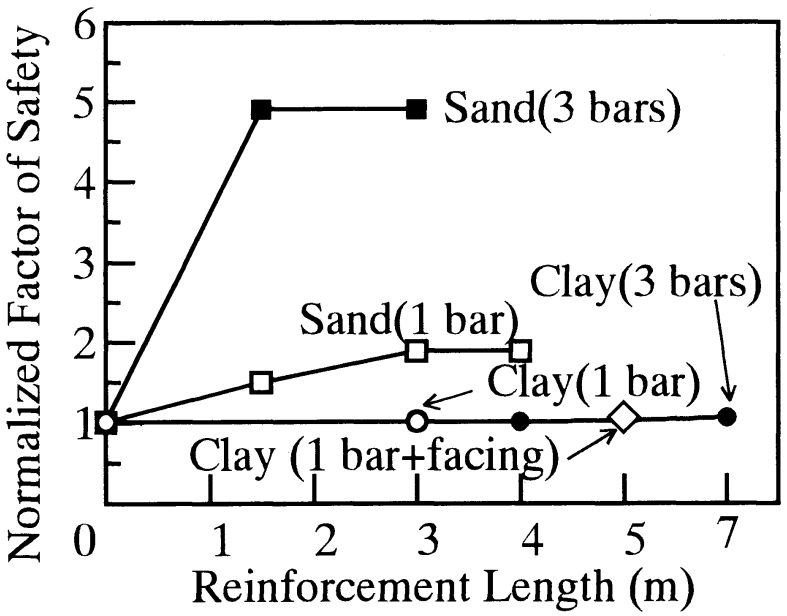

Figure 4.41 Computed factor of safety versus reinforcement length in a reinforced frictional soil and comparisons with the normalized safety factors for purely cohesive clay slopes.

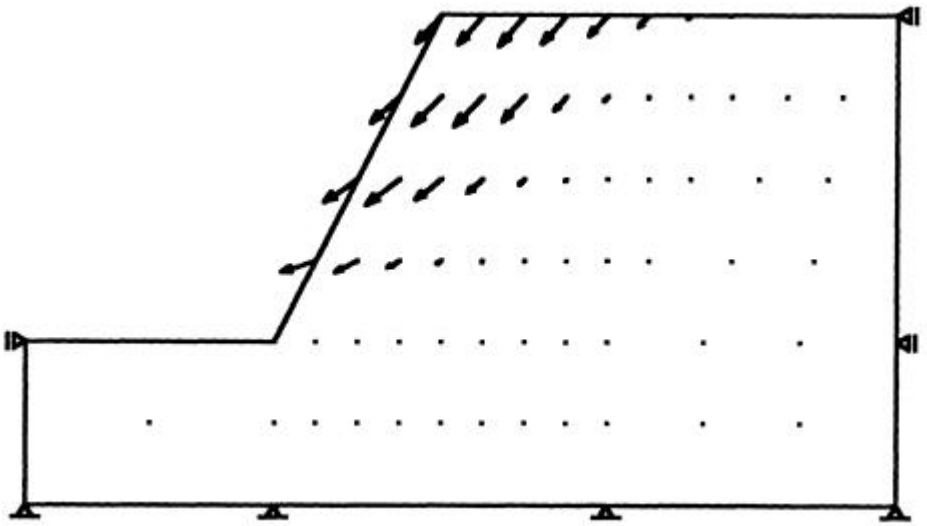

(a) Velocity Vectors

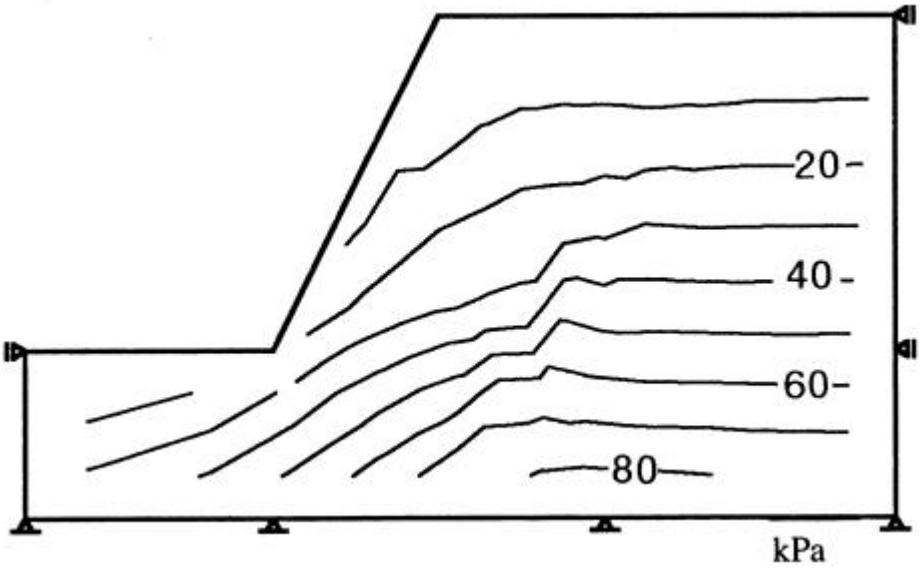

(b) Mean Stress Distributions

Figure 4.42 Velocity field, principal stress orientations and mean confining stress contours in a frictional soil (c-ϕ) without any reinforcing material.

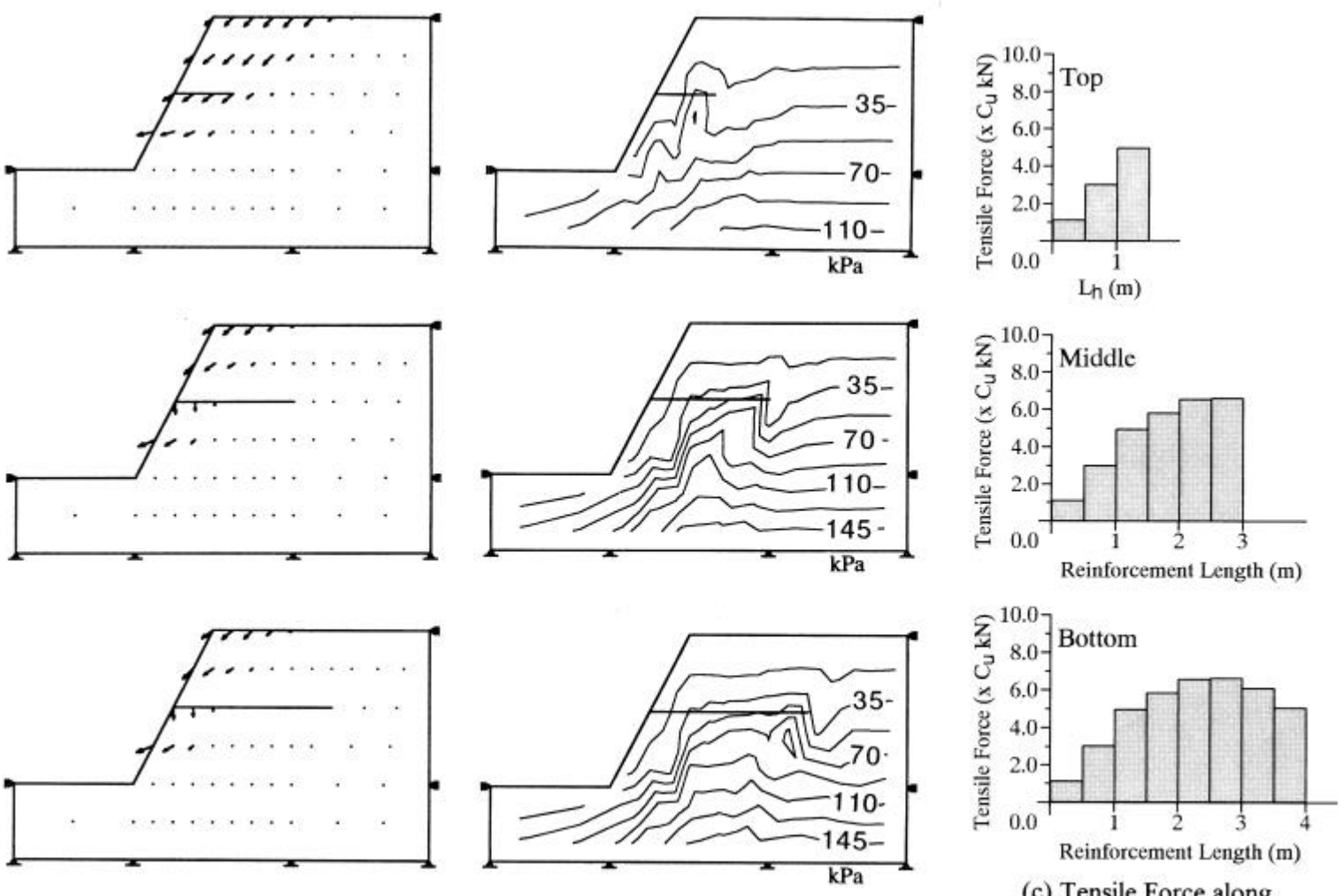

(a) Velocity Vectors (b) Mean Stress Distributions (c) Tensile Force along Reinforcement Length

Figure 4.43 Velocity field, mean confining stress contours and axial force along reinforcements of different lengths in case of frictional soil (c-ϕ).

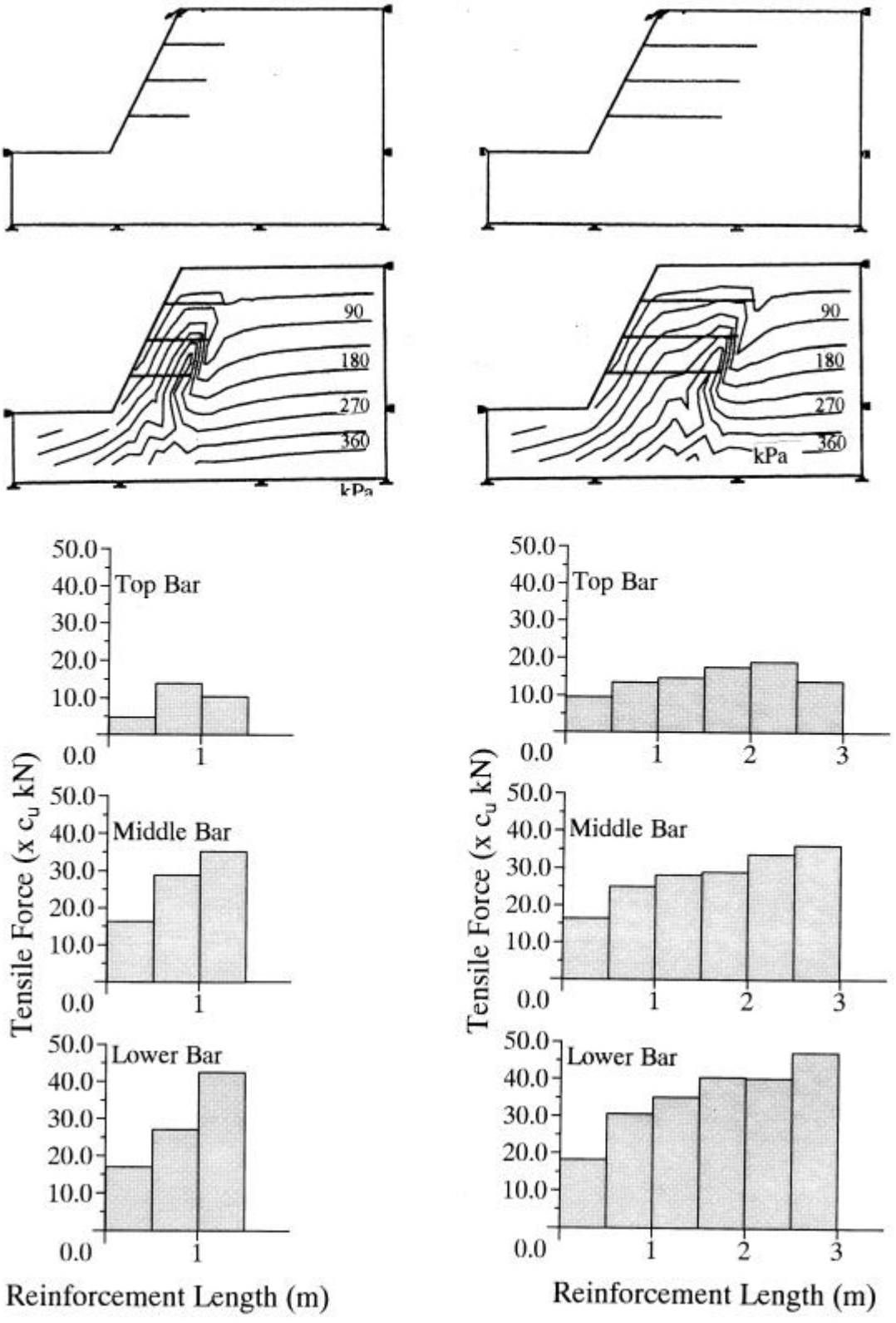

(a) Short Reinforcements (L=1.5m) (b) Long Reinforcements (L=3.0 m)

Figure 4.44 Effect of multiple reinforcements on velocity field; mean confining stress contours and axial force distribution (*c*-*f* material).

4.4 SUMMARY AND CONCLUDING REMARKS

The numerical method formulated in the previous chapter, Chapter III, by introducing a new concept of computation of bearing capacity/safety factor, distribution of the axial and the shear forces (/bending moment) in reinforcing members as well as velocity vectors and stress distribution in reinforced soil structures is investigated and the features/capability of the methodology is demonstrated through some typical reinforced soil engineering structures. The effects of tensile reinforcements and flexural materials are coupled in the conventional rigid plastic finite element method by introducing a set of constraint conditions of "*no-length change*" and "*no-bending condition*" of the soil element nodes corresponding to reinforcing members at the limit equilibrium state of the soil mass.

The proposed concept is tested numerically in one set of bearing capacity problems and two sets of slope stability problems with strip footing loading and gravity loading, respectively. The following conclusions are drawn through the present study:

1. The "*no-length change*" and "*no-bending*" conditions in the soil mass at the limit equilibrium state can be introduced in the plastic energy dissipation minimization problems. In this case, the Lagrange multipliers corresponding to the constraint condition of no-length change and no-bending condition represent respectively the axial force and the shear force in the reinforcing material per unit length.
2. In the bearing capacity problem of purely cohesive clay, a set of optimum reinforcement positions are obtained depending on the footing type. The maximum effect on the bearing capacity in the reinforced homogeneous clay mass is about 13% larger compared with the unreinforced case and 25% in the case of clay having linearly increasing shear strength with depth.
3. In the slope stability case, reinforcements have contrast effect on the safety factor of the problem depending on the soil type, i.e. purely cohesive clay or frictional (c-ϕ) material. The increase in safety factor in the frictional soil is quite higher than the purely cohesive clay due to the differences in the mechanism of reinforcements depending on the soil type. In frictional material, the bar acts like an anchor while in the purely cohesive clay the bar does not show such effects. Such effect was clearly explained through the velocity field, the mean confining pressure and the axial force distribution in the reinforcement.

4) For the first time, the effect of rigid panel facing is included in the stability analysis. The proposed method could explain well the effect of flexural rigidity of the facing. It can be explained with the axial and the shear force developed in the facing.

CHAPTER V MODEL TESTS AND THEORETICAL ANALYSIS

5.1 GENERAL

In Chapter III, reinforced soil systems at the working load and at the limiting equilibrium state were newly formulated based on the linear elastic plastic finite element method (LEFEM) and the rigid plastic finite element method (RPFEM), respectively, by introducing some new concepts on the mechanism of reinforcing the soil mass. In Chapter IV, salient features of the formulation were demonstrated through a few typical reinforced soil-engineering problems under ideal material properties and boundary conditions. The applicability of the proposed methodology is clearly verified through such ideal problems and present chapter is intended to support the applicability of the methodology into real reinforced soil structures with diverse material properties and boundary conditions.

To fulfill the aforesaid objective, a set of medium-sized 1g model tests, carried out during this research work is explained. Firstly, the model test set-up and test conditions are outlined. Then, observed behaviors of these model tests from initial loading to the ultimate failure state are explained in detail concerning various aspects of these structures. Latter, the proposed numerical methodology is tested by simulating the model test results. It will be shown that the numerical methodology proposed in this research can nicely simulate the real observed behavior of the reinforced soil structures which provides confidence enough for the practicing engineers to implement the methodology in the design and analysis of such complex real reinforced soil structures.

Applicability of the proposed numerical methods is examined through analyzing the results of a series of medium scale 1g model tests of the reinforced soil slopes. These slopes are about 1m

high and made of sandy soil fill, in which the reinforcing steel bars and slope facing members are installed. Deformation of the slope and the failure modes are monitored during the vertical load application on top of the slope. Advantages and limitations of the aforementioned analysis methods are assessed using these observations of the real model test.

5.2 OUTLINE OF MODEL TESTS

5.2.1 Description of Test Facility

An overview of the reinforced soil model test facility is given in Fig.5.1. The principal structural components of the facility were four rigid concrete walls of 200mm thickness and a rigid floor. Plan and sectional elevation of the test facility along with loading arrangements are shown in Fig.5.2. Stability of the concrete walls against translation was provided by 25mm diameter anchor rods/bolts as shown in Figs.5.1 & 5.2. Additional lateral stability was secured by bolting the two I-beams at the bottom of the wall. The inside surface of the walls were faced with Teflon sheets and detailed explanation is given at a later section.

Loading System

Loading on the soil was applied through a rigid steel plate (500 mm x 900 mm) considering it as an equivalent rigid rough footing. The bottom surface of the footing plate was made rough by attaching rough sandpaper. A hydraulic jack manually operates this loading system. Lower end of the load cell pushes the footing (i.e., loading plate) and the other end is fixed on the horizontal I-beam. Reaction force developed on the I-beam is finally transferred to the rigid floor through a I-beam-column setup. Figure 5.1 shows the details of the loading system.

Side Wall Friction

The friction between soil mass and the wall surface is made very smooth by the following treatments: (1) Teflon sheets (1mm thick) were stuck firmly on the wall surfaces and then grease was applied over these sheets. (2) The greased surface was further covered by another soft silicon mixed paper sheet that can tear under very low stresses. Because of such very low wall friction and rigidly fastened concrete walls, all the model tests are considered as "plane strain" tests.

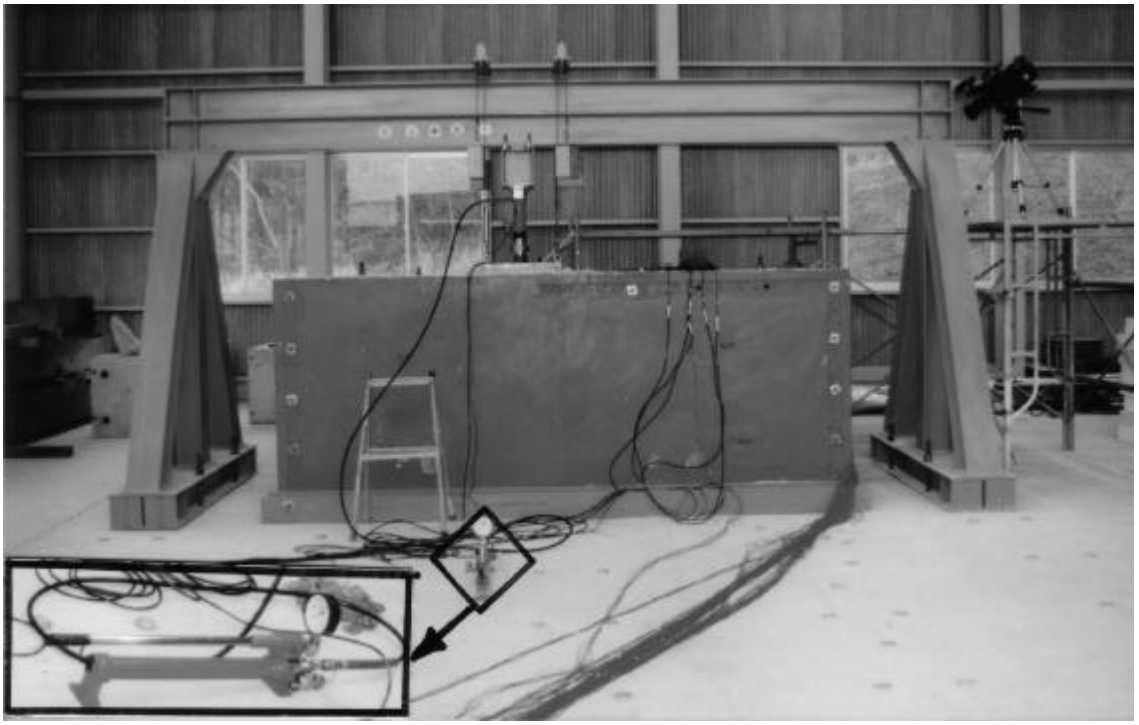

(a) Front view of the model setup

(b) Inside view of the model and model set up when the concrete wall was removed

Figure 5.1 Inside and outside views of model test set-up.

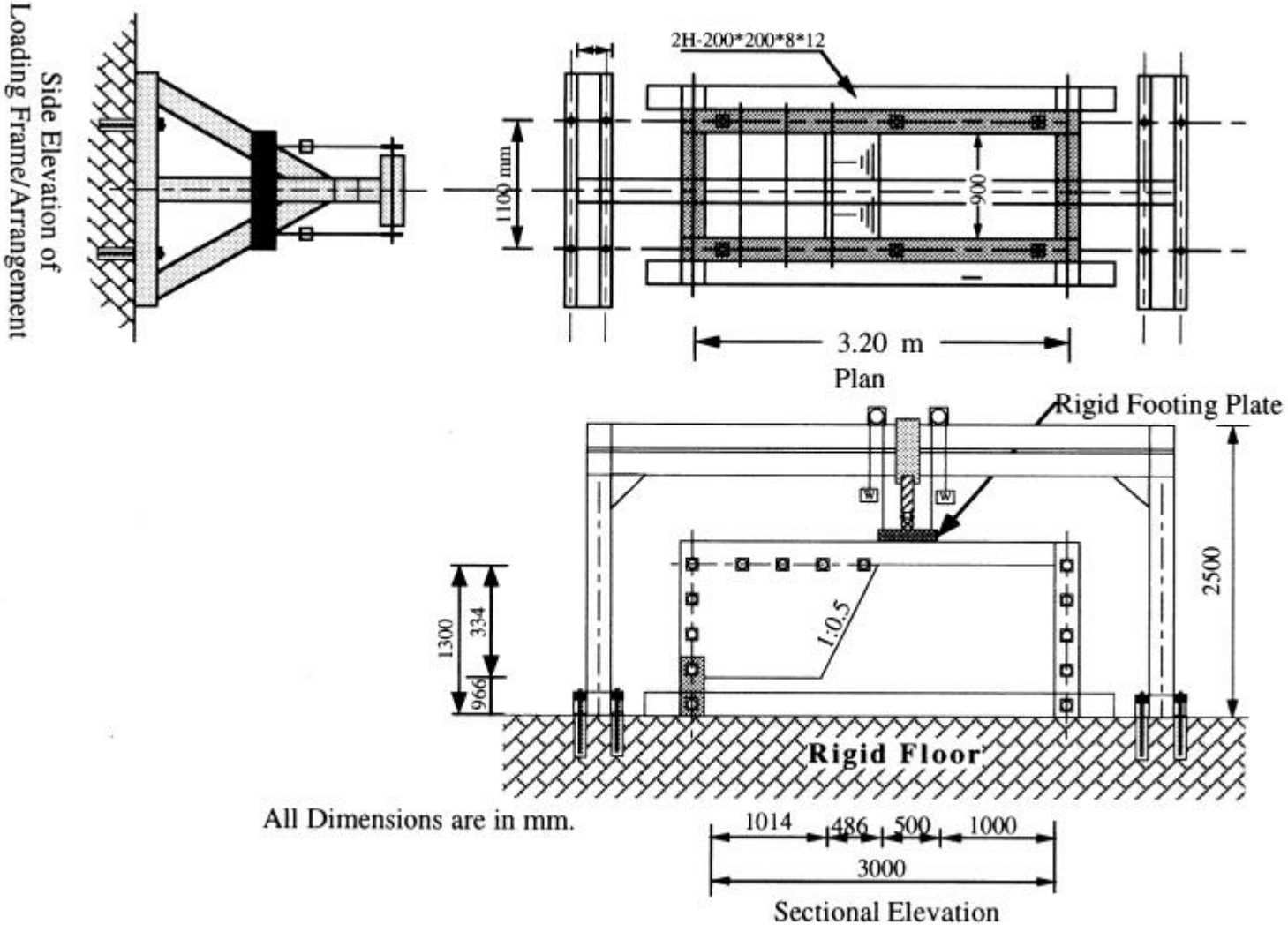

Figure 5.2 Plan, sectional elevation and side elevation of the model test facility.

Instrumentation

Models were instrumented to measure the following items during the complete loading operation (Fig.5.3):

(1) Load (loading stress)- A load cell installed at the center of the loading plate measured the load, and the loading pressure was an average of the load per unit area.

(2) The vertical settlement of the loading plate,

(3) The axial strain in reinforcements and

(4) The horizontal movement of the facing panels or slope face.

Slip surface and the total deformation of the model slopes at failure were observed by removing a concrete sidewall after complete loading operation.

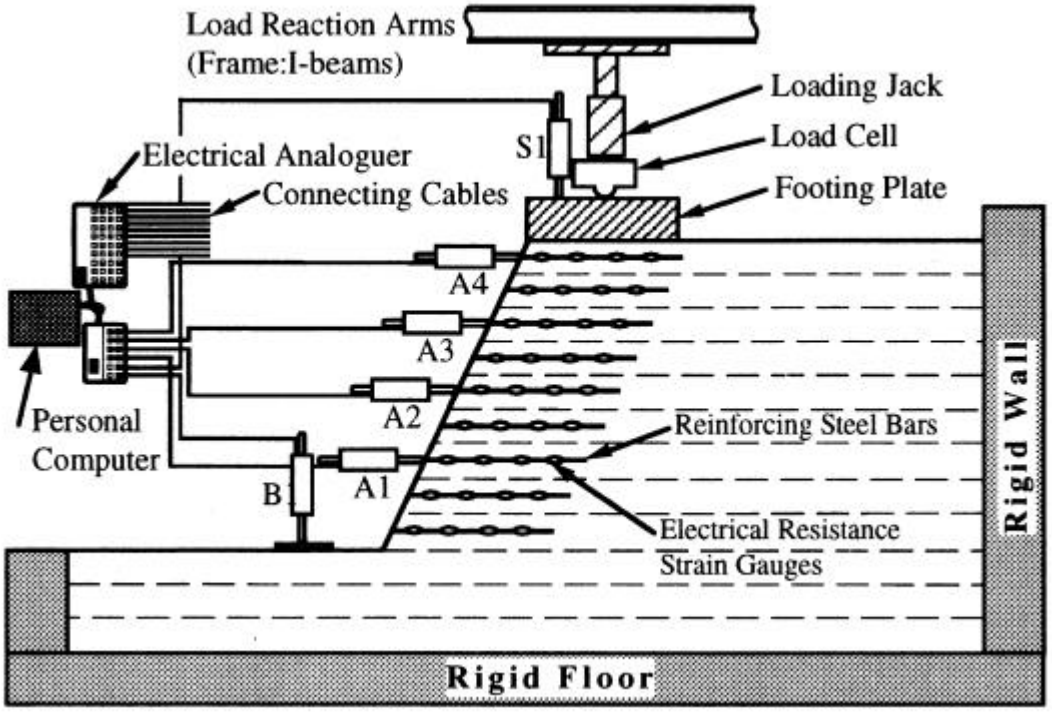

Figure 5.3 Details of instrumentation and measurements

5.2.2 Testing Materials

Fill Material *- Sand*

The fill material (soil) used was classified as silty-sand (SM). The grain size distribution for this material is given on Fig. 5.4. The optimum moisture content (OMC) was determined by standard compaction test. The compaction test results are plotted in Fig. 5.5. Some physical and mechanical test results are presented in Table 5.1.

Table 5.1 Physical and mechanical properties of fill material

Material Parameters	Values
Specific gravity, G_S	2.716
Maximum dry density, γ_{max}, kN/m^3	18.34
Optimum moisture content, w_{opt} (%)	12.80
Cohesion, c, kN/m^2 (CD Triaxial Test)	0.0
Angle of internal friction, ϕ, (deg.)	35^o
Particles passed the 2mm sieve (grain size analysis)	100 %
Particles passed the 0.074 mm sieve	18.2%
Uniformity coefficient	27.1
Coefficient of Curvature	3.48

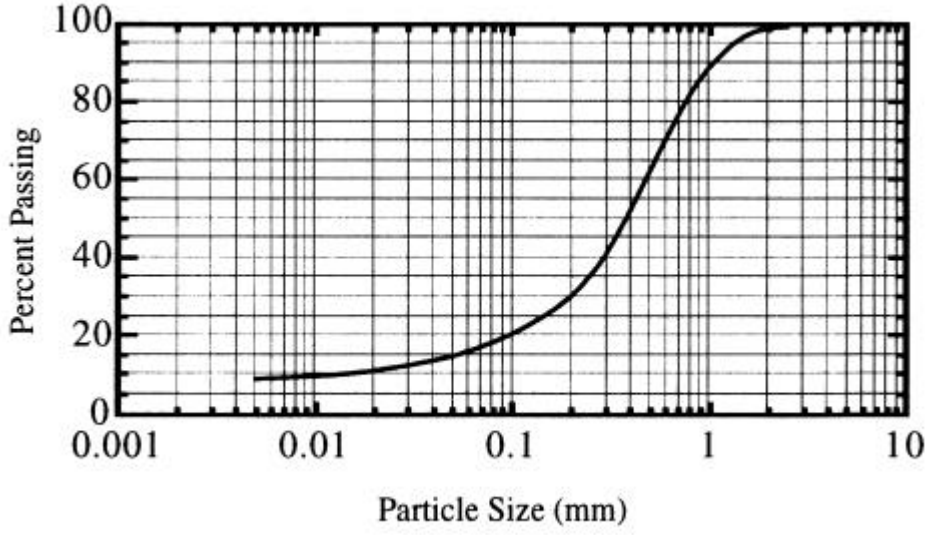

Figure 5.4 Grain size distribution of fill sand

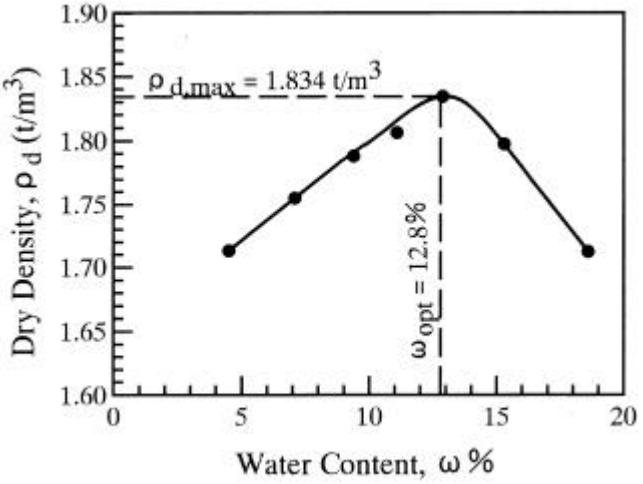

Figure 5.5 Optimum moisture content of the fill sand.

Reinforcing Material

Reinforcing material laid in all the reinforced soil models were 3mm diameter steel bars. These steel bars are considered inextensible compared to the strain developed in the soil mass (*see* Bathrust, 1987). Length of reinforcements for the first eight models (Types A~H) was equal to footing width, 500mm. The length of reinforcements is increased to 700 mm in the last two I and J models (i.e. 9th and 10th). This is to investigate effects of different reinforcement lengths on the behavior of the reinforced soils. Reinforcements were made rough by gluing sands on the surface (e.g. Fig.5.6).

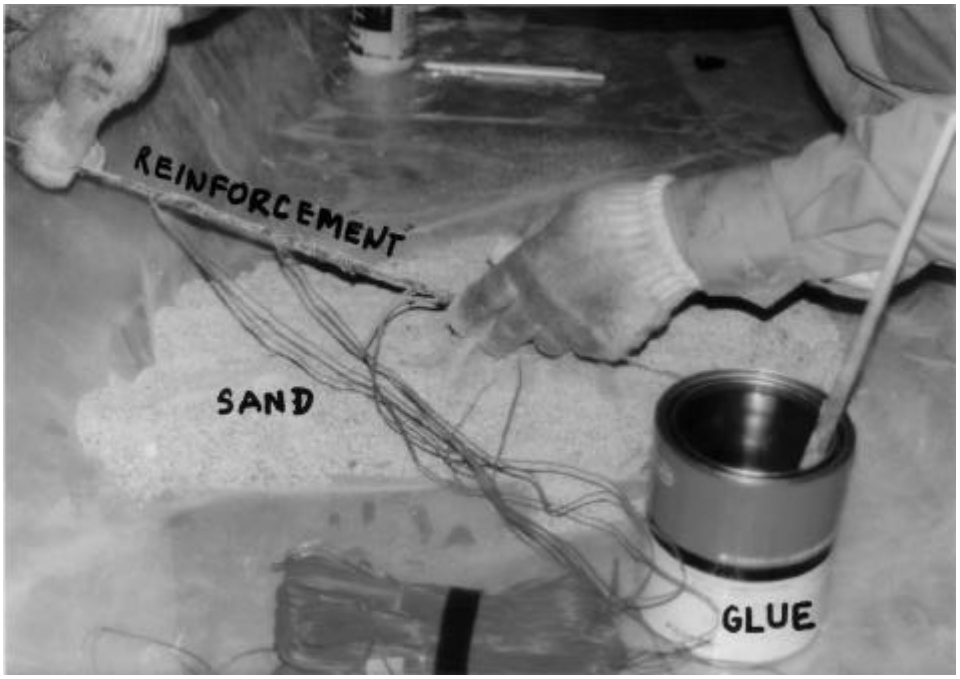

Figure 5.6 The surface of the reinforcing steel bars was made rough by gluing sands on the surface.

Facing Material

The facing panels were acrylic resin boards (Fig.5.7). Two types of facing thicknesses, thin and thick, are adopted. Thin type panels had thickness equal to 3mm while thick type panels were 5mm thick. Purpose of these facing types is to investigate effects of flexural rigidity in bending due to the earth pressure. In the present context of models and magnitude of the induced stresses (earth pressure), the latter type (5mm thick) is considered rigid to resist the lateral earth pressure developed during the loading. Figure 5.8 shows a typical configuration of facing panels for the mild slope models. Every reinforcing bar was rigidly bolted at the center of facing panels (Fig.5.7). The facing panels overlap each other in the lateral direction as shown in Fig.5.8, but just touch each other in the vertical direction.

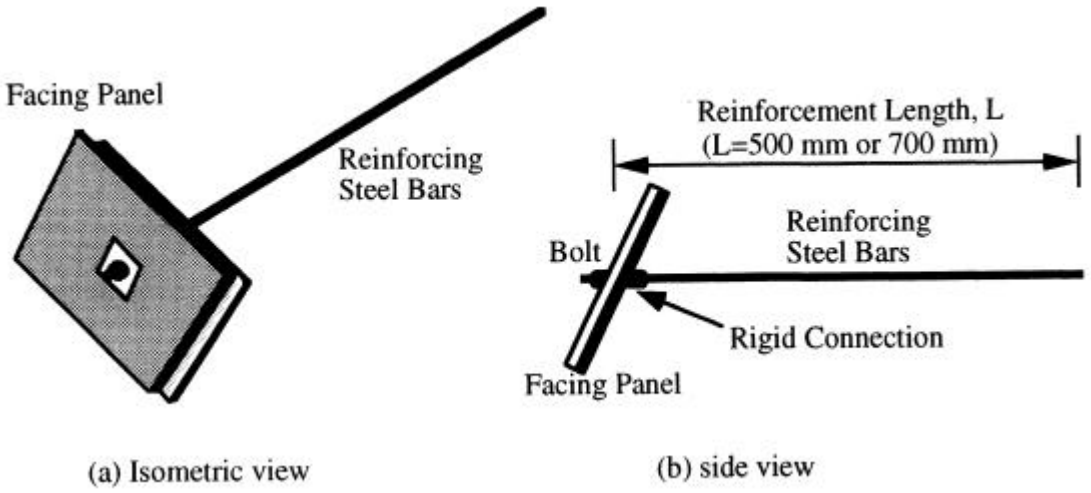

Figure 5.7 Facing panel and reinforcement connection.

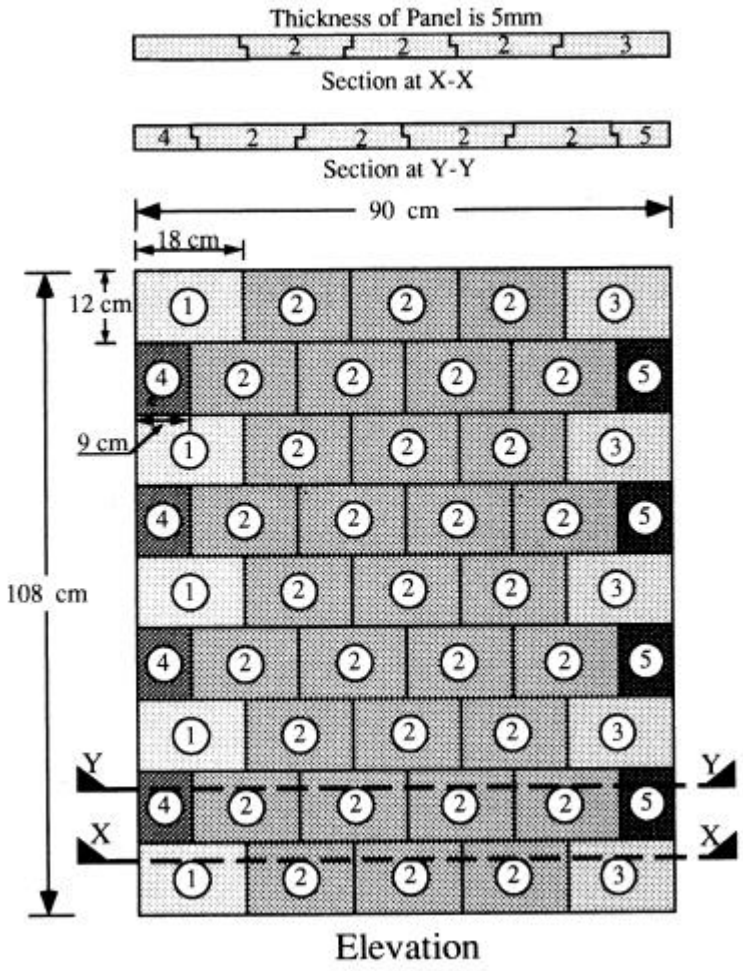

Figure 5.8 Details of a typical panel-facing configuration.

5.2.3 Construction of Model Slopes

Three series of model tests were constructed with two slope grading. The first series was on mild slope models with 1:0.5 (*vertical*: horizontal) slope gradient and the latter two series were on steep slope models with 1:0.2 gradient of slope face. Dimensions of various components of model set-up (test facility) have been already explained in the preceding sub-section. Similarly, details of a typical model slope and boundary conditions are also illustrated in Fig.5.9. As the total length and breadth of all the models were kept equal to 3,000mm and 900 mm, respectively. Position of the loading plate also remained same for all other model tests, thus the top-horizontal-platform was always 1,500 mm. Meanwhile, the 966 mm slope height in mild slope models (*see* Fig.5.9) was changed to 941 mm for the steep slope models.

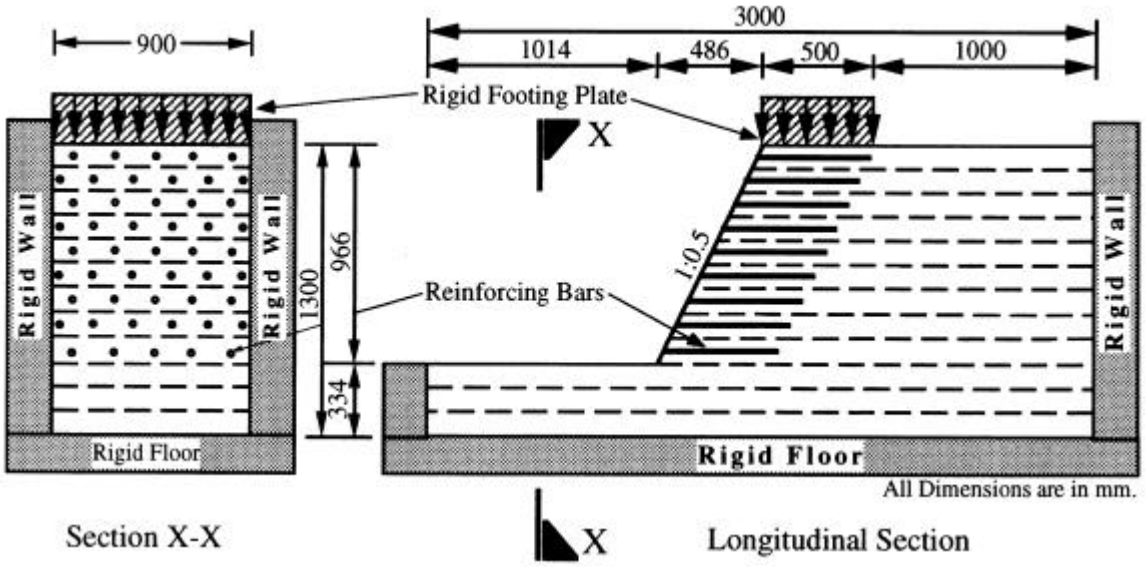

Figure 5.9 Typical model test configuration with reinforcement details.

The construction sequence adopted for all models was as follows: (1) First moisture content of the soil fill was determined (Fig.5.10a). Additional amount of water was added to the soil in order to maintain 10% water content in the soil fill (Fig.5.10a~b). The soil-water mix was homogenized on a large mixer (Fig.5.10c). Thus, weight of the soil and water content in the soil before and after mixing the additional water were properly monitored. (2) The homogenized moist soil was immediately moved to the set-up (Fig.5.10c) and spread. To achieve an uniform unit bulk weight throughout the model, filling and compaction of the soil were carried out in several stages (incremental lifts). The total soil weight required to each lift is calculated beforehand (e.g. Fig.5.11a). Thus, all models consist of three incremental lifts in the base part that extends from the front wall to the wall on the back. Likewise, the remaining height in the mild slope models consist of

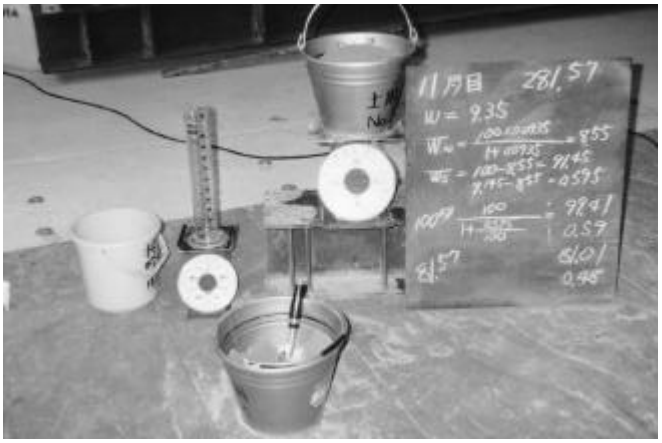

(b) 10% moisture content in the model was obtained by adding the net deficit water.

(a) Monitoring of the moisture content in the fill soil material

(c) Soil water mix was homogenized in a large mixture, subsequently transported to the model set-up for filling and compaction.

Figure 5.10 Quality control and monitoring of fill soil during the model preparation.

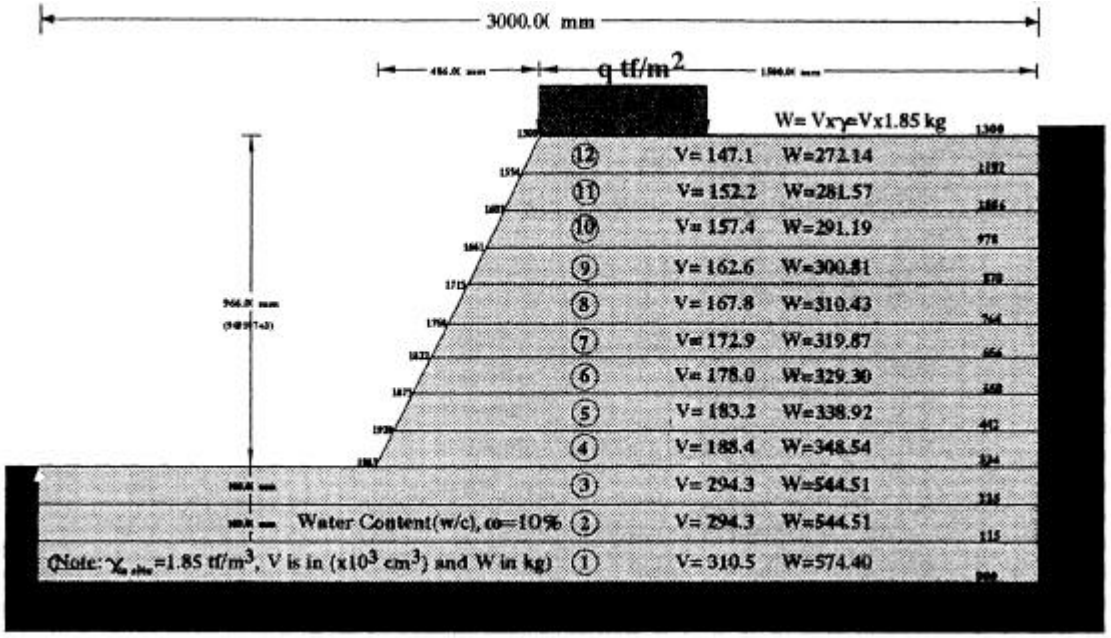

(a) Actual amount of soil required to every individual lift was exactly calculated

(b) Compaction of soil using hammer. (c) Verifying the in-situ density of soil mass

Figure 5.11 Filling and compaction of soil was carried out in several incremental lifts and density of compacted soil was fully monitored.

nine incremental lifts while only eight incremental lifts constitutes in the steep slopes. Each lift was compacted by a wooden tamper of 10 kgf weight until the lift thickness and an uniform unit bulk weight of 18.1 kN/m^3 (at water content, w_w=10%) was obtained (*see* Fig.5.11b). At the time of compaction, the face of the slope was rigidly supported by wedge shaped detachable EPS(expanded polystyrene) blocks (see Fig.5.12). These supports were released only after full height of the model is completed.

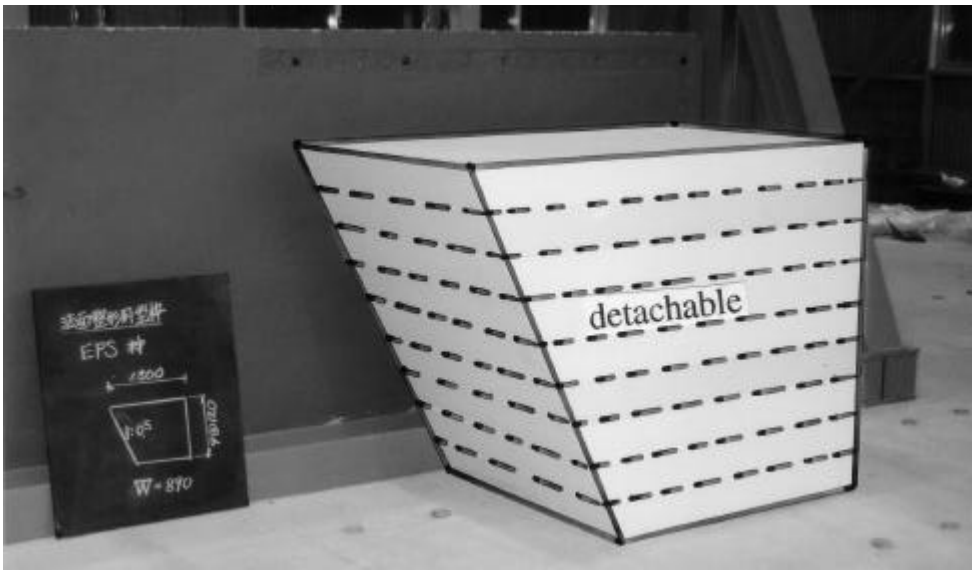

(a) A View of EPS blocks.

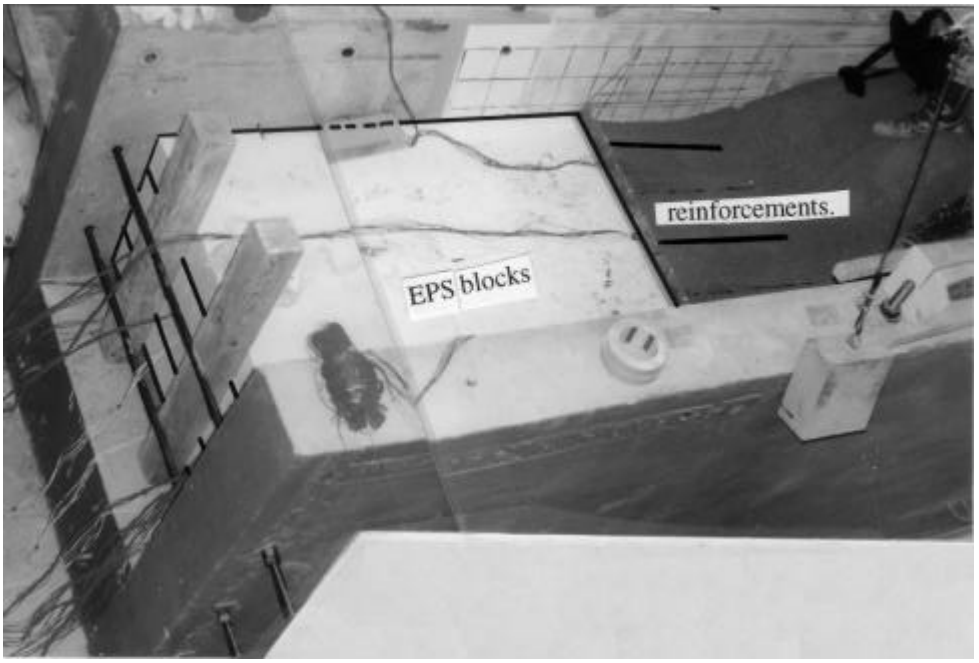

(b) EPS Blocks are fixed in position to support the slope face.

Figure 5.12 Temporary support system during construction phase consists of EPS Blocks.

5.2.4 Test Conditions

Table 5.2 presents the overall model test scheme. The reinforcements were 3mm diameter and 500mm long steel bars (last two models, i.e. 9th and 10th, have 700 mm bars) whose surface was coated by gluing the fill sand. Five and six reinforcements were alternately placed at every mid height of the lifts, (Fig.5.9). As mentioned before, the facing panels were acrylic resin boards of either thin type (thickness 3mm) or thick type (5mm thick). Latter type facing, i.e. 5mm thick, is considered rigid in resisting the bending moment developed due to lateral earth pressure. The connection between a panel and a reinforcing bar was rigid, thus angle at the bar-panel connection is assumed constant throughout loading.

Table 5.2 Model test scheme.

Model#	Face Slope	Reinforcements	Facing Panels	Bar Length
A	Mild Slope 1V:0.5H	Non-reinforced	No-facing	-
B		Reinforced		500 mm
C			5mm thick	
D			3mm thick	
E	Steep Slope 1V:0.2H	Non-reinforced	No-facing	-
F		Reinforced		500 mm
G			5mm thick	
H			3mm thick	
I			No-facing	700 mm
J			5mm thick	

Footing loads, vertical settlements of the loading plate, the axial strains along reinforcements and the horizontal movement of the facing panels or slope face were measured as explained before. A load cell installed at the center of the loading plate measured the load, and a loading pressure is an average of the load per unit area. Loading plate was assumed an equivalent rigid rough footing under plain-strain condition. Slip surface and the total deformation of the model slopes at failure were observed by removing a concrete sidewall after complete loading operation.

5.3 TEST RESULTS AND DISCUSSIONS

In this section, the behavior of individual model tests observed during loading, post-failure observations on the reinforced soils, the reinforcing bars and the facing materials are discussed. The main discussion will concentrate on the settlement of footing plate versus footing load relation; horizontal movement of the slope, development of cracks and slip surfaces, then finally the ultimate failure slip surface at the end of loading. Developments of the axial strains along the reinforcements at different loading levels are also discussed.

5.3.1 Observation of Model Tests

Failure surfaces observed by removing a concrete sidewall at the end of each test are presented in Figure 5.13. Salient features of each test observed from an initial loading to the ultimate failure are as follows:

Type A (*plain type*): As soon as the loading operation was commenced, some relatively dry sand started rolling down on the slope surface. The gradual increase in the footing load resulted tilting of the footing plate towards the slope face. Subsequently, a horizontal crack on an upper part of the slope face was observed. As soon as the footing load approached the upper limit, another big crack appeared on the lower part of the slope surface. Ultimately, the soil mass within the slip zone continued flowing, thus failure occurred. Figure 5.13(a) shows that the failure surface is shallow and is confined near the slope face covering almost full height of the slope.

Type B (*reinforced without facing*): When the load reached 170kPa, a horizontal crack appeared on the second layer (from top) and subsequently another crack also appeared around the middle of the slope height. At this moment, the loading plate tilted like in the case of Type A. A narrow strip of soil mass around the second layer collapsed at a footing load of 270kPa. A new horizontal crack appeared on the toe of the slope at 290 kPa loading level. Figure 5.13(b) shows that there are three major slip surfaces; and many local failure surfaces are confined within the most outward failure zone. During first half of the loading, only the shallow failure zone seemed to exist, which was similar to Type A. Development of several such shallow slips didn't cause an ultimate failure of the slope, it is because of the reinforcing effect on the soil mass. The final failure was due to the deep failure initiated from the inner end of the footing.

Type C (*reinforcement with thick facing*): The facing panels discussed in earlier sub-sections are installed as facing on the slope. Panels were rigidly attached to the reinforcements. The facing is considered strong enough to resist the earth pressure developed due to the loading. The thick panel facing, therefore, is considered very rigid in resisting the bending moment due to the earth pressure. Consequently, nothing outside the facing could be noticed through out the loading period. The local slip surfaces .

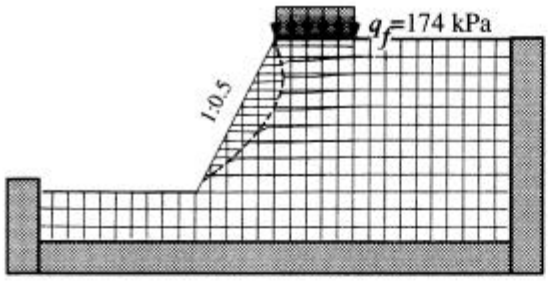

(a) **Type A:** *Unreinforced plain slope*

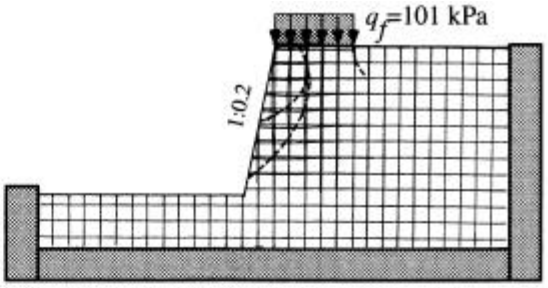

(a) **Type E:** *Unreinforced plain slope*

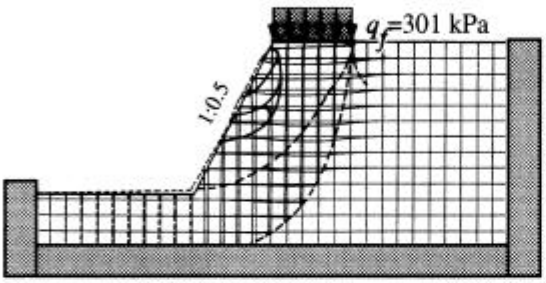

(b) **Type B:** *Reinforced soil without Facing*

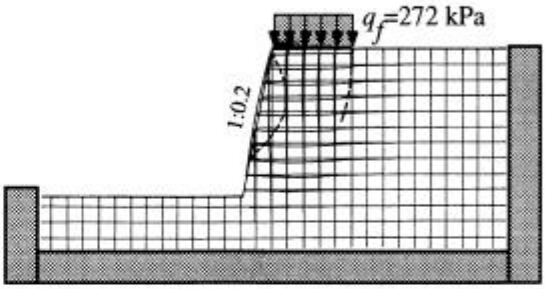

(b) **Type F:** *Reinforced soil without Facing*

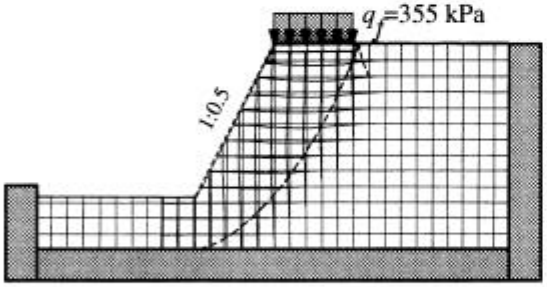

(c) **Type C:** *Reinforced soil with 5mm thicl Facing*

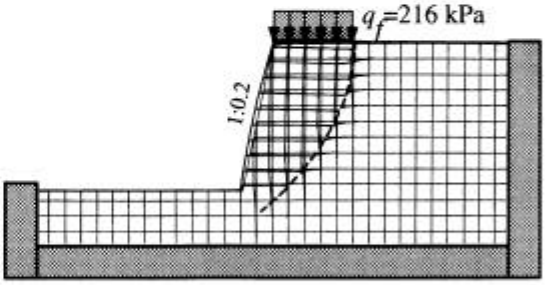

(c) **Type G**: *Reinforced soil with 5mm thick Facing*

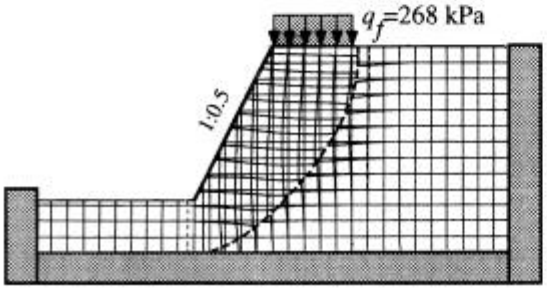

(d) **Type D:** *Reinforced Soil with Thin Type (3mm) Facing*

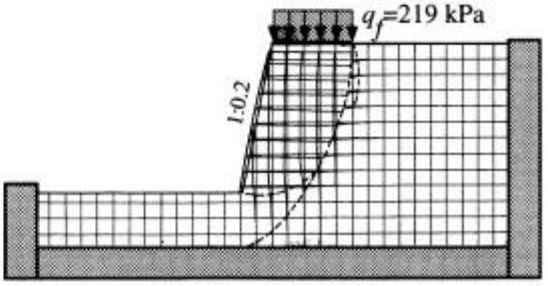

(d) **Type H**: *Reinforced Soil with Thin Type (3mm) Facing*

Figure 5.13 Failure surfaces and velocities observed at the end of each test (*mild slope models*)

Figure 5.14 Failure surfaces and velocities observed at the end of each test (*steep slope models*).

close to the facing observed in Type B model were not experienced in this model (Type C). The ultimate failure surface (Figure 5.13c) is passing through inner ends of all the reinforcing bars, such that the slip surface behind the reinforced zone is almost parallel to the slope face. Such failure mode may be classified as a block failure.

Type D (*reinforcement with thin type facing*): This model is almost same as in the previous model, Type C. The difference lies in only the thickness of the facing panels. The facing panels in this model are 2mm thinner than the panels in the previous model, Type C. Objective of these models with different panel thickness is obviously for comparative studies on the response of the reinforced soils due to varying flexural rigidities of facing panels. In this model (as in Type C) also there was hardly any noticeable change on the slope facing. Figure 5.13(d) confirms non-existence of any local slip surface (or cracks) around the facing, unlike several local slip surfaces observed close to the facing in Type B model. The ultimate failure surface behind the reinforced zone is nearly parallel to the slope face. Such failure mode may also be classified as a block failure.

Figure 5.14 shows the failure slip surfaces observed at the end of loading of the models having steep slope. The tendency of each test, i.e. plain slope (Type E), reinforcement without facing (Type F) and reinforcement with facing (Types G and H), is almost similar to the respective mild slope models. In the case of Type E (Fig. 5.14), the shallow failure occurred in the lower face of the slope is so big that the loading procedure could not continue at the early stage of loading. Figure 5.14(b) shows that the failure surface initiated from the inner end of footing does not pass through the bottom or below the slope. Fig. 5.14(c) shows that Type G exhibits block type failure as similar as Type C. Similarly, Type H is similar to Type D failure modes.

Type I (*reinforced without facing***)**: In this model, soil is reinforced with 700 mm long reinforcements; 200 mm longer than the width of loading plate. Other details remained same as in the sixth model test (Type F). As the slope didn't have any special facing materials, some fine cracks were seen some time after the loading operation was commenced. Once the footing load reached to 150 kPa, a relatively big first horizontal crack appeared on the slope face located around the 4th layer (from top). The soil started rolling down in small patches. Likewise, another horizontal crack appeared around the middle of the slope height as early as the footing load reached to 228 kPa. At this moment, the loading plate tilted towards the slope face, like in Type F (or Type B). The loading plate and the soil within the failure zone, subsequently, started flowing with decreasing load cell pressure. The slope ultimately failed when the footing load reached 261kPa. Displacement field and the failure surfaces observed by removing a concrete side wall, as shown in Fig.5.15a, reveals that distinct failure surfaces exist only close to the slope face (unlike Type B). The ultimate failure in Type B model was probably due to propagation of the ultimate failure surface, initiated at the inner end of the footing. In Type I model, such failure surface even if initiated at inner end of the footing, was restrained by the long reinforcements

against further propagation. Besides, the second slip (i.e., close to face) ultimately resulted excessive settlement of the footing and consequent reduction of the footing load was considered the ultimate failure state of the model.

Type J (*reinforcement with facing*): In this model, the rigid type, i.e. 5mm thick, facing panel were rigidly connected with 700 mm steel bars. Other details remained same as in model Type G. At the low footing load, nothing could be noticed outside the slope facing. As the footing load was gradually increasing, some time the sound of the facing panel cracking could be heard. The high earth pressure and the high axial force in the reinforcements resulted stress concentration at the bar-panel connection and high bending moment on the panel board, which resulted crushing of some panels with violent sound. Before reaching the ultimate failure state many panels burst out, however, no distinct slips/cracks were observed on the slope face. Figure 5.15(b) confirms that there was no local failure near the facing as well, which is quite different compared to the Types C or G tests. Swelling of a patch close to toe, as seen in Fig. 5.15(b), is due to the breaking of the facing panels close to the toe.

Based on these observations of the failure surfaces, it is clear that the reinforcement bar is effective by preventing the ultimate collapse due to local failure occurred close to the surface. Such local failures are avoided when these reinforcing bars are connected with the rigid panel facing. Rigid panel facings attached with the long reinforcements are much more effective in strengthening the soil mass.

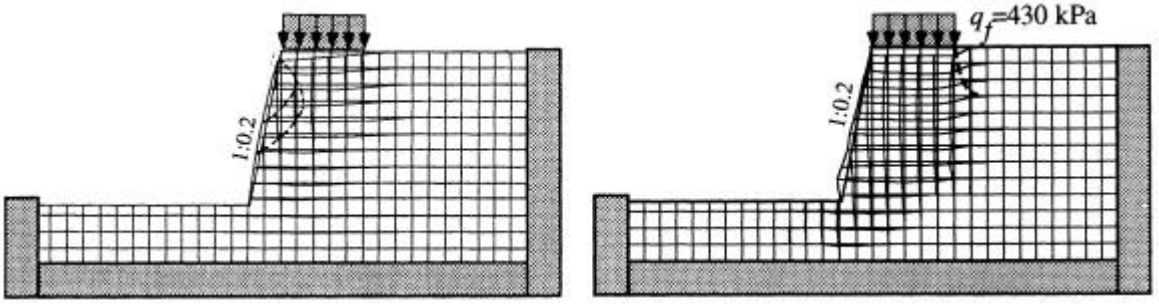

Type-I (*Reinforced without Facing*) **Type-J** (*Reinforced with 5mm thick Panel Facing*)

Figure 5.15 Failure surfaces and velocities observed at the end of the steep slope models (*700 mm long reinforcement cases*).

5.3.2 Failure Load and Vertical Displacement

Figure 5.16 shows the footing load versus the footing settlement relationships recorded during the loading tests on the mild slope models and Figs. 5.17 & 5.18 are the footing load-settlement relationships for the steep slope models with 500 mm and 700mm long reinforcing steel bars, respectively. In the case of the mild slope models (Fig. 5.16) the effect of the reinforcement and the panel facing can be observed from the start of loading to the failure stage. The first tangent line is steeper with increasing order for Types A, B, D and C. The steepest tangent is in the reinforced soil model with thick panel facing. The reinforcement and the panel facing exhibits significant effect in restraining the displacements. Failure loads corresponding to the models of Types B, C and D are very high compared with the Type A, which reveal that the reinforcement and the panel facing are effective on the stability of slopes. Furthermore, Types B and C (or D) show that there is considerable footing settlement before reaching the ultimate failure state.

Nature of the first tangent line in steep models (Fig. 5.17) is similar to the mild slope models explained in the previous paragraph. Models with facing (Types G & H) have higher footing load for the given footing settlements, but the ultimate failure load in Type G (also Type H) model could not reach the failure load in the reinforced soil without facing (Type F) case. Type F (as in Type B) exhibits considerable footing settlement before reaching the ultimate failure state. Overall, the reinforcements whether connected with facing or not, are very effective on improving the stability of slopes.

The vertical settlement versus the footing load relationships for the steep slope models reinforced with long reinforcements (700 mm long) is presented in Fig. 5.18. The slope of the first tangent line is very similar to the slope in Type F model. Type I (like in Type B) exhibits considerable footing settlement before reaching the ultimate failure state. The nature of the first tangent lines is similar to the first tangent lines in preceding models (i.e. steep slope models with 500mm long bars). The model reinforced with long reinforcements connected to the rigid panel facing (Type J) shows the steepest first tangent line to the load-settlement curve, likewise it has significantly high failure load compared to all other models (A~I). Thus, the long reinforcements when connected to the rigid facing are very much effective on improving the slope stability.

5.3.3 Axial Strains and Lateral Displacement

Figures 5.19, 5.20 and 5.21 show the lateral displacements of slope surface and the axial strains in the reinforcing bars recorded during loading. At the same loading level, the reinforcement and the facing panel are considerably effective not only in controlling the vertical settlement but also in reducing the lateral displacement. The effect is much higher, especially, in the reinforcements connected to the facing. A significant outward movement

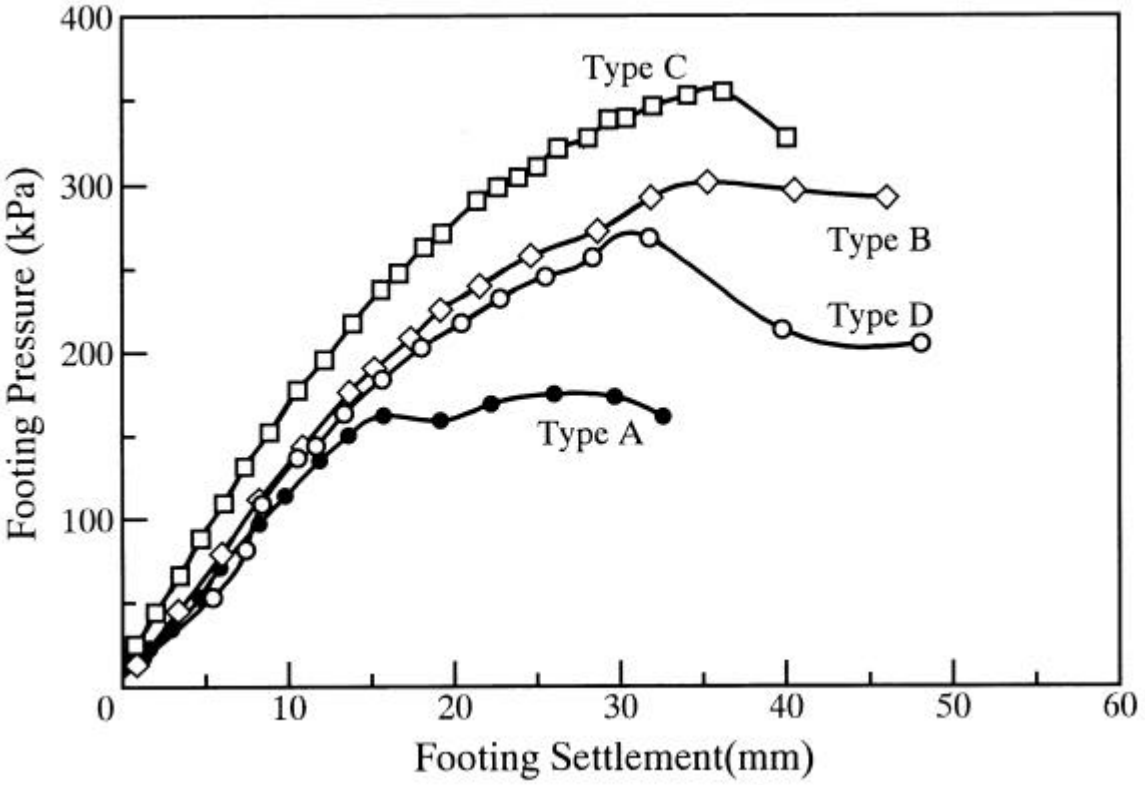

Figure 5.16 Footing settlement versus footing pressure relations for the mild slope (1V:0.5H) models.

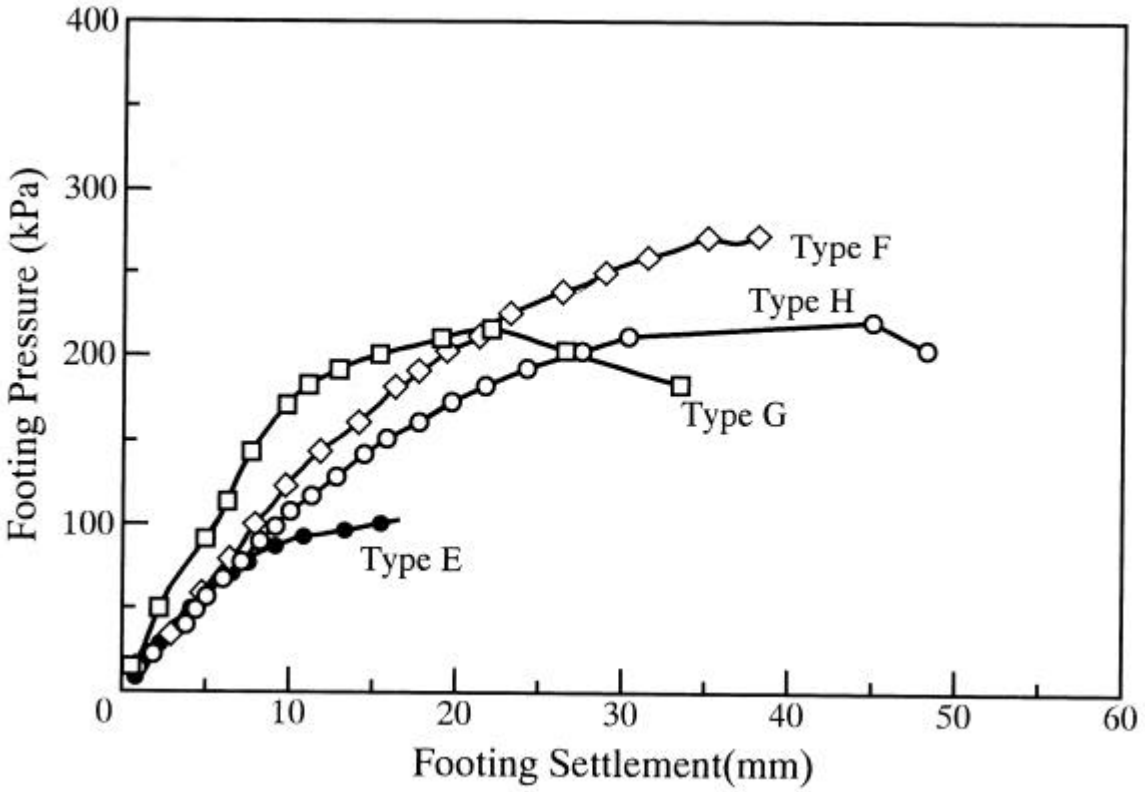

Figure 5.17 Footing settlement versus footing pressure relations for the steep slope (1V:0.2H) models.

at the middle of the slope height due to the local failure could be observed in reinforced slopes without facing; i.e. Types B, F and I; while a progressive rotation pushed out from the footing to the slope toe is significant in the panel faced models, i.e. Types C, D, G, H and J.

The axial strains in the case of Types C, D, G, H and J are large compared to the axial strains in the case of Types B and E. Furthermore significant axial strains developed at the face side of the reinforcing bars in the former types can be clearly observed. In all the cases, a peak in the axial strain distribution curve can be seen moving towards inner direction as the reinforcement position moves lower and lower. Sometimes, the axial strain distribution curve showed twin peaks, especially, for the reinforcements positioned at lower elevations (close to toe).

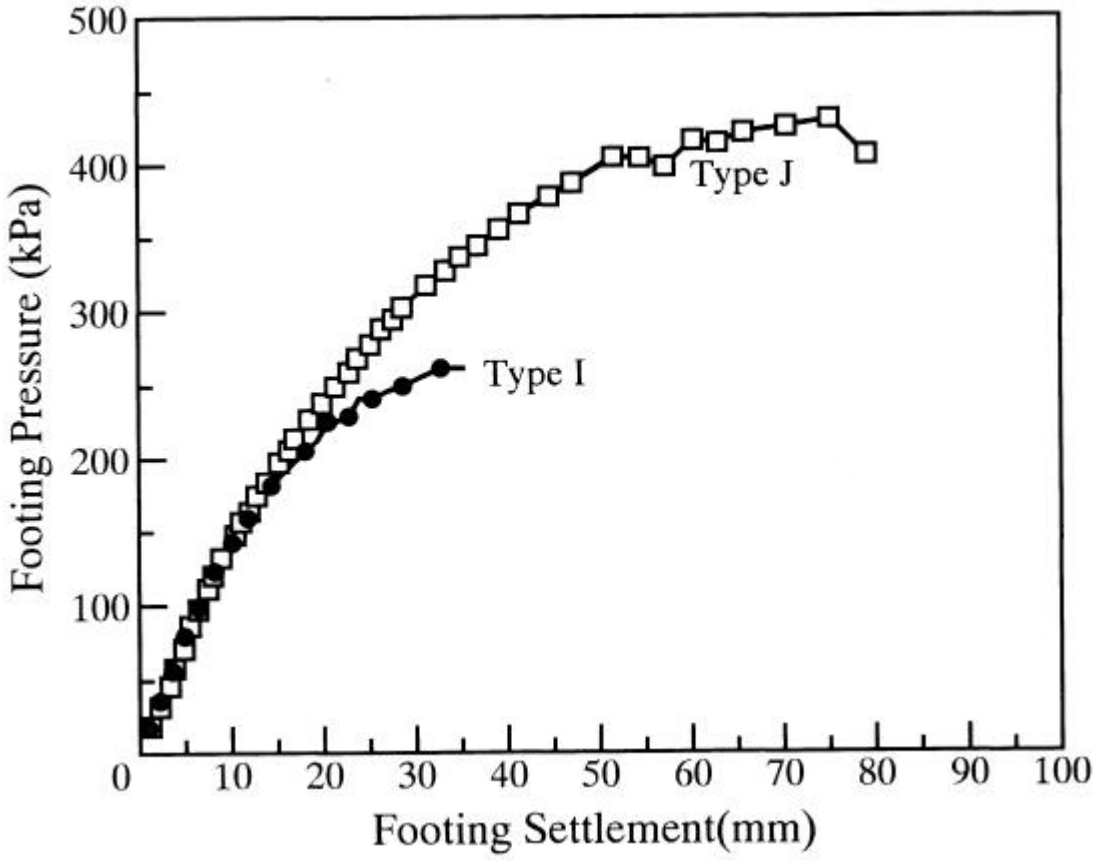

Figure 5.18 Footing settlement versus footing pressure relations for the steep slope (1V:0.2H) models with 700 mm long reinforcements.

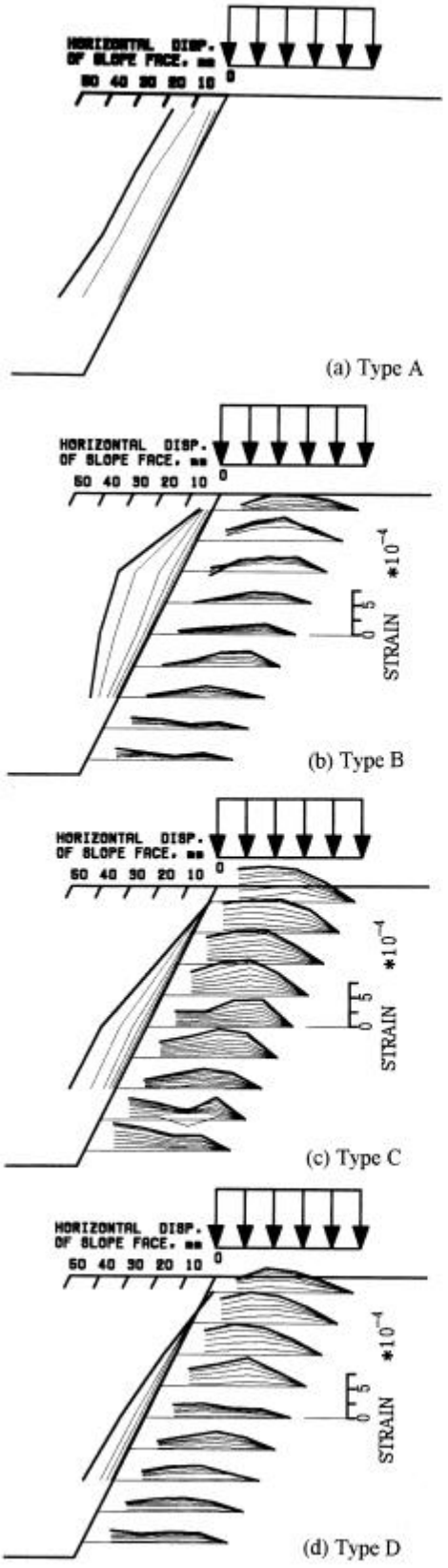

Figure 5.19 Observed axial strain distributions (*mild slope models*).

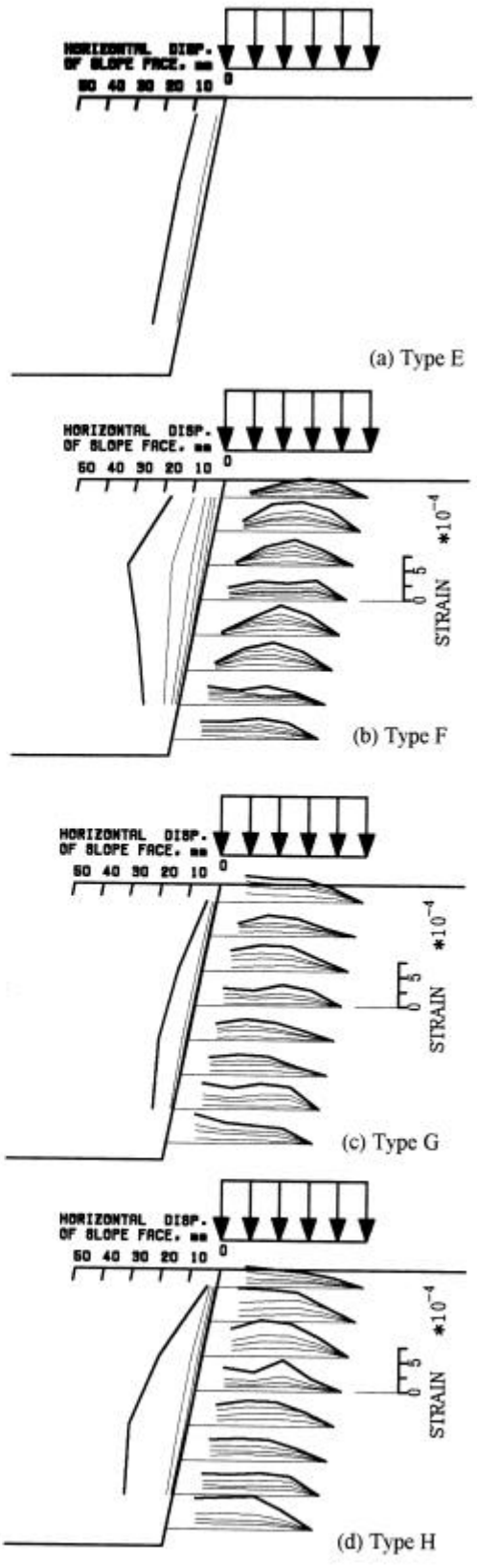

Figure 5.20 Observed axial strain distributions (*steep slope models*).

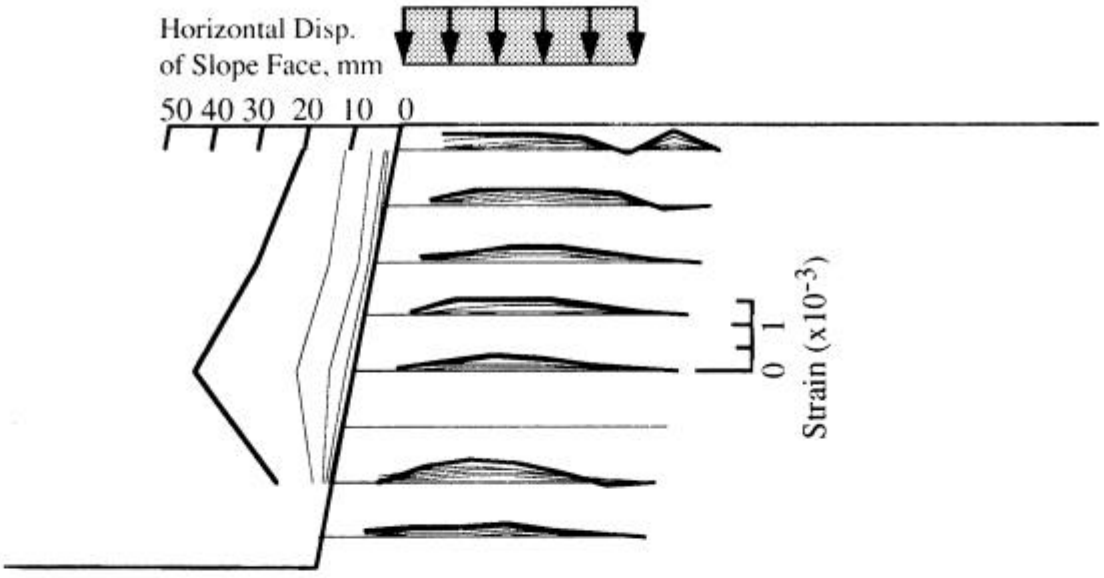

(a) Model Type I

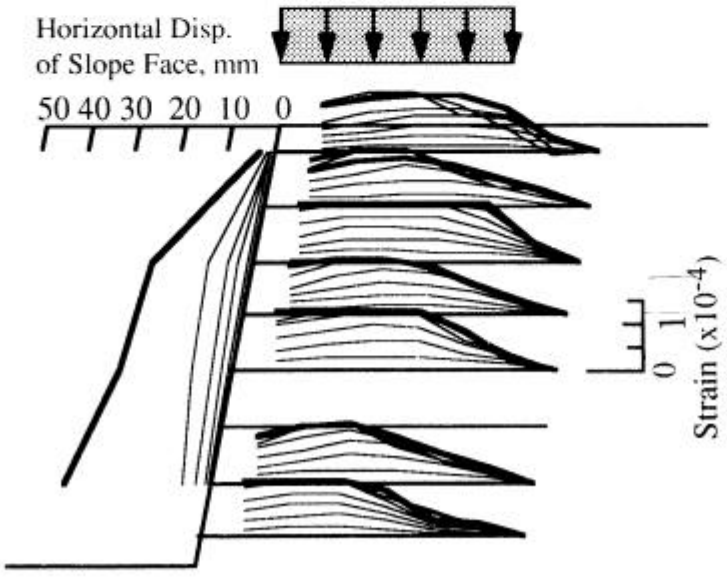

(b) Model Type J

Figure 5.21 Observed axial strain distributions along reinforcing bars in the steep slope models with 700 mm long reinforcing bars.

5.4 NUMERICAL SIMULATION OF MODEL TEST RESULTS

5.4.1 Outline of Numerical Simulations

The numerical simulation work is performed using the linear elastic finite element method (LEFEM) and the rigid plastic finite element method (RPFEM). In both the cases, constraint conditions on the displacements and the velocity fields are introduced, respectively as mentioned in the earlier chapter (Chap. III). In this research, the LEFEM is used to investigate the first tangent line on the vertical settlement versus the footing load relationship, while the RPFEM is employed to compute the ultimate failure footing load. Finite element arrays used in these analyses are shown in Fig. 5.22. A rigid rough loading condition is assumed, which restrains the displacement or velocity under the footing to move only in vertical direction. Another assumption being made here is regarding the friction between floor and soil mass. Firstly, in the mild slope cases the friction on the floor appeared considerably high which prompted the floor nodes be considered as restrained nodes. However in the later models, especially, the steep models (E~J), such assumption of frictional boundary exhibited conservative tendency of results. Therefore, roller (sliding) type boundary conditions were assumed concerning the floor nodes in all the steep slope models.

Numerical methods (LEFEM and RPFEM) are employed to simulate the reinforced soil model test results presented in the previous sections. The linear constrained conditions newly introduced in this study have also been incorporated into these numerical methods to model the effect of the reinforcements and facing on soil mass. Effect of a reinforcement is modeled by imposing the first constrained condition of "*no-length change*" on the distances between successive soil nodes along the reinforcement (thick lines in Fig. 5.22). Likewise, the effect of facing panel is modeled by imposing an additional linear constrained condition of the "no-bending" condition (corollary: "*no-angle change*") on the angle formed by the three successive soil nodes along the facing panel; in addition to the former "*no-length change*" condition. The latter constrained condition, "*no-bending*", is employed only to incorporate the effect of a rigid facing material, i.e. Types C and G.

Soil properties required in the LEFEM as well as the RPFEM are obtained by back analysis of the first model test (i.e. Type A) on unreinforced plain slope. These material parameters are presented in Table 5.3. Regarding LEFEM, assumption of Poisson's ratio equal to 0.3 resulted good matching of the Young's modulus with the first tangent line in the Type A model test. Likewise regarding RPFEM, assumption of the frictional angle equal to 25^{o} and cohesion (given in the table) resulted good matching of the computed failure load with the failure load observed at the end of the model test (i.e. Type A). Soil properties obtained through back analysis of the first model test (Type A) are used in the numerical investigations of all the remaining model tests selected for the numerical simulations (Types A, B and C among the mild slope models and

Types E, F and G models among the steep models). Details of the models selected for the numerical simulations employing the proposed numerical method are summarized in Table 5.4.

Table 5.3 Material parameters obtained by performing back analysis.

Linear Elastic Analysis
$\nu = 0.3$
E= 7000 kPa
Rigid Plastic Analysis
$\phi = 25^{o}$
c = 20 kPa

Table 5.4 Model Tests selected for Numerical Simulations

Model#	Face Slope	Reinforcements	Facing Panels	Bar Length.
A	Mild	Unreinforced	no-facing	-
B	Slope	Reinforced		500 mm
C	1V:0.5H		5mm thick	
E	Steep	Unreinforced	no-facing	-
F	Slope	Reinforced		
G	1V:0.2H		5mm thick	500 mm

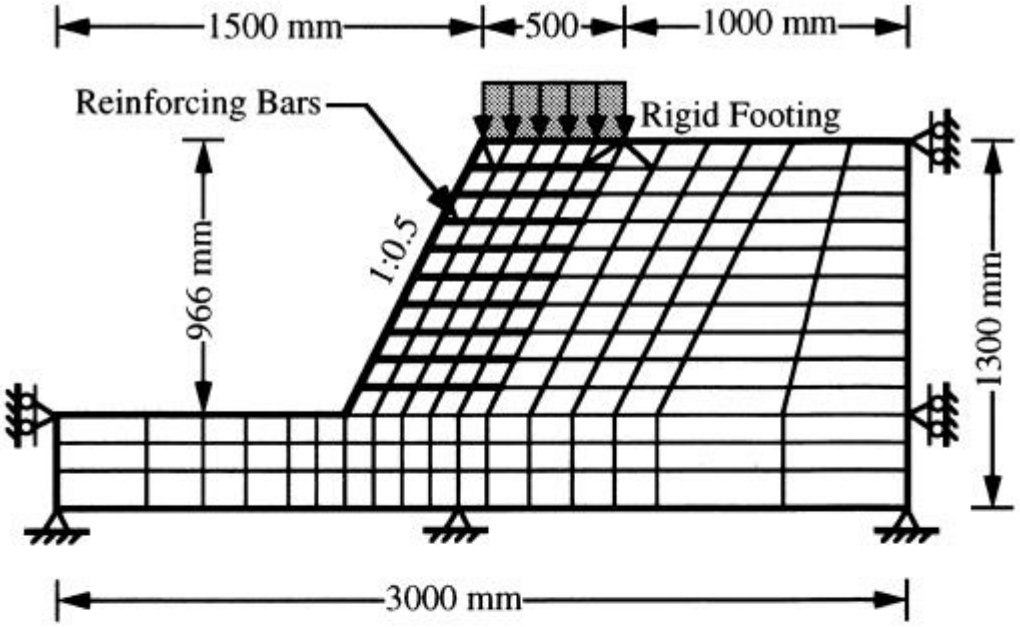

(a) Mild Slope

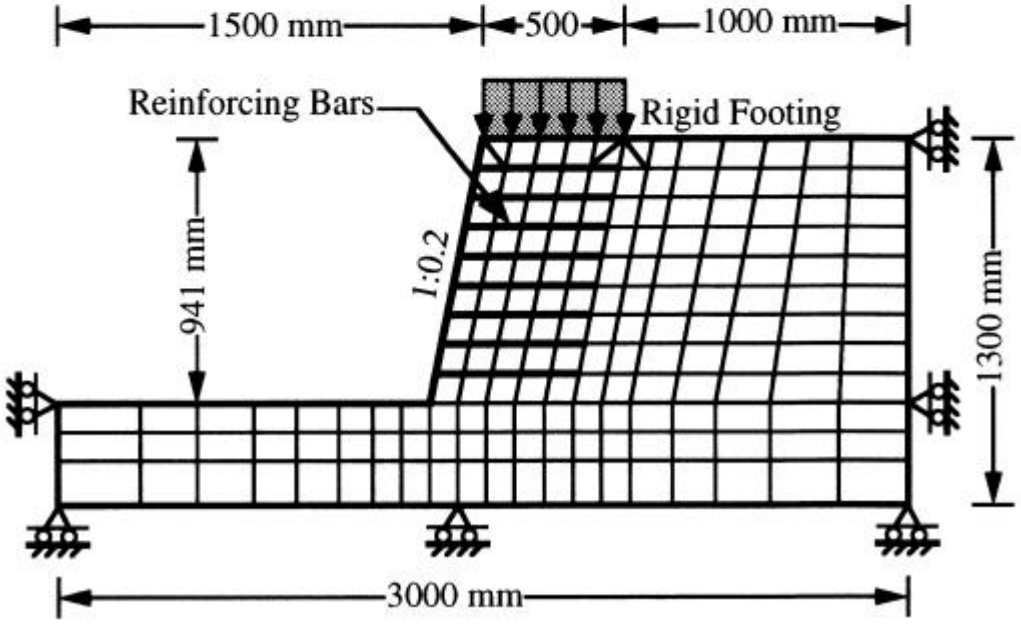

(b) Steep Slope

Figure 5.22 Finite element discretization for the numerical simulation of the model test results.

5.4.2 Results and Discussions

Load-Settlement Relation:

At the outset, the vertical displacement versus the footing stress relations for the mild slope calculated through the proposed numerical method is discussed. The simulated first tangent lines and failure loads are compared with the corresponding model test results in Fig. 5.23. This figure also shows that the effects of both the reinforcement and the facing panel can be approximately modeled without changing the soil parameter but by incorporating the proposed constraint conditions of no-length change as well as no-bending into these finite element methods. Likewise, the results corresponding to all the steep slope models (Types E~G) presented in Fig. 5.24, clearly demonstrate that the effect of restraining soil deformations (i.e. the first tangent line) could be nicely simulated with the same soil parameters used in the mild slope models. Moreover, the effect of reinforcement alone on stability of the Type F model (i.e. reinforced slope without facing) could be simulated very well. Since the failure load recorded in Type G model test (reinforced soil with rigid facing) was significantly lower than the failure load for Type F model (without facing), such a result cannot be explained/simulated through the proposed numerical method (**RPFEM**) where the plastic energy to be minimized is influenced by the additional constraint conditions imposed on panel facing, i.e., "*no length change*" plus "*no bending*" conditions.

Displacement and Velocity Fields

Figures 5.25 and 5.26 illustrate the computed displacement fields for the mild and the steep slope models respectively. As mentioned earlier, these computations are based on the LEFEM. In these figures, the displacement vectors are significantly enlarged for clarity. The computed displacement fields for the Types A and B may not be clearly distinguished, but, the difference between the displacement fields for Types B and C is comparatively clear. The constraint conditions imposed on the facing panel forced the nodal displacements along the attached reinforcement to follow the facing panel displacements. Therefore, the displacement vectors within the reinforced region are aligned parallel to the corresponding facing displacements (Figs. 5.25~5.26). This might be the reason why the failure slip surfaces observed in Types C and G models were narrow compared to the failure surfaces in Types B and F, respectively (ref. Figs. 5.13 and 5.14). Such a behavior could not be explained through the RPFEM because it always considers the soil mass as incompressible at the limit state. Figures 5.27 & 5.28 shows the velocity fields obtained based on RPFEM corresponding to mild slope and steep slope models, respectively.

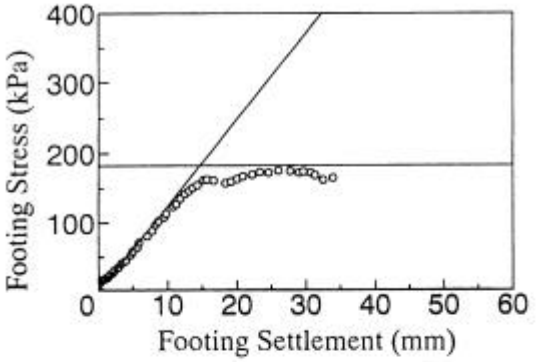

(a) Unreinforced Model, **Type A**

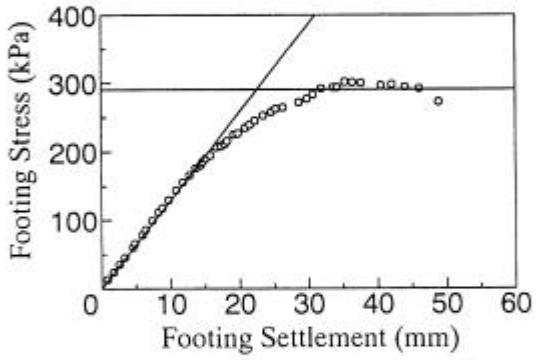

(b) Reinforced Model, **Type B**

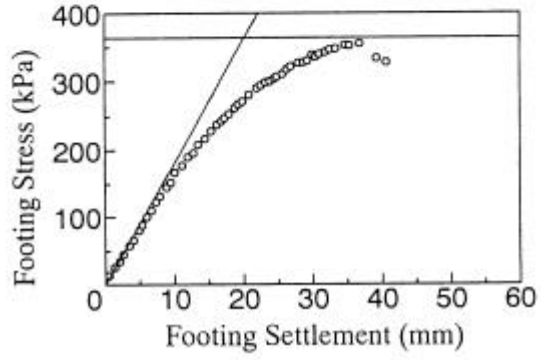

(c)**Type C:** (Panel Facing,5mm thick)

Figure 5.23 Computed and observed footing pressure-settlement relations (*Mild slope models*)

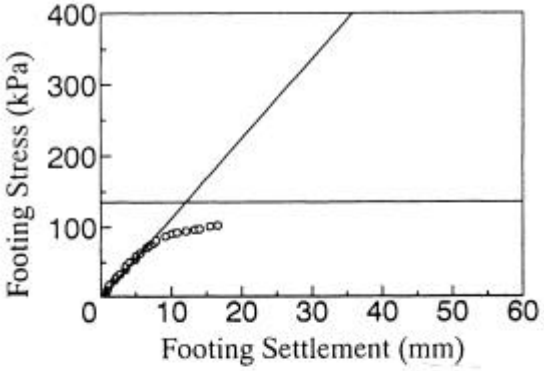

(a) Unreinforced Model, **Type E**

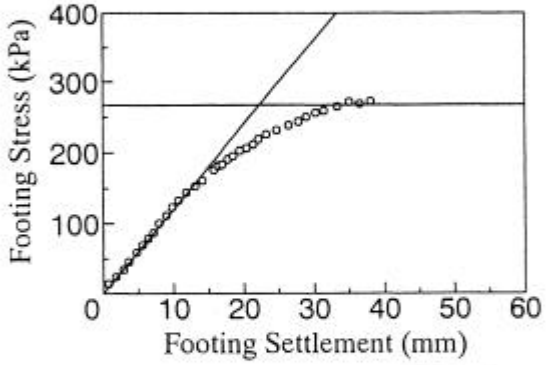

(b) Reinforced Model, **Type F**

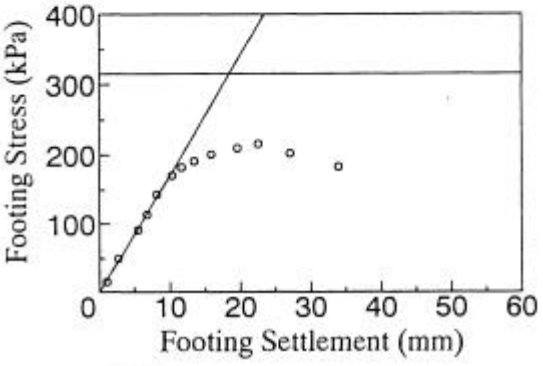

(c) **Type G**:(Panel Facing,5mm thick)

Figure 5.24 Computed and observed pressure-settlement relations (*Steep slope models*)

Figure 5.25(a) and 5.26(a) illustrate that the failure mode of the unreinforced model slopes can be well simulated. The plastic region in reinforced soils (Types B and F) extends toward the toe of the slope (e.g. Figs. 5.27b and 5.28b), similar to the observed failure surfaces. Besides, the constraint conditions imposed on the slope facing forced the plastic region in the soil mass to extend beyond the toe, e.g. Figs. 5.27 & 5.28.

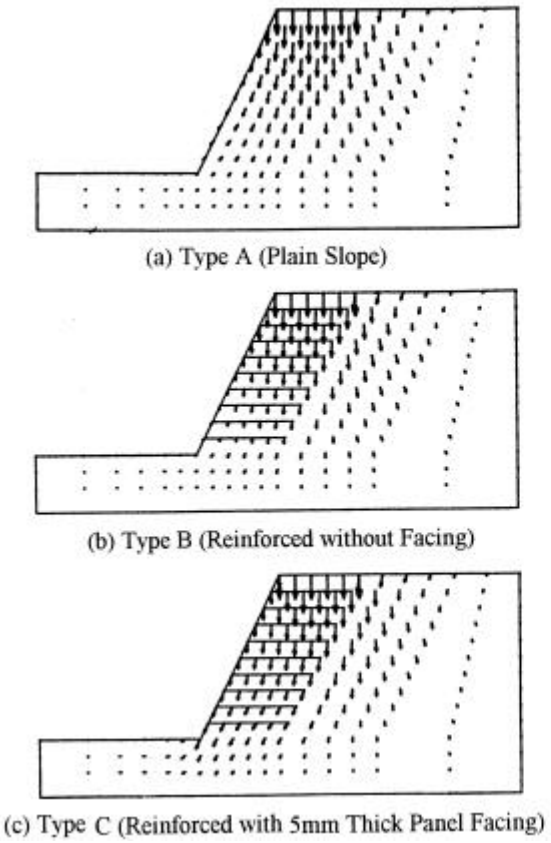

Figure 5.25 Computed displacement field using LEFEM (*Mild slope models*)

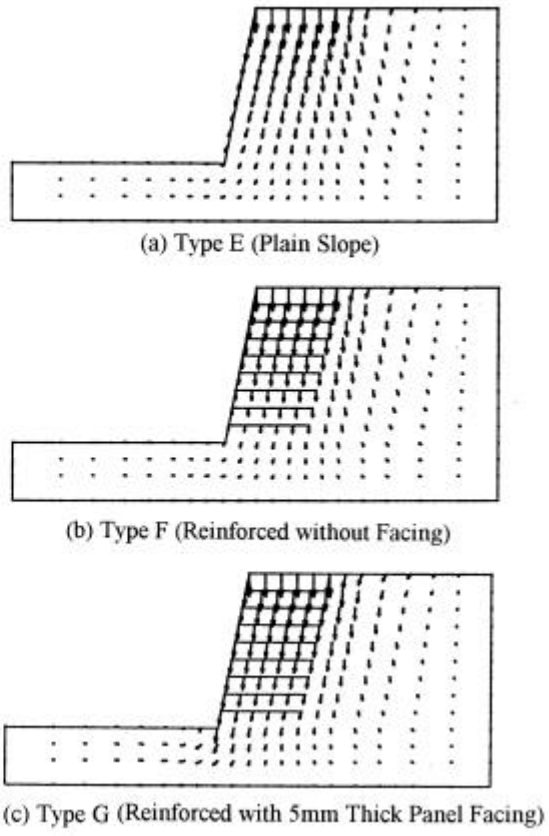

Figure 5.26 Computed displacement field using LEFEM (*Steep slope models*)

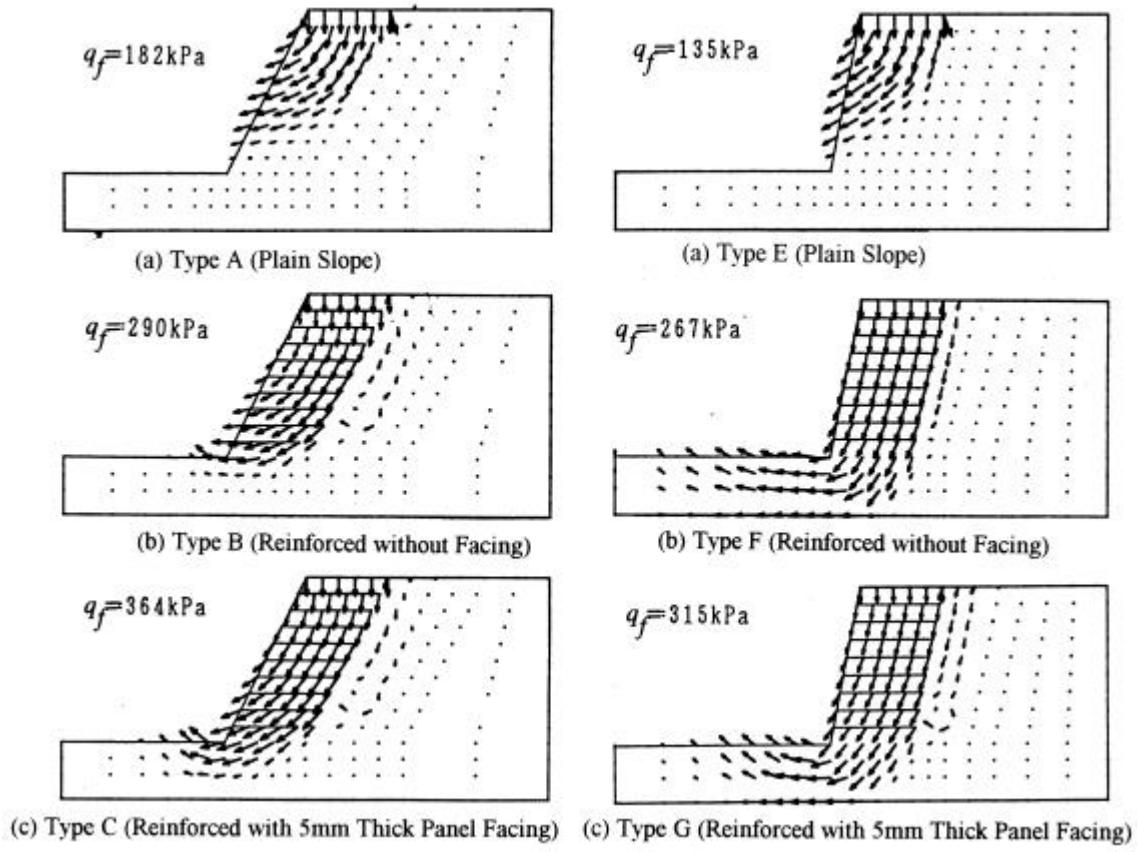

Figure 5.27 Computed velocity field using RPFEM (*Mild slope models*)

Figure 5.28 Computed velocity field using RPFEM (*Steep slope models*)

Mean Stress Distribution

Figures 5.29 & 5.30 shows the computed mean stress distributions at the limit state based on RPFEM. Reinforced soils (Types B and F) exhibit relatively high stress concentration towards the face side of reinforcements. This tendency is more clear in Type C model where the high stress concentration is appeared just behind the panel facing as illustrated in Figs. 5.29~30. In the plain slope models, a relatively high stress concentration is observed around inner edge of the footing. However, the high stress concentration in the reinforced soil mass was moved towards outer edge of the footing. This could be the reason for tilting of the footing plate in the unreinforced model tests (ref. Fig. 5.13a and 5.14a).

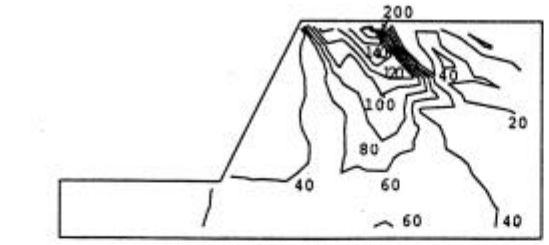

(a) Type A (Plain Slope)

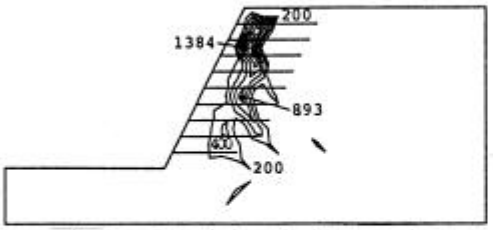

(b) Type B (Reinforced without Facing)

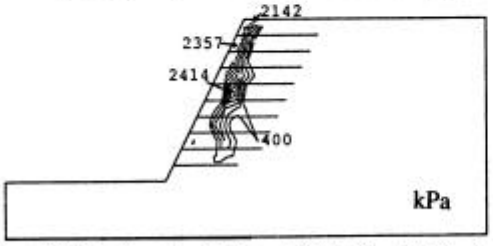

(c) Type C (Reinforced with 5mm Thick Panel Facing)

Figure 5.29 Computed mean confining stress contours (*mild slope models*).

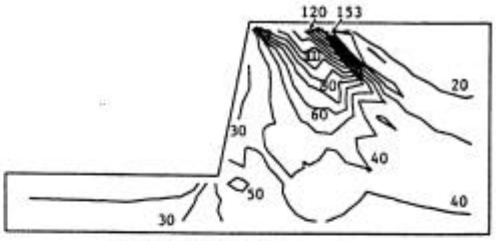

(a) Type E (Plain Slope)

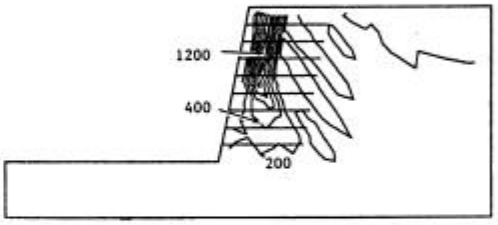

(b) Type F (Reinforced without Facing)

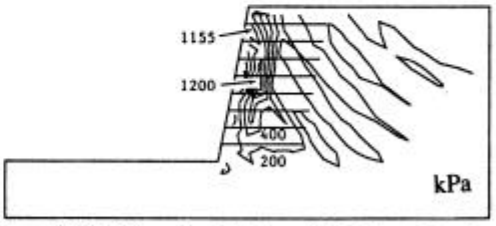

(c) Type G (Reinforced with 5mm Thick Panel Facing)

Figure 5.30 Computed mean confining stress contours (*steep slope models*).

Axial Force Distributions

The computed tensile force distributions at failure based on RPFEM and the axial strain distributions recorded in the model tests are shown in Figs. 5.31 and 5.32 for the reinforced mild slope and the steep slope models, respectively. It should be noted that the axial force is calculated per unit width. Though the calculated distributions are quite approximate because of the coarse finite element array, the axial strain distribution pattern along the reinforcement recorded in the model tests could be well explained by the computed tensile force distribution (e.g. a position of peak, shifting of peak positions away from slope face in lower positioned bar, appearance of twin peaks in the lower positioned bars, etc.)

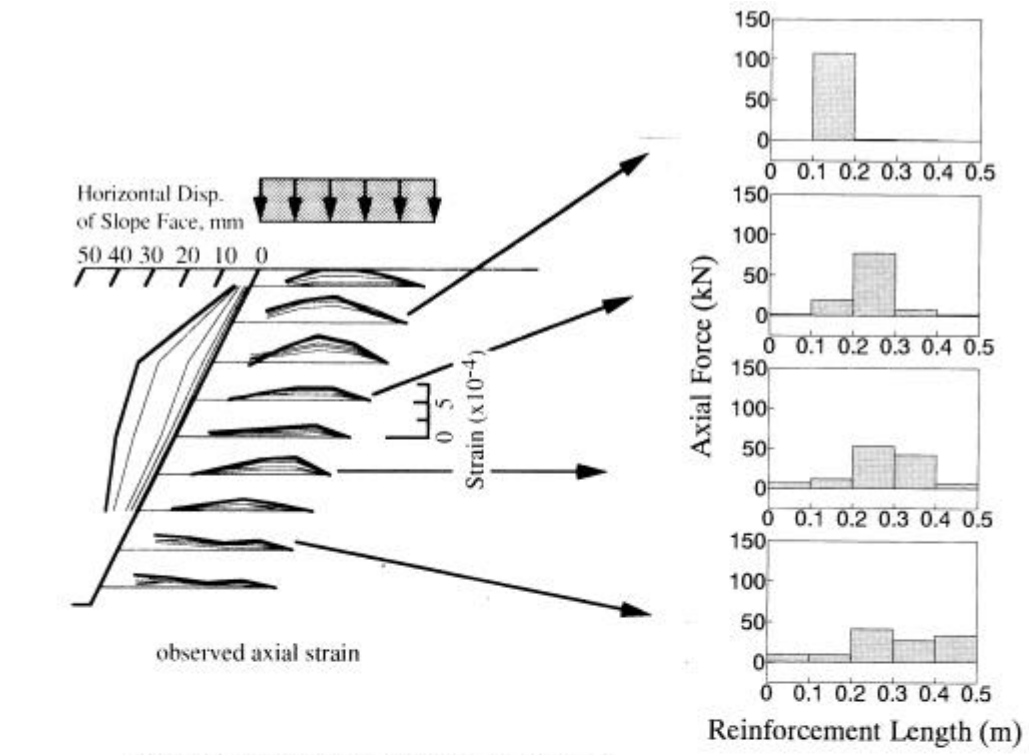

(a) Type B (Reinforced without Facing)

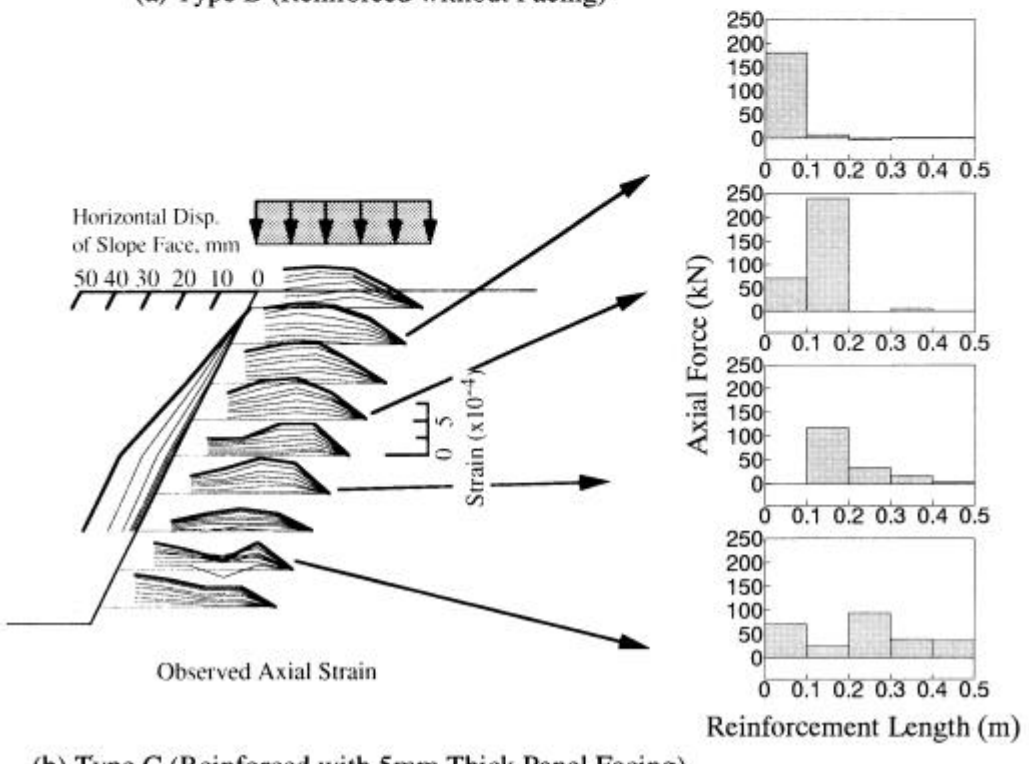

(b) Type C (Reinforced with 5mm Thick Panel Facing)

Figure 5.31 Comparing the computed axial force distribution pattern with the observed axial strain distribution along reinforcements in *mild slope models*.

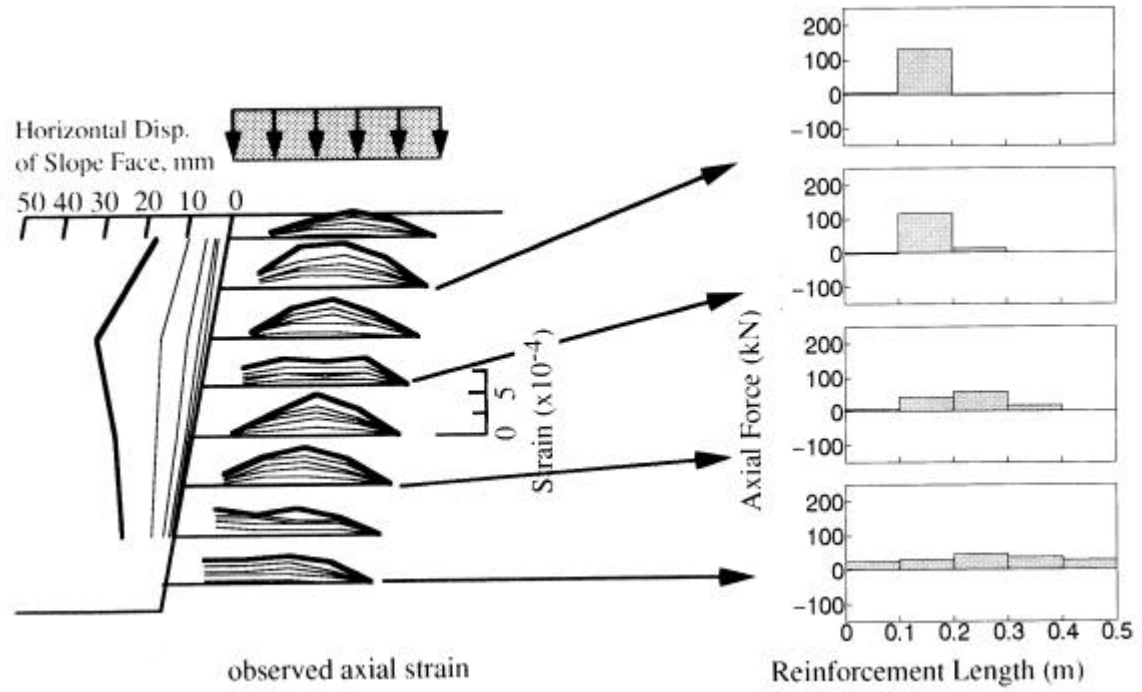

(a) Type F (Reinforced without Facing)

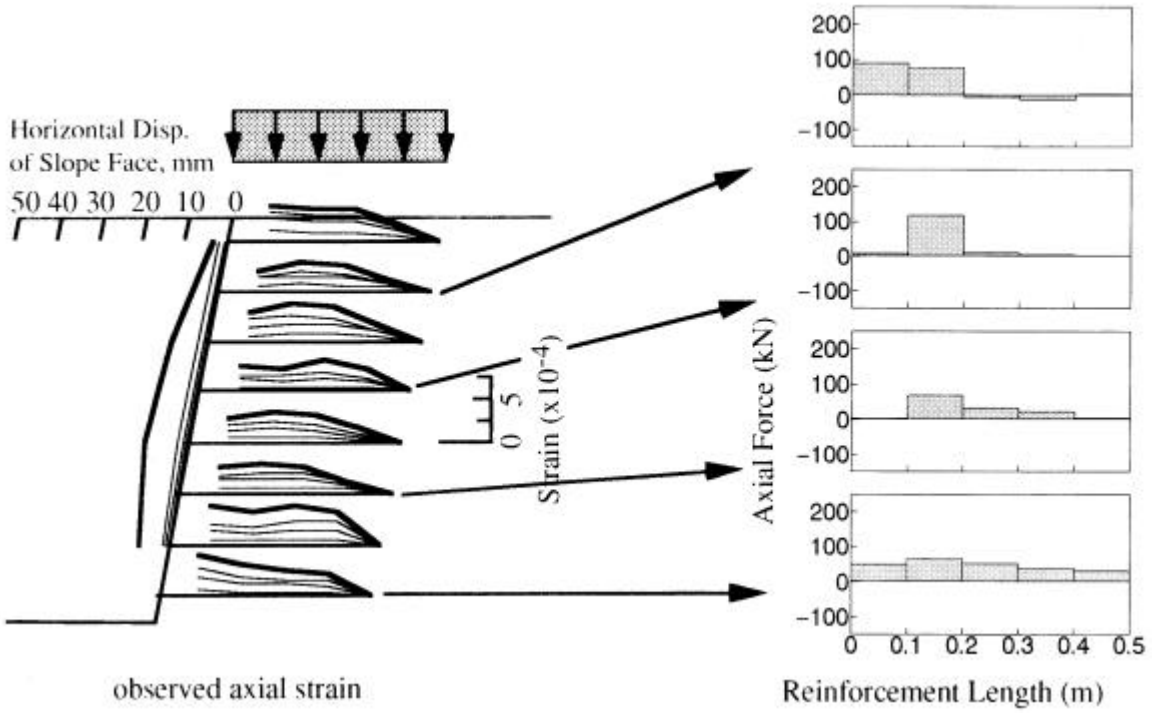

(b) Type G (Reinforced with 5mm Thick Panel Facing)

Figure 5.32 Comparing the computed axial force distribution pattern with the observed axial strain distribution along reinforcements in *steep slope models*.

5.5 SUMMARY AND CONCLUDING REMARKS

Series of the model tests on plain, reinforced and panel-faced slopes were explained in detail. Models were prepared under two types of slope face grading. Behavior of these models from initial loading to the ultimate failure was illustrated. Numerical simulations were carried out based on the linear elastic finite element method and rigid plastic finite element method where the newly introduced constraint conditions (in Chap. III) have been incorporated into these numerical methods. The following conclusions are drawn through the present study.

1. The model test results clearly show that there is a substantial change in the response of the soil to the applied stresses when the soil media is reinforced. Mode of the lateral and vertical displacement of the soil mass from the initial loading to the failure stage shows excellent improvement in response of the soil mass with respect to the applied external stresses. Model test results are well supported by the numerical simulations.
2. The first tangent line in the footing pressure-settlement curves and failure load reveals that the reinforced slope is more effective when facing panels are installed. The numerical analysis confirms such features.
3. Higher axial strain distributions in the reinforcements exhibits improved efficiency of the reinforcing bars when the facing panels are attached. This too is also supported by numerical analysis.

CHAPTER VI EXCAVATION OF CLAY GROUND

6.1 GENERAL

Foundation works may require a relatively deep excavation with vertical sides. The sides may be supported by sheet pile walls or diaphragm walls, which can be braced by means of horizontal or inclined struts. The ground movements which will occur around the excavation, e.g. settlement of the ground surface adjacent to the excavation, lateral movement of the vertical supports, heave of the base of the excavation must be considered in the design, especially if the excavation is close to the existing structures. To a large extent, the aforesaid movements are interdependent because they are the result of strains in the soil mass due to the stress relief when excavation takes place.

The magnitude and the distribution of the aforesaid ground movements depend on the type of soil, the dimensions of the excavation and details of the construction, and they depend to a large extent on the mode of deformation of the supporting systems. The magnitude of the ground movements can be minimized by installing rigid struts or rigid vertical piles (e.g. sheet piles, 'I' shaped steel sections, etc.). Recent developments on *in-situ reinforcing techniques* (e.g., soil nailing) have shown a significant success. In this study, the effect of such supporting systems, horizontal or vertical reinforcing members, on the soil mass is investigated employing the methodology presented in the Chapter III.

The behavior of the soil mass is clearly shown to be directly dependent on the mode of resistance offered by these reinforcing members. This is demonstrated through the computed axial force and the bending moment distributions in the reinforcing members. Here, the vertical reinforcements are distinguished either as axial members, e.g. concrete wall or as a bending member (e.g. 'I' shaped steel sections). A new concept on the positioning of such reinforcing members is also newly proposed.

6.2 OUTLINE OF THE EXCAVATION PROBLEM

An excavation problem of a homogeneous purely cohesive clay ground, as shown in Fig. 6.1, is considered in this chapter. Material properties (strength parameters) for the clay at the limit state are chosen in such a way that the computed safety factor of the excavated homogeneous soil mass (without having any reinforcing materials) comes out to be unit (Fs=1.00). The soil constants are c_u=27.6 kPa, γ_t=16.3 kN/m^3. Analyses in the next sections will be carried out under gravity loading, i.e. due to self-weight of the soil, and no additional surcharge loading is applied. Thus the problem represents a typical excavation on an open ground without any surcharge loading.

Two types of reinforcing materials are considered in the present excavation problem. Firstly, the reinforcement is inserted horizontally (e.g. nailing). Latter, the reinforcing materials like 'I' shaped steel-sections or sheet piles, which exhibit flexural rigidity are vertically embedded into the soil mass. Such a rigid flexural material can easily be driven vertically into the clay ground before starting the excavation or the construction work. In both the cases, the behavior of the reinforced soil is investigated for various lengths and positions of a single reinforcement as well as multiple reinforcements.

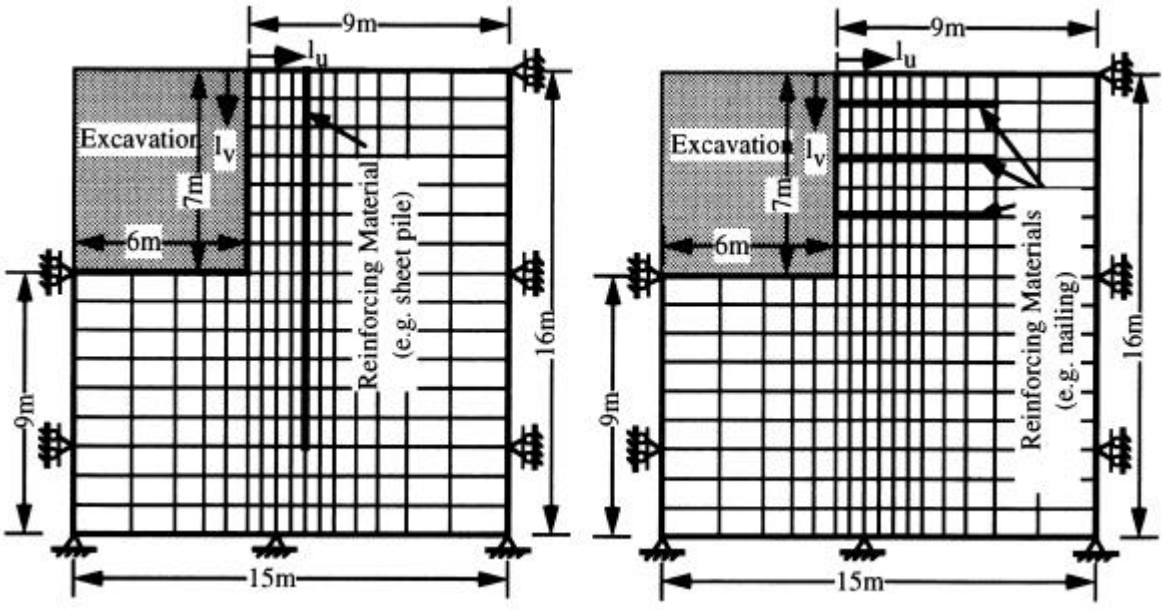

Figure 6.1 Schematic diagram showing details of the excavation problem and the finite element discretization with typical boundary conditions.

The RPFEM is employed in the analysis of the excavation problems outlined in this section. Figure 6.1 illustrates the finite element discretization of the analysis area with the boundary conditions. Because of the symmetry, only the right half is discretized. The outer boundaries around the excavation are located far enough so that they have negligible effect on the soil mass to be analyzed. Thus the boundaries were kept enough distance away from the farthest end of the longest reinforcements. The left (due to symmetry) and the right vertical boundaries were confined laterally and the bottom horizontal boundary was confined both laterally as well as vertically.

The results of the numerical analyses are presented in the subsequent sections. Basically, the computed factor of safety, the velocity field of the soil mass and the axial force distributions along the reinforcements are illustrated. The bending moment is also presented in the case of vertical reinforcements.

6.3 ANALYSIS OF PLAIN EXCAVATION

At the outset, the factor of safety and the nodal velocities were computed for the plain excavation without having any reinforcing members or external supports, e.g. scaffoldings or struts. As mentioned before, the strength parameters of soil were chosen to get the factor of safety, Fs=1.0, for the unreinforced as well as the unsupported excavation. Figure 6.2 shows the velocity field at the limit state of the soil mass. It clearly shows that a slip type of failure mode is distinct. The failure slip surface passes through the toe. The heaving effect is not so significant on the trench floor.

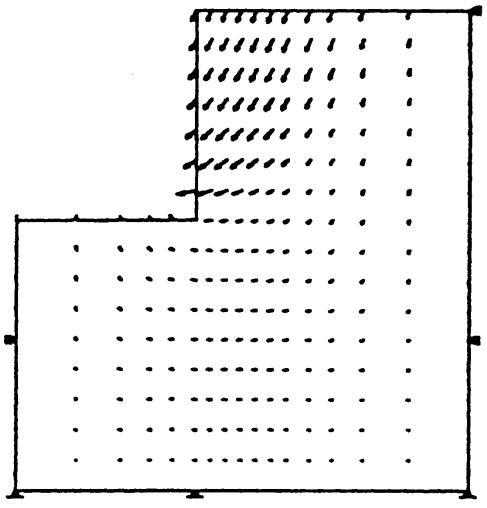

Figure 6.2 Effect of excavation on velocity field of the unreinforced soil mass at limit state.

6.4 EXAMPLE 1: HORIZONTAL REINFORCEMENT

Two excavation problems are dealt with the reinforcement of the soil by horizontal reinforcing material (e.g. nailing). Firstly the soil is reinforced with horizontal reinforcement alone, that is, without any facing material on the vertical sides. Secondly, the vertical cut face is covered by a set of rigid facing panels attached to several reinforcements. Both the cases are illustrated in Fig. 6.3. In both the types, the numbers of reinforcements are three and six, respectively, representing the coarse and the close spacing.

The computed factors of safety corresponding to all these individual examples are tabulated in Table.6.1. Obviously, the densely reinforced soil with rigid panel facing, produced the highest safety factor. The densely reinforced soil without facing material exhibits higher safety factor compared to the soil with panel facing attached to the coarse spaced reinforcements. It reveals that the spacing of reinforcements is also important in addition to the existence of a facing material.

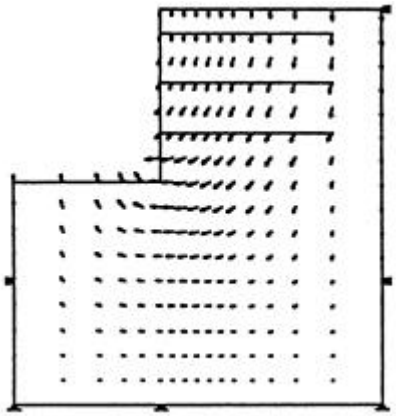

(a) Three reinforcements without facing

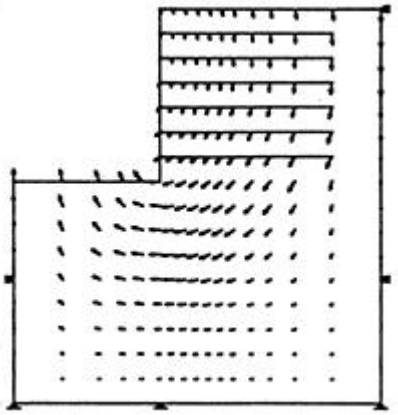

(b) Six reinforcements without facing

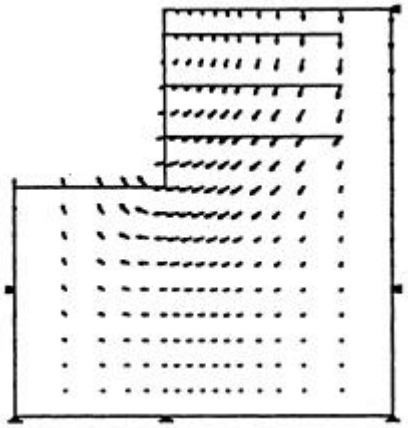

(c) Three reinforcements with facing

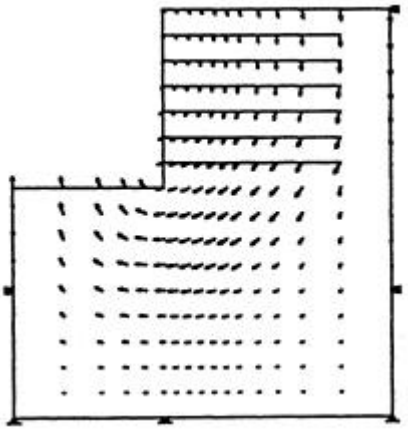

(d) Six reinforcements with facing

Figure 6.3 Effect of horizontal reinforcements on the velocity field of the soil mass.

Table 6.1 Computed safety factor for the horizontal reinforcement cases

Types	Factor of Safety, F_S
Unreinforced case	1.000
Three Reinforcements without facing	1.126
Three Reinforcements connected to facing	1.133
Six Reinforcements without facing	1.203
Six Reinforcements connected to facing	1.207

6.5 EXAMPLE 2: VERTICAL REINFORCING MEMBERS

Rigid reinforcements, e.g. 'I' shaped steel-sections, sheet piles; have been embedded vertically to resist the lateral earth pressure developed due to the excavation of a clay ground. These reinforcements are embedded into the soil before commencing the ground excavation work. The horizontal reinforcements, in the previous examples, resist the lateral earth pressure by developing the tensile force in reinforcements because of the soil-reinforcement interactions; likewise, the rigid vertical reinforcements resist the earth pressure through the bending resistance developed along the length. Such vertical members are, therefore, considered flexural members (bending elements). These rigid flexural sheet piles are modeled by imposing the "*no-length change*" along with the "*no-bending*" conditions. These constraint conditions are incorporated into the RPFEM and all the numerical examples presented in this section are also based on the RPFEM.

In this example, firstly, the effect of the reinforcement length on the soil mass at the limit state is investigated; subsequently effect of the reinforcement position is studied. At the end of this section, the effect of multiple reinforcements is compared with these former two cases.

6.5.1 Effect of Reinforcement Length

Firstly, a single reinforcement is vertically embedded into the soil mass at different lateral positions. The computed factor of safety for the excavation problems with a single reinforcement positioned at l_u=1.5m (away from the front face) is presented in Fig.6.4. The reinforcement up to 3m height does not exhibit any noticeable changes in the factor of safety of the soil mass. As the reinforcement height is further increased beyond 3m, the safety factor linearly increases with respect to length increment as shown in Fig.6.4. The computations are made for the reinforcement length of maximum 13m. Additional computation of the factor of safety is carried out for the multiple reinforcement cases. Figure 6.4 reveals that the soil reinforced with multiple reinforcements resembles similarity with the single reinforcement case. The rate of increase of factor of safety with increasing reinforcement height in multiple (two or three) reinforcement case

is higher than the former example. Even then, the absolute increase in the factor of safety, for all the examples explained so far, is convincing because the maximum increment is about 20% higher than the unreinforced excavation problem.

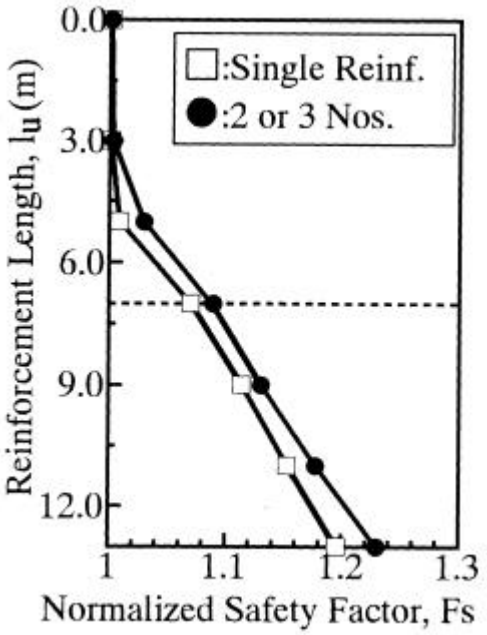

Figure 6.4 Variation in the factor of safety of the soil mass with respect to the changes in the reinforcement length.

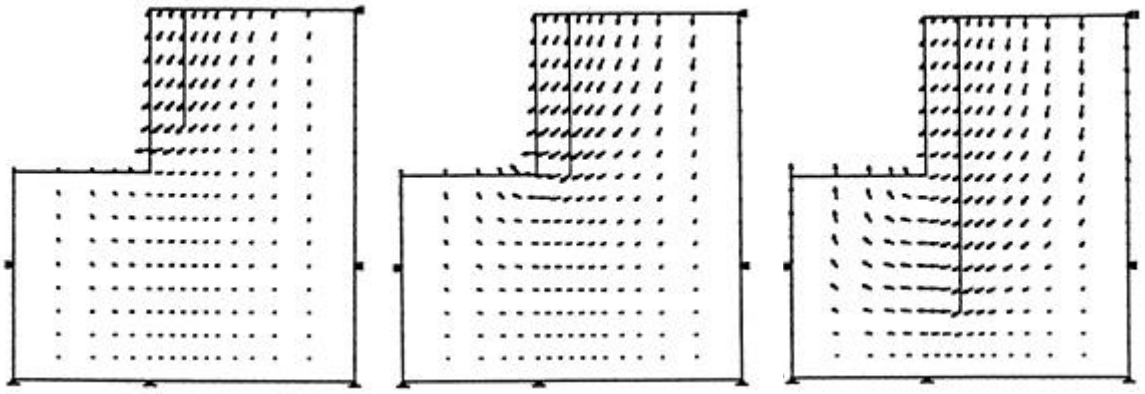

(a) l_V=5 m (b) Reinforcement Length, l_V=7 m (c) l_V=13 m

Figure 6.5 Effect of reinforcement length on the plastic flow of the soil mass at limit state.

The computed nodal velocity vectors corresponding to single reinforcement with lengths l_V=5m, 7m and 13m cases are presented in Fig.6.5. If the lower end of the reinforcements is above the toe, then the slip (passing through the toe) type failure mode is distinct. The failure mode is gradually changed to heaving of the trench floor as the reinforcement extends below the toe. It is clear through the velocity field presented in Fig. 6.5. For short reinforcements, the velocity vectors on the trench floor are not significantly large and are relatively large on the cut above toe. For very long reinforcement, relative magnitude of the velocity vectors is reversed, i.e. velocities on the vertical face get smaller, and velocities on the trench floor become vertical and have large magnitude. This demonstrate that a long rigid reinforcement is effective on resisting the lateral earth pressure developed due to excavation of the ground, such resistance directly comes from the flexural (bending) rigidity of the vertical piles.

Axial tensile force distributions in the reinforcements plotted in Fig. 6.6(a), correspond to various reinforcement lengths: 3m, 5m, 7m..... and 13m. When the reinforcements are shorter (=5m) than the depth of excavation, then the axial force distribution along reinforcements have peaks close to lower end of the reinforcements. The length of reinforcement when extended downward beyond the toe level, the positions of such peaks approach close to the toe level. The magnitude of the axial forces along reinforcements also gradually increases as the reinforcement length is extended.

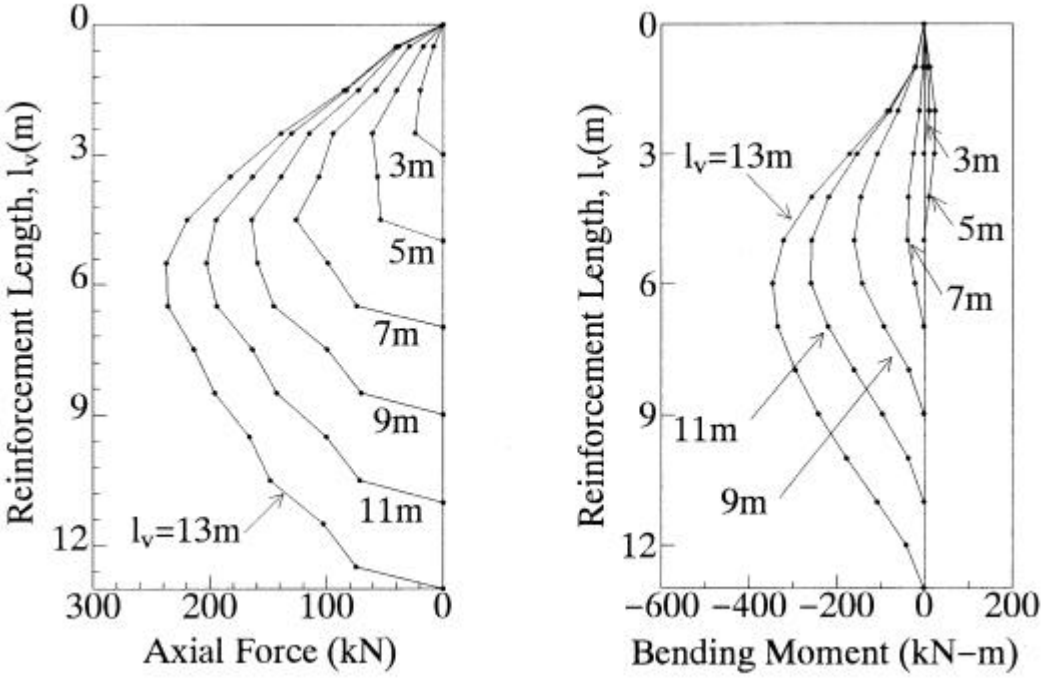

(a) Axial Force Distributions (b) Bending moment distributions

Figure 6.6 Effect of reinforcement length on the axial force and bending moment distributions along the reinforcement length.

Likewise, the bending moment on the reinforcement also increases as the reinforcement length increases (Fig. 6.6b). The shorter reinforcements (=5m) show bending with convex (tension side) on the trench side, and the longer reinforcements (=7m) exhibit bending towards the trench that is reverse to the former case. The reason for the short reinforcements (=5m) not showing any effect on the factor of safety (Fig.6.4) may be attributed to such (reverse) bending characteristics of the reinforcements. Soil exhibits some sort of clamping effect on reinforcements extending below toe, thus, the reinforcements act like a simple beam with yielding support. This bears similarity with the conventional analysis.

6.5.2 Effect of Multiple Reinforcements

Multiple reinforcements are embedded into the soil. Firstly, two reinforcements are embedded at l_u=0.5m and 2.5 m, then, three reinforcements at l_u=0.5m, 1.5 m and 2.5 m are embedded. The effect of length of multiple reinforcements (2 and 3 numbers) on the safety factor of soil mass have been already illustrated in the previous subsection (i.e. Fig.6.4). The examples described in this section have only one set of reinforcement length, l_V=13m. These two examples are compared with the excavation problem having single 13 m long reinforcement discussed in the preceding sub-section (Fig. 6.7).

The safety factor, the nodal velocities, the axial force and the bending moments are computed. Computed safety factors are presented in Table 6.2. The safety factor variation between two reinforcements case and single reinforcement case is not as significant as compared with the difference between the single reinforcement case and the unreinforced excavation. Likewise, the factor of safety in the three-reinforcement case remains almost equal to the two-reinforcement case.

The velocity fields (*see* Figs. 6.8a & 6.9a) in these aforesaid multiple reinforcements (two or three numbers) cases do not exhibit any significant differences from the single reinforcement case (Fig. 6.7a). The axial force distribution observed in the single reinforcement example, placed at l_u=0.5 m is almost similar to the reinforcement placed at the same position (l_u=0.5m) in the two or three reinforcement cases (Fig. 6.8~6.9).

The bending moment results shown in Figs.6.8 (b~c) are quite interesting. In the multiple reinforcement cases, the farthest reinforcement exhibits the highest bending moment compared to the reinforcements embedded close to the excavation. The bending moment in reinforcements embedded close to the face is almost nil, thus the total bending moment is resisted by the outer reinforcement placed at l_u=2.5m away from the front face in the two reinforcement case. The pattern of bending moment distribution in the three-reinforcement case is also similar to the two reinforcements case. The two reinforcements close to the face (l_u=0.5m and 1.5m) do not exhibit any significant resistance to the bending moment.

Table 6.2 Computed safety factor for the vertical reinforcement cases

Types	**Factor of Safety, F_S**
Unreinforced case	1.000
Single Reinforcements at l_u=0.5 m	1.126
Two Reinforcements at l_u=0.5 and 2.5m	1.133
Three Reinforcements at l_u=0.5, 1.5 & 2.5m	1.207

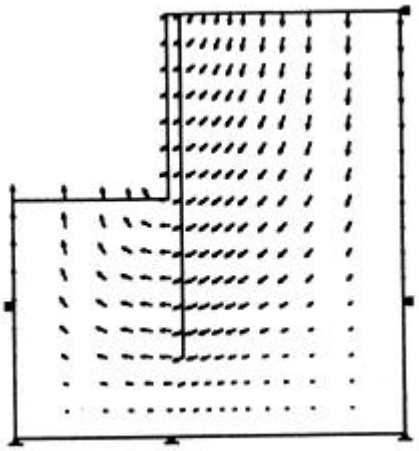

(a) Velocity Field

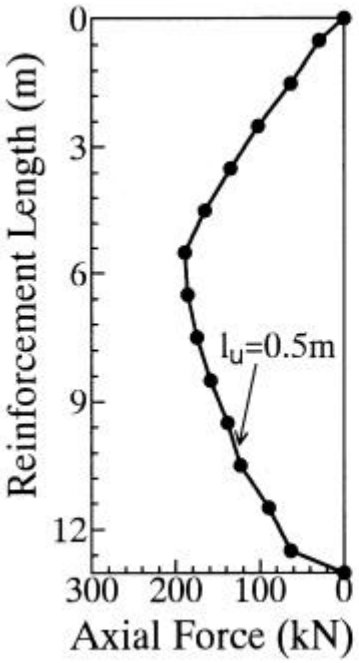

(b) Axial Force Distributions.

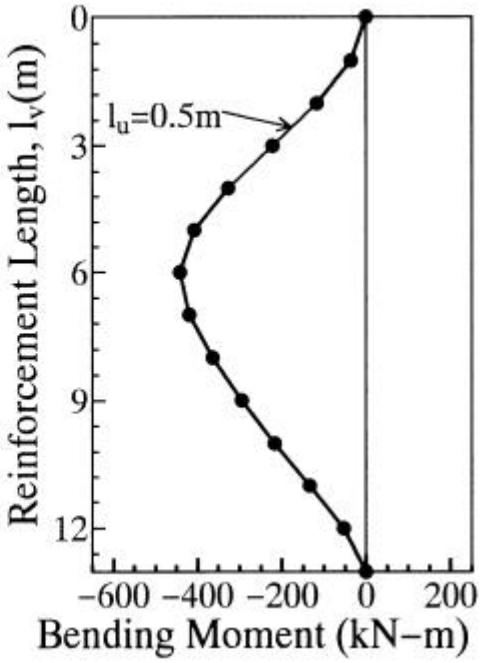

(c) Bending Moment Distributions.

Figure 6.7 Velocity field of the soil mass, axial force and bending moment distributions along a reinforcement embedded at l_u=0.5m.

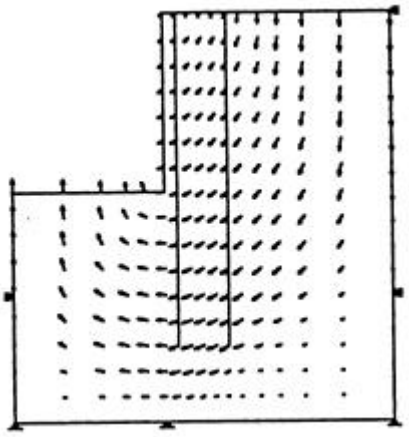

(a) Velocity Field

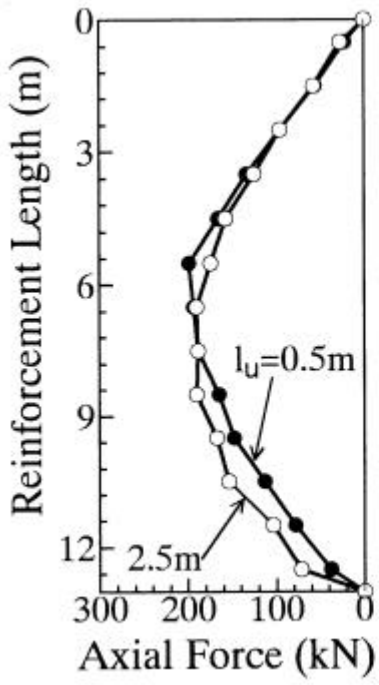

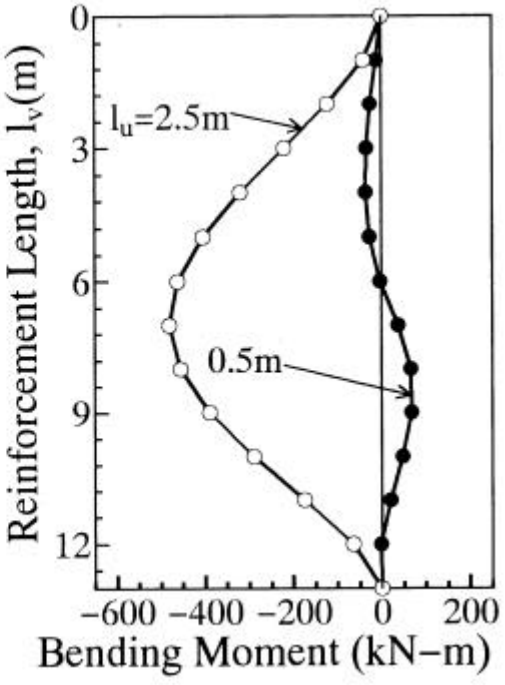

(b) Axial Force Distributions.

(c) Bending Moment Distributions.

Figure 6.8 Multiple reinforcements induced effects on velocity field of the soil mass, axial force and bending moment distributions along reinforcements. (*two-reinforcements case*)

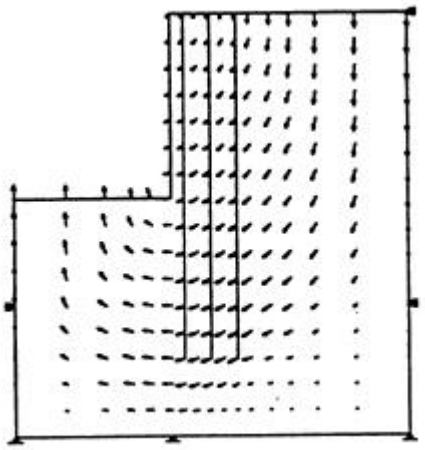

(a) Velocity Field

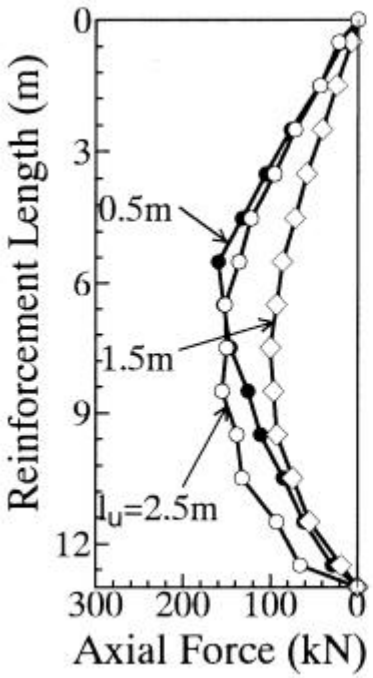

(b) Axial Force Distributions.

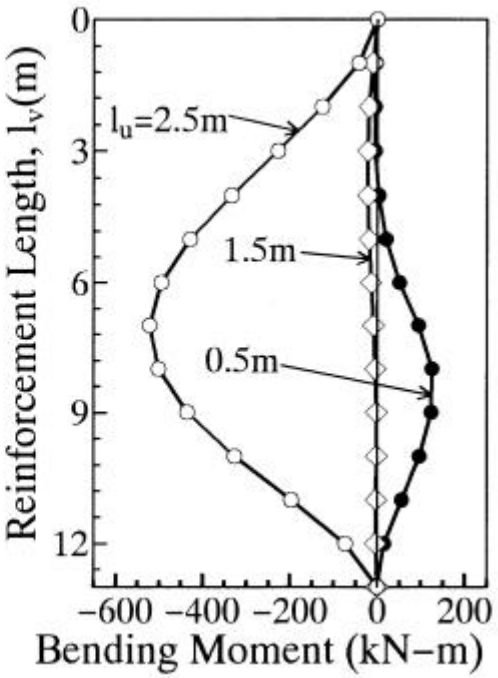

(c) Bending Moment Distributions.

Figure 6.9 Multiple reinforcements induced effects on velocity field of the soil mass, axial force and bending moment distributions along reinforcements. (*three-reinforcements case*)

6.5.3 Effect of Lateral Position of Reinforcement

In order to observe the effect of lateral position of the reinforcement, the position of a single 13m long vertical reinforcement is moved in the lateral direction. At first its position is on the edge (vertical face of the excavation), l_u=0.0 m in Fig. 6.1a, and the farthest position is 4.5 m away from the vertical face. Thus there were altogether nine positions, i.e. l_u= 0.0, 0.5m, 1.0m, 1.5m, 2.0m, 2.5m, 3.0m, 3.75m and 4.5m (*ref*. Fig. 6.1a)

The computed factor of safety for all these positions is presented in Fig. 6.10. The factor of safety for the reinforcement positions upto l_u= 3m (i.e., l_u=0~3m) remained almost constant. Moving the reinforcement position further beyond 3m (away from the face) results gradual decrease in the factor of safety of the soil mass, which finally behaves like an unreinforced plain excavation problem.

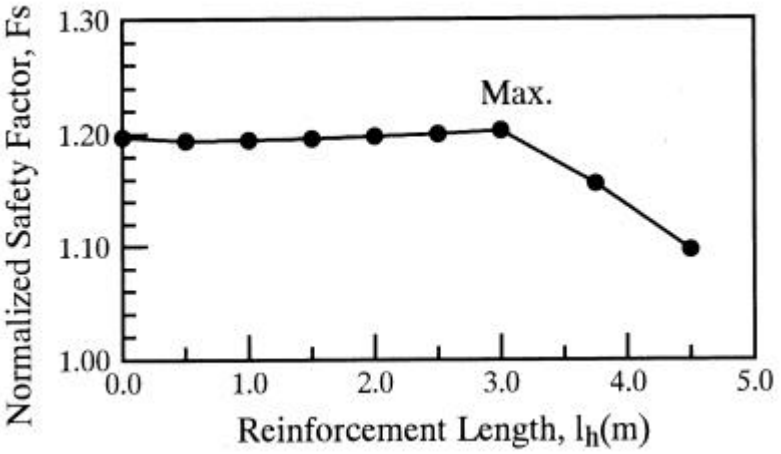

Figure 6.10 Variation in the safety factor with respect to different lateral positions, l_u (m) of reinforcement.

The computed nodal velocity vectors corresponding to l_u=0.5, 3.0m and 4.5 m are presented in Fig. 6.11. Reinforcements embedded close to the excavation, restrains velocity vectors around the face. Moving the reinforcement position away from the cut face extends the failure region. Likewise, the velocities on the trench floor get smaller. Further movement of the reinforcement virtually tends to behave like an unreinforced soil where the plastic flow of the soil mass at the limit state is significant only above the toe, i.e., comparing the Fig. 6.2 with 6.11(c).

The axial force and the bending moment distributions along the reinforcements are plotted in Fig. 6.12. Similarly, the peak values in the distributions corresponding to each reinforcement positions are presented in Fig. 6.13. These figures reveals that the axial force in the reinforcement gradually increases when the reinforcement position is moved away from the excavation face while the bending moment distribution along the reinforcement increases in reverse order, that is, the bending moment distributions corresponding to the reinforcement positions close to the slope face have higher magnitudes. This latter feature may be attributed to the lateral earth pressure

causing the bending. The lateral earth pressure on the reinforcements positioned close to the outer boundary approaches the earth pressure at rest condition (K_o). In such cases, net lateral earth pressure acting on either side of reinforcements is negligible.

Overall conclusion is that the reinforcement which offer high flexural resistance should be positioned as close to the excavation face as possible, and the reinforcements which do not resist bending moment but offer high resistance to the axial force should be placed little away from the excavation face (nearly at the point intersected by a line inclined 60^o to horizontal and passing through the toe.)

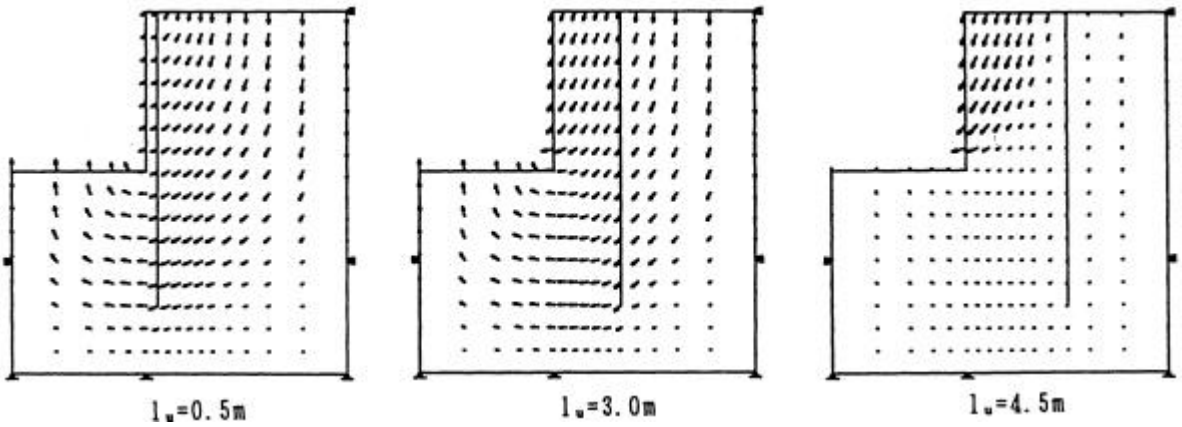

Figure 6.11 Effect of lateral positioning of reinforcement on the plastic flow of soil mass.

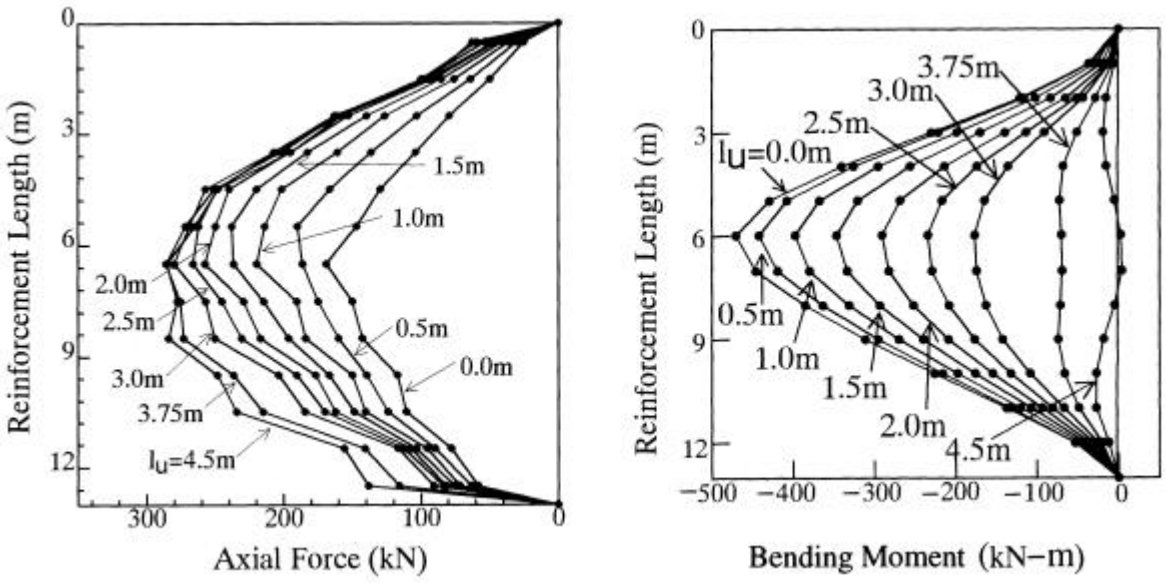

(a) Axial Force Distributions. (b) Bending Moment Distributions.

Figure 6.12 Effect of the lateral position of a vertical reinforcement on the axial force and bending moment distributions along its length.

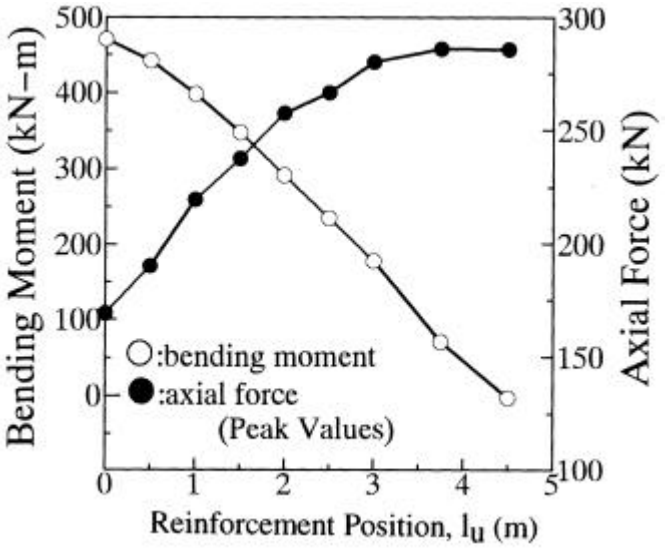

Figure 6.13 Variation in the peak values in the axial force and bending moment distributions with respect to different lateral positions, l_u (m) of the reinforcements.

6.7 SUMMARY AND CONCLUDING REMARKS.

The following conclusions are drawn through the present study.

1) Unreinforced plain excavation problem at the limit state exhibits slip failure surface passing through the bottom of the excavation.
2) Reinforcing the excavation by horizontal reinforcements (e.g. nailing) increases the safety factor of the soil mass. Reinforcement spacing is important in improving the overall safety factor of the soil mass while it provides additional safety against local failure of soil close to the excavation face.
3) Performance of the vertical reinforcements depends on the length and the position of the reinforcements. The reinforcements should be longer than the depth of excavation and very long reinforcements restrain the plastic flow of soil (at limit state) around the cut face, provided the reinforcements are close to the vertical cut. The reinforcements close to the face resists the lateral earth pressure due to the bending resistance and if the position is moved away from the face then the reinforcements exhibit high axial force while decreasing the bending effect. Thus, the reinforcements placed close to face must offer high flexural resistance and the reinforcements far away from face should offer high resistance to axial force, but the flexural resistance may not be so essential.
4) The failure mode of the soil is heaving when long reinforcements are embedded close to the excavation face, and moving the reinforcements away from face exhibits slip failure mode on the soil mass above the toe just like in the case of the unreinforced plain excavation problems.

CHAPTER VII CONCLUSIONS

7.1 CONCLUSIONS

The existing methods for the analysis and the design of reinforced soil structures show a wide spectrum. Realizing the need of a unique, simple and a realistic tool for the analysis and design of simple to complex reinforced soil structures, a method which presents a new concept of computation of bearing capacity/safety factor, distribution of axial and shear (/bending) forces as well as velocity vectors and stress distribution in reinforced soil structures, is presented and is demonstrated through some typical soil engineering problems and a set of prototype model test results.

The detailed conclusions presented below are drawn through the present study in addition to the concluding remarks made under the individual chapters.

1. The mechanism of the reinforcement and the facing can be modeled by introducing the two new linear constraint conditions, "*no-length change*" and "*no-bending*", in the energy functions. Lagrange multipliers corresponding to these constraint conditions represent the axial force and the shear force (/bending moment) in the reinforcing material per unit length, respectively.
2. The improvement on the safety factor is quite high in the frictional soil (c-ϕ) compared to the purely cohesive clay.
3. The reinforcement acts like a soil anchor in the frictional (c-ϕ) soil due to significantly high stress concentrations and can be explained through the velocity and the axial force distributions. The assumption of same axial force distribution pattern irrespective of the fill

material (clay or sandy) in the conventional method of analysis is not acceptable (at-least theoretically) and could be the main reason behind the conservatism in these design and analysis methods. The reinforcement force depends on the mean confining pressure, therefore, the reinforcement force should be considered as an internal stress developed due to the soil-reinforcement interaction.

4. The effect of the rigidity of a facing material can be explained by the bending moment developed in the facing.

5. The model test results clearly show that there is a substantial change in the response of the soil to the applied stresses when the soil media is reinforced. Mode of the lateral and the vertical displacement of the soil mass from the initial loading to the failure stage are significantly improved by the reinforcements.

   The effectiveness of the soil reinforcement (with and without facing) can be explained through the first tangent line in the footing pressure-settlement relationship and the failure load.

6. Through the numerical investigations on the behavior of a clay excavation problem, a new concept on the positioning of vertical reinforcements has been recommended depending on the reinforcement types. The reinforcements exhibiting high resistance to the axial force should be positioned away while the reinforcements exhibiting high bending resistance be positioned close to the excavation.

Overall, the proposed methodology exhibits promising features and wide applicability for the analysis and design of complex reinforced soil structures. It provides enough confidence for the practicing engineers so that this methodology may be adopted in the practice for the analysis and design of the real reinforced soil structures.

REFERENCES

American Society of Civil Engineer(1978): *Symp. on Earth Reinforcement*, April 27, 1978, USA, pp.900.

Asaoka, A. and T. Kodaka(1992): Seepage Failure Experiments and their Analyses of Loose and Medium Dense Sands, *Soils and Foundations*, Vol. 32(3), p. 117-129.

Asaoka, A. and T. Kodaka(1993); "Soil Profile Construction and Mesh Generation for the Rigid Plastic Finite Element Computation of Clays", *Proceedings of the 6th International Conference on Constitutive Modeling of Soils*, UK, Oct., 1992. Eds. Pande et al.

Asaoka, A., S. Ohtsuka and M. Matsuo(1990): Coupling Analysis of Limiting Equilibrium State for Normally Consolidated and Lightly Overconsolidated Soils, *Soils and Foundations*, Vol. 30(3), p. 109-123.

Asaoka, A., T. Kodaka and G. Pokharel (1994): Stability Analysis of Reinforced Soil Structures using Rigid Plastic Finite Element Method, *Soils and Foundations*, Vol. 34(1), p. 107-118.

Asaoka, A., T. Kodaka and G. Pokharel (1994): "Numerical Analyses and Model Tests of Reinforced Soil at Limit Equilibrium State", *Proceedings of the Symposium on Soil Mechanics and Foundation Engineering*, Aug., 1993. JSSMFE Chubu Branch. pp. 135-142.

Asaoka, A., T. Kodaka and G. Pokharel (1994); " Rigid Plastic Finite Element Computation of the Stability of Reinforced Soil", *Proceedings of the 8th International Conference on Computer Methods in Geomechanics*, USA, May, 1994 Eds. Siriwardane et al., pp.1319-1324.

Asaoka, A., T. Kodaka and G. Pokharel (1994); "Simplified Method of Solving Reinforced Soil System", *Proceedings of the Asian Regional Conference on Soil Mechanics and Foundation Engineering*, China, Sept., 1995 (in press)

Asaoka, A. and S. Ohtsuka (1987): Bearing Capacity Analysis of a Normally Consolidated Clay Foundation, *Soils and Foundations*, Vol. 27(3), p. 58-70.

Asaoka, A., S. Ohtsuka and M. Matsuo (1990): Coupling Analysis of Limiting Equilibrium State for Normally Consolidated and Lightly Overconsolidated Soils, *Soils and Foundations*, Vol. 30(3), p. 109-123.

Atkinson, J.H. and P.L. Bransby(1978): *The Mechanics of Soils - An Introduction to Critical State Soil Mechanics*, McGraw Hill, London.

Basset, R.H. and H.C. Last(1978): Reinforced Earth below Footings and Embankments. *ASCE Symposium on Earth Reinforcement*, pp. 222-231, Pittsburgh, April 1978.

Bolton, M.D. (1989): Reinforced Soil Laboratory Testing and Modeling. Performance of Reinforced Soil Structures, *Proc. Intl. Reinforced Soil Conference*, Editors McGown et al., 1989, Thomas Telford.

Bolton, M.D. and P.L.R. Pang (1982): Collapse Limits of Reinforced Earth Walls, *Geotechnique*, Vol. 32(4), pp.349-367.

Bonaparte, R. and G.R. Schmertmann (1987): Reinforcement extensibility in Reinforced Soil Wall Design, *UREHHCLQJVRI WKH1 $72 $ GYDQFH5HVHDUFK: RUNVKRS RQWKH 'Application of Polymeric Reinforcement in Soil Retaining Structures*,' Kingston, Ontario, Canada June 8-12, 1987", Eds. Jarret and McGown, pp.365-407.

Bruce, D.A. and R.A. Jewell(1986): Soil Nailing Application and Practice- Part I, *Ground Engineering* , Vol. 19(11), pp. 10-15.

Bruce, D.A. and R.A. Jewell(1987): Soil Nailing Application and Practice- Part II, *Ground Engineering* , Vol. 20(1), pp. 21-33.

British Dept. of Transport(1978): Reinforced Earth Retaining Walls and Bridge Abutments fro Embankments, *Technical Memo* BE3/78.

Broms, B.B. (1988): Fabric Reinforced Retaining Walls, *Proc. of Intl. Geotechnical Symp. on Theory and Practice of Earth Reinforcing*, Is Kyushu, Japan, Balkema, pp. 3-31.

Chapius, R. (1972). Rapport de recherche de DEA. Institut de Mécanique de Grenoble (unpublished internal report).

Chen, W.F. and X.L. Liu (1989): Limit Analysis in Soil Mechanics, Elsevier.

Drucker, D.C. (1951): A More Fundamental Approach to Plastic Stress-strain relations, *Proc. 1st US. Nat. Congr. Appl. Mech*, p.487

Davis, E.H. and J. R. Booker(1973): The Effect of Increasing Strength with Depth on the Bearing Capacity of Clays, *Geotechnique*, 23(4),pp. 551-563.

Gens, A., I. Carol and E.E. Alonso(1989): An Interface Element Formulation for the Analysis of Soil-Reinforcement Interaction,*Computer and Geotechnics*, Vol. 7(2), pp.133-151.

Goodman, R.E., R.L. Taylor and T.L. Berkke (1968): A Model for the Mechanics of Jointed Rock, *J. Soil Mech. Found. Div*., ASCE, Vol. 94(3), pp. 637-659.

Gourc, J.P. (1993): Keynote Lecture: Geosynthetic in embankments, review of theory, *Proc. of the Intl. Symp. on Earth Reinforcement Practice*, Nov. 11-13, 1992 (Editors: Ochiai, H., S. Hayashi & J. Otani); A. A. Balkema, Vol. II, pp. 773-800.

Fannin, R.J. and S. Hermann (1990): Performance Data for a Propped Reinforced Soil Wall. *Canadian Geotechnical Journal*, Vol. 27(5), pp. 676-686.

Hada, M., Y. Taguchi and K. Kagawa (1988): Application of RBSM Analysis on Earth Reinforcement Method, *Proc. of Intl. Geotechnical Symp. on Theory and Practice of Earth Reinforcing*, Is Kyushu, Japan, Balkema, pp. 395-400.

Hausmann, M.R.(1976): Strength of Reinforced Soil, *Australian Road Research Board, Proceedings*, (8), 1-8, Session 13, 1976.

Ho, S.K. and R. K. Rowe. (1992): Finite Element Analysis of Geosynthetic Reinforced Soil Walls. *Gyosynthetic '93 Conference*, Vancouver, Canada..

Huang, C.C. and F. Tatsuoka(1994): Stability Analysis for Footings on Reinforced Sand Slopes, *Soils and Foundations*, Vol. 34(3), pp. 21-37.

Ingold, T.S. (1982): *Reinforced Earth*, Thomas Telford Ltd., London.

Jarret, P.M. and McGown(eds) (1988): The Application of Polymeric Reinforcement in Soil Retaining Structures, *Proceedings of the NATO advance Research Workshop on the* '*Application of Polymeric Reinforcement in Soil Retaining Structures*,' Kingston, Ontario, Canada June 8-12, 1987", Eds. Jarret and McGown, pp.637.

Jewell, R.A. (1992): Keynote Lecture: Links between the testing, modeling and design of reinforced soil, *Proc. of the Intl. Symp. on Earth Reinforcement Practice*, Nov. 11-13, 1992 (Editors: Ochiai, H., S. Hayashi & J. Otani); A. A. Balkema, Vol. II, pp. 755-772.

Jewell, R.A. (1988): Reinforced Soil Wall Analysis and Behavior, *Proceedings of the NATO advance Research Workshop on the 'Application of Polymeric Reinforcement in Soil Retaining Structures*,' Kingston, Ontario, Canada June 8-12, 1987", Eds. Jarret and McGown, pp.365-407.

Jones, C.J.F.P. (1994): Economic Construction of Reinforced Soil Structures, *Proc. of the Intl. Symp. on Recent Case Histories of Permanent Geosynthetic-Reinforced Soil Retaining Walls*, Tokyo, Nov. 6-7, 1992 (Editors: Tatsuoka, H. and Leshchinsky, D.); A. A. Balkema, pp. 103-106.

Juran, I. and F. Schlosser(1978): Theoretical Analysis of Failure in Reinforced Earth Structure, *Proc. of Symp. on Earth Reinforcement*, ASCE, 1978, pp.528-555.

Kalikan, V. and F. Xi (1992): Finite Element Analysis of Geosynthetically Reinforced Walls, *A Paramtetric Study. Rept. No. 92-5*, Civil Engineering Department, Univ. of Delaware, Newark, DE.

Kodaka,T., A. Asaoka and G. Pokharel (1994); "Analysis of Reinforced Soil Structures introducing Some Linear Constraint Conditions on Velocity and Deformation", *Proceedings of the International Conference on Structural and Geotechnical Engineering*, Hongkong, Nov. 1994. Eds. Lee et al.

Kodaka,T.(1993); Study on Bearing Capacity of Composite Ground based on Soil-Water Coupling Limiting Equilibrium Analysis, *Doctoral Thesis*, Nagoya University, Japan, March, 1993. pp.1-153.

Kodaka,T., A. Asaoka and G. Pokharel (1995); " Model Tests and Theoretical Analysis of Reinforced Soil Slopes with Facing Panels", *Soils and Foundations*, Vol. 35(1), pp..(in press).

Koiter, W.T. (1962): General Theorems for Elastic-Plastic Solids, *Progress in Solid Mechanics*, Edited by Sneddon, I.N. and R. Hill, 1962.

Leshchinsky, D.(1992): Keynote Lecture: Issues in geosynthetic-reinforced Soil, *Proc. of the Intl. Symp. on Earth Reinforcement Practice*, Nov. 11-13, 1992 (Editors: Ochiai, H., S. Hayashi & J. Otani); A. A. Balkema, Vol. II, pp. 871-897.

Madhav, M.R. and N.K. Pitchumani (1992): Settlement Reduction due to Extensible Reinforcement Strip, *Proc. of the Intl. Symp. on Earth Reinforcement Practice*, Nov. 11-13, 1992 (Editors: Ochiai, H., S. Hayashi & J. Otani); A. A. Balkema, Vol. I. pp. 631-636.

McGown, A., K.Z. Andrawes, M.M. Al-Hasani (1978): Effect of Inclusion Properties on the Behavior of Sand. *Geotechnique*, Vol. 28(3). pp. 327-346.

McGown, A., K.Z. Andrawes and K.C. Yeo(Eds.) (1990) *Proc. of the International Reinforced Soil Conference*, Sept. 10-12, 1990, Glasgow, Scotland. Thomas Telford Ltd.

Mitchell, J.K.(1981), Soil Improvement, *State-of-the-Art Report, Session 12, Tenth Int'l Conf. on SMFE*, Stockholm, Sweden, June 15-19, 1981.

Muramatsu, M, K. Nagura, T Sueoka, K. Suami and Kitamura(1992): Stability analysis for reinforced cut slopes with a rigid facing, *Proc. of the Intl. Symp. on Earth Reinforcement Practice*, Nov. 11-13, 1992 (Editors: Ochiai, H., S. Hayashi & J. Otani); A. A. Balkema, Vol. I. pp. 503-508.

Murata, O., M. Tateyama and F Tatsuoka(1992): Loading tests of geosynthetic reinforced soil retaining walls and their stability analyses, *Proc. of the Intl. Symp. on Earth Reinforcement Practice*, Nov. 11-13, 1992 (Editors: Ochiai, H., S. Hayashi & J. Otani); A. A. Balkema, Vol. I. pp. 385-390.

Nagao, A., Kitamura, T. and J. Mizutani(1988): Field Experiment on Reinforced Earth and its Evaluation using FEM analysis, *Proc. of Intl. Geotechnical Symp. on Theory and Practice of Earth Reinforcing*, IS Kyushu, Japan, Balkema, pp. 395-400.

Oka, F, A. Yashima, Iwasaki and J. Nagaya (1992): Numerical Analysis of the Behavior of Clay Foundation Beneath Reinforced Embankment, *Proc. of the Intl. Symp. on Earth Reinforcement Practice*, Nov. 11-13, 1992 (Editors: Ochiai, H., S. Hayashi & J. Otani); A. A. Balkema, Vol. I. pp. 665-670.

Otani, J., H. Ochiai and S. Hayashi (1992): Restraining effect of Geogrid Reinforced Soil in Finite Element Analysis, *Proc. of the Intl. Symp. on Earth Reinforcement Practice*, Nov. 11-13, 1992 (Editors: Ochiai, H., S. Hayashi & J. Otani); A. A. Balkema, Vol. I. pp. 147-150.

Ochiai, H., Hayashi S. and J. Otani(Eds.) (1992): Earth Reinforcement Practice, *Proc. of the Intl. Symp. on Earth Reinforcement Practice*, Nov. 11-13, 1992, A. A. Balkema, Vol. I & II.

Onodera, S, S Naemura, A. Nakane and S. Maruo(1992): A design method for steep reinforced embankment with geotextiles, *Proc. of the Intl. Symp. on Earth Reinforcement Practice*, Nov. 11-13, 1992 (Editors: Ochiai, H., S. Hayashi & J. Otani); A. A. Balkema, Vol. I. pp. 391-396.

Rimoldi, P. (1988): A Review of Rield Measurements of the Behavior of Geogrid Reinforced Slopes and Walls, *Proc. of Intl. Geotechnical Symp. on Theory and Practice of Earth Reinforcing*, Is Kyushu, Japan, Balkema, pp. 571-578.

Roscoe, K.H. and J.B. Burland(1968): Mechanical behavior of an Idealized 'wet' clay, in J. Heyman and F.A. Leckie (eds.), *Engineering plasticity* (Cambridge: Cambridge University Press), pp. 535-609.

Roscoe, K.H., A.N. Schofield and A. Thurairajah(1963): Yielding of Clays in States Wetter than Critical, *Geotechnique*. Vol. 13(1), p. 211-240.

Rowe, R.K. and S. K. Ho. (1992): Keynote Lecture: A review of the behavior of reinforced soil walls, *Proc. of the Intl. Symp. on Earth Reinforcement Practice*, Nov. 11-13, 1992 (Editors: Ochiai, H., S. Hayashi & J. Otani); A. A. Balkema, Vol. II, pp. 801-830.

Schlosser, F.(1990): Mechanically Stabilized Earth Retaining Structures in Europe, *Design and Performance of Earth Retaining Structures, Geotechnical Special Publication No. 25,* ASCE, Lambe and Hansen (eds.) pp. 347-378.

Schlosser, F. and P. Delage(1987): Reinforced Soil Retaining Structures and Polymeric Material, *Proceedings of the NATO advance Research Workshop on the 'Application of Polymeric Reinforcement in Soil Retaining Structures*,' Kingston, Ontario, Canada June 8-12, 1987", Eds. Jarret and McGown, pp.3-68.

Schlosser, F., H.M. Jacobsen, and I. Juran(1981): Soil Reinforcement. General Report. Speciality Session 5, *Proceedings of the 8th European Conference on Soil Mechanics and Foundation Engineering* (3), pp. 1159-1180, Helsinki .

Schlosser, F. and I. Juran (1979): Paramèteres de calcul des sols artificiellement améliorés: rapport général Séance 8., *Proceedings of the 8th European Conference on Soil Mechanics and Foundation Engineering*, pp. 1-29, Helsinki .

Schlosser, F. and N.T. Long (1972): Comport de la Terre Armée dans les Ouvragés de souténement, *Proceedings of the 5th European Conference on Soil Mechanics and Foundation Engineering*, Vol. 1, pp. 299-306, Madrid, 1972.

Sekiguchi, H. and H. Ohta (1977): Induced Anisotropy and Time Dependency in Clays, *Proc. 9th ICSMFE*, Speciality Session-9, Tokyo, pp. 475-484.

Smith, I.M. and P. Segrestin (1990): Inextensible Reinforcements versus externsible ties- FEM Comparative Analysis of Reinforced or Stabilized Earth Structures, *Proc. of the Intl. Symp. on Earth Reinforcement Practice*, Nov. 11-13, 1992 (Editors: Ochiai, H., S. Hayashi & J. Otani); A. A. Balkema, Vol. I pp.425-430.

Taga, N; S. Tayama, S. Uehara and Y. Doi (1992): Stability Nomograms for Reinforced Earth with Steel Bars against Shallow Sliding of Steep Slopes, *Proc. of the Intl. Symp. on Earth Reinforcement Practice*, Nov. 11-13, 1992 (Editors: Ochiai, H., S. Hayashi & J. Otani); A. A. Balkema, Vol. I & II. pp. 549-554.

Tamura, T., S. Kobayashi and T. Sumi(1984): Limit Analysis of Soil Structure by Rigid Plastic Finite Element Method, *Soils and Foundations*, Vol. 24(1), p. 34-42.

Tamura, T., S. Kobayashi and T. Sumi(1987): Rigid Plastic Finite Element Method for Frictional Material, *Soils and Foundations*, Vol. 27(3), p. 1-12.

Tatsuoka, F. (1992): Roles of Facing Rigidity in Soil Reinforcing, Theme Lecture for IS Kyushu, *Proc. of the Intl. Symp. on Earth Reinforcement Practice*, Nov. 11-13, 1992 (Editors: Ochiai, H., S. Hayashi & J. Otani); A. A. Balkema, Vol. I & II. pp. 831-870.

Vidal, H. (1966): La Térré arméé (un nouvéau matériau pour lvs travaux pblics). *Annalés de l'ITBTP*, n^{O} 223-224, Juillet-Aout .

Yako, M.A. and B.R. Christopher (1987): Polymerically Reinforced Retaining Walls and Slopes in North America, *Proceedings of the NATO advance Research Workshop on the 'Application of Polymeric Reinforcement in Soil Retaining Structures*,' Kingston, Ontario, Canada June 8-12, 1987", Eds. Jarret and McGown, pp.365-407.

Yang, Z. (1972): Strength and Deformation Characteristics of Reinforced Sand, *Ph.D. Thesis*, UCLA.

Yamanouchi, T., N. Miura and H. Ochiai(eds) (1988): *Proc. of the Intl. Geotechnical Symp. on Theory & Practice of Earth Reinforcement*, Nov. 1988, Kyushu, A.A. Balkema.

Zienkiewicz, O. and R.L. Taylor (1989): *The Finite Element Method, Basic Formulation and Linear Problems*, McGraw Hill, Vol. I, 4th Ed.